TU Delft

Delft University of Technology

Ice-induced vibrations of offshore wind turbines

An exploration of scaling, hybrid testing, and numerical simulations

Hammer, T.C.

DOI
10.4233/uuid:b3b5eb45-1581-44b6-975b-05a7ac74de8e

Publication date
2024

Document Version
Final published version

Citation (APA)
Hammer, T. C. (2024). *Ice-induced vibrations of offshore wind turbines: An exploration of scaling, hybrid testing, and numerical simulations* . [Dissertation (TU Delft), Delft University of Technology].
https://doi.org/10.4233/uuid:b3b5eb45-1581-44b6-975b-05a7ac74de8e

Important note
To cite this publication, please use the final published version (if applicable).
Please check the document version above.

Copyright
Other than for strictly personal use, it is not permitted to download, forward or distribute the text or part of it, without the consent of the author(s) and/or copyright holder(s), unless the work is under an open content license such as Creative Commons.

Takedown policy
Please contact us and provide details if you believe this document breaches copyrights.
We will remove access to the work immediately and investigate your claim.

This work is downloaded from Delft University of Technology.
For technical reasons the number of authors shown on this cover page is limited to a maximum of 10.

Ice-induced vibrations of offshore wind turbines

An exploration of scaling, hybrid testing, and numerical simulations

Ice-induced vibrations of offshore wind turbines

An exploration of scaling, hybrid testing, and numerical simulations

Dissertation

for the purpose of obtaining the degree of doctor
at Delft University of Technology
by the authority of the Rector Magnificus prof. dr. ir. T.H.J.J. van der Hagen,
Chair of the Board for Doctorates,
to be defended publicly on
Friday 22 November 2024 at 10:00 o'clock

by

Tim Christopher HAMMER

Master of Science in Water Management, Environmental and Coastal Engineering,
Leibniz University Hannover, Germany,
born in Flensburg, Germany.

This dissertation has been approved by the promotors.

Composition of the doctoral committee:

Rector Magnificus,	chairperson
Prof. dr. A.V. Metrikine,	Delft University of Technology, promotor
Dr. ir. H. Hendrikse,	Delft University of Technology, copromotor

Independent members:

Dr. T.S. Nord	Norwegian University of Science and Technology, Norway
Prof. dr. A. Bekker,	Stellenbosch University, South Africa
Dr. R.U.F. von Bock und Polach,	Hamburg University of Technology, Germany
Prof. dr. J. Tuhkuri,	Aalto University, Finland
Prof. dr. ir. J.W. van Wingerden,	Delft University of Technology, Netherlands

This work is co-financed by Siemens Gamesa Renewable Energy and by TKI-Energy by the 'Toeslag voor Topconsortia voor Kennis en Innovatie (TKI's)' of the Dutch Ministry of Economic Affairs and Climate Policy under grant reference TKITOE_WOZ_1906_TUD_SHIVER.









Keywords: dynamic ice-structure interaction, model ice, model testing, multi-modal vibration, hybrid testing, hardware-in-the-loop, scaling laws, dynamic ice loads, ice tank, ice crushing, model-scale, intermittent crushing, frequency lock-in

Printed by: Gildeprint - Enschede

Front & Back: Adobe Illustrator

Copyright © 2024 by T.C. Hammer

ISBN 978-94-6384-610-3

An electronic version of this dissertation is available at
https://repository.tudelft.nl/.

CONTENTS

Summary **9**

Preface **11**

1 Ice-induced vibrations of offshore structures **1**
1.1 Ice-induced vibration regimes . . . 3
1.2 Model ice and scaling of ice-induced vibrations . . . 5
1.3 Model-scale experiments of ice-induced vibrations . . . 8
1.4 Numerical simulation of ice-induced vibrations . . . 9
1.5 Ice-induced vibrations of offshore wind turbines . . . 10
1.6 Design of offshore wind turbines for dynamic ice loads . . . 11
1.7 Objective and scope . . . 12
1.8 Reading guide . . . 13

2 Scaling ice-induced vibrations by combining replica ice modeling and preservation of kinematics **17**
2.1 Motivation . . . 17
2.2 Introduction . . . 20
2.3 Methods . . . 21
2.3.1 Replica modeling . . . 21
2.3.2 Preservation of kinematics during dynamic ice-structure interaction 22
2.3.3 Scaling factors . . . 23
2.4 Model ice . . . 25
2.4.1 Crushing . . . 25
2.4.2 Ductile-to-brittle transition speed and velocity effect . . . 26
2.4.3 Standard scaling parameters . . . 27
2.5 Scaling effects . . . 28
2.5.1 Aspect ratio . . . 29
2.5.2 Shape . . . 30
2.6 Validation . . . 32
2.6.1 Molikpaq event . . . 33
2.6.2 Norströmsgrund (NSG) Lighthouse events . . . 34
2.7 Discussion . . . 37
2.7.1 Scaling verification . . . 37
2.7.2 Validation . . . 39
2.7.3 Data Reliability . . . 40
2.7.4 Application . . . 40
2.7.5 Limitations . . . 41
2.8 Conclusion . . . 41

3 Hardware-in-the-Loop experiments in model ice for analysis of ice-induced vibrations of offshore structures **45**
3.1 Introduction . . . 45
3.2 Method . . . 48
3.2.1 Hardware-in-the-Loop testing . . . 48
3.2.2 Hardware and numerics . . . 49
3.2.3 Numerical simulations . . . 50
3.3 Results . . . 53
3.3.1 Critical delay . . . 57
3.3.2 Mitigation of Instabilities . . . 60
3.4 Discussion . . . 61
3.4.1 Ice-structure coupling . . . 61
3.4.2 Applicability . . . 62
3.5 Conclusion . . . 63

4 Ice-induced vibrations of offshore wind turbines **67**
4.1 Introduction . . . 67
4.2 Methods . . . 68
4.2.1 Structural model and wind load . . . 68
4.2.2 Hardware-in-the-Loop system . . . 71
4.2.3 Scaling . . . 73
4.3 Results . . . 74
4.3.1 Constant Deceleration Tests . . . 74
4.3.2 Constant Ice Drift Speed Tests . . . 74
4.4 Discussion . . . 79
4.4.1 Generalization of Results . . . 81
4.4.2 Limitations . . . 81
4.5 Conclusion . . . 82

5 Effect of wind-ice misalignment on ice-induced vibrations **85**
5.1 Introduction . . . 85
5.2 Experimental campaign . . . 86
5.2.1 Misalignment angles . . . 86
5.3 Wind-ice misalignment . . . 87
5.4 Wind-induced structural motion . . . 91
5.4.1 Inline motion . . . 91
5.4.2 Crosswise motion . . . 92
5.5 Discussion . . . 99
5.5.1 Effects of wind-ice misalignment on the development of ice-induced vibrations . . . 99
5.5.2 Ice Deformation and Crushing at the Side of the Structure . . . 99
5.5.3 Generalization of Results . . . 100
5.5.4 Data Reliability . . . 100
5.5.5 Sensitivity of results to local changes in ice properties and equipment malfunction . . . 100
5.6 Conclusion . . . 103

6 Implications of ice-induced vibrations for the design of offshore wind turbines 107
6.1 Introduction . . . 107
6.2 Classification of ice-induced vibrations regimes of offshore wind turbines 108
6.3 Fully-coupled ice-structure interaction simulations . . . 111
6.3.1 Ice model . . . 111
6.3.2 Wind turbine model . . . 112
6.3.3 Simulation matrix . . . 113
6.3.4 Numerical ice-induced vibrations regimes . . . 114
6.3.5 Bending Moments along the Support Structure . . . 114
6.3.6 Qualitative ice model validation . . . 114
6.3.7 Conclusion . . . 115
6.4 Ice model coupling effects on ice-induced vibrations of an offshore wind turbine . . . 118
6.4.1 Comparison of local maximum bending moments in idling . . . 118
6.4.2 Comparison of beta-plots in idling . . . 119
6.4.3 Comparison of time series in idling . . . 121
6.4.4 Comparison of local maximum bending moments in operation . . . 122
6.4.5 Linearized structural model . . . 123
6.4.6 Discussion . . . 123
6.4.7 Conclusion . . . 125
6.5 Ice-induced vibrations of "XXL" turbines . . . 126
6.5.1 Method . . . 126
6.5.2 Experimental results . . . 127
6.5.3 Multi-modal interaction . . . 130
6.5.4 Discussion . . . 132
6.5.5 Limitations . . . 132
6.5.6 Conclusion . . . 133
6.6 Discussion . . . 133
6.7 Conclusion . . . 137

7 Discussion & Conclusion 139
7.1 Multi-modal (ice-structure) interaction . . . 140
7.2 Scaling of ice-induced vibrations . . . 142
7.2.1 Scaled time- and rate-dependent behavior of ice . . . 142
7.2.2 Scaled structural frequencies . . . 144
7.2.3 Scaling laws and the future of ice model testing . . . 146
7.3 Expected results of full-scale measurements . . . 147
7.4 Engineering confidence . . . 148
7.5 Conclusion . . . 148

Epilogue 151

Acknowledgements 153

A Appendix **157**
A.1 Numerical ice model 157
A.1.1 Modeling approach 157
A.1.2 Input parameters 158
A.1.3 Initial roughness and ice failure 160
A.1.4 Limitations and Discussion 160

B Appendix **161**
B.1 A scaling example of ice-induced vibrations 161

Bibliography **163**

Samenvatting **179**

List of Publications **181**

Curriculum Vitae **183**

SUMMARY

The worldwide demand for energy independence and renewable energy has led to plans for offshore wind farms in cold regions such as the Baltic Sea in Europe and the Bohai Sea in China. In such regions, the presence of floating sea ice poses a risk to installed offshore structures such as offshore wind turbines.

An offshore structure experiences significant ice-induced loads once the drift ice crushes against the vertical interface of that structure at the water level. Eventually, the structure starts to vibrate and to interact with the ice, influencing the ice crushing and ice loading processes. The ice-structure interaction and accompanying ice-induced vibrations have historically led to the (partial) failure of offshore structures.

There are no full-scale data to investigate ice-induced vibrations of offshore wind turbines yet. Furthermore, doubts exist if insights derived from ice-induced vibrations events of oil and gas platforms, lighthouses, or channel markers can be transferred to offshore wind turbines, as structural properties of the latter differ significantly in comparison to those of offshore structures installed in the past. For similar reason, namely a lack of full-scale data, numerical models for simulation of ice-induced vibrations of offshore wind turbines could not be validated yet. Also, insights derived from small-scale experiments investigating the general development of ice-induced vibrations are limited, as experiments in ice tank facilities resulted in ice failure modes and ice-induced vibrations that did not match real-world observations.

The objective of this thesis was to generate and analyze a benchmark model-scale data set of offshore wind turbines experiencing ice-induced vibrations.

To achieve this objective, a scaling method has been developed which allowed to investigate offshore wind turbines in model ice experiments. The method was based on the hypothesis that ice-induced vibrations are mainly based on the ice failure mode (crushing) and the time- and rate-dependent properties of the ice; and can be scaled based on the mean ice load level. A cold model ice was developed which showed similar rate-dependent behavior as sea ice, and which resulted in crushing failure when tested. Applying the scaling resulted in full-scale structural response amplitudes and frequencies. Thereby, practical limitations related to testing structures with low natural frequencies in an ice tank facility (e.g., 0.15 Hz for an offshore wind turbine) have been overcome through the innovative use of hybrid simulations in model ice.

Hybrid simulations combine physical load measurements with numerical simulations. In this thesis, only the structural interface in contact with the ice was tested physically,

while the full structural model was implemented numerically. Measured ice loads at the structural prototype during the experiments could thus be used to solve for the full-scale structural response numerically, which was eventually imposed by two electrical actuators.

Results of the experiments unveiled the development of multi-modal ice-induced vibrations of an offshore wind turbine under dynamic ice loading. In total four types of ice-induced vibrations were observed: intermittent crushing, multi-modal ice-structure interaction-I, multi-modal ice-structure interaction-II (also known as frequency lock-in), and continuous brittle crushing. Increased numerical aerodynamic damping and wind-induced deflections affected but did not change the characteristics of these ice-induced vibrations significantly.

Experiments for misalignment of wind-ice loading directions revealed the effect of low aerodynamic damping in the ice loading direction on the development of ice-induced vibrations, and demonstrated that wind-induced deflections were constrained by the ice.

The applied ice-structure interaction model was qualitatively validated by comparison of experimental results and numerical simulations. Though the effect of ice confinement has to be added to accurately model the interaction in misaligned scenarios and may significantly influence the estimations of structural fatigue. Further analysis showed that maximum bending moments are related to the development of multi-modal ice-structure interaction regimes. These regimes are not recognized based on past experience and are as such not included in standard guidelines for the design of offshore wind turbines under dynamic ice loading. A comparison between fully-coupled and sequential simulations showed that the latter encountered difficulties in accurately simulating (design-driving) multi-modal ice-structure interaction regimes.

PREFACE

I conducted my first experimental study in a multi-directional wave and current basin, focusing on exploring the effect of marine growth on the hydrodynamics around an offshore wind turbine monopile foundation during my bachelor thesis. Subsequently, during my master thesis, I investigated the wave-dampening potential of floating vegetation-based islands through full-scale experiments in a large wave flume. Upon learning about the opportunity to investigate ice-induced vibrations of offshore wind turbines using model ice experiments, I assumed that I could transfer my experience from test campaigns on hydrodynamics to the field of ice-structure interaction.

Within the first two months of my PhD journey, I quickly realized my misconception about ice being solely frozen water: I encountered a lack of substantial data on structures affected by ice-induced vibrations; the application of conventional scaling laws presented numerous challenges during model ice experiments; and advanced numerical ice models were just recently implemented in the offshore wind industry. Another setback was that planned ice tank experiments faced multiple delays due to COVID-19 restrictions. In the end, the experiments of the first SHIVER model test campaign in 2021 collided with my first (online) conference. This is why my first conference presentation took place in a small office above the Ice and Wave tank at Aalto University in Finland and was followed by several hours of ice tank experiments conducted at -11°C. Unexpectedly, my presentation (and our paper) was rewarded with the best student paper award, a moment that overwhelmed me to the extent that I accidentally broke my (already cold-strained) glasses due to nervousness.

Bringing a new pair of glasses (and a spare one), I was leading the second SHIVER model test campaign in the Ice and Wave tank at Aalto University in 2023. This time we brought red hats for all participants (two years before they were blue), continuing the legacy of our nickname: the Smurfs. While we successfully gathered data that eventually helped us to answer our research questions, I'll especially remember the small gestures of the team, involving an Easter Bunny leaving traces of chocolate eggs for us, an old friend joining the experiments, or the appearance of a Schwarzwälder Kirschtorte in the heart of Finland on my birthday.

Among other things, the experimental results of these two SHIVER model test campaigns are presented in this thesis, which is a result of luck, dedication, and care from my 'ice family' and partner during the often isolated but adventurous time.

Tim Christopher Hammer
The Hague, November 2024

1

ICE-INDUCED VIBRATIONS OF OFFSHORE STRUCTURES

These ice floes have peculiar habits. Sometimes they lie as quiet as can be, though cut apart by creeks or large fjords; at other times they travel with a speed so swift and violent that a ship with a fair wind behind is not more speedy; and when once in motion, they travel as often against the wind as with it.

Anonymous, The King's Mirror: Speculum regale-Konungs skuggsjá, ca. 1250, published by Library of Alexandria

Prime ministers of eight countries which surround the Baltic Sea have agreed on the combined ambition to install at least 19.6 GW offshore wind capacity in the Baltic Sea by 2030, seven times the current capacity (2.8 GW[1]), and recognized a total potential of up to 93 GW offshore wind capacity when signing the Marienborg Declaration (The Baltic Sea Energy Security Summit, 2022). Up to 85 GW of the total potential offshore wind capacity are estimated to be deployed by 2050 (WindEurope, 2019). However, offshore wind turbines built in such cold regions like the Baltic Sea in Europe or in the Bohai Sea in Asia, or even in the Netherlands (Figure 1.1) can have a distinct challenge in comparison to other wind farm installations: namely, sea ice.



Figure 1.1: The author of this thesis taking an ice core from the landfast ice in the Ijsselmeer during the winter of 2021. Offshore wind turbine foundations of the Fryslân wind park can be seen in the background.

Offshore structures in cold regions must be designed to withstand different features of sea ice, such as ridged, rafted, and level ice drifting against the foundation (Løset *et al.*, 2006). This thesis focuses on level and big floe ice (only stress limited), which is common in areas of ongoing offshore wind farm development. For level ice, the ice loads and the corresponding structural responses are driven by the failure mode of the ice: bending or buckling of the ice leads to moderate loads, while structures exposed to crushing ice experience higher loads. For vertically sided structures, such as offshore wind turbines

[1] 4.7 GW includes wind farms under construction, 10.2 GW includes areas with consent authorized, and roughly 62 GW includes areas with a consent application submitted (November 2024). This additional information is not included in the source but may provide further insight.

with monopile foundations, the design focuses on high loads caused by ice crushing failure, as ice most likely fails in compression when moving against the vertical side of the structure. Note that 'crushing failure' envelopes all failure processes (e.g., pulverization, spalling, or radially cracking of the ice that occur once associated load drops occur.

The crushing of ice and associated loads highly depend on the structural motion during the ice-structure interaction. Processes involved can cause ice-induced vibrations (IIV) (Hendrikse, 2017), which have resulted in structural damage and critical incidents for offshore structures in the past. Ice-induced vibrations of offshore structures have been recorded for multi-leg structures in the Cook Inlet (Blenkarn, 1970; Peyton, 1968) and the Bohai Sea (Xu *et al.*, 2020; Yue and Bi, 2000), lighthouses and channel markers in the Baltic Sea (Engelbrektson, 1977; Määttänen, 1975a; Määttänen, 1975b; Nordlund *et al.*, 1988), and an oil and gas platform (Molikpaq) in the Beaufort Sea (Jefferies and Wright, 1988). The most recent data come from two full-scale measurement campaigns on the Nörstromsgrund lighthouse in the Gulf of Bothnia. The LOLEIF (*Validation of LOw LEvel Ice Forces*) project (Schwarz and Jochmann, 2001) and the follow-up STRICE (*measurements on STRuctures in ICE*) project (Kärnä and Qu, 2009) instrumented the lighthouse with load panels around a portion of the circumference of the structure. Photographs of the Molikpaq platform and the Nörstromsgrund lighthouse are shown in Figure 1.2.

Next, a description of ice-induced vibrations regimes that have been observed during full-scale events is given in Section 1.1. Following that, model ice types, scaling laws, and conducted model-scale experiments focusing on ice-induced vibrations are presented in Sections 1.2 to 1.3. After that, ice crushing models for numerical analysis of ice-induced vibrations are briefly listed in Section 1.4. The penultimate section of the introduction (Section 1.6) describes how ice-induced vibrations are considered in the design standards of offshore structures. Finally, the explicit scope of this thesis, posed research questions and a reading guide are presented in Section 1.7 and Section 1.8.

1.1. ICE-INDUCED VIBRATION REGIMES

Ice-induced vibrations can be classified into intermittent crushing, frequency lock-in and continuous brittle crushing for offshore structures like oil- and gas platforms, channel markers, or lighthouses (Hendrikse and Nord, 2019; Kärnä *et al.*, 2010; Määttänen, 2015; Nord *et al.*, 2015b; Sodhi, 2001; Ziemer, 2019). Typically these regimes are related to a constant indentation or 'drift' velocity of the ice. Time histories of the different regimes for a single-degree-freedom-structure representation of an offshore structure can be found in Figure 1.3. The three regimes are classified as follows.

Intermittent crushing

This quasi-static regime shows long phases of load build-up with severe, rapid load drops upon global ice failure. After a load drop, the structure crushes through the ice with a high relative velocity between the structure and the ice. The high relative velocity results in short phases of brittle crushing. Once the structure moves in the same direction as the ice, contact might be lost. During the decay of the structural vibration, several events of



(a) Molikpaq platform at the Beaufort Sea. The photograph was extracted from Timco *et al.* (1999).

(b) Norströmsgrund lighthouse in the Baltic Sea. The photograph was extracted from Nord *et al.* (2018). Photograph courtesy of Kari Kolari.

Figure 1.2: Two offshore structures exposed to sea ice.

contact loss can occur, resulting in load drops to zero or more specifically to the sum of remaining external loads. The frequency of global ice failures is well below the natural frequency of the structure.

Frequency lock-in

The structural displacement is quasi-harmonic. The relative velocity between the structure and the ice shows an oscillating pattern, with the trough reaches a (near-)zero value. 'Shortly'[2] after the trough, load peaks occur. For phases of higher relative velocity, short phases of brittle crushing of the ice occur. The periodicity of the structural displacement and ice load is governed by the eigenfrequency of the structure.

Continuous brittle crushing

The ice load is characterized as a stochastic crushing process around a roughly constant mean value[3]. The order of load magnitude is lowest of all ice-induced vibration regimes. The load signal has no obvious periodicity, and neither does the ice-induced structural displacement. The structural displacement is typically characterized by a small-amplitude oscillation of the structure around a mean displacement. Relatively high and nearly constant relative velocity between structure and the ice occurs.

[2] Refer to Owen (2024) for further description of 'shortly'.

[3] This statement is limited to model-scale observations. In reality, the mean value would fluctuate due to inhomogeneous conditions in the sea ice.

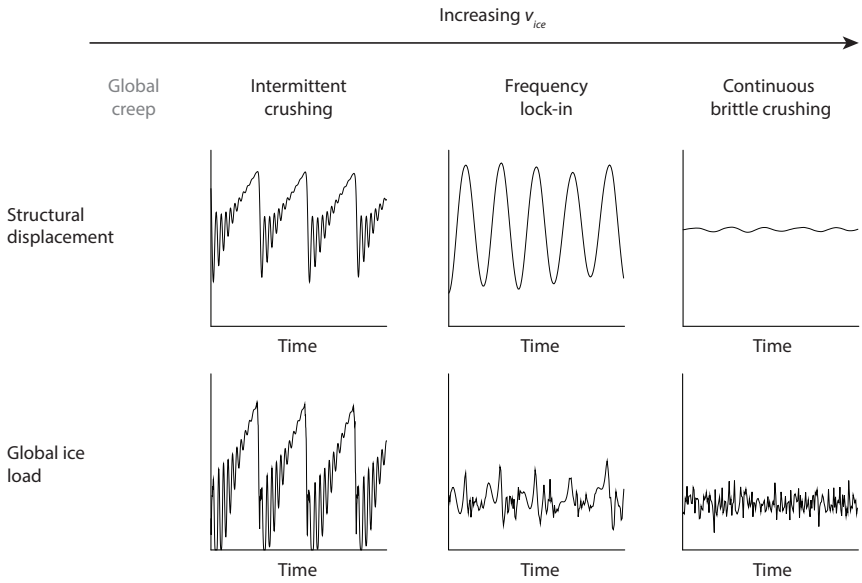


Figure 1.3: Ice-induced vibration regimes modeled for a single degree of freedom structure representation by Hendrikse and Nord (2019).

1.2. MODEL ICE AND SCALING OF ICE-INDUCED VIBRATIONS

The scarcity of full-scale data on offshore structures has inhibited quantitative validation of numerical models. Consequently, researchers generated data in model-scale experiments to further substantiate existing ice models and to reveal the fundamental mechanism(s) causing ice-induced vibrations eventually improving constitutive ice models and applied scaling techniques.

Most of those experiments were conducted in small scale, downscaling the offshore structure and sea ice, respectively. The most common scaling method for ice-induced vibrations of vertically sided offshore structures combines Froude $Fr = v/\sqrt{gL}$ (ratio between inertial (velocity, v) and gravitational forces (gravity g, and length L)) and Cauchy $Ca = \rho v^2/E$ scaling (ratio between inertial (velocity v and density ρ) and elastic forces (elastic modulus, E)) as mentioned by von Bock und Polach and Molyneux (2017). Recent model scale experiments aiming to investigate ice-induced vibrations of a vertically sided offshore wind turbine structure confirm this statement (Tian *et al.*, 2019).

The Cauchy scaling implies a weakening of the model ice to adapt for the small-scaled structural geometries when applying Froude scaling (Palmer and Dempsey, 2009). To create 'weak' columnar model ice, saline solutions were used when growing model ice

in ice tank experiments. Bringing the ratio between Young's modulus E and the flexural strength of the model ice σ_f closer to the scaling application range, the ice, after freezing, was further annealed, which is commonly called ice tempering (Schwarz, 1975). For control of the brittleness of the model ice, air bubbles were trapped in the ice, and scraper systems were applied, while latter method did not proof itself (Evers and Jochmann, 1993). Further, the effect of varies chemical dopants on the mechanical properties of the model ice were investigated (e.g., urea-doped model ice (Hirayama, 1983; Timco, 1980)), peaking in the development of the EG/AD/S model ice that combined multiple dopants (that is, ethylene glycol, aliphatic detergent, and sugar) (Timco, 1986). To save freezing time when thicker model ice was required, granular model ice types were developed, which were created by spraying fine droplets onto the super-cooled surface, forming a thin layer of ice. This layering technique resulted in an ice growth from the top (Enkvist and Makinen, 1984). The granular model ice was further tuned by adding an ethanol solution, resulting in granular ethanol model ice (Jalonen and Ilves, 1990).

In summary, model ice in its traditional form is based on Cauchy and Froude scaling and was tailored to investigate brittle failure at high strain rates. The Cauchy scaling considers an ice strength value related to an elastic force component, which is based on Young's modulus E of the ice (e.g., elastic control factor by Huang *et al.* (2007)). However, since both saline and freshwater ice exhibit non-elastic behavior under loading scenarios relevant for ice-induced vibrations (Cole and Durell, 1995; Owen *et al.*, 2023a; Wei *et al.*, 2022), the suitability of considering only an elastic force component is questionable. Yap (2011) also emphasized that "strength is a function of several known [and unknown] factors" and von Bock und Polach and Molyneux (2017) pointed out that corresponding relative speeds during ice-structure interaction on vertically sided offshore structures "may be in the ductile region, which again presents a challenge for model basins, as Froude-Cauchy scaling does not apply, as strain rate scales [in such] system[s]".

It can be noted that once the Froude scaling can be disregarded, since gravitational forces can be considered insignificant during the crushing of ice on a structure with a vertical interface, there is no need for artificial weakening of the ice (Palmer and Dempsey, 2009). Adapting this idea, Ziemer (2021) developed an improved crushing model ice (ICMI) to reduce the influence of flexural deformation during crushing and to improve the scalability of local loads and the development of the contact area. The procedure of the model ice generation consists of different cooling phases. In one of those cooling phases, the water is kept in motion by use of wave makers, resulting in a high level of ramification of the growing ice crystals during the final cooling (freezing) phase. However, the adjustability of the ICMI to reach certain target behavior was not fully explored.

A trivial and somehow provocative statement was provided by Palmer and Dempsey (2009) who concluded that "[s]ea ice is best modelled by real saline ice". However, Palmer and Dempsey (2009) also elaborated on the idea by Atkins and Caddell (1974), who proposed to scale the fracture of ice instead of applying Cauchy scaling. One year later Palmer *et al.* (2010) suggested scaling ice-induced vibrations similarly to vortex-induced vibrations. A similar concept was proposed by Huang *et al.* (2007) who introduced a rate

control factor which had already been brought forward by Izumiyama and Uto (1997) in form of the Strouhal number. Although the Strouhal number is commonly employed to scale vortex-induced vibrations, its applicability to the phenomenon of ice-induced vibrations remains a subject of debate. For ice, there is nothing equivalent to the Strouhal frequency, which defines the frequency of vortex-shedding on a rigid and immovable cylinder in a steady flow. The loads on rigid and immovable structures experiencing ice crushing are aperiodic with no apparent eigenfrequency (for a recent example see the work from van den Berg *et al.* (2022)).

Sodhi (1992) noticed during indentation tests with freshwater ice that the relative velocity between the structure and the ice should not be scaled, as he found that the effective pressures measured on small and large structures were similar when indentation rates were kept unscaled. Kamesaki *et al.* (1996) introduced the dimensionless compliance effect to scale ice-induced vibrations[4]. The 'compliance effect' aligns with the conclusion of Sodhi (1992), suggesting that velocity should be preserved. Sodhi (1992) suggested using replica modeling for investigating ice-structure interaction in small-scale experiments. In replica modeling, geometrically similar structures, providing identical materials at corresponding locations as in full-scale, are tested (Baker *et al.*, 1991). Ignoring the fact that it is practically impossible to test with identical materials, and applying this scaling to ice-induced vibrations, this form of modeling predicts that the effective mean pressure at the ice-structure interface must be similar. Based on the study by Sodhi (1992), Yap (2011) applied replica modeling while achieving velocity similarity by scaling the time and the amplitude of the structural displacement with the same geometrical scaling factor, which was based on the Cauchy number.

Focusing on the scaling of the dynamic behavior of a structure in ice, Määttänen (1979) stated that an "exact geometric scaling is not necessary: it is required that the dynamic behaviour - natural modes and frequencies - follows that of full scale structure.". However, also Määttänen (1979) faced the challenge on how to scale the stress rate over ice strength leading to scaling parameters that were not "entirely self-consistent" as pointed out by textciteTimco1984. Picking up the thought of time-preservation, Ziemer (2021) preserved time in model-scale experiments assuming that the strain rate governs ice-induced vibrations of vertically sided structures. Ziemer (2021) scaled the amplitude of the structural displacement, assuming length-independent ice failure. However, the conclusion of Ziemer (2021) favored velocity preservation over strain rate preservation to achieve representative ice-induced vibrations. Even if the strain rate of a drifting ice sheet is considered during scaling, the identification of a reference length to determine that strain rate in an indentation scenario is challenging. However, preservation of structural response velocity requires full-scale structural responses, which in turn require full-scale geometric scaling in ice tank experiments—thereby cycling the problem back to the initial discussion.

In summary, and after application of the Buckingham Pi theorem (see Section 2.1), it remains unknown which physical parameter(s) control(s) the mechanism(s) causing

[4] A recent insight is that the observed compliance effect can be explained by the (relative) velocity effect between the structure and the ice (Owen *et al.*, 2023b).

ice-induced vibrations of vertically sided structures. Literature suggests that the relative velocity between the structure and ice should not be scaled in model-scale tests. Even further, neither the structural displacement amplitude nor time should be scaled. Not scaling time implies not scaling frequency, necessitating heavy or flexible structures in test facilities, which could exceed the structural size, mass, and noise limits of those facilities.

1.3. MODEL-SCALE EXPERIMENTS OF ICE-INDUCED VIBRATIONS

Several model-scale tests were conducted to reproduce and analyze the development of ice-induced vibrations of specific structures such as the JZ-20-2 multi-leg structure (Timco *et al.*, 1992), the Great Belt West bridge (Christensen *et al.*, 1995; Timco *et al.*, 1995), and the Molikpaq structure (Cornett and Timco, 1998; Sodhi, 2001). Other model-scale tests focused on the general development of ice-structure interaction, validation of numerical models, and derivation of dimensionless numbers for prediction of ice-induced vibrations (Hendrikse *et al.*, 2018; Huang *et al.*, 2007; Kärnä and Jochmann, 2003; Kärnä and Muhonen, 1990; Määttänen, 1979; Määttänen *et al.*, 2012; Sodhi, 1991; Toyama *et al.*, 1983; Yue *et al.*, 2006).

One of the first experiments to investigate ice-induced vibrations of a structure representation including two degrees-of-freedom was performed by Määttänen (1983). The author found that the structure would vibrate in the lowest natural mode until the velocity became too high for the first mode to follow, resulting in vibrations of the second natural frequency (or higher). Other small-scale experiments of a cylindrical structure in model ice showed that steady-state vibrations would occur at the lowest eigenfrequency (Kärnä *et al.*, 2003). Further small-scale experiments were conducted by Määttänen *et al.* (2012) to analyze the effect of multiple structural mode excitation on the magnitude of identified forces during ice-induced vibrations. From those data, Nord *et al.* (2013) found that the maximum ice force occurred when the structure was vibrating in multiple structural frequencies simultaneously. Extending this finding, Nord *et al.* (2015a) showed that the transition velocity, at which the structural response shifted from first to second mode oscillations, increased with reduced structural stiffness and reduced superstructure mass. However, once the setup stiffness was changed by adjusting clamps, so was the natural frequency, which is why the conclusion of Nord *et al.* (2015a) should rather be that the intensity of second mode oscillation increased with a reduced structural stiffness, reduced superstructure mass, and reduced structural frequency. A similar comment was already given by Hendrikse (2019) when analyzing the conclusions by Huang *et al.* (2007). This underlines the challenge of isolating effects caused by structural parameters on the ice-induced vibrations during small-scaled experiments in model ice.

Another challenge was to keep a constant low indentation velocity when moving a structure into the ice as mentioned by Määttänen (1983). Böhm *et al.* (2022) showed that the stiffness of the integral test-setup is affecting the absolute test velocity significantly. They also argued that insufficient control of the indenter motion is affecting the velocity,

making it deviate from the intended velocity. A variation of the test velocity interferes with the ice-structure interaction process and thus affects the experimental data significantly.

One of the two main challenges during the performance of small-scaled experiments for offshore structures was that only the first two vibration modes of structures could be scaled when a geometrical scaling of the structure was required (Määttänen, 1983; Määttänen *et al.*, 2012; Stange *et al.*, 2020). The second main challenge was that the ice often failed in unwanted failure modes (e.g., buckling or bending) when vertically sided structures were tested, which was also related to the aspect ratio and softness of the ice (Barker *et al.*, 2005; Hendrikse *et al.*, 2018; Tian *et al.*, 2019). The occurrence of unwanted failure modes has been described to be related to the disregarding of the non-linear flexural behavior of the model ice during application of the Cauchy scaling (von Bock und Polach *et al.*, 2019).

1.4. NUMERICAL SIMULATION OF ICE-INDUCED VIBRATIONS

Accompanying the analysis of historical full-scale events and small-scale experiments, numerical crushing ice models have been developed to predict the development of ice-induced vibrations when coupled to a structural model. The ice models can be separated by three main mechanisms implemented, which are ordered historically:

Mechanism 1 Quasi-forced-vibrations

- by a characteristic ice failure length (Gagnon, 2011; Matlock *et al.*, 1969; Sodhi, 1995).

Mechanism 2 Self-excitation

- by a global ice strength which depends on the loading rate; often referred to as 'instantaneous negative damping' approach (Blenkarn, 1970; Määttänen, 1978).
- by local ice failure pressures which depend on 'instantaneous negative damping' (Kärnä *et al.*, 1999).

Mechanism 3 Spatial synchronization

- by contact area variation due to elastic, delayed-elastic and viscous ice behavior (Hendrikse and Metrikine, 2015) (see also Appendix A).

Here quasi-forced vibrations (Mechanism 1) differ from forced vibrations as the time signal is not fully predesribed, however the oscillator cannot control the oscillation phase of external loading due to a preset of ice element succession. In contrast, for Mechanism 2, it is only the oscillator that controls the oscillation phase of the external loading. By that definition, Mechanism 2 and 3 both result in a self-excitation of the structure. However, for Mechanism 3, the structure and ice first must spatially (locally) synchronize before allowing the structure to influence the temporal oscillation phase of the external loading.

1.5. ICE-INDUCED VIBRATIONS OF OFFSHORE WIND TURBINES

The Baltic Sea is attractive for the installation of offshore wind farms as it provides high average wind speeds, shallow waters, reasonable maintenance distances, and short distances to the markets. However, building wind turbines in cold regions like the Baltic Sea requires the consideration of sea ice floes drifting against the foundation causing ice-induced vibrations of the offshore wind turbine. The only published full-scale ice action event of an offshore wind turbine exposed to sea ice exists for a foundation equipped with a cone at the water level to mitigate the development of ice-induced vibrations (Wang *et al.*, 2022; Yu *et al.*, 2020). Ice-induced vibrations of offshore wind turbines with a vertical ice-structure interface have not been recorded or published *yet* to the knowledge of the author. This is mainly because of recent, relatively mild winters in Europe and Asia and few structures on monopiles so far being installed and monitored at locations where sea ice can develop (Figure 1.4).

However, the absence of evidence is not evidence of absence. Over the last decades, it has become clear that structures with a relatively high 'compliance' are more prone to severe ice-induced vibrations (Kamesaki *et al.*, 1996). Comparing offshore wind turbines with lighthouses, channel markers, and oil and gas platforms which have experienced ice-induced vibrations in the past, it is to be expected that in similar ice conditions, offshore wind turbines will develop a more severe dynamic response (Gravesen and Kärnä, 2009; Hendrikse, 2024; Knut *et al.*, 2023). The reason for that concern is that offshore wind turbines have low eigenfrequencies, relatively large vibration amplitudes at the ice-action point, experience significant, simultaneous environmental loading (e.g., wind and ice), and have relatively low and state-dependent damping. Here the term 'state', in the state-depending damping, is referring to the production scenario of the wind turbine. For example an idling wind turbine, when compared to an operational turbine, experiences less aerodynamic damping.

Focusing on numerical simulations, numerous numerical ice crushing models have been used in coupled simulations for prediction of ice-induced vibrations of offshore wind turbines, while mainly two ice models have been applied in the offshore wind industry in Europe (Hendrikse and Nord, 2019; Kärnä *et al.*, 1999) (Former can be found in Appendix A). However, ice models in application of offshore wind turbines could not be validated against full-scale data yet.

Model-scale experiments which specifically investigated ice-induced vibrations of offshore wind turbines, or tried to validate the developed numerical models for such analysis, encountered challenges related to scaling. These experiments resulted in ice buckling or bending rather than crushing in the tests with vertical structures (Barker *et al.*, 2005; Tian *et al.*, 2019). Other experiments only focussed on the first global bending mode of the turbine (Tian *et al.*, 2019). The experiments of Wu *et al.* (2018) did not consider the structural dynamics at all, treating the offshore wind turbine as rigid.



(a) Offshore wind turbines in the offshore wind farm *Nissum Bredning Vind* during the winter of 2018. Photograph courtesy of Siemens Gamesa Renewable Energy.



(b) Offshore wind turbine foundations of *Windpark Fryslân* during the winter of 2021. Photograph courtesy of Windpark Fryslân.



(c) Offshore wind turbines in the Bohai Sea. Photograph courtesy of Prof. Qu Yan from the South China University of Technology.



(d) Offshore wind turbines in the offshore wind farm *Tahkoluoto* in Reposaari (Baltic Sea, Finland). Photograph courtesy of Cody Owen.

Figure 1.4: Photographs of offshore wind turbine(s) (foundations) in cold regions.

1.6. DESIGN OF OFFSHORE WIND TURBINES FOR DYNAMIC ICE LOADS

Ice-induced vibrations (i.e., intermittent crushing, frequency lock-in, and continuous brittle crushing) are considered in the design guidelines for offshore wind turbines (IEC 61400-3-1, 2019). The IEC 61400-3-1 (2019) refers regularly to the ISO 19906:2019(E) (2019), which regulates the design of arctic offshore structures related to the petroleum and natural gas industries. Three preferable approaches to consider dynamic ice loads on offshore wind turbines are proposed by the IEC 61400-3-1 (2019):

1. Analysis of statistical [full-scale] data from similar structures in similar ice conditions.
2. Application of sufficiently advanced numerical models including the dynamics of the structure, the dynamics of the ice, and their interaction.
3. Usage of [model-scale] measurements.

However, and as mentioned before, full-scale data of offshore wind turbines with a vertically sided interface at the ice action point do not exist to the knowledge of the author (approach 1). Insights from full-scale events of offshore structures like oil and gas platforms, lighthouses or channel markers may be inapplicable for offshore wind turbines, which have different structural properties, and are exposed to different, multi-directional environmental loading. Also, dynamic properties offshore wind turbines are affected by the state of operation. Developed numerical models (approach 2) have not been extensively validated for their capacity to predict the interaction between ice and offshore wind turbines owing to the same absence of full-scale data. Structural limitations of test facilities (approach 3) inhibited the testing of structure representations with low eigenfrequencies and multiple structural modes[5]. Large structure could also excite the surroundings and increase the noise-to-signal ratio of measurements. The lowest eigenfrequency of an offshore structure tested in model ice was 2.3 Hz (Yap and Palmer, 2013) according to my knowledge. Application of existing scaling methods in tests with vertically sided structures often resulted in ice buckling rather than ice crushing.

1.7. OBJECTIVE AND SCOPE

Offshore wind turbines, given their structural properties, are expected to experience severe ice-induced vibrations. However, full-scale events neither have been observed nor published yet and thus predictions of existing numerical models could not yet been validated. Model-scale experiments, aiming to investigate ice-induced vibrations of offshore wind turbines, have been inconclusive as structures with low natural frequencies would exceed the capacity of test facilities (i.e., size and weight limits), while geometrical scaling introduced scaling effects (e.g., buckling) compromising the validity of conducted experiments.

In the absence of full-scale testing capabilities, the main goal of this work was thus to demonstrate how offshore wind turbines behave under dynamic ice loads in small-scale experiments. In total four research questions (RQ) have been formulated and are addressed in this thesis, collectively serving to achieve the primary objective of this thesis.

RQ1: How can ice-induced vibrations of vertically sided offshore structures be scaled?

RQ2: How can offshore structures with low and multiple eigenfrequencies be tested in ice tank experiments?

RQ3: What types of ice-induced vibrations can an offshore wind turbine experience?

RQ4: What is the effect of wind-ice misalignment on the development of ice-induced vibrations of offshore wind turbines?

This thesis first addresses RQ1 given the challenges of scaling ice-induced vibrations in the past. Next, RQ2 is addressed, investigating a method to test representations of

[5] Uncertainty persists regarding whether researchers considered it necessary to conduct investigations involving structures with lower frequencies, as the application of state-of-the-art scaling may have discouraged such exploration.

offshore structures in ice tank facilities considering low, and multiple structural eigenfrequencies. Once a scaling method was established and validated with existing full-scale data, model ice experiments with offshore wind turbines were conducted to answer RQ3 and RQ4. The gained insights were used to investigate how ice-induced vibrations may affect the design of offshore wind turbines.

For clarification of the limitations: The present thesis is solely focusing on the hypothetical loading scenario of a uniform and isotropic flat level ice floe with consistent thickness. The ice floe drifts and continuously introduces crushing forces against a single vertically sided offshore wind turbine support structure. In the present thesis, failure modes like creep and buckling and mechanical forms of sea ice, such as ridged or rafted ice are disregarded. Furthermore, the effect of crushed ice in the form of rubble or ice extrusion is not explicitly considered in the present study. For a more comprehensive overview of the different ice failure modes and mechanisms, the reader is referred to Blanchet *et al.* (1988), Hendrikse and Metrikine (2016a), Jordaan (2001) and Timco (1991). Offshore wind turbine specifics like the rotation of the blades, aerodynamics, soil dynamics, or other foundation types are discussed but not investigated.

1.8. READING GUIDE

The main aspect of each chapter is presented in bold font. In addition, a short description of each chapter is given. At the end of the present section, specific reading tracks are recommended.

Chapter 2 **Derivation, verification, and validation of a scaling approach for ice-induced vibrations.**

This chapter explores the development of a scaling method for replicating full-scale ice-induced vibrations of vertically sided offshore structures. Rigid indenter tests and ice-induced vibrations experiments on structures with different shape and diameter are performed to verify the scaling method. Validation of the scaling method is aimed at by reproducing ice-induced vibrations of the Molikpaq platform and Norströmsgrund lighthouse in model ice experiments.

Chapter 3 **Analysis of hybrid simulations in model ice.**

This chapter explores the applicability of hybrid testing in model ice to investigate ice-induced vibrations of offshore structures. In total, 204 hybrid tests are analyzed to investigate the robustness and performance of such. Additional experiments are performed to determine the delay that can cause instabilites of specific experiments.

Chapter 4 **Experimental investigation of ice-induced vibrations of offshore wind turbines.**

This chapter describes model ice tank experiments of a 14 MW offshore wind turbine on a monopile foundation exposed to crushing ice representative for conditions in the Southern Baltic Sea. Experiments are conducted by applying the scaling method presented in Chapter 2, utilizing hybrid simulations as presented in Chapter 3.

Chapter 5 **Experimental analysis of wind-ice misalignment scenarios for offshore wind turbines under dynamic ice loading**.

This chapter explores the impact of misalignment between wind and ice loading directions on the development of ice-induced vibrations of offshore wind turbines. Furthermore it is experimentally investigated how ice influences the structural vibrations perpendicular to the ice drift direction under misaligned conditions.

Chapter 6 **Numerical and experimental studies on the implications of ice-induced vibrations on the design of offshore wind turbine support structures.**

First, this chapter introduces a classification matrix aimed at identifying ice-induced vibration regimes of offshore wind turbines. Second, a dynamic ice-structure interaction case study of a 14 MW offshore wind turbine in the Southern Baltic Sea was performed, unveiling key regimes for the Ultimate Limit State design. A comparison between experimental data (Chapter 4) and numerical results was performed to qualitatively validate the applied numerical model. Next, comparative analyses between sequential and fully-coupled simulations were performed to investigate the potential effect on the design loads when simplified design methods are applied. Finally, ice tank experiments with structures providing artificially increased mode shape amplitudes were performed to investigate the development of ice-induced vibrations of future offshore wind turbines.

The final chapter discusses the findings presented in this thesis and addresses the research questions specifically.

To close the introduction, recommended reading tracks are provided based on assumed reader interests (combinations possible):

1. "The (Arctic) offshore (wind) engineer" : Chapters 1 and 4 to 7.
2. "The dynamicist" : Chapters 1, 3, 4, and 7.
3. "The experimentalist" : Chapters 1 to 3 and 7.
4. "The material scientist" : Chapters 1, 2, and 7.
5. "The numericist" : Chapters 1, 6, and 7.
6. "The extremist" : Chapters 1 to 7.
7. "The passerby" : Chapters 1 and 7.



2

SCALING ICE-INDUCED VIBRATIONS BY COMBINING REPLICA ICE MODELING AND PRESERVATION OF KINEMATICS

This chapter addresses the first research question on how to scale ice-induced vibrations of offshore structures. The first section addresses an attempt to identify a dimensionless number for the specific case of ice-induced vibrations of structures with a vertical interface at the ice action point and thus builds the motivation to develop a new scaling approach. The main part of the chapter derives, verifies and validates a scaling method for application to ice-induced vibrations of vertically sided offshore structures such as offshore wind turbines with a monopile foundation. During the validation process, ice-induced vibrations as documented for the Molikpaq platform and the Norströmsgrund lighthouse were reproduced in model scale experiments. Note that verification and validation processes involved the application of hybrid simulations which are explicitly investigated in Chapter 3.

2.1. MOTIVATION

Chapter 1 showed that it has proven challenging to define a meaningful physical equation for the problem of ice-induced vibrations which could serve as a basis for defining

This chapter has been published by **Cold Regions Science and Technology** as *Scaling ice-induced vibrations by combining replica ice modeling and preservation of kinematics* in 2024 (Hammer *et al.*, 2024). A summary of the experiments and structural models can be found in the supplementary material of the journal publication. Note that the first section was published in the **Proceedings of the 26th International Conference on Port and Ocean Engineering under Arctic Conditions** as *A 2D test setup for scaled real-time hybrid tests of dynamic ice- structure interaction* in 2021 (Hammer *et al.*, 2021) and was added here for contextualization. Redundant sections in the introduction have been removed or merged. Textual passages may vary. Data for this chapter have been collected during **the second SHIVER model test campaign** and have been published separately (Hammer and Hendrikse, 2023a). Data from other sources are indicated as such.

important dimensionless quantities which in turn can be used for scaling. Most of the developed models for simulating ice-induced vibrations contain some empirical or phenomenological component, which does not allow the equations to be fully expressed in terms of physical quantities. Furthermore, certain theories assume that the ice behaves in a purely elastic and brittle manner, whereas other theories include viscoelastic and viscoplastic deformation components in the ice, associated with the development of damage, microcracking, recrystallization, etc., though often only in an approximate manner. Such differences lead to different sets of dimensionless numbers governing the problem of ice-induced vibrations.

Here it was chosen to (re-)derive the relevant dimensionless numbers involved in the dynamic interaction. The rederivation results in a list of relevant variables, assuming the structure can be represented by multiple modes of oscillation, each with its natural frequency ω_i, damping ratio as a fraction of critical ζ_i, and modal mass m_i:

$$[\omega_1, \zeta_1, m_1, \ddot{x}, \dot{x}, x, w, h, v_{\text{ice}}, E_1, \sigma_c, d, \eta, E_2]$$

where x is the displacement of the structure at the ice action point in the direction of ice loading, overdots represent derivatives with respect to time, w is the projected width of the interaction zone, h is the ice thickness, v_{ice} is the ice drift speed, E_1 is a modulus of elasticity defining the elastic deformation of ice under compressive loading, σ_c is a representative crushing strength, d is the average grain size of the ice, η is a material coefficient of viscosity, and E_2 is the elastic modulus defining the viscoelastic deformation. Note that higher modes are not included here as these can be made dimensionless in terms of their relative ratio to the first mode.

Table 2.1: Dimensional matrix for the problem of ice-induced vibrations, assuming the deformation of the ice to be governed by elastic and viscoelastic components, and fracture to be brittle in local zones defined by strength and grain size as governing parameters. Higher modes are omitted since they can be made dimensionless by their relative ratio to the first mode natural frequency, mass, and damping ratio.

Dim	m_1	ζ_1	ω_1	$\ddot{x}$	$\dot{x}$	x	w	h	v_{ice}	E_1	σ_c	d	η	E_2
M	1	0	0	0	0	0	0	0	0	1	1	0	1	1
L	0	0	0	1	1	1	1	1	1	-1	-1	1	-1	-1
T	0	0	-1	-2	-1	0	0	0	-1	-2	-2	0	-1	-2

The dimensional matrix shown in Table 2.1 is obtained from the identified important variables. Application of the Buckingham Pi theorem[1], choosing σ_c, ω, and d as repeating variables (as these are of interest during the tests), results in the set of 11 dimensionless parameters defined in Equation (2.1). A grain size was chosen here, rather than the more commonly used ice thickness, because local behavior of the ice to be considered more important and it may be better represented by grain size, or any other characteristic length or dimension at or below that scale, rather than ice thickness when it comes to

[1] historically correct: *the method of dimensions*

crushing. One could also consider to use a length scale associated with dislocations in the ice (Cole and Durell, 1995) instead or any other scale that is significantly smaller than the geometrical scale of the diameter.

$$\pi_{1..10} = \left[\frac{\sigma_c d}{m\omega^2}, \frac{\zeta \ddot{x}}{d\omega^2}, \frac{\dot{x}}{d\omega}, \frac{x}{d}, \frac{w}{d}, \frac{v_{\text{ice}}}{d\omega}, \frac{E_1}{\sigma_c}, \frac{h}{d}, \frac{\eta\omega}{\sigma_c}, \frac{E_2}{\sigma_c} \right] \tag{2.1}$$

Some relevant groups can be recognized that already have been proposed in the literature, such as the compliance ratio $\pi_1\pi_6 = \frac{\sigma_c d w}{m\omega^2 d} = \frac{\sigma_c h w}{kh}$ from the work by Kamesaki *et al.* (1996), the parameter proposed by Palmer *et al.* (2010) to govern dynamic ice-structure interaction $\frac{\pi_7}{\pi_8} = \frac{v_{\text{ice}}}{h\omega}$, the 'Strouhal number for ice' introduced by Izumiyama and Uto (1997) given by $\pi_1\pi_5\pi_6\pi_8 = \frac{\sigma_c w h \omega}{k v_{\text{ice}}}$, the Elasticity control factor $\pi_1\pi_8\pi_9 = \frac{E_1 h}{k}$, and the rate control factor $\frac{\pi_6}{\pi_7} = \frac{w\omega}{v_{\text{ice}}}$ by Huang *et al.* (2007).

It is interesting to note that all earlier proposed dimensionless numbers can be obtained when assuming the problem to be a purely elastic-brittle problem, in which the grain size or a characteristic length for local failure does not play a role, excluding d, η, and E_2 as relevant parameters. In such a scenario, it would be appropriate to ensure that for the model ice, the ratio $\pi_8 = \frac{E_1}{\sigma_c}$ is maintained, and scaling of the other important variables follows by introducing some geometrical scale factor. The ratio $\frac{E_1}{\sigma_c}$ can be relatively well controlled, as shown in the review by Lau *et al.* (2007).

Focusing on the viscoelastic component, two additional dimensionless numbers have been introduced in Equation (2.1), one of which is purely ice-related, $\pi_{11} = \frac{E_2}{\sigma_c}$, and the other links the ice and structural properties, $\pi_{10} = \frac{\eta\omega}{\sigma_c}$. This last number is probably the most critical, as it relates the rate-dependent ice behavior to the dynamics of the structure. If the problem were purely elastic and brittle, a change in natural frequency, assuming the damping ratio and stiffness of the structure remain constant, would only result in a change in $\pi_7 = \frac{v_{\text{ice}}}{d\omega}$. This suggests that for a higher natural frequency, a higher ice drift speed would be required to obtain similar results between two tests or when comparing full-scale and model-scale results. However, the introduction of $\frac{\eta\omega}{\sigma_c}$ shows that when changing the natural frequency, we would have to additionally change either the viscosity or strength of the ice to achieve a similar result. The effect on basin tests for ice-induced vibrations would be significant, as the ratio $\frac{\eta}{\sigma_c}$ for model ice is typically neither measured nor controlled.

The grain size is the only geometrical parameter that is typically not controlled in ice tank experiments. However, it is not known if or to what extent the ice grain size governs the interaction problem. In any case, it is assumed that the physical mechanism for ice-induced vibrations is on a scale much smaller than the geometrical scale of the structural prototype. This would allow to apply a different scaling approach where natural frequency and velocity are not scaled, and only a sufficiently high ratio $\frac{w}{d}$ and $\frac{h}{d}$ must be maintained to avoid interaction with a single grain.

Thus, it is concluded that the complete scaling of the problem is not an option. However,

this does not imply that basin tests should be disregarded. On the contrary, many basin tests exhibit interaction regimes observed for full-scale structures, indicating that the governing physics are present to some degree, regardless of how the ice is adjusted for the basin setting. This is an interesting observation in itself. It is believed that many general trends in the interaction can be understood from basin tests, provided that structures with different properties are tested under the same model ice conditions so that clear trends can be captured.

2.2. INTRODUCTION

The literature presented in Chapter 1 indicated that ice-induced vibrations are primarily controlled by the energy transfer between ice and structure which is mainly, from the ice perspective, defined by the magnitude of the ice forces on the structure. Furthermore, the magnitude of the ice forces during interaction has been shown to be strongly dependent on the relative velocity between ice and structure. At low relative velocities higher forces are observed, which is referred to as the velocity effect (Izumiyama *et al.*, 1994; Jefferies *et al.*, 2008; Kamesaki *et al.*, 1996; Kärnä *et al.*, 2008; Määttanen, 1981; Owen *et al.*, 2023b; Singh *et al.*, 1990; Sodhi, 2001; Tsuchiya *et al.*, 1985). This effect is also observed on completely rigid structures, for which the relative velocity becomes just the ice drift speed, where the highest global forces are typically obtained at a transition speed (e.g., Inoue and Koma (1985) and Takeuchi *et al.* (2001)) in a range of $0.08\,\mathrm{mm\,s^{-1}}$ to $0.9\,\mathrm{mm\,s^{-1}}$. This (ductile-to-brittle) transition speed is here defined as the indentation speed at which the macroscopic creep changes to a fracture dominated failure of the ice. This transition speed and the associated high ice forces when compared to the forces for indentation velocities far exceeding the transition are key properties of the ice.

It was found from numerical simulations that ice-induced vibrations could be controlled by variation of the mean ice load: the phenomenological ice model for simulation of ice-induced vibrations of vertically sided structures considers the mean load level to 'scale' the input parameters to different conditions (Hendrikse and Nord, 2019) (see also Appendix A). Interestingly, Sodhi (1992) found that the effective pressures measured on small and large structures were similar when the indentation rates were kept unscaled. Combining the insights from the numerical model which has been shown to reproduce many observations related to ice-induced vibrations, and the experimental observation, one can arrive at the idea to use the mean load (i.e., mean pressure assuming that the physical mechanisms of ice-induced vibrations develop on a significantly smaller scale than the geometrical scale) for scaling purposes.

Thus, it was assumed that the relative velocity between the structure and the ice, together with the mean ice load, control the energy transfer and the rate of energy transfer between ice and structure during interaction. It then follows that if the time-dependent and rate-dependent model ice properties can be kept within similar ranges as those observed for sea ice, full-scale ice-induced vibration events should be reproduced in a model scale setting when the structural model is adjusted to compensate for the lower mean load at scale compared to reality. The result would then be a structural response of

full-scale magnitude and in real time in the model basin setting.

This chapter aims to introduce and validate a scaling method that can be applied to reproduce representative ice-induced vibrations of offshore structures with vertical sides in model-scale experiments. For this purpose, a replica modeling technique was applied in combination with a preservation of the kinematics during the ice-structure interaction, in line with suggestions from literature (Sodhi (1991)). The scaling method considered four main aspects: the kinematics during ice-structure interaction; the degree to which the ice can resist higher loading at low velocities prior to failure (velocity effect); the existence of a transition speed; and the mean ice load level.

Contrary to other scaling methods, this scaling method underlines that it is unknown how to scale the time- and rate-dependent behavior of ice, or how to scale the amplitude of structural oscillation without affecting the development of ice-induced vibrations in an uncontrolled manner, which is why a preservation of the kinematics is applied. Similarity of structure shape, aspect ratio, Young's modulus, compressive strength, ice mass, local peak ice pressure at high speed (i.e., brittle crushing peak loads), surface friction, and ice temperature are assumed to not be required to achieve representative ice-induced vibrations in model ice experiments.

2.3. METHODS

A representative scaled test for ice-induced vibrations is further defined as a test in which the regimes of ice-induced vibrations (i.e., frequency lock-in and intermittent crushing) develop as observed during full-scale ice-induced vibration events or other reference data with their characteristics preserved (e.g., Hammer *et al.* (2022) and Hendrikse (2019)), and with global loads and structural kinematics qualitatively similar to those of full-scale ice-induced vibration events. A key characteristic is that an ice floe slowing down against a relatively flexible structure can cause a transition from continuous brittle crushing to frequency lock-in and ultimately to intermittent crushing (Jefferies and Wright, 1988; Peyton, 1968). Here the relative increase in global peak loads (in comparison to other IIV), should be captured, as well as the increase in period of the saw-teeth as the ice drift speed decreases. Experience has shown that the latter two aspects have not developed in 'standard' model ice, most likely due to the tendency of the ice to bend or buckle under high loading (e.g., Hendrikse *et al.* (2018)).

2.3.1. REPLICA MODELING

Replica modeling uses a model dimensionally similiar to the full-scale structure, with identical materials placed at corresponding geometric positions (Baker *et al.*, 1991). This approach can be understood as preserving the effective mean ice pressure as shown by conducted experiments (Sodhi, 1992) and application in scaling (Yap, 2011). If the mechanism(s) causing ice-induced vibrations originate at a small scale in the ice (Cole, 2021; Hendrikse, 2019; Owen, 2024), then the finding of Sodhi (1992) seems to be reasonable when the specimen is much larger than the ice grain size. It is assumed that the effective

mean pressure preservation is achievable when the ratio of structural diameter (D) to grain size (D_{gr}) is relatively large: $D/D_{gr} > 25$ (Hirayama *et al.*, 1974) and only when testing at mass-unaffected velocities[2].

2.3.2. PRESERVATION OF KINEMATICS DURING DYNAMIC ICE-STRUCTURE INTERACTION

The literature presented in Chapter 1 indicates that neither the structural displacement amplitude nor time should be scaled, which leads to a preservation of the kinematics during the dynamic ice-structure interaction. Here the term preservation is defined as a state in which (the targeted) physical quantities are kept at the full-scale value. To preserve kinematics during interaction, the relevant kinematic properties of the ice *and* of the offshore structure[3] must therefore be kept at full-scale.

ICE

The transition speed and the velocity effect are central to the development and scaling of ice-induced vibrations of vertically sided structures (Hendrikse and Nord, 2019). The model ice was therefore required to have a similar transition speed and show a similar velocity effect as sea ice. The transition was associated with the ice drift speed that led to the highest standard deviation in rigid indenter experiments of sufficient duration. This definition aligns with Takeuchi *et al.* (2001), who determined the transition speed by visually confirming reduced prominence of low-frequency load peaks in the signal. The standard deviation was chosen as a transition speed classification criterion as it considers the change of load peak prominence when no mass effects (i.e., ice extrusion) are influencing the mean load.

STRUCTURE

A hardware-in-the-loop system was used in the experiments to achieve full-scale kinematics of the offshore structure during the ice-structure interaction (Figure 2.1). The system is combining physical measurements with numerical simulations.

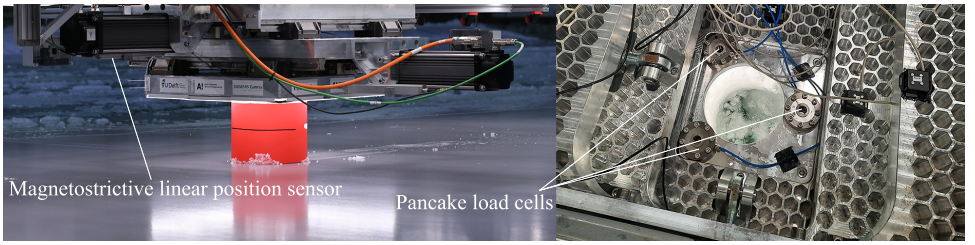


Figure 2.1: Left: physical prototype and actuators of the test setup. Right: Top view on the pancake load cells once the aluminum pile was removed.

[2] This does not imply that the grain is the physical driver of the phenomenon.

[3] The offshore structure includes the dynamic structure and material as well as the support structure during testing.

In our case, the test setup consists of a physical prototype, equipped with ice load measurement devices, and a numerical model for predicting the structural response of offshore structure. The test setup helps to preserve relative velocity, without requiring large structure models in the ice tank. Before testing, a numerical structure model (e.g., a file containing scaled structural properties of a specific offshore structure) was uploaded to the numerical model. As the physical prototype was moved through the ice sheet, the measured ice load was used as input for the numerical model. The numerical model solved the dynamic equations in real time using a Euler-Cromer method to determine the structural displacement of the offshore structure, which was then applied on the physical prototype by an electrical actuator. The application of a test setup led to a "decoupling" between oscillation and substructure, as suggested by (Määttänen, 1983), (Timco, 1984), and Ziemer (2021). Three separate load cells (2960–2962-2965 low-profile (pancake) load cells SENSY S.A, 6040 Jumet, Belgium) were positioned between the aluminum pile and the moving tables (Figure 2.1) to determine the ice-induced bending moments. The vertical load component was disregarded when calculating horizontal ice loads in ice load direction F_y, as vertical components were small relative to the horizontal loads. Displacements in ice drift direction (d_y) were measured with a magnetostrictive linear position sensor. The aluminum test pile accommodated the connection of red 3D-printed adapters (Figure 2.2), which allowed investigation of geometrical scale effects using different shape and diameter of indenters without increasing the mass of the physical prototype or increasing manufacturing cost and time significantly. The suitability of using 3D-printed structures made of polylactic acid for model tests of vertically sided structures in model ice was explored by Petry *et al.* (2023). The global stiffness was determined to 18 $\mathrm{MN\,m^{-1}}$ (0.45 mm deformation under 8 kN loading). Minimizing the risk of local damage, selective laser sintering (SLS) of polyamide 12 was favored over the tested fused deposition modeling technique used in Petry *et al.* (2023). Material similarity of the physical prototype (consisting of aluminum or polyamide 12) and the offshore structures (constructed from steel or concrete) was assumed when assessing the crushing of ice against a vertical side. This means that neither material used in the experiments yielded significantly, which would, on the one hand, change the relative velocity between structure and ice and, on the other hand, affect the test setup control. For the same reason it was essential to maintain the support structure stiffness of the fully-integrated test setup (Böhm *et al.*, 2022). Both the aluminum and 3D prints were designed so that the local deformation under maximum loading was negligible. After manufacturing, the SLS-prints were painted red to enhance better visual contrast with the model ice. Tested substructures can be seen in Figure 2.2 and further specifications of the substructures can be found in Table 2.2. The reader is referred to Chapter 3 for further details on the developed test setup and measurement systems.

2.3.3. SCALING FACTORS

While the simulation and presentation of the global ice drift speed is straightforward by moving a structure with the full-scale speed through the model ice, maintaining structural kinematics is more complex. To address this challenge, a hybrid setup was employed, enabling the scaling of structural properties in a numerical domain while testing a "decoupled" physical prototype in an ice tank (see Chapter 3). Assuming mean

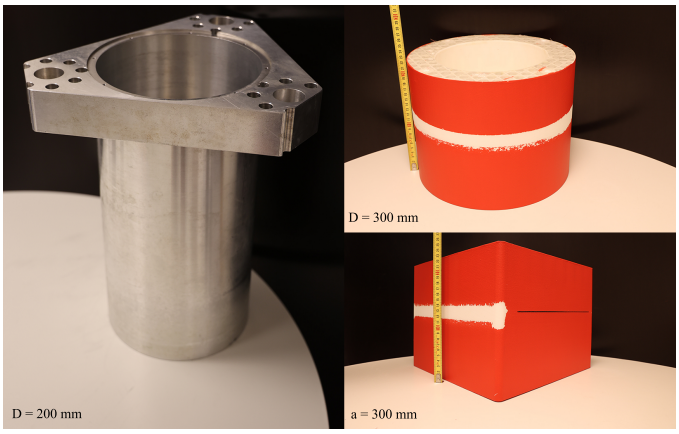


Figure 2.2: Left: Aluminum pile. Top right: Cylindrical (C) SLS-print. Bottom right: Rectangular (R) SLS-print.

Table 2.2: Specification of investigated physical prototypes.

Structure	Material	D (a)	Height	Aspect ratio	Application	Technical drawings*
		[mm]	[mm]	[-]	[-]	
Pile	Aluminium	200	378	8	Rigid, Molikpaq, NSG Lighthouse	SM2.pdf
SLS-C	Polyamide 12	300	230	12	Rigid	SM3.pdf
SLS-R	Polyamide 12	(300)	230	12	Rigid	SM4.pdf

*Supplementary material (Hammer *et al.*, 2024)

ice pressure preservation, the structural properties of the full-scale structure (e.g., mass, damping, and stiffness) were scaled to account for the difference in the loaded area between full- and model-scale. A scale factor λ_F between the measured quasi-static mean ice load measured on the physical prototype in model ice experiments ($\bar{F}_m$) and the quasi-static mean ice load of the full-scale event ($\bar{F}_f$) was applied to scale the structural properties in the numerical model implemented in the hybrid simulations:

$$\lambda_F = \frac{\bar{F}_f}{\bar{F}_m}. \tag{2.2}$$

The mean model ice load $\bar{F}_m$ was determined through an ice load measurement from a rigid indenter test at an ice drift speed of $100\,\mathrm{mm\,s^{-1}}$ for a 1.5 m crushing length at the start of each separate test run through the ice sheet. Note that the controlled indenter speed (carriage speed) is interpreted as ice drift speed in this thesis. The value of $100\,\mathrm{mm\,s^{-1}}$ was chosen to reflect the upper bound of rate-independent mean pressure as found by Sodhi (1992). A summary of the applied scaling factors is provided in Table 2.3. Mean ice loads as measured during rigid indenter experiments in four model ice sheets are shown in Figure 2.3. The rigid indenter experiments were performed by moving the actuators at a constant speed below $10\,\mathrm{mm\,s^{-1}}$, and by driving the carriage for higher indentation speeds. Low and high speeds were alternated to assure ice with a rough

interface when starting an indentation test with a relatively low indentation speed. This is considered more representative of a true interaction scenario with a structure where the relative speed always changes. Mean ice loads as measured during rigid indenter experiments in four model ice sheets are shown in Figure 2.3. The chosen speed for scaling (i.e., 100 mm s^{-1}) is at the upper limit of ice drift speeds resulting in minor rate effects (grey area). The boundaries of the grey area are set for ice drift speeds that did not exceed a median load variation of ±15 % when compared to the chosen median load as measured for an ice drift speed of 100 mm s^{-1}.

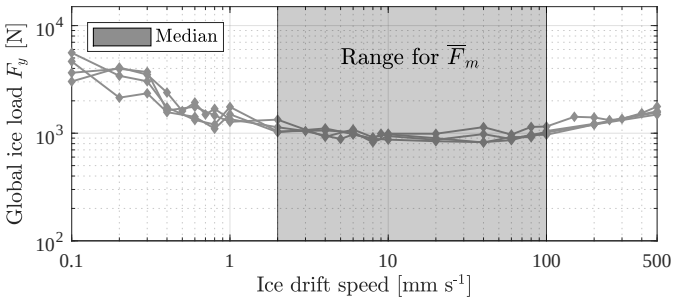


Figure 2.3: Global ice loads based on rigid indenter experiments in four cold model ice sheets measured during the second SHIVER model test campaign.

The full-scale mean load $\bar{F}_f$ can be extracted from project reports, estimated by design guidelines, or be simulated with ice models coupled to rigid structures (see Section 2.7.4).

2.4. MODEL ICE

2.4.1. CRUSHING

Model ice experiments were conducted in the Ice and Wave tank of the Aalto University in Espoo, Finland. The ethanol-doped model ice used in this thesis was produced by spraying a fine mist through water nozzles in 60 cycles at an air temperature of −10.5 °C, following the growth of an initial carrying ice layer for 20 min. Using a carriage speed of 0.16 m s^{-1} while spraying, the total spraying time was 225 min. Subsequently, the ice underwent 150 freezing degree hours at a constant temperature of −12 °C. The ice was maintained at −11 °C during testing. This ice type is henceforth referred to as cold model ice. The experiments were conducted with a sprayed ice thickness of 25 mm. The reader is referred to Figure 2.4 to find vertical ice cross-sections. The sprayed ice grain size in these figures is visually estimated to be in the order of 1 mm. It is worth noting that von Bock und Polach *et al.* (2013) defined the highest probable grain size as 0.68 mm for ethanol-doped model ice in the same Ice and Wave tank, using the same spraying nozzles.

Table 2.3: Scale factors based on the scale factor λ_F.

Physical quantity	Unit	Scale factor applied
General		
Length	[m]	1*
Time	[s]	1
Structure		
Frequency	[s^{-1}]	1
Damping ratio	[-]	1
Mass-normalized mode shape	[$kg^{-0.5}$]	$\lambda_F^{-0.5}$
Mass	[kg]	λ_F
Stiffness	[$N m^{-1}$]	λ_F
Damping	[$N s m^{-1}$]	λ_F
Ice		
Ice drift speed	[$m s^{-1}$]	1
Mass	[kg]	~1 at micro scale
Mean brittle crushing force**	[N]	λ_F
Strength	[$N m^{-2}$]	< 1 (discussed in Section 2.4.3)
Transition speed from ductile- to brittle failure	[$m s^{-1}$]	~1 (discussed in Section 2.4.2)
Thickness	[m]	Section 2.5.1
Aspect ratio	[-]	Section 2.5.1

*The length scaling applies to response not to geometry.
**Determined for a crushing length of 1.5 m at an ice drift speed of 100 mm s^{-1} as described above.

2.4.2. DUCTILE-TO-BRITTLE TRANSITION SPEED AND VELOCITY EFFECT

The (ductile-to-brittle) transition speed is here defined as the indentation speed at which the macroscopic creep changes to a fracture dominated failure of the ice. Results of rigid indenter tests in the cold model ice are shown in Figure 2.5. The cold model ice manages to resist increased load levels at the lowest ice drift speeds (velocity effect). A transition speed of 0.1 mm s^{-1} is identified for the cold model ice. It should be noted that the value could theoretically be lower as the standard deviation was highest for the lowest ice speed tested. However, it can be assumed that the transition speed is almost reached as a levelling trend for lowest tested ice drift speed can be observed (see also Figure 2.3. The cold model ice exhibits similar transition speeds as sea ice, comparing the identified transition speed to those observed in sea ice 'close' to the location of the full-scale scenarios (0.08 mm s^{-1} to 0.17 mm s^{-1}, see Table 2.4), or of freshwater ice in the laboratory (0.06 mm s^{-1} to 0.11 mm s^{-1} (Wu *et al.*, 1976). Indentation experiments in sea ice (Inoue and Koma, 1985; Takeuchi *et al.*, 2001), documenting a range of 0.08 mm s^{-1} to 0.9 mm s^{-1} for the transition speed, support the transition speed results found for uni-axial compression strength tests.

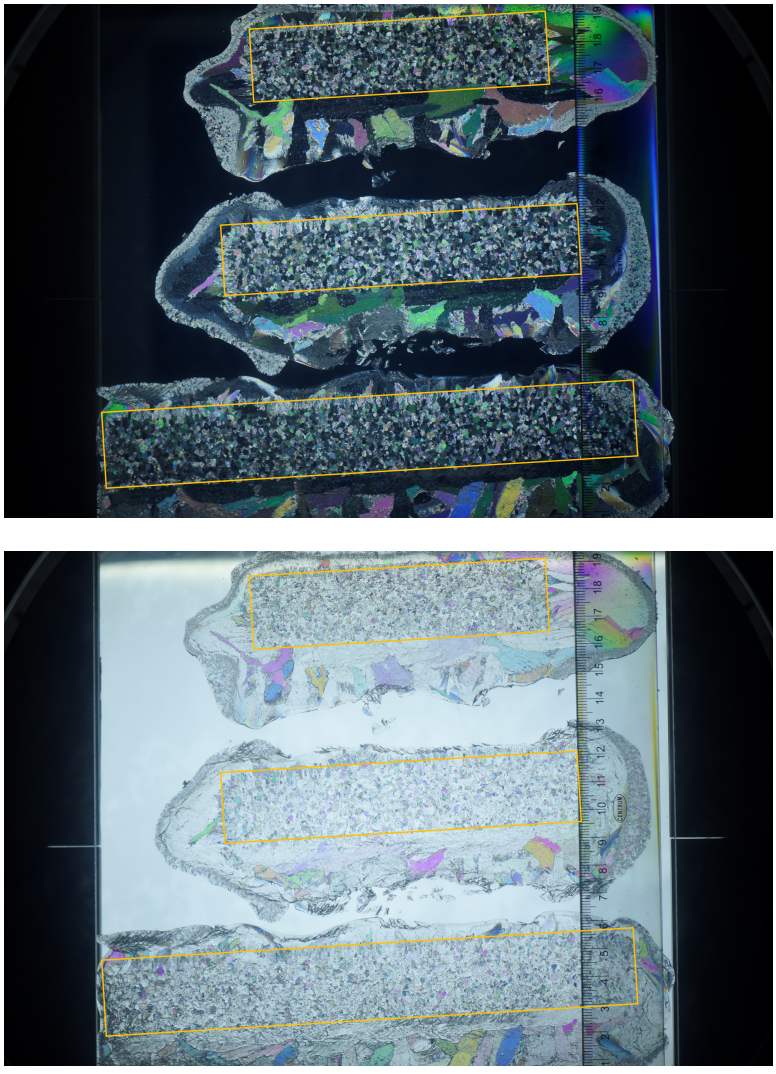


Figure 2.4: Thin sections in parallel- and in cross-polarized light (≈ 1 mm thick) of the cold model ice during the second SHIVER model test campaign. The sprayed ice layer is framed. Photograph courtesy of Cody C. Owen.

2.4.3. STANDARD SCALING PARAMETERS

Although not considered in the scaling, Young's modulus and compressive strength were tested and put into relation with full-scale data, as they are standard parameters and analysis creates a better comparability to existing scaling methods and ice types. Compressive in-situ strength tests, flexural in-situ strength tests, and Young's modulus measurements

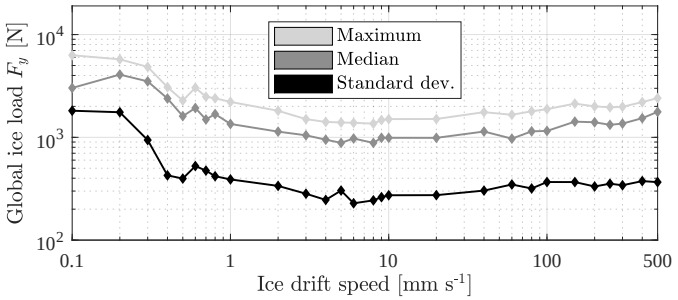


Figure 2.5: Ice loads from rigid indenter tests for cold model ice. Rigid experiments were performed with the aluminum pile (D = 200 mm) and an ice thickness of 25 mm.

were conducted at least once per day for the cold model ice in accordance with the ITTC (2021). Comparison of field measurements (see Table 2.4) with material properties as measured in the ice tank (see Table 2.5) reveals that the compression strength σ_c of the cold model ice, although relatively high, is still lower than the compressive strength of sea ice. Similarly, the Young's modulus of the cold model ice, although relatively high, is lower than measured values in sea ice. It is important to put this result into perspective. To the knowledge of the author, no ice property measurements exist for the dates of full-scale events which were aimed to be simulated in the ice tank. Properties from similar locations and times were extrapolated to the investigated cases which increases uncertainty in the comparison. But most importantly, achieving elastic similarity was of secondary interest in the present study, as the primary concern was to preserve kinematics. Furthermore, strength tests in model scale are complex, as pressure-area, geometry, grain size, and stress functions may form co-dependencies (von Bock und Polach and Ehlers, 2015) (see also Section 2.1).

Table 2.4: Examples of mechanical sea ice properties. Transition speed v_t is based on uniaxial compression strength tests. Ice temperature is T and Young's modulus E.

Ice Type	Location	T	v_t	σ_c	E	σ_f	D_{gr}	Reference (Testing date)
		[°C]	[mm s^{-1}]	[MPa]	[MPa]	[kPa]	[mm]	[mm]
Sea ice floe	Bay close to NSG Lighthouse	-1	0.09–0.17	3.91–5.12	4–6	-	5	Fransson (2004) (15.04.2003)
Sea ice	Bay of Bothnia, Baltic Sea	-	-	0.65–1.98	-	321–472	-	Suominen *et al.* (2013) (22-24.03.2012)
Rafted sea ice block	Beaufort Sea	-11	0.08	1.04–4.04	4.5	-	2–12	Frederking and Timco (1983) (06.01.1982)

2.5. SCALING EFFECTS

Next, it is investigated if the assumption to neglect similarity of the structure shape and aspect ratio when scaling for ice-induced vibrations can be verified. Rigid indenter and

Table 2.5: Model ice properties as measured according to the ITTC (2021).

Date and sub-structure	Ice Type	T	v_t	σ_i^*	σ_c	σ_f	E	h	
		[°C]	[mm s^{-1}]	[kPa]	[kPa]	[kPa]	[GPa]	[mm]	
06.04.2023 Pile	Cold	−11	0.1	1567	678.1	491.7	3810	25	Figure 2.5
12.04.2023 SLS-Print-R	Cold	−11	0.2	1776	709.1	484.3	4152	25	Figure 2.6
25.04.2023 SLS-Print-C	Cold	−11	0.1	1656	1054	544.6	5012	25	Figure 2.8

*The crushing strength σ_i is based on Equation 5 in Section 6 of the ITTC guideline (2021), using a contact factor of 0.7 and maximum force measurements during rigid indenter tests, and is given as reference to the compression strength.

dynamic ice-induced vibration experiments of structures with two different aspect ratios and structure shape have been conducted and analyzed.

2.5.1. ASPECT RATIO

Experimental results of rigid indenter tests for substructures with diameters (D) of 200 mm and 300 mm are shown in Figure 2.6. Changing from a smaller to a larger diameter had no discernible effect on the transition speed or velocity effect. The ratios between the standard deviation and median ice load (F_{std}/F_{median}) remained similar for both tested substructures. Notably, these substructures both exhibited a slightly increasing ratio for low ice drift speeds, and a decreasing ratio for higher ice drift speeds. This trend was more pronounced with increased structural diameter. This observation might be associated with the ice failure type. Typically, two ice failure types are distinct: at a high relative velocity between structure and ice, the ice fails randomly and non-simultaneously in time and space along the structural surface, often related to local peak pressure generation and small contact area. At a low relative velocity, the ice fails simultaneously, synchronized in time and space along the surface of the structure, which often leads to higher global peak loads and increased contact area. For non-simultaneous ice failures, the averaging of random processes over a larger area led to a reduction in the ratio. In cases of ice drift speeds corresponding to simultaneous ice failure, the increased area appeared to enhance the likelihood of simultaneous loading and consequent global load peak generation. Extrapolating this finding to full-scale dimensions, an increased standard deviation for experimental data can be expected when compared to full-scale data. However, this effect is negligible here as the suggested scaling method is based on the central tendency of the brittle crushing load and not on the peak pressures or loads.

Investigating the effect of a change in the aspect ratio on the development of ice-induced vibrations, dynamic ice-induced vibration experiments of structures with two different aspect ratios were conducted in the cold model ice. The comparison of time series of four dynamic ice-induced vibration regimes in Figure 2.7 (one regime per row)

showed that scaling effects related to the change in aspect ratio for the two tested diameters (i.e., aspect ratio change from 8 to 12) on the ice-induced vibrations were negligible.

Note that the ice thickness is not targeted in the scaling. A value is chosen, which results in crushing of the cold model ice (e.g., aspect ratio < 12) and that would not exceed the maximum load capacity of the test setup at maximum ice loads.

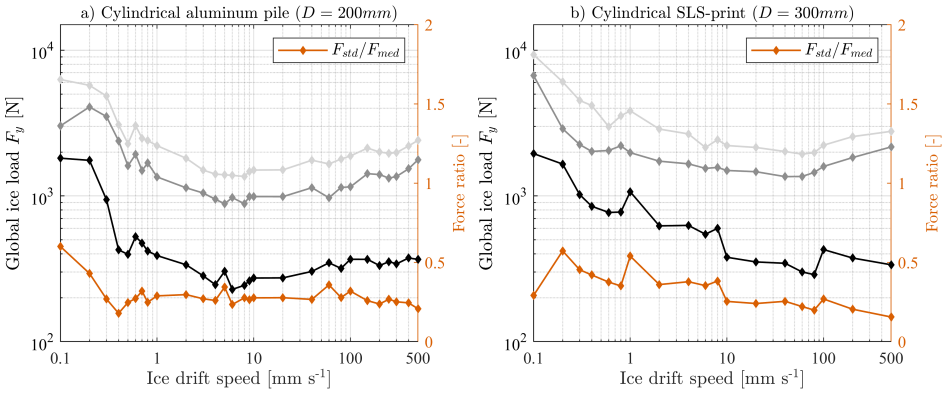


Figure 2.6: Statistical measures derived from rigid indenter tests for structures of similar shape but different diameter. Note that the same color scheme for the statistical values was used as in Figure 2.5.

2.5.2. SHAPE

The results from rigid indenter tests with two different shapes are depicted in Figure 2.8. The use of a rectangular SLS-print or a cylindrical SLS-print did not significantly shift the transition speed or affect the velocity effect. However, the rectangular SLS-print exhibited higher maximum loads when compared to the cylindrical SLS-print with the same nominal area at the ice interface (i.e., 9.7 % higher peak loads). This discrepancy in loads was attributed to the greater resistance of ice to move around the rectangular SLS-print, leading to higher confinement, which is a common observation (see Table 27 of Korzhavin (1962)). However, it was observed that low ice drift speeds resulted in radial crack formation when testing the rectangular SLS-print. This crack formation was presumably linked to high stress concentrations at the corners of the SLS-print. The high stress concentration could also explain the chipping of red paint at the corners of the SLS-print during crack formation (refer to Figure 2.2).

Investigating the effect of a change in shape and aspect ratio on the development of ice-induced vibrations, dynamic ice-induced vibration experiments of structures with two different aspect ratios and shapes were conducted in the cold model ice. The comparison of time series for three dynamic ice-induced vibration regimes in Figure 2.9 (one regime per row) shows that scaling effects related to the change in shape and aspect ratio for the two tested diameters and shapes (i.e., aspect ratio change from 8 to 12; cylindrical to

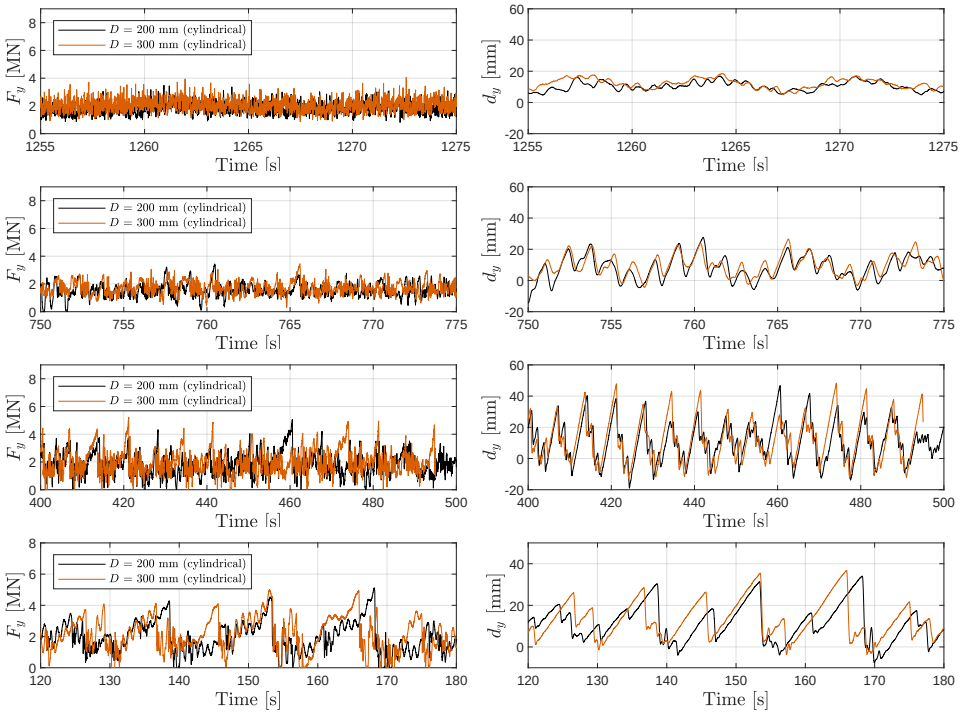


Figure 2.7: Time series of dynamic ice-induced vibrations experiments for two structures with different diameter. For better comparability ice load levels have been scaled to full-scale.

rectangular) on the ice-induced vibrations were negligible. However, it was noted that radial cracks at the corners of the rectangular SLS-print occurred.

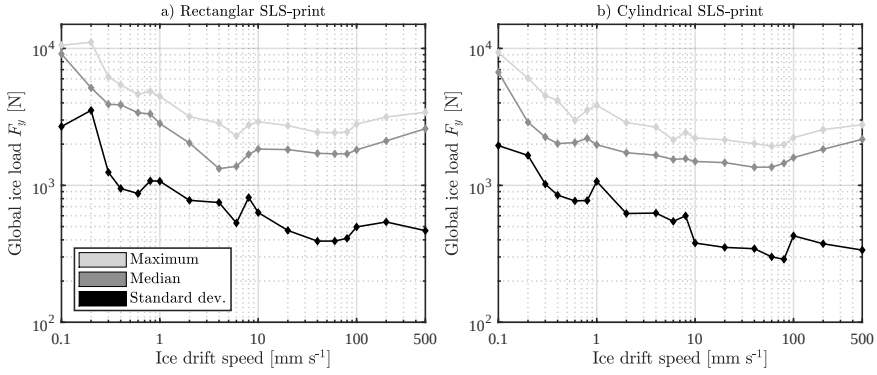


Figure 2.8: Results of rigid indenter tests for two different structural shapes with the same effective width.

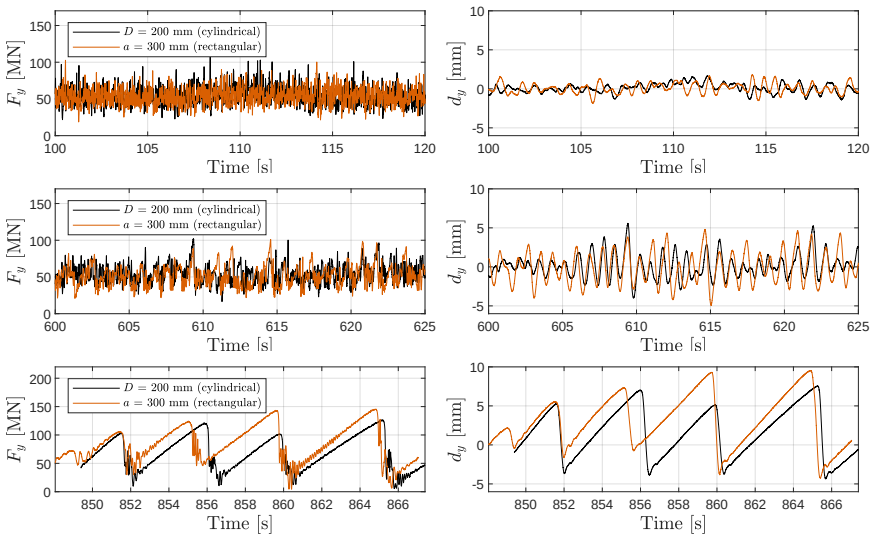


Figure 2.9: Time series of dynamic ice-induced vibrations experiments for two structures with different shape and diameter. For better comparability ice load levels have been scaled to full-scale.

2.6. VALIDATION

Finally, the suggested scaling method is applied to investigate if representative ice-induced vibrations of offshore structures can be reproduced by ice tank experiments. Experimental findings were compared to full-scale events. Acknowledging the presence of uncertainties in the environmental data of the full-scale dataset, it is imperative to recognize that this section serves the purpose of identifying if the ice-induced regimes can be predicted qualitatively, rather than striving to achieve a quantitative match with the data. However, to generate a qualitative comparison, classification criteria are applied to identify the ice-induced vibration regimes that developed. The criteria established to classify ice-induced vibration regimes R_{IIV} draw upon the classification framework for ice-induced vibrations of offshore wind turbines (see Hammer *et al.* (2022)). Thus, intermittent crushing (ICR), multi-modal (ice-structure) interaction (MMI), frequency lock-in (FLI), and continuous brittle crushing (CBR) have been categorized through the application of the following formula:

$$R_{IIV} = \begin{cases} ICR & \text{if periodicity}^* \text{ and } T_{\text{peak}} < 0.5 \cdot T_{\text{nat},1} \\ ICR \text{ or } FLI \text{ (or } MMI) & \text{if periodicity}^* \text{ and } 0.5 \cdot T_{\text{nat},1} < T_{\text{peak}} < CI(1) \cdot T_{\text{nat},1} \\ FLI \text{ (or } MMI) & \text{if periodicity}^* \text{ and } CI(1) \cdot T_{\text{nat},1} < T_{\text{peak}} < CI(2) \cdot T_{\text{nat},1} \\ & \text{and } v_{\text{rel}}^{**} < v_1 \\ CBR & \text{if no apparent periodicity}^*. \end{cases} \tag{2.3}$$

Here T_{peak} is the peak period of structural response (i.e., structural acceleration) as manifested in the measurements, while $T_{nat,i}$ signifies the natural period associated to the mode i of the numerical structure model. A coupling interval (CI) is introduced to incorporate the effects of added mass and damping on the period of vibration (here CI = [0.8, 1.2]). The periodic relative velocity between structure and ice is defined as v_{rel}. The velocity v_1 is the largest ice velocity at which a load peak increase caused by simultaneous ice failure can be measured in rigid indenter experiments.

Ice-induced vibrations as experienced by two full-scale offshore structures were simulated by applying the scaling method introduced in this work: the Norströmsgrund lighthouse (NSG lighthouse) and the Molikpaq platform (Molikpaq).

2.6.1. MOLIKPAQ EVENT

The Molikpaq platform experienced notable ice-induced vibrations on the 12th of May, 1986, while operating in the Beaufort Sea, as documented by Jefferies and Wright (1988), and analyzed by Gagnon (2012) and Owen and Hendrikse (2021). The full-scale mean brittle crushing ice load from intact ice involved in the dynamic process ($\bar{F}_{\text{f}}$) was estimated as 50 MN. This estimation is based on the load measurement during the Molikpaq event as visualized in Gagnon (2012). As demonstrated by Gagnon, a static baseline load (i.e., ice rubble force) of roughly 100 MN should be subtracted from the total load signal to get an estimation of the mean brittle crushing ice load.

To simulate the ice-induced vibration event of the Molikpaq platform, experiments were conducted using a decelerating 'ramped' ice drift speed (v_{ice}) as also the ice floe during the event slowed down when crushing against the structure. The starting ice drift speed was based on the documented full-scale ice drift speed of 85 mm s^{-1} (Kärnä, 2011b). Given that experiments for the Molikpaq event during the first SHIVER model test campaign showed that ice drift speeds between 85 mm s^{-1} and 55 mm s^{-1} predominantly result in continuous brittle crushing and considering the limitations of crushing length in ice tank experiments, the velocity ramp was initiated at an ice drift speed of 55 mm s^{-1} during the experiments. The ice decelerated at a constant rate of approximately 0.066 mm s^{-2}. The acceleration in full-scale was non-linear which could not be captured in the ice tank. Therefore, it was settled on an estimate for the deceleration around where ICR happened (last minute of the full-scale signal (see Gagnon (2012))), understanding that this would lengthen the periods of CBR and FLI in the signal (if occurring) compared to full-scale. Although the ice mainly crushed against the flat north side of the Molikpaq platform, a cylindrical structure was used during the experiments to avoid radial cracks, as those cracks are unknown to be representative of those in full-scale.

The time series of the experiments were low-pass filtered with a cut-off frequency of 5 Hz and 50 Hz for the acceleration and ice load, respectively. The cut-off frequency for

*Periodicity of structural response.

**When investigating MMI also higher mode vibrations must be investigated to distinguish superposed high frequency oscillations from higher mode lock-in vibrations

the acceleration was chosen with respect to the highest structural frequency considered in numerical structure modeling. After filtering, data were resampled to the original sampling rate of 50 Hz to improve comparability between time series of the model-scale and full-scale measurements. The full time series of the postprocessed global ice load F_y and structural acceleration at waterline (WL) for the Molikpaq event are shown in Figure 2.10 to Figure 2.13.

The experimental results of the 'deceleration test', involving ice drifting against the Molikpaq and here slowing down against the aluminium pile, are compared in Figure 2.10 to three burst files included in the full-scale data. It should be noted that the CBR and FLI data, originally presented as a single CBR burst by Kärnä (2011a), have been separated. When zooming in on the three distinct regimes (Figure 2.11 for CBR, Figure 2.12 for FLI, and Figure 2.13 for ICR), it can be shown that all regimes have been representatively reproduced. The overprediction in the standard deviation of the ice load during continuous brittle crushing is assumed to be caused by the upscaling of non-simultaneous failure peaks (see Section 2.5.1). Also, response periods simulated in the experiments are slightly longer than in full-scale as the ice floe deceleration was underestimated.

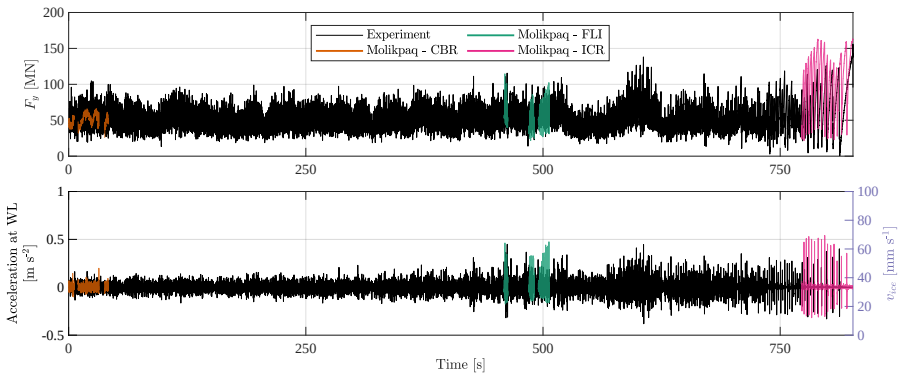


Figure 2.10: Experimental results (Hammer and Hendrikse, 2023a) in comparison to IIV of the Molikpaq platform as extracted from Kärnä (2011a).

2.6.2. NORSTRÖMSGRUND (NSG) LIGHTHOUSE EVENTS

The NSG lighthouse is situated in the Bothnian Bay, located in the Northern Baltic Sea. Full-scale measurements of ice loads and structural acceleration for the lighthouse were conducted during the STRICE test campaign between 2000 and 2003 (Kärnä and Jochmann, 2003). Postprocessed data from the ice-induced vibration events on the 4th of April 2002, 25th of March 2003, and 9th of April 2001 were analyzed in the ice-induced vibrations Joint Industry Project (JIP) (Kärnä, 2011a). For validation purposes, ice loads and accelerations recorded during these events were used in the present study. The full-scale mean brittle crushing ice loads ($\bar{F}_f$) of 0.377 MN, 1.559 MN and 1.011 MN, along with constant ice drift speeds (v_{ice}) of 30 mm s^{-1}, 50 mm s^{-1} and 100 mm s^{-1}, respectively, were extracted from the project report. Due to uncertainty in full-scale ice

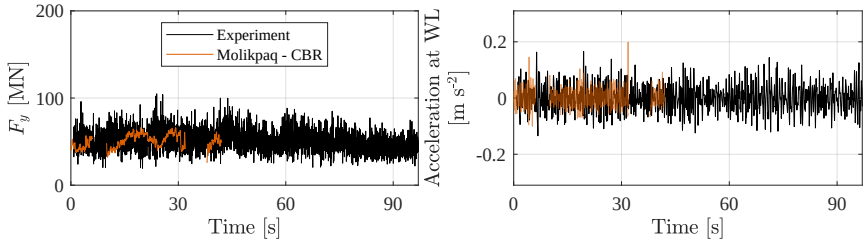


Figure 2.11: Comparison of experimental results (Hammer and Hendrikse, 2023a) and full-scale data of the Molikpaq event 12.05.1986 at high ice drift speed (continuous brittle crushing) as extracted from Kärnä (2011a).

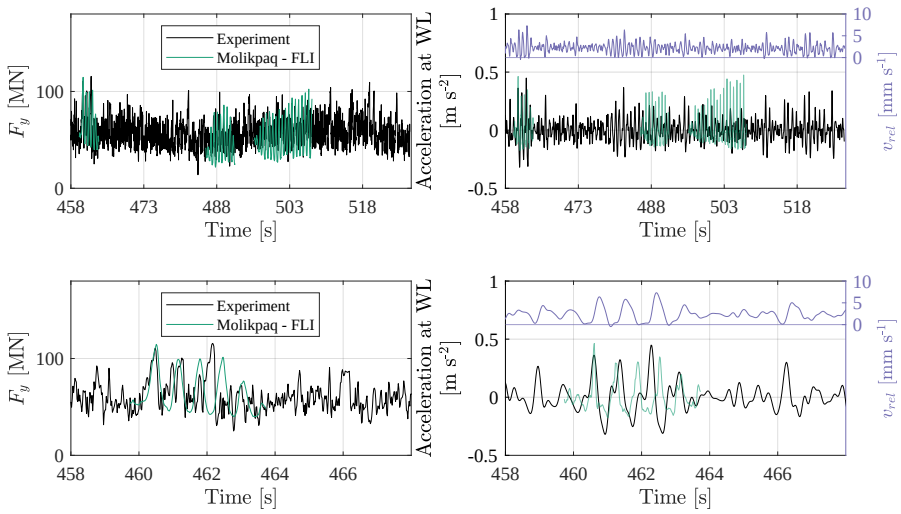


Figure 2.12: Top row: Comparison of experimental results (Hammer and Hendrikse, 2023a) and full-scale data of the Molikpaq event 12.05.1986 at intermediate ice drift speed (bursts of amplified load and response representative for frequency lock-in) as extracted from Kärnä (2011a). Bottom row: Close up.

drift speed measurements (Kärnä, 2011a), experiments were conducted with ice drift speeds at, above, and below the full-scale ice drift speeds documented. Tests for the NSG Lighthouse were performed exclusively with the aluminum pile.

The time series of the experiments were low-pass filtered with a cut-off frequency of 30 Hz for both acceleration and ice load of the NSG Lighthouse. The cut-off frequency for the acceleration was chosen with respect to the highest structural frequency considered in the numerical structure model. After filtering, data have been resampled to the original sampling rate of 30 Hz to improve comparability between time series of the model-scale

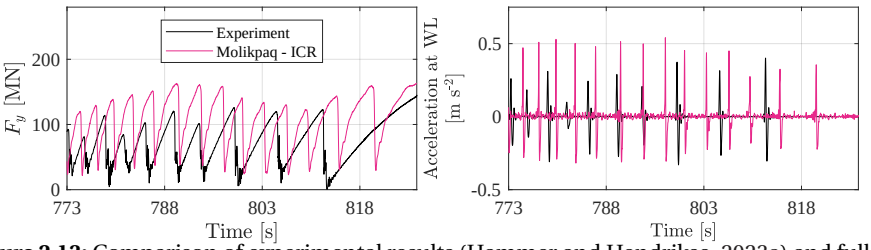


Figure 2.13: Comparison of experimental results (Hammer and Hendrikse, 2023a) and full-scale data of the Molikpaq event 12.05.1986 at low ice drift speed (intermittent crushing) as extracted from Kärnä (2011a).

and full-scale measurements. The full time series of the postprocessed global ice load F_y and structural acceleration at waterline (WL) are shown in Figure 2.14 to Figure 2.16.

Focusing on the experimental results for the ice-induced vibration event of the NSG lighthouse on the 04.04.2002 in Figure 2.14, tendencies towards frequency lock-in can be found. However, those vibrations are not as pronounced as observed in full-scale. Experimental results for the ice-induced vibration event of the NSG lighthouse on the 25.03.2003 in Figure 2.15 show a short lock-in burst starting at $t = 45$ s, which is also visible by the higher load peaks in the load signal. Neither vibrations of the NSG lighthouse in full-scale nor vibrations as measured in experiments were sustained. Experimental results in Figure 2.16 cannot be validated as no tendency to frequency lock-in occurred. This finding is discussed in Section 2.7.

A summary of the experimental results for the Molikpaq platform and NSG lighthouse is provided in Table 2.6. The experiments managed to successfully reproduce the regimes of ice-induced vibrations observed in full-scale (i.e., ICR, FLI/MMI, and CBR) except for the frequency lock-in event on 09.04.2001. The primary difference observed between the model-scale experiments and full-scale events was that the NSG lighthouse frequency lock-in events could only converge at lower ice drift speeds compared to those documented in the full-scale events (see Table 2.6).

The selected full-scale events were chosen as these were seen as most representative full-scale events of ice-induced vibrations. Additional details of the experiments conducted for the Molikpaq and the NSG lighthouse can be found in Table 1 and Table 2 in the supplementary material of Hammer *et al.* (2024) including corresponding velocity profiles and implemented dynamic structural models. Note that the structural properties in the structural files, which also can be found in the supplementary material, were scaled for the measured mean ice load ($\bar{F}_{\mathrm{m}}$) during the experiments. A summary of the full-scale events can be found in Kärnä *et al.* (2013), from which the table of selected validation cases was reproduced in Table 3 in the supplementary material of Hammer *et al.* (2024).

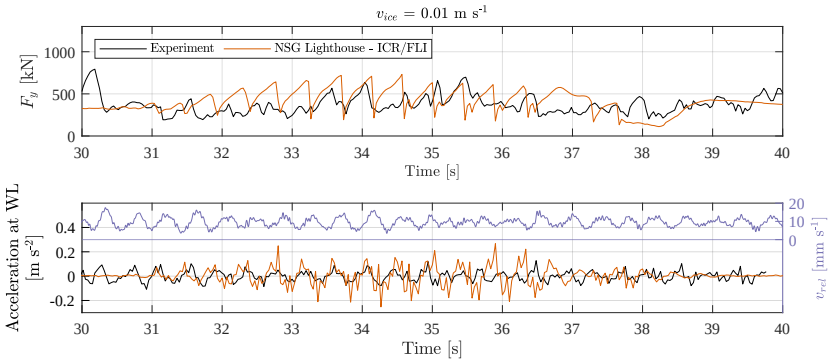


Figure 2.14: Experimental results (Hammer and Hendrikse, 2023a) in comparison to the ice-induced vibration-event of the NSG Lighthouse on the 04.04.2002 as extracted from Kärnä (2011a).

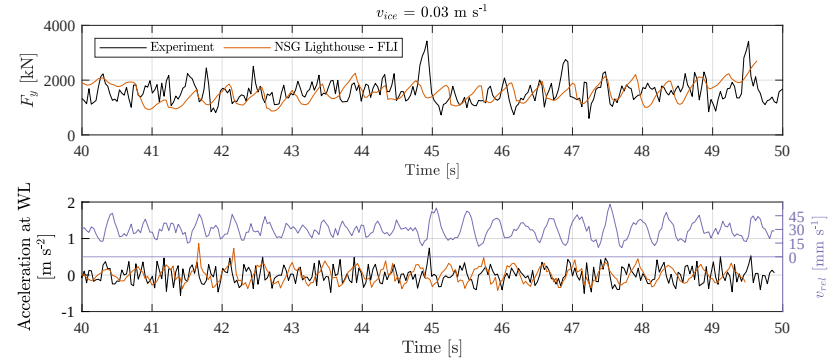


Figure 2.15: Experimental results (Hammer and Hendrikse, 2023a) in comparison to the ice-induced vibration-event of the NSG Lighthouse on the 25.03.2003 as extracted from Kärnä (2011a).

2.7. DISCUSSION

2.7.1. SCALING VERIFICATION

The present study aimed to verify the proposed scaling technique for the application of ice-structure interaction of vertically sided structures. The cold model ice failed purely in crushing and produced a load increase at lower ice drift speeds (velocity effect). Other types of model ice, such as the *wave model ice* developed by Ziemer (2021), also have been shown to fail in crushing. If these model ice types can demonstrate a velocity effect and transition speeds comparable to sea ice, they could potentially be utilized for applying the presented scaling method. Note that the transition speed, in the present thesis, is defined as the indentation speed at which the macroscopic creep changes to a fracture dominated failure of the ice. However, there is limited full-scale data from indentation tests on this transition speed. For that reason results obtained from uniaxial compressive strength tests are also considered, indicating that the transition speed, as defined in this

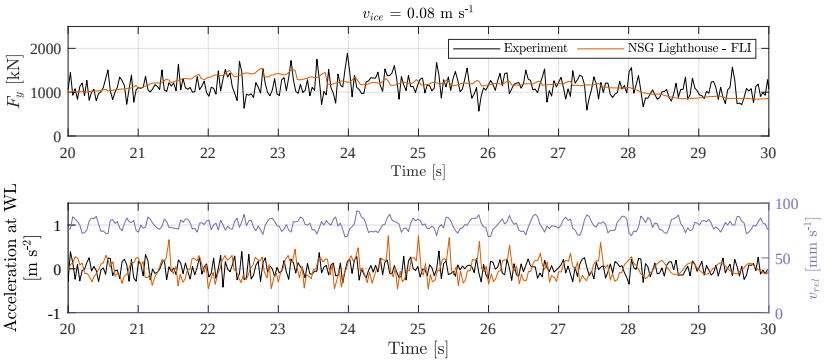


Figure 2.16: Experimental results (Hammer and Hendrikse, 2023a) in comparison to ice-induced vibration-event of the NSG Lighthouse on the 09.04.2001 as extracted from Kärnä (2011a).

Table 2.6: Summary of validation cases. Note that the second column is based on data from the second SHIVER model test campaign (Hammer and Hendrikse, 2023a).

Event	Date	Regimes based on Kärnä (2011a)	v_{ice} [mm s^{-1}]	R_{IIV}	v_{ice} [mm s^{-1}]
Molikpaq	12.05.1986	CBR	>85	CBR	>30
	12.05.1986	"Phase locked"	85>v_{ice}>10	FLI	30>v_{ice}>10
	12.05.1986	ICR	<10	ICR	<10
NSG Lighthouse	04.04.2002	ICR/FLI	30	FLI/CBR	10
	25.03.2003	FLI	50	FLI/CBR	30
	09.04.2001	FLI	100	CBR	80

work, and the transition speed based on the measurement of strain rate measurements might correlate. However, it remains unknown how to define strain rate in the context of an indentation experiment, and whether the transition from macroscopic creep to fracture coincides with the 'ductile-to-brittle' transition observed in small-scale material tests. It is even most likely that the transition speed chosen for scaling is in fact controlled by a more fundamental ice property, such as the ice temperature.

During the verification process, the requirement for elastic and strength similarity was relaxed. This decision was based on the understanding that achieving similar elasticity and strength in ice might not be essential when attempting to reproduce ice-induced vibrations. As the present study managed to reproduce full-scale events while relaxing the elastic and strength similarity, this approach seems to be reasonable. Results indicated that no significant aspect ratio effect occurred in the experiments. Nonetheless, the difference between the investigated physical prototypes diameter was small (aspect ratio change from 8 to 12). Experiments with a larger diameter are expected to manifest scaling effects in the magnitude of the standard deviation due to averaging of high-pressure zone formation for a larger area. This scaling effect could explain the different magnitude of the standard deviation of ice loads during continuous brittle crushing of the Molikpaq

platform (Figure 2.11- left). However, representative ice-induced vibrations can still be achieved as the scaling method is based on the mean ice load level and not on peak pressures. The rectangular print led to the formation of radial cracks during testing. However, no further analysis regarding crack frequency, formation, propagation, or their representativeness for ice-induced vibrations of the Molikpaq platform was performed. The cylindrical pile already yielded representative outcomes.

2.7.2. VALIDATION

While the model-scale results were representative of the Molikpaq event, the results for the Norströmsgrund lighthouse require some further discussion. Frequency lock-in of the NSG lighthouse model for environmental conditions applied as documented for the 9th of April 2001 was not observed in the ice tank. A challenge here is that the NSG lighthouse as a relatively stiff structure, almost never experienced long sustained frequency lock-in events, as, for example, observed for the more flexible structures in the Bohai Bay (Yue *et al.*, 2002). Given the non-linearity of the ice-structure interaction, the initial conditions play a significant role in cases where sustained lock-in is not possible. As seen during the experiment simulating the event on the 25th of March (see Figure 2.15), the tendency to frequency lock-in only occurred for part of the time. This is very representative of the full-scale scenario, but also shows how difficult it is to use these full-scale data for validation as one cannot generate specific initial conditions in an ice tank. Such initial conditions have been reported upon by Bjerkås (2006), for example, as smooth ice edges interacting with the lighthouse because of previous radial cracking. Thus, relaxing the input parameters, results of an experiment scaled for a higher full-scale ice load (2 MN), as tested in the first SHIVER model test campaign (Hendrikse *et al.*, 2022a), was used for comparison in Figure 2.17. It can be seen that frequency lock-in of the NSG lighthouse does occur in the cold model ice. This is indicative that the experiments conducted are at the boundary between no frequency lock-in and sustained frequency lock-in which corresponds well to the actual full-scale observations. It is not a challenge to obtain sustained lock-in signals in an ice tank, the challenge is to achieve a boundary regime where the ice load magnitude is just insufficient for sustained frequency lock-in, but in certain cases of specific initial conditions (high peak load, slightly thicker than average ice) can cause short bursts of vibrations.

Notably, there is some uncertainty with respect to the full-scale load levels due to only partial instrumentation of the waterline of the NSG lighthouse with load panels. In addition, recordings of a camera attached to the structure were used to define the ice drift speeds. The authors of the report themselves acknowledged the potential for an overestimation of the documented ice drift speeds (Kärnä, 2011a). Testing for too high ice drift speeds promotes continuous brittle crushing over frequency lock-in. The accuracy of ice drift speed inputs could be achieved by applying an ice drift tracking routine on available video footage (Nord *et al.*, 2018).

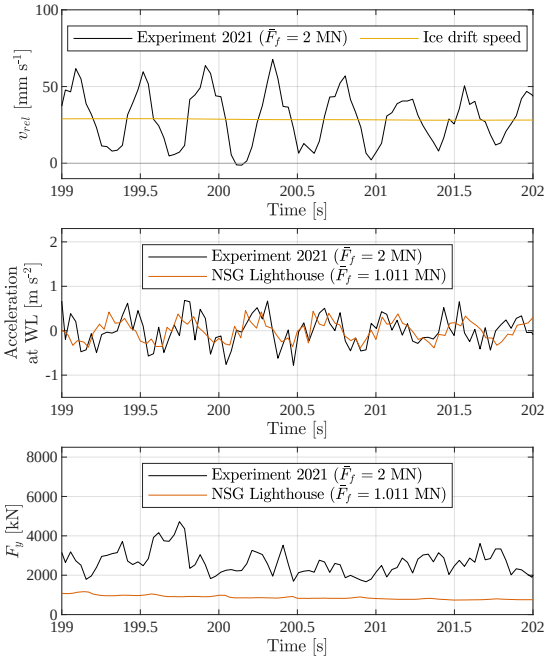


Figure 2.17: Experimental results of the relative velocity and structural acceleration at water level (WL) as measured in the experiments of the first SHIVER model test campaign for the NSG Lighthouse scaled with $\bar{F}_f$ = 2 MN (Hendrikse *et al.*, 2022a) as recorded in the full-scale event on the 09.04.2001 Kärnä (2011a).

2.7.3. DATA RELIABILITY

To assess the reliability of the load data, a comparison between median ice loads obtained from a direct shear load measurement (see sensor 4 in Figure 3 in Hammer *et al.* (2021)) and the identified, horizontal ice loads was conducted. The comparison results are presented in Figure 1 of the supplementary material of Hammer *et al.* (2024), revealing a good agreement between the two measurements. Within the same figure, vertical loads appear minor in contrast to horizontal loads. Consequently, it was assumed that no significant upward or downward ice movement occurred during the crushing model scale experiments. This observation is corroborated by the paint removal on the prints (refer to Figure 2.2), indicating that the model ice exerted force against the structure at the anticipated interaction point mainly. The shortening of the aluminum pile and the utilization of honey-combed SLS-prints minimized masses affecting load cell measurements. The contribution of inertial loading was thus negligible.

2.7.4. APPLICATION

The applicability of the suggested scaling method is contingent upon the quality of the environmental load envelope (same holds for numerical simulations). Once these conditions are known, the full-scale mean (or alternatively, median) brittle crushing ice

load can, for example, be estimated utilizing eq. A.8–21 of ISO 19906:2019(E) (2019). Alternatively, the full-scale mean ice load can be extracted from an ice model simulation during continuous brittle crushing with a rigid structure (e.g., by application of the model presented in Appendix A). The scaling as applied to test the Molikpaq structure in model ice (Section 2.6.1 is presented as example in Appendix B.

Finally, it is emphasized that the scaling method was exclusively applied for two full-scale structures. Comprehensive and synchronized high-resolution measurements of ice load and structural displacement of an offshore structure facing crushing ice loads, along with synchronized environmental data (e.g., ice drift speed measurements), would be invaluable for further evaluation of the proposed scaling method. The limited access to full-scale data constitutes the most significant constraint of the present study, together with limited full-scale data revealing the transition speeds for rigid indenter experiments.

2.7.5. LIMITATIONS

The investigated scaling method can be applied to offshore structures subjected to predominantly crushing ice loads. As highlighted in the introduction, other dominant failure modes would likely not allow omission of global mass similarity. Also, at higher ice drift speeds, ice extrusion prevents the neglection of mass similarity. The scaling method is thus only valid when the mean ice load, used for scaling, is rate-unaffected (see Figure 2.3). The scaling approach does not focus on local peak pressures or exact peak loads during high-speed crushing. Thus, it is not critical that the aspect ratio scale effect inhibits a qualitative reproduction of the high frequency peaks during continuous brittle crushing. Another limitation of the study is the requirement of a mean ice load estimation for applying the scaling. However, mean loads can be estimated by ice models coupled to rigid structures. Additionally, it is crucial to underscore that the approach was verified for structures with relatively low first natural frequencies (0.15 Hz to 2.5 Hz). Whether structures with higher frequencies can be assessed in a similar manner remains to be tested.

2.8. CONCLUSION

The combination of replica modeling (i.e., effective pressure preservation at relevant scale) and preservation of kinematics during ice-structure interaction has been applied as a scaling technique for investigating ice-induced vibrations of vertically sided offshore structures in ice tank experiments. Based on recent theoretical developments, the kinematics during ice-structure interaction, the transition speed, the velocity effect and the mean brittle ice crushing load level were chosen to define the energy transfer to the structure and thus controlling the mechanism of ice-induced vibrations. It has been proposed that the (here: ethanol-doped) model ice must fail in crushing and demonstrate both the existence of a transition speed and velocity effect for rigid structures. The transition speed macroscopic creep changes to a fracture dominated failure of the ice was adopted as a reference property of the ice, defining its time- and rate-dependent behavior. The ratio between the full-scale and the model-scale mean brittle crushing ice load was used to scale numerical structure properties. Thorough rigid indenter experiments in

combination with ice-induced vibrations experiments of structures with different aspect ratio and shape were conducted to verify the scaling approach. No observable scaling effects on the velocity effect, transition speed, and development of ice-induced vibrations were found when varying between a cylindrical and rectangular shape of same width, or when changing the aspect ratio in a range between 8 and 12. The proposed scaling technique was qualitatively validated by performing novel ice tank experiments to reproduce the full-scale ice-induced vibrations experienced by the Molikpaq platform and the Norströmsgrund lighthouse. Regrettably, the lack of well-documented, synchronized, and high-frequency sampled full-scale measurements on structures susceptible to ice-induced vibrations continues to hinder a quantitative validation of scaling approaches, though the results obtained in the experiments are promising.


Shiver
TUDelft
SIEMENS

3

HARDWARE-IN-THE-LOOP EXPERIMENTS IN MODEL ICE FOR ANALYSIS OF ICE-INDUCED VIBRATIONS OF OFFSHORE STRUCTURES

In the present chapter, the development and applicability of a hybrid test setup in model ice is described and analyzed. It is investigated if offshore structures with low and multiple eigenfrequencies could be tested in ice experiments. The robustness and performance of 204 hybrid simulations in model ice is investigated while the main analysis focuses on outliers in the results. Additional experiments were performed to determine the critical delay of offshore structures tested in the experiments.

3.1. INTRODUCTION

Offshore structures interacting with level sea ice crushing against the vertical interface of the structure can result in highly non-linear ice-induced vibrations of the offshore structure (Hendrikse, 2019). The analysis of these vibrations is challenging, stemming from the non-existence or proprietary availability of comprehensive full-scale data, inadequacies in scaling laws, or restricted capabilities of test facilities for large-scaled experiments. In the past, test setups developed for experimental analysis of ice-induced vibrations consisted of clamping mechanisms, different spring configurations, and modular mass

This chapter has been published in **Scientific Reports** as *Hardware-in-the-Loop experiments in model ice for analysis of ice-induced vibrations of offshore structures* in 2024 (Hammer and Hendrikse, 2024b). Textual passages may vary. Data for this chapter have been collected during **the second SHIVER model test campaign** and have been published separately (Hammer and Hendrikse, 2024a). Data from other sources are indicated as such.

blocks to adjust the physical structural stiffness and mass of the test setup (Hendrikse *et al.*, 2018; Määttänen, 1983; Ziemer and Evers, 2016). However, these setups reached their limits when it came to investigate offshore structures, such as offshore wind turbines, as setups could not achieve the required lowest natural frequencies due to the load, size, and noise capacities during ice tank or basin experiments.

Modern experiments more regularly consider the application of hybrid testing techniques for analysis of rate-dependent loading scenarios of offshore structures. Those techniques minimize the components of a scaled physical structural model, achieving this by dividing the structure into both physical and numerical components. This approach allows for the translation of intricate physical structural elements into the numerical domain, with only those parts directly affected by the environmental hazard being physically represented. In the fields of mechanical and aerospace engineering, particularly in applications like flight simulator development, hybrid testing techniques are often known as hardware-in-the-loop simulations (Palacio-Betancur and Gutierrez Soto, 2023). When the concept was transferred to the field of civil engineering, the term pseudo-dynamic testing was introduced (Hakuno *et al.*, 1969; Takanashi *et al.*, 1975). The initial form of hybrid testing involved a clear separation of two phases, one dedicated to the application of loads and the other to calculate the structural response. This division of phases characterized the method as a quasi-static testing approach. To circumvent the recuperation of reversible processes during the calculation phase, a continuous pseudo-hybrid testing method was introduced (Takanashi and Ohi, 1983), meaning that the physical test setup was accompanied by actuators that prevented motion discontinuity. Subsequently, fast continuous pseudo-dynamic testing methods emerged. For these methods, the time scale between calculation and real-time operation converged, leading to real-time pseudo dynamic testing (Nakashima *et al.*, 1992). The main differences between hardware-in-the-loop systems and real-time hybrid simulations is that latter consists of an outer loop establishing a dynamic feedback loop based on the simulated and measured output.

In hardware-in-the loop systems, the physical prototype generates a force while the response of the physical prototype is generated in the numerical domain, involving a numerical solver, which can be implemented explicitly or implicitly. An explicit solver, on the one hand, is relatively straightforward to implement and requires lower computational resources. On the other hand, an implicit solver is more complicated but offers the advantage of unconditional stability of the numerical model (Palacio-Betancur and Gutierrez Soto, 2023). The numerical output is imposed on the physical prototype by electrical or hydraulic actuators, which can be tailored to work for a single axis or multiple axes (Bonnet, 2006; Najafi *et al.*, 2020). The loop introduces delays due to communication between the computer, servo-controller, and data acquisition system (Carrion and Spencer, 2007). However, it has been observed that the most critical source of delay is attributed to the actuator itself (Zhao *et al.*, 2003). The concern arises from the phase shift between the numerical and actual responses, which results in a counterclockwise energy hysteresis, signifying an irreversible energy gain in the system, commonly referred to as negative damping (Horiuchi *et al.*, 1999). If this accumulated energy leads to instability of the system, it can significantly reduce the performance and accuracy of the system. To identify and predict instability of the system, a critical time delay can be formulated. The

formulation is typically derived by solving the characteristic equations of delay differential equations, applicable to both single-degree-of-freedom representations of structures ((Wallace *et al.*, 2004; Zhou *et al.*, 2023a)), and multi-degree-of-freedom representations of structures (Gao and You, 2019; Maghareh *et al.*, 2016). Once a system provides a delay larger than the critical delay, the system can be expected to become unstable.

Hybrid test setups have found adaptation in various disciplines, serving diverse applications, including the modeling of seismic events McCrum and Williams (2016)); active, tuned or liquid damper (Chen and Chen, 2023; Liu *et al.*, 2024; Wu and Song, 2019; Zhang *et al.*, 2019); hydrodynamics (e.g., floating offshore wind turbines) (Bachynski *et al.*, 2016; Luan *et al.*, 2018; Sauder *et al.*, 2016; Sun *et al.*, 2022; Thys *et al.*, 2018); aerodynamics (Ruffini *et al.*, 2020; Wu and Song, 2019; Zhang *et al.*, 2019); fire (Abbiati *et al.*, 2020; Mergny and Franssen, 2022; Wang *et al.*, 2019); geotechnical centrifuges (Kong *et al.*, 2015); coupled seismic and hydrodynamic events (Neumann *et al.*, 2023; Zhou *et al.*, 2023b); bridge piers (Park *et al.*, 2023); vehicles (Witteveen and Koller, 2023); neuroscience (Amaducci *et al.*, 2019); biomedical engineering (Insam *et al.*, 2021); or the deployment of a parachute for a Mars space shuttle (Linderholt *et al.*, 2020).

So far, hybrid testing techniques mainly have been applied in scenarios when the externally applied forces could be controlled. The effect of the structural response on the external force was either zero or insignificant and thus structural responses quasi-static or harmonic. For ice-induced vibrations neither the force nor the forcing frequency can be predefined or accurately be predicted - the system must consider highly non-linear and almost instantaneous frequency and magnitude variations in the loading (and thus response). Due to the unpredictability of the response even small delays in system could lead to a zero phase margin within the open loop and thus instability of the system.

The objective of this study was to analyze the robustness, performance and limitations of a test setup developed for hardware-in-the-loop simulations in model ice (HILSI). The novel application of HILSI would introduce several advantages: properties of the offshore structure could be varied numerically; multi-degree-of-freedom representations of structures in ice could be investigated and multi-axial ice loading be simulated. But most important the method would allow to test structures with relatively low natural eigenfrequencies typical of heavy or tall offshore structures like for example offshore wind turbines in model ice experiments.

The study begins by introducing and explaining the hybrid test setup developed. Next, 204 separate experiments are investigated to analyze the robustness and performance of HILSI. Outliers are analyzed in greater detail. Furthermore, the critical delay of tested offshore structures is experimentally determined and compared to an analytically calculated delay. Finally, the results are discussed, and a conclusion is provided.

3.2. METHOD

3.2.1. HARDWARE-IN-THE-LOOP TESTING

In the present study, the full offshore structure has been simplified during the Hardware-in-the-Loop experiments as illustrated in Figure 3.1. The idea of the developed system was that only the small ice loaded strip of the full-scale structure is modelled physically. The mass of this strip is insignificant in comparison to the mass of the full-scale structure. It was thus decided to simplify the physical prototype to a rigid, geometrical interface that can crush the ice while providing insignificant damping and mass. Thus neither stiffness, mass, nor damping were assigned to the physical prototype and it became effectively a single point with negligible mass. The pile was manufactured from thin-walled aluminium to minimize the mass while deforming less than 10 micrometer under estimated maximum ice loading.

The structural model and potential wind load are both handled numerically. Motion of the physical prototype was imposed by two electrical actuators. The complete hardware was mounted to a carriage of the Ice and Wave tank of the Aalto University. While it is feasible to push ice sheets against a stationary structure, the chosen approach was to move the entire test setup through a stationary ice sheet instead. This decision was influenced by the existing infrastructure of ice tanks, which are often tailored for maneuvering ship models through stationary ice sheets. Consequently, these ice tanks frequently feature a carriage designed to traverse rail systems along an ice channel or attached to a bridge which extends across an entire basin to allow for bi-directional movement. Utilizing a support frame (see Figure Figure 3.2a), the developed setup was affixed to the carriage of the tank and then moved through the ice as depicted in Figure 3.2b. A narrow open channel can be seen in Figure 3.2b as the physical prototype (i.e., the aluminum pile) crushes through the ice.

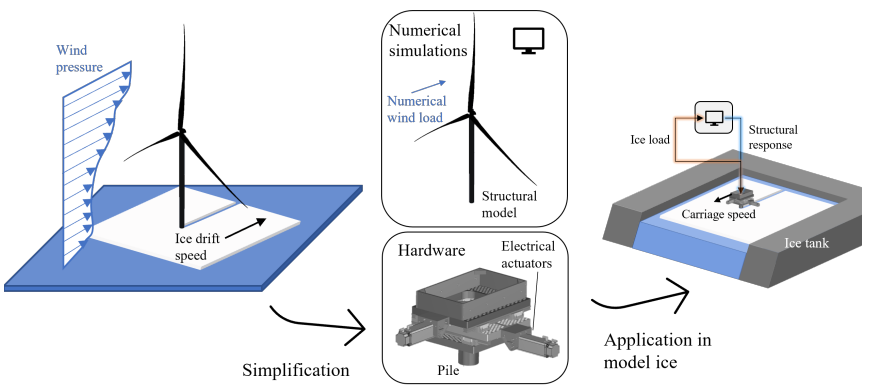
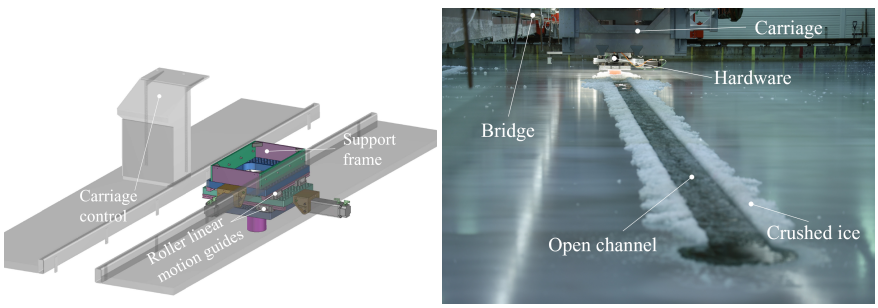


Figure 3.1: The full problem of an offshore wind turbine under wind and ice loading was simplified to a hardware-in-the-loop system.

3.2.2. HARDWARE AND NUMERICS

The primary components of the hardware comprised three aluminum plates (see Figure 3.3). The upper plate was rigidly bolted to the carriage by installation of an additional support frame (Figure 3.2a). In contrast, the two lower plates were capable of uni-directional movement, enabled by the installation of four caged roller linear motion guides. These guides were designed to minimize friction within the system. To further reduce the overall system mass and subsequently lessen the inertial load experienced by the actuators and recorded by the implemented sensors for ice load identification, a honeycomb hollowing pattern was milled into the aluminum plates. This weight reduction also ensured compliance with the load limits of the carriage-bridge system.



(a) Schematic of the hardware attached to the carriage.

(b) Photograph of an open water channel after performing HILSI in an ice tank.

Figure 3.2: Application of a hardwrae-in-the-loop sytem in model ice.

The bi-axial displacements of the two lower plates were precisely monitored using magnetostrictive displacement sensors T(BIW0007-BIW1-A310-M0250-P1-S115, Balluff B.V., 5232 BC 's-Hertogenbosch, The Netherlands). Two different ice load measurement systems in combination with two different aluminum piles were employed during the development of the hardware-in-the-loop system. In the first design[1], an aluminum pile featured two weakened rings to accommodate the installation of 16 strain gauges. This configuration allowed for the closest possible measurement of ice load to the waterline Hammer *et al.* (2021). The second design[2] utilized a shorter aluminum pile fitted with three load cells (2960-2962-2965 low-profile pancake load cells, SENSY S.A., 6040 Jumet, Belgium) at the flange of the pile Figure 3.4a. The shorter pile facilitated the use of 3D-printed adapters (Figure 3.3), which allowed for the adjustment of the interface shape, diameter, and slope of the physical prototype. The application of 3D-printed materials for conducting ice crushing experiments was investigated in advance by Petry *et al.* (2023). To capture the dynamics of the physical prototype, four accelerometers were strategically placed: one inside the pile (ADXL326, Analog Devices Inc., Wilmington MA 01887, USA) and one probe (ADXL327, Analog Devices Inc., Wilmington MA 01887, USA) each at the bottom, center, and top plate, as depicted in Figure 3.4b. Additionally, axial load measurements were carried out at the connection point between the top plate and

[1] First SHIVER model test campaign
[2] Second SHIVER model test campaign

the electrical actuators, utilizing VST5000 S-type load cells (HENK MAAS Weegschalen B.V., 4264 AW Veen, The Netherlands). This load measurement served for redundancy and verification of static load measurements. To document the setup from different angles, two cameras (GoPro Hero 9) were positioned to record video footage along each axis.

Two displacement-controlled electrical integrated motor actuators (GSX50-1005-MKR-SB5-358-G2, ACTUATION DIVISION - EXLAR Corporation, Eden Prairie MN 55346, USA). For computation, a Teensy USB Development Board (Version 3.6, PJRC) was installed. During the experiments, a PID controller (SD6 servo drive controller, STÖBER Antriebstechnik GmbH + Co. KG, Pforzheim, Germany) was used to enforce the boundary conditions between the numerical and physical prototype. The verification of the functionality of the control system was carried out by replicating predefined displacement time series in dry test experiments (Hammer *et al.*, 2021). During those experiments, the controller settings were tailored to each actuator separately to improve the overall performance. No outer loop control was implemented. Within the carriage, both motors of the controller were situated. Additionally, the software and data acquisition were overseen and managed from this location. The carriage is riding on twin rails and four dual bogies in total. The carriage is propelled by a rack-and-pinion system with two drive pinions.

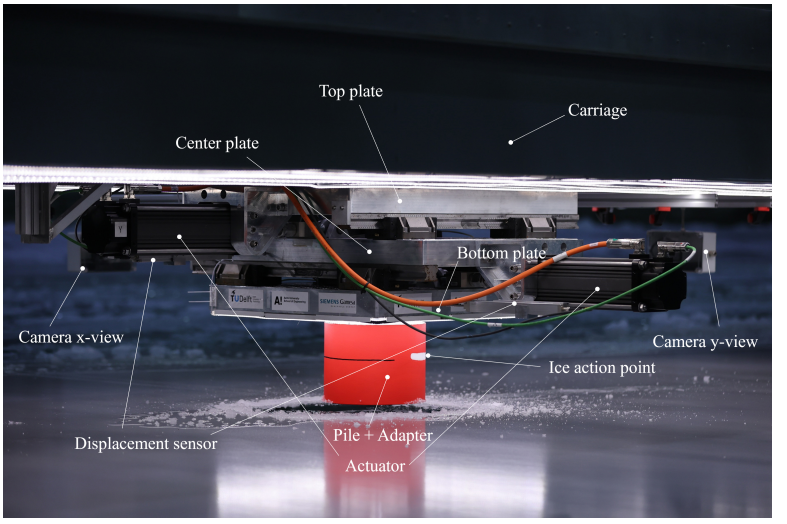
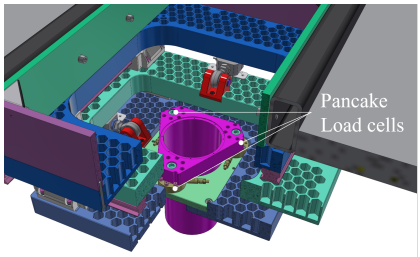


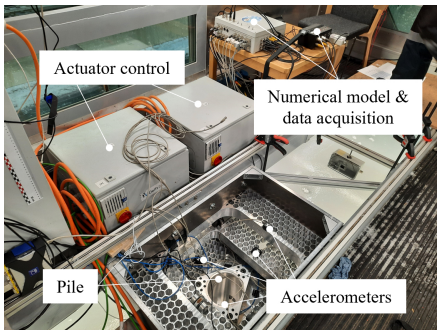
Figure 3.3: Photograph of the developed test setup during the second SHIVER model test campaign.

3.2.3. NUMERICAL SIMULATIONS

The offshore structures were represented by linearized single- or multi-degree-of-freedom models in the modal domain. These models encompassed structural properties, including frequency, damping, and mass-normalized modal amplitudes in both the x- and y-direction at the point of ice action. The structural models were truncated and com-



(a) Cross section of the physical prototype.



(b) Photograph of the hardware installed during the experiments.

Figure 3.4: Visualization of the developed test setup for hybrid tests in model ice.

prised structural frequencies up to 20 Hz to reduce the computational complexity and thus the internal simulation time. The value was also chosen as ice loads typically do not excite higher frequencies (see A.8.2.6.1.5 ISO 19906:2019(E) (2019)). Furthermore, the numerical model allowed for the application of external loads $F_{y;ext}$ and $F_{x;ext}$ at locations distinct from the ice action point, affecting the structural displacements in the x- and y-direction, respectively. For example, this facilitated the inclusion of wind loading at the tower top of an offshore wind turbine. The equations of motion in the modal domain are as follows:

$$\ddot{w}_i(t) + 2\zeta_i\omega_i\dot{w}_i(t) + \omega_i^2 w_i(t) = \begin{bmatrix}\phi_{i,x;ice} & \phi_{i,y;ice}\end{bmatrix}\begin{bmatrix}F_{x;ice}\\ F_{y;ice}\end{bmatrix} + \begin{bmatrix}\phi_{i,x;ext} & \phi_{i,y;ext}\end{bmatrix}\begin{bmatrix}F_{x;ext}\\ F_{y;ext}\end{bmatrix} \tag{3.1}$$

Here, w_i represents the modal displacement of mode i, and the over-dots signify derivatives with respect to time. ζ_i denotes the damping ratio as a fraction of critical damping, and ω_i stands for the natural frequency. $\phi_{i,x;ice}$ and $\phi_{i,y;ice}$ are the mass-normalized modal amplitudes of mode i at the ice point and $\phi_{i,x;ext}$ and $\phi_{i,y;ext}$ on any other external point respectively, satisfying the equation:

$$\boldsymbol{\phi}_i^T \cdot \boldsymbol{M} \cdot \boldsymbol{\phi}_i = 1. \tag{3.2}$$

Here, $\boldsymbol{M}$ refers to the mass matrix, and $\boldsymbol{\phi}_i$ represents the mass-normalized mode shape vector for mode i. Note that Equation (3.1) does not consider any contribution of the physical prototype as the pile was designed to behave as a rigid interface of negligible mass to crush the ice. The prototype displacement at the water line d_y as measured by the displacement sensors at time t_j at iteration j shown in Figure 3.3, is:

$$d_y(t_j) = x(t_j - \tau) \tag{3.3}$$

whereas

$$x(t_j) = \sum_{i=1}^{n} \phi_{i;x;ice} \cdot w_i(t_j); \tag{3.4}$$

τ is the delay between the output signal and the measured displacement. The equations were solved in each iteration j using the semi-implicit Euler-Cromer method with a time step size (Δt) of 10^{-4} s:

$$\ddot{w}_i(t_j) = \begin{bmatrix} \phi_{i;x;ice} & \phi_{i;y;ice} \end{bmatrix} \begin{bmatrix} F_{x;ice}(t_j) \\ F_{y;ice}(t_j) \end{bmatrix} + \begin{bmatrix} \phi_{i;x;ext} & \phi_{i;y;ext} \end{bmatrix} \begin{bmatrix} F_{x;ext}(t_j) \\ F_{y;ext}(t_j) \end{bmatrix} - 2\zeta_i \omega_i \dot{w}_i(t_j) - \omega_i^2 w_i(t_j) \tag{3.5}$$

with

$$\dot{w}_i(t_{j+1}) = \dot{w}_i(t_j) + \Delta t \cdot \ddot{w}_i(t_j) \tag{3.6}$$

and

$$w_i(t_{j+1}) = w_i(t_j) + \Delta t \cdot \dot{w}_i(t_{j+1}). \tag{3.7}$$

The execution time for the time-stepping function was approximately 55 µs for the structural model with the highest number of modes.

CONSTANT DELAY COMPENSATION

After analysis of initial experiments in the ice tank, the delay τ between the measured pile position and position in the control system was quantified to be 4-5 ms. To address this delay, a constant delay compensation was implemented to predict the structural position forward by a time interval of Δt_{fp} equal to 5 ms:

$$\dot{w}_{i;\text{fp}}(t_j) = \dot{w}_i(t_j) + \Delta t_{\text{fp}} \cdot \ddot{w}_i(t_j) \tag{3.8}$$

$$w_{i;\text{fp}}(t_j) = w_i(t_j) + \Delta t_{\text{fp}} \cdot \dot{w}_{i;\text{fp}}(t_j) \tag{3.9}$$

Here, $w_{i;\text{fp}}$ corresponds to the forward-predicted modal displacement. The forward-predicted output has been generated by substitution of $w_{i;\text{fp}}$ in Equation (3.4).

Two simplified flow charts, illustrating the signal flow in the system, are presented in Figure 3.5.

SCALING

The applied scaling method was described in Chapter 2. However, a short summary is given here. The scaling method combines replica modeling and preservation of kinematics during testing. More specifically, the replica modeling results in a mean pressure similarity, while the preservation of kinematics denies any scaling of time components (either of the structure or of the ice). The mean pressure similarity allows to scale the numerical structural properties based on the ratio between a measured model-scale and an estimated full-scale mean ice load. For example, the numerical mass, stiffness and

damping (m, k, c) are significantly but equally reduced when a large full-scale mean ice load (e.g., caused by a thick full-scale ice sheet) is tested for. The damping ratio ζ and structural eigenfrequency f remain unchanged since both numerical stiffness and mass are scaled by the same factor.

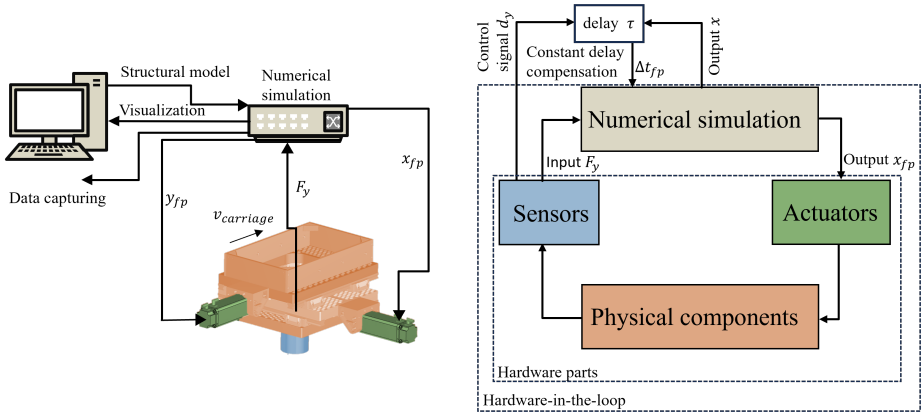


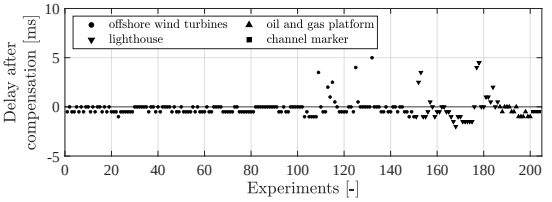
Figure 3.5: Signal flow charts illustrating the signal flow of the hardware-in-the-loop simulations. The box flow chart has been adapted from Lee and Tu (2014).

In the next section, the robustness and performance of the HILSI is analyzed. It should be noted that the delay shown in the following two sections, if not stated otherwise, is the delay before application of the constant forward prediction.

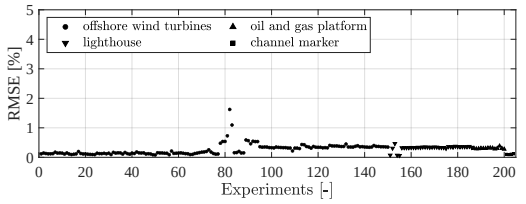
3.3. RESULTS

To assess the robustness and performance of the HILSI, the delay, the normalized root mean square error (RMSE), and the peak tracking error between the measured pile position and the position in the control system were calculated for 204 experiments, as illustrated in Figure 3.6. Notably, the developed setup demonstrated robust performance, with the majority of experiments showing a delay after compensation with a constant forward predicted time interval of approximately 0 to -0.5 ms, a normalized RMSE < 0.6 %, and a peak tracking error < 1 %, even when numerous parameters, such as the numerical structure, measurement system, physical prototype or ice type were altered. Note that the negative delay can be explained by the application of a constant delay compensation (Δt_{fp} = 5 ms). The delay was calculated by identifying the maximum cross-correlation between the measured displacement and the output signal of the numerical model. To mitigate static fluctuations, a moving mean offset was applied. The window had a bin size of 2 s. The sampling rate during the experiments was set to 2 kHz. The RMSE and peak tracking error were calculated as J2 and J3 in a benchmark control problem for real-time hybrid simulations (Silva *et al.*, 2020).

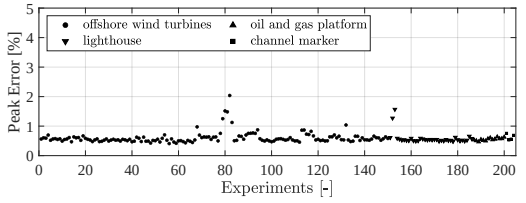
Exceptions indicate that the stability of the system was not unconditional for all experiments. It was found that the outliers in Figure 3.6 can be categorized into two distinct



(a) Delay after compensation for experiments with numerical structural models for offshore wind turbines, a lighthouse, an oil and gas platform and a channel marker.



(b) Normalized root mean square error (RMSE) for experiments with numerical structural models for offshore wind turbines, a lighthouse, an oil and gas platform and a channel marker.



(c) Peak tracking error for experiments with numerical structural models for offshore wind turbines, a lighthouse, an oil and gas platform and a channel marker.

Figure 3.6: Performance parameters for 204 experiments of the hybrid test in model ice.

groups. The first group of exceptions (Experiments 177-187) was linked to warm model ice tests. In warm model tests, the mean model ice load was significantly lower than during cold model tests. Loads of small magnitude, induced by background vibrations (e.g, caused by the motor of the actuator), did consequently start to affect the ice load identification. Thus it is assumed that the high critical delays are caused by the low signal-to-noise ratio, an effect which can lead to undesired performance of hybird tests (Palacio-Betancur and Gutierrez Soto, 2023). The second group was associated with experiments aiming to simulate harsh ice conditions for a lighthouse structure (Experiments 113-117, 125-126) and offshore wind turbines (Experiments 152-153). Those experiments are further analyzed in the next section.

Results for the normalized root mean square error and peak tracking error are shown in Figure 3.6b and Figure 3.6c. Here two groups of outliers can be identified. One group is related to experiments that also resulted in outliers in the result of the measured delay

(Experiments 152, 153). The second group is related to experiments of a smaller and thus stiffer offshore wind turbine (Experiments 78-83). These experiments did not result in a high delay of the HILSI. The error only manifested at higher test speeds, amplifying with each incremental rise in test velocity. It is assumed that the errors increased as one of the eigenfrequencies of that particular numerical structure was similar to the eigenfrequency of the carriage (~ 3.5 Hz). However, the magnitudes of both errors are still insignificant (RMSE < 2 %, Peak tracking error < 2.1 %), which is why the following analysis is focusing on the outliers found for the delay.

One example of instability for a lighthouse experiment is shown in Figure 3.7. Notably, measured delays of 10-12 ms were observed upon the initiation of HILSI in open water when a numerical model of a lighthouse was implemented. Exponential growth in the measured 'ice load' and structural displacement can be observed, particularly in the vicinity of a frequency close to 40 Hz. Note that the 'ice load' in open water is initiated by small load amplitudes and measured inertia of the pile. This frequency is in the range of the natural frequency of the physical prototype, as a power spectral density of the measured pile accelerations during a separate rigid indentation experiment in Figure 3.8 shows. Interestingly, once the aluminum pile was dragged through the ice for the lighthouse test ($t > 299$ s in Figure 3.7), the delay in the HILSI decreased by approximately 25%. Simultaneously, the occurrence of high-frequency load and response reduced significantly. After all it seems that once the physical prototype was in contact with the ice, the coupled system was less prone to instabilities. The physical prototype being in contact or not in contact with the ice can also explain the two highest peaks ($f_1 = 37.9$ and $f_2 = 43.4 Hz$) in the frequency swarm of the PSD of the pile acceleration of the physical prototype as shown in Figure 3.8. The effect of ice-structure coupling on the overall HILSI stability is further discussed in Section 3.4.

Another experiment from the second outlier group (i.e., large delays for experiments aiming to test harsh ice conditions) resulting in a significant delay is depicted in Figure 3.9. This figure illustrates an experiment of an offshore wind turbine simulation under harsh ice conditions. When compared to the time series of the lighthouse experiment shown in Figure 3.7, the offshore wind turbine exhibited vibrations with a frequency close to 20 Hz. Only towards the end of the experiment did the vibration frequency converge to the eigenfrequency of the physical prototype, approximately in the range of 30-40 Hz. However, the experiment was prematurely terminated to prevent damage to the equipment. It remains a matter of speculation why the offshore wind turbine, scaled for harsh ice conditions, experienced vibrations at a frequency slightly higher than the highest numerically modeled eigenfrequency, whereas the experiment with a model of a lighthouse resulted in vibrations with a frequency equal to that of the physical prototype. One possible explanation is based on the fact that the highest eigenfrequency of the offshore wind turbine is higher than any modeled eigenfrequency of the lighthouse, and thus more prone to excitation by high frequency loads.

In summary, the majority of the experiments demonstrated delays that were either shorter or equal to the time increment applied in the constant forward prediction method. However, a few instances of longer delays were attributed to low signal-to-noise ratios and scaling of the HILSI. Since the reasons for the instabilities resulting from the scaling for

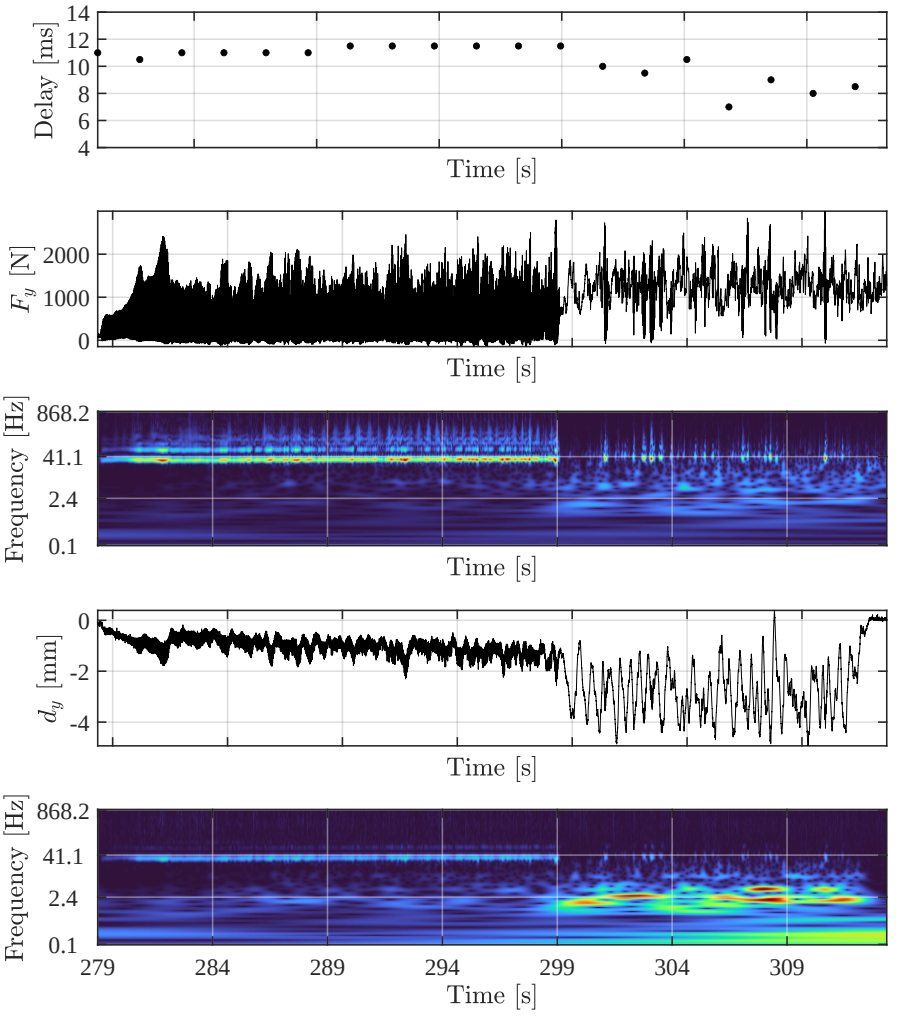


Figure 3.7: Measured delay during an experiment in the first test campaign of a lighthouse scaled for harsh ice conditions. Additionally time series and corresponding wavelet transformation of the measured ice load F_y and structural displacement d_y are shown. The setup first moves through open water (279 to 299 s) and then crushes through the model ice (299 to 313 s). Test ID 451.

harsh ice conditions remain unclear, the subsequent investigation will focus on exploring the critical delays of the implemented numerical structures.

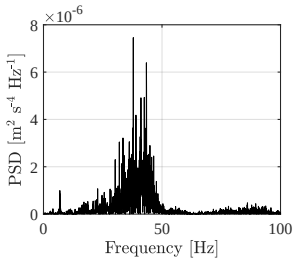


Figure 3.8: Power spectral density of the measured acceleration inside of the pile during a rigid indenter experiments through the ice. Test ID 514.

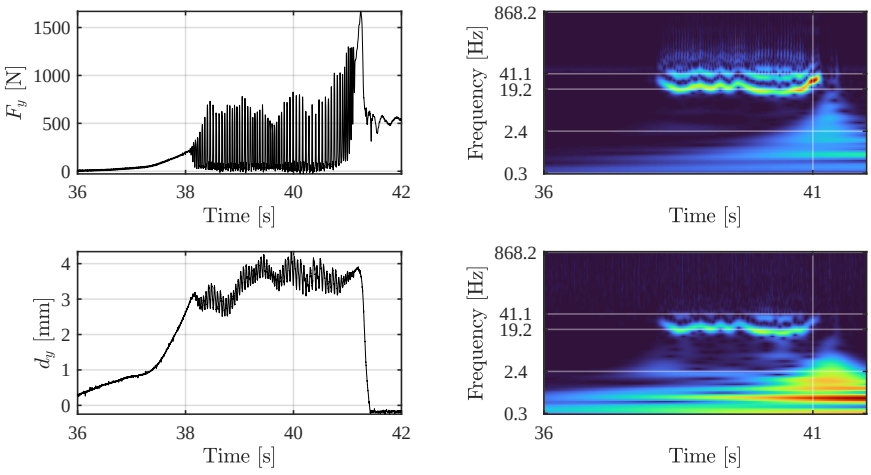


Figure 3.9: Results of HILSI when a numerical model of an offshore wind turbine was scaled for harsh ice conditions and implemented. Test ID 241.

3.3.1. CRITICAL DELAY

The critical delay was experimentally identified to identify why specific numerical representations of structures became unstable while others remained stable during the experiments. The critical delay is the threshold beyond which a system accumulates more energy than it can dissipate. Subsequently, efforts were made to seek an analytical solution to approximate the critical delay.

EXPERIMENTAL CRITICAL DELAY

Identifying a critical delay was a challenging task due to the need to test a range of numerical structure models, passing the transition from unstable to stable (or vice versa) HILSI. This transition was crucial to approximate a critical delay experimentally. As such, experiments were conducted with numerical models of a lighthouse and two offshore wind turbines, incrementally lowering the numerical stiffness and mass, equivalent to

scaling for harsher ice conditions until HILSI instability was observed.

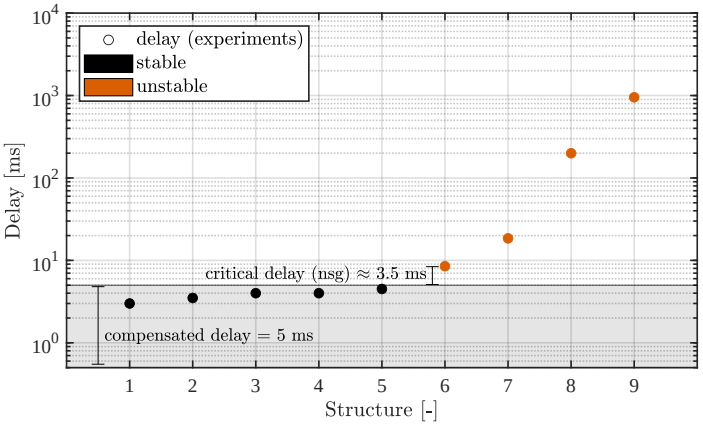


Figure 3.10: Experimental results for implemented numerical models of the lighthouse (nsg) scaled for nine different ice conditions from mild to severe. Test ID 81, 87, 84, 534, 533, 532, 531, 529, 530.

Experimental results for nine different full-scale ice mean loads are shown in Figure 3.10. Before testing, the implemented numerical model of a lighthouse was scaled to the ice mean load respectively. Each numerical structure model was tested in a separate experiment, resulting in one measured delay per 'Structure' (Figure 3.10). Experiments that resulted in a delay exceeding 5 ms are highlighted in orange. The delay was identified based on the maximum cross-correlation between the measurement of the pile position and the equivalent value in the control system. Prior to cross-correlation, the quasi-static component of the time series was removed by subtracting the moving mean for a window of 2000 data points. The final experimental critical delay was obtained by subtracting the forward-predicted time (5 ms) from the experimental delay for unstable experiments. However, the critical delay can only be approximated when the HILSI approaches the threshold of instability, and yields an overestimation in other cases. On the threshold of instability, Structure 6 in Figure 3.10 exhibited a delay of 8.5 ms. After subtracting the implemented forward prediction, the actual experimental critical delay is 3.5 ms. Additionally, the critical delay was experimentally identified for two numerical models of offshore wind turbines. The two different types of offshore wind turbines are designated NREL and Reference, with the former exhibiting significantly greater stiffness compared to the latter. The experimental critical delay was found to be 2 ms for the NREL offshore wind turbine. A delay of 1 ms was identified for the Reference turbine, respectively. It is worth noting that the critical delay may vary for the same numerical structural model when tested under different mean model-scale ice loads during the experiments.

ANALYTICAL CRITICAL DELAY

For evaluation of the experimentally identified critical delays, the authors chose to apply an analytical instability criterion formulated by Wallace *et al.* (2005)[3]:

$$\omega_n \tau \frac{k_s}{k} < 2\zeta. \tag{3.10}$$

In this inequality the stiffness k_s represents the stiffness of the physical test setup and is assumed to be constant for the time being. τ is the delay of the system, ω_n, k and ζ are numerical model parameters, namely the natural frequency, stiffness and damping ratio respectively. It is apparent that the left-hand side (LHS) of Equation (3.10) increases as numerical structural stiffness decreases. When the LHS surpasses the right-hand side, the real part of the solution for the characteristic equation of the delay differential equation becomes positive, leading to a condition of instability (Wallace *et al.*, 2005)[4]:

$$\tau = \begin{cases} \tau & \omega_n \tau \frac{k_s}{k} < 2\zeta \\ \tau_{crit} & \omega_n \tau \frac{k_s}{k} = 2\zeta \end{cases} \tag{3.11}$$

First, the analytical critical delay was calculated based on Equation (3.11) for the structures that were used to approximate an experimental critical delay. Thereby, the stiffness of the physical prototype k_s was computed using the natural frequency obtained from accelerometer measurements (Figure 3.8). For calculation of the critical delay, the second peak of ($f_2 = 43.4 Hz$) was utilized as it was assumed to be the coupled frequency between structure and ice. This assumption is discussed in Section 3.4. The mass of the physical prototype (i.e., aluminum pile) was specified as 5 kg. The analytical solution yielded a critical delay of 3.7 ms for the lighthouse, 2.3 ms for the NREL offshore wind turbine and 0.5 ms for the Reference offshore wind turbine respectively. The close match between the critical delays and the experimental results, as shown in Table 3.1, is remarkable, especially considering that the experimental delay can only be approximated and that the analytical critical delay is based on an equation for single-degree-of-freedom structure. The analytical critical delay was computed for every structural mode of each individual structural model. However, for clarity, only the smallest calculated value is presented here, as this value corresponds to the point at which the first shift in stability occurs. As the critical delay matches well with the experimental delay for which instability was observed, the criterion is also used to estimate the critical delays of the numerical representations of an oil and gas platform and a channel marker, which had been tested during the two test campaigns.

Due to their unique combination of structural properties, offshore wind turbines and the tested channel marker are predisposed to exhibit instability during HILSI experiments. When scaling numerical structure models for harsh ice conditions, the relatively low numerical stiffness places the system in a precarious state close to instability. Minor perturbations during the experiments can cause system instability, manifesting as high-

[3] It should be noted that the criterion was derived for a single-degree-of-freedom structural representation, and thus does not consider the coupling of the eigenvalues via the external forcing term (i.e., ice load).

[4] Notable, Equation (3.10) is based on the assumption that τ is small

Structure	Critical Delay	
	Experimental [ms]	Analytical [ms]
Lighthouse	3.5	3.7
NREL OWT	2.0	2.3
Reference OWT	1.0	0.5
Oil and gas platform	-	<36
Channel marker	-	<0.5

Table 3.1: Critical delays of investigated offshore structures.

frequency vibrations that impose substantial accelerations on the actuators, resulting in an increase in the measured delays. HILSI with a numerical model of the channel marker implemented were not seen to result in instability as the numerical models were scaled only for relatively mild ice conditions during the experiments.

3.3.2. MITIGATION OF INSTABILITIES

Experiments involving numerical models of offshore structures scaled for harsh sea ice conditions regularly resulted in HILSI instability. To mitigate such occurrences, three general measures can be implemented. First, experiments can be conducted with a larger model-scale mean ice load, which reduces the scaling factor (the ratio between full-scale and model-scale mean ice load). This, in turn, results in less downscaling of the numerical stiffness, increasing the critical delay. Achieving a larger model-scale mean ice load can be accomplished by increasing the compressive strength of the model ice, installing a physical prototype with a larger projected width or increasing the ice thickness. However, the challenge of this approach is that very high loads cannot be accommodated without compromising the control systems or structural integrity of the test facilities. Second, the numerical (modal) representation of the offshore structures can be truncated to enhance stability (Miraglia *et al.*, 2020). While this approach involves modifying the original numerical model, it has proven effective in cases where the critical delay was primarily affected by higher structural modes. Truncating these modes eliminates instability and increases the critical delay. Alternatively, the propensity for higher structural mode instability can be mitigated by applying supplementary modal damping to the identified critical modes (Maghareh, 2017). Third, various control methods are available to alleviate and offset time delays, including techniques such as nominal extrapolation, phase-lead compensation, model-based compensation, derivative feed-forward, inverse compensation, virtual coupling, smith regulator, fuzzy logic, three variable control, infinite impulse response, impedance matching, passivity-based or adaptive compensation. A detailed explanation of these methods can be found in the work of Palacio-Betancur and Gutierrez Soto (2023).

By combining all three measures (1: scaling for a higher mean load, 2: truncating the numerical model, 3: constant delay compensation), stable HILSI simulating the

NREL offshore wind turbine in harsh sea ice conditions have been achieved (Figure 3.11). Note that the same offshore wind turbine model as in Figure 3.9 was investigated, which resulted instantly in instability and led to an abortion of the experiment. But now, the numerical structure model was truncated and the numerical structural properties were scaled for a slightly higher mean model ice load level.

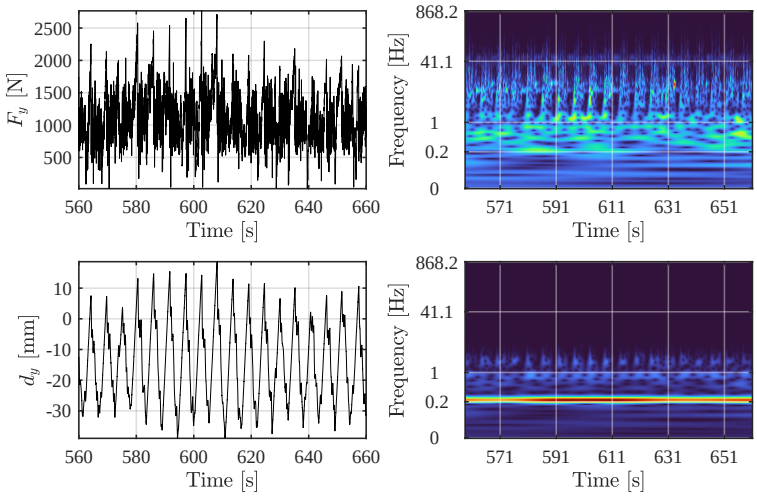


Figure 3.11: Stable HILSI for a numerical model of an offshore wind turbine was scaled for harsh ice conditions. Test ID 498.

3.4. DISCUSSION

3.4.1. ICE-STRUCTURE COUPLING

In the preceding analysis, the stiffness of the physical prototype, denoted as k_s, was presumed to remain constant. However, an examination of the time series from an experiment with a numerical representation of a lighthouse scaled to emulate harsh sea ice conditions (Figure 3.7), raised the question if the stiffness of the physical prototype during testing was inherently constant. The clear differentiation between the two phases of critical delays in Figure 3.7 suggests that the delay reduction is likely linked to the physical coupling of the ice to the physical prototype, effectively increasing the stiffness of the coupled physical prototype ($k_{s;\text{coupled}}$). The two highest peaks observed in the frequency swarm of the measured pile acceleration (Figure 3.8) support this hypothesis: a 25 % reduction in the delay τ, when expressed in Equation (3.11) while other variables remain constant, implies a proportionate increase in the stiffness of the coupled physical prototype ($k_{s;\text{coupled}}$). Given the insignificance of the mass of the model ice, the coupled eigenfrequency of the physical prototype would be roughly 15 % higher than the eigenfrequency of the physical prototype when not in contact with the ice. Notably, the two frequencies of maximum PSD in the acceleration signal (Figure 3.8) differ by 15 %. The same difference can also be found when the measured frequency during instability ($\approx$ 20 Hz) in (Figure 3.9) is compared to the highest modelled frequency of 17.31 Hz. Therefore,

it is reasonable to surmise that the eigenfrequency of the physical prototype when coupled to the ice was $\omega_{s;\text{coupled}} = f_2 = 43.4\,\text{Hz}$, while otherwise, $\omega_{s;\text{uncoupled}} = f_1 = 37.9\,\text{Hz}$. However, the swarm of frequencies in Figure 3.8 also shows that the contact is not binary. The ice-structure contact is time varying and thus is the PSD. Nevertheless, it can be stated that the coupling between the physical prototype and ice reduces the delay of the system by increasing the coupled stiffness of the physical prototype during ice-structure interaction. The ice acted as a natural measure to mitigate the instability of the HILSI.

3.4.2. APPLICABILITY

The developed hardware-in-the-loop setup enables to perform HILSI for analysis of offshore structures subjected to crushing ice conditions. However, the analysis has unveiled certain limitations associated with these simulations. It was observed that the approach adopted led to instability of HILSI when a combination of harsh ice conditions and flexible numerical representations of structures were investigated. While this discovery clearly imposes a constraint on HILSI, it is worth noting that the combination of a flexible structure and severe ice conditions is unlikely to occur in reality, as design for such conditions would typically result in stiff offshore structures to be able to satisfy design requirements in standards. There is also room for debate about whether such stiff offshore structures should still be represented by a multi-degree of freedom model, as high frequencies might not be excited and, consequently, may not be a concern for the offshore structure design. The application of HILSI involves a trade-off between achieving physical accuracy and considering design constraints. For example, in the context of offshore wind turbines, it remains crucial to include higher structural modes in the numerical domain. However, Figure 3.9 demonstrated that an eigenfrequency of 17 Hz, when scaling the numerical model of an offshore wind turbine for harsh ice conditions, was present in an unstable response of the structure. Additionally, structural frequencies close to the eigenfrequency of the carriage should be excluded from the numerical structure models, as severe carriage vibrations were observed in such experiments.

Over the course of two model test campaigns, single-degree- and multi-degree-of-freedom structural representations with frequencies ranging from 0.15 Hz to 17.31 Hz were successfully tested. Models of offshore wind turbines were examined under full-scale ice loads of approximately 2.2 MN in mild ice conditions and around 7.8 MN in harsh ice conditions. For harsh ice conditions, stable HILSI were only achieved by employing a truncated structural model of the stiffer NREL wind turbine at increased model-scale mean ice loads. HILSI with structural representations of a lighthouse implemented, were successfully tested scaled for ice loads ranging from mild to severe ($\approx$ 0.4 to 2-4 MN). The highest full-scale ice load scaled for was 75 MN for an oil and gas platform.

In summary, the versatility of the HILSI allows for the coverage of a wide spectrum of level ice scenarios in mild ice conditions, while addressing more severe ice conditions may require the application of methods to mitigate the risk of HILSI instability. Physical substructural diameters were constrained to a low ratio between diameter and model ice thickness which prevented model ice buckling. It is important to note that the HILSI were performed with a specific focus on ice-structure interaction and ice-induced vibrations,

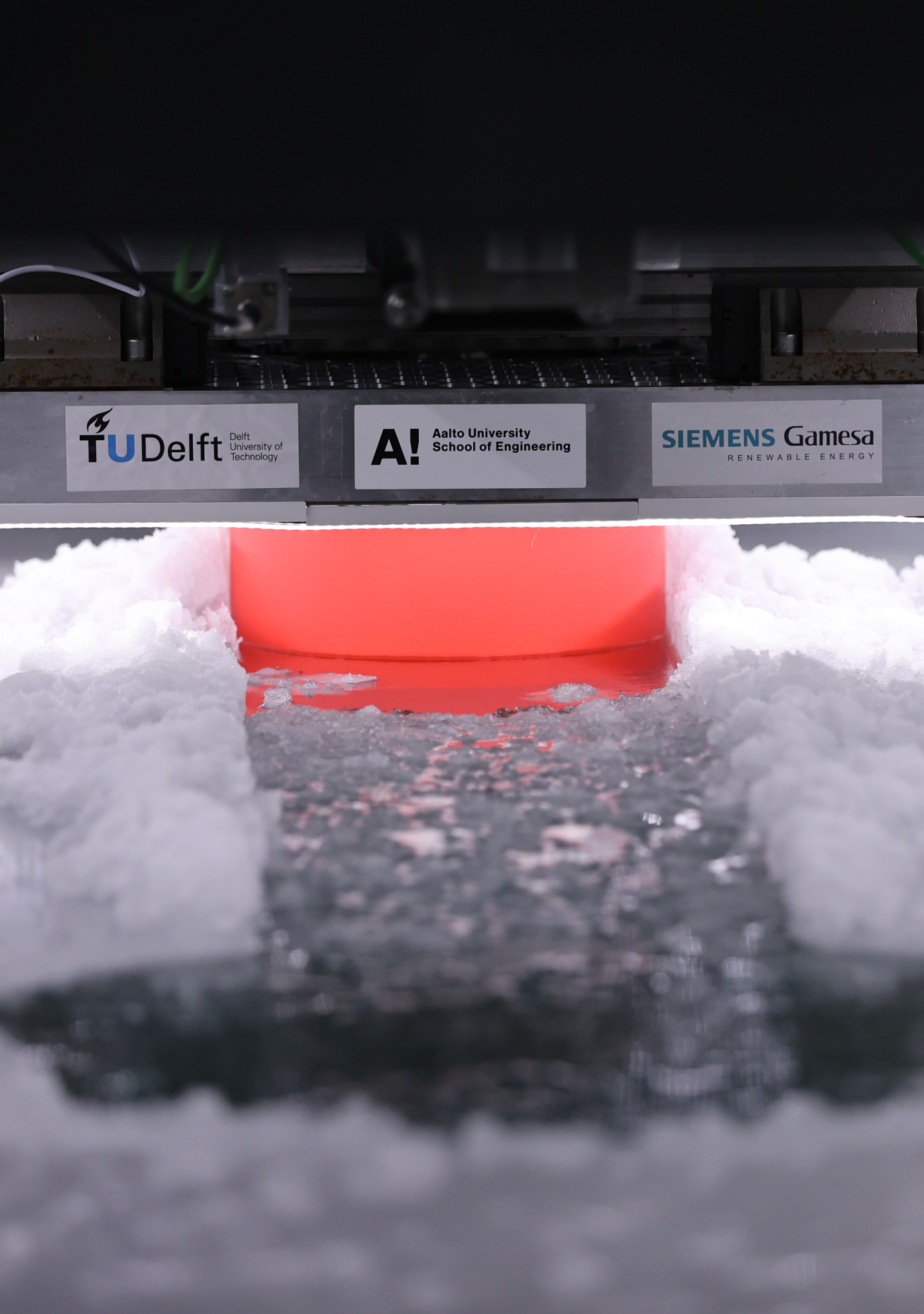
which implies crushing failure of ice for which good results were obtained. HILSI may not be suitable for investigating ice load scenarios exceeding those encountered in harsh ice conditions. For example, it seems questionable if ridge ice loads acting on an offshore wind turbine could be simulated without experiencing instabilities of the HILSI. But before experimentally delving into ridge loads for slender structures, it is imperative to gain a comprehensive understanding of whether dynamic ice-structure interactions should be considered in such scenarios.

The test setup lacks the capability to handle horizontal ice loads when significant vertical loads are present, as the horizontal ice load identification process disregarded the vertical components to solve the over-determined load measurement system. Furthermore, it is unknown how HILSI perform when ice loads, stemming from an ice action event with a significantly varying (or unknown) ice action point, are considered (e.g. during ice bending or for 'thick' ice). This limitation arises from the implementation of a static arm for horizontal load identification. To fully capture the acting forces, it would be necessary to employ a 6-DOF load cell or to develop a compensation algorithm for determining the variation in the static ice load through numerical means.

3.5. CONCLUSION

Prior to this study, hybrid testing techniques had not been explored for investigating ice-structure interaction of offshore structures with relatively low natural frequencies. The need for such techniques stems from challenges associated with the scaling for dynamic ice-structure interaction and exceeding capacities of test facilitates when testing of offshore structures like offshore wind turbines is required. The present study elaborated on the developed hybrid testing technique based on hardware-in-the-loop simulations and presented the implemented constant delay compensation. 204 experiments were analyzed to evaluate the robustness and stability of hardware-in-the-loop simulations in model ice (HILSI) under various conditions. It was only in cases where numerical structural properties were adjusted to accommodate substantial full-scale mean ice loads that the observed delays exceeded the critical thresholds. The large delay prompted the development of instability as confirmed by analyzing the time series of load and structural response. The performance of HILSI also reduced when model ice that resulted in significant lower mean ice loads, was tested, as a low signal-to-noise ratio emphasized the presence of background noises. Furthermore, it was discovered that the stiffness of the physical prototype was changing due to the interaction with the ice. During periods of ice crushing, HILSI resulted in reduced delays and hence a lower likelihood of becoming unstable. Thus, ice-structure coupling led to a mitigation of instability of HILSI by increasing the physical prototype stiffness. Finally, critical delays were experimentally determined and confirmed by a simplified analytical solution, substantiating the assumption that the reduction in the numerical stiffness caused the instabilities of the HILSI. However, testing with higher model-scale mean ice loads and truncation of the numerical structural models improved the stability of HILSI and allowed to run stable experiments of an offshore wind turbine under harsh ice conditions.

In summary, the applied hybrid testing technique demonstrated robust and stable simulations of offshore wind turbines, lighthouses, oil and gas platforms, and channel markers in model ice tank experiments aimed at capturing ice-induced vibrations due to crushing of ice. The developed hardware-in-the-loop setup allowed to maintain the full-scale structural eigenfrequencies and structural displacements of offshore structures, while enhancing versatility in adjusting structural properties and substructural shapes to investigate the dependency of structural properties, shape and aspect ratio on the development of ice-induced vibration regimes. The present study lays the foundation for a broader application of hybrid testing techniques in model ice experiments.


TU Delft
Delft University of Technology
A!
Aalto University
School of Engineering
SIEMENS Gamesa
RENEWABLE ENERGY

4

ICE-INDUCED VIBRATIONS OF OFFSHORE WIND TURBINES

This chapter aims to investigate the types of ice-induced vibrations that can develop when an offshore wind turbine with a vertically sided interface at water level is subject to ice loads caused by crushing level ice. The chapter presents results from experiments aiming to generate representative ice-induced vibrations of offshore wind turbines by applying the scaling method developed in Chapter 2. The experiments aimed to model the interaction of an idling and operational 14 MW turbine with ice representative of a 50 year return period for Southern Baltic Sea conditions. Hybrid testing allowed the incorporation of the specific modal properties of an offshore wind turbine at the ice action point, as well as virtual wind loading (see Chapter 3).

4.1. INTRODUCTION

The applicable design standard IEC 61400-3-1 (2019) emphasizes the importance of considering dynamic ice-structure interaction for offshore wind support structure design in cold regions. Three different approaches to consider dynamic ice loads in the support structure design are proposed by the IEC 61400-3-1 (2019): Analysis of ice action data from similar structures in similar ice conditions; application of sufficiently advanced numerical models including the dynamics of the structure, the dynamics of the ice and their interaction; or usage of (model-scale) measurements. The challenges for these three methods have been explained in detail in Chapter 1. The challenge is that data from similar structures in similar ice conditions do not exist. Numerical models are being used, but these have not been extensively validated for their capacity to predict the interaction

This chapter has been published by **Marine Structures** as *Dynamic ice loads for offshore wind support structure design* in 2023 (Hammer *et al.*, 2023). Redundant chapters in the introduction and methods have been removed. The numerical analysis has been transferred to section Chapter 6. Textual passages may vary. Data for this chapter have been collected during **the first SHIVER model test campaign** and have been published separately (Hendrikse *et al.*, 2021; Hendrikse *et al.*, 2022a). Data from other sources are indicated as such.

between ice and offshore wind turbines owing to the same shortage of data.

In the present chapter, the results from ice tank tests aiming to simulate the interaction of a 14 MW offshore wind turbine in ice conditions representative of severe conditions (50 year return period) in the Southern Baltic Sea are presented. The goal of the experiments was to answer the question: which regimes of ice-induced vibrations can develop for an offshore wind turbine in these conditions? Both an idling and operational turbine were tested applying a hybrid testing technique to obtain some insight into the effect of combined wind and ice loading on the development of ice-induced vibrations.

The experimental campaign is first briefly introduced, where reference is made to a more detailed description in Hendrikse *et al.* (2022a). Data from the campaign used in this paper are publicly available from Hendrikse *et al.* (2021). The ice and wind turbine model used for the numerical simulations are introduced with reference to existing literature. The experimental results are presented with a focus on the regimes of ice-induced vibrations that developed during the tests. A comparison between idling and operational cases is made to assess the effect of wind loading on the interaction of the structure with the ice. Finally, a discussion covers generalization of the results and limitations of the experiments.

4.2. METHODS

4.2.1. STRUCTURAL MODEL AND WIND LOAD

In June 2021 basin tests were conducted at the Aalto Ice and Wave tank aimed to simulate the dynamic interaction between a drifting ice sheet and an offshore wind turbine on a monopile foundation. Structural properties of the implemented offshore wind turbine model in the hybrid test setup are based on a 14 MW offshore wind turbine. The full offshore wind turbine model had been developed for numerical simulations of ice-structure interaction of offshore wind turbines in the Bonus Horizontal axis wind turbine Code (BHawC) from Siemens Gamesa Renewable Energy as presented in Chapter 6. The offshore wind turbine is based on a (steel) monopile foundation and has a full-scale diameter of 7.5 m at the mean sea level (MSL). The interface between tower and transition piece is at 14 m above MSL, the tower top is roughly at 134 m above MSL. The offshore wind turbine has been designed for a water depth of 30 m, resulting in the pile tip at 62 m below MSL. Scaled, linearized structural modal properties, as shown in Table 4.1 are derived by a modal analysis of a lumped mass model derived from the full offshore wind turbine model in BHawC. Mode shapes for the first twelve global bending modes of the simplified structural model are shown in Figure 4.1. The mode shapes underline the symmetry of the offshore wind turbine structure as amplitudes in Fore-Aft (FA) and Side-Side (SS) direction are similar over height. The frequency response functions at MSL are shown for loads applied at MSL and TT in Figure 4.2.

The choice to not incorporate the full rotor-nacelle assembly (RNA) and blade-wind interaction in the numerical part of the hybrid test setup was made as the expectation was that the most important effects on the ice-structure interaction would result from the

added aerodynamic damping and the wind-induced motions of the support structure. The latter effects could be modeled with a simplified structural model. This implies that a full non-linear offshore wind turbine simulation was not achieved here, though it is argued that effects of the non-linear interaction between wind and blades combined with the ice-structure interaction can be investigated in the numerical domain once an ice crushing model has been established which accurately captures the effects observed and described in the following two chapters.

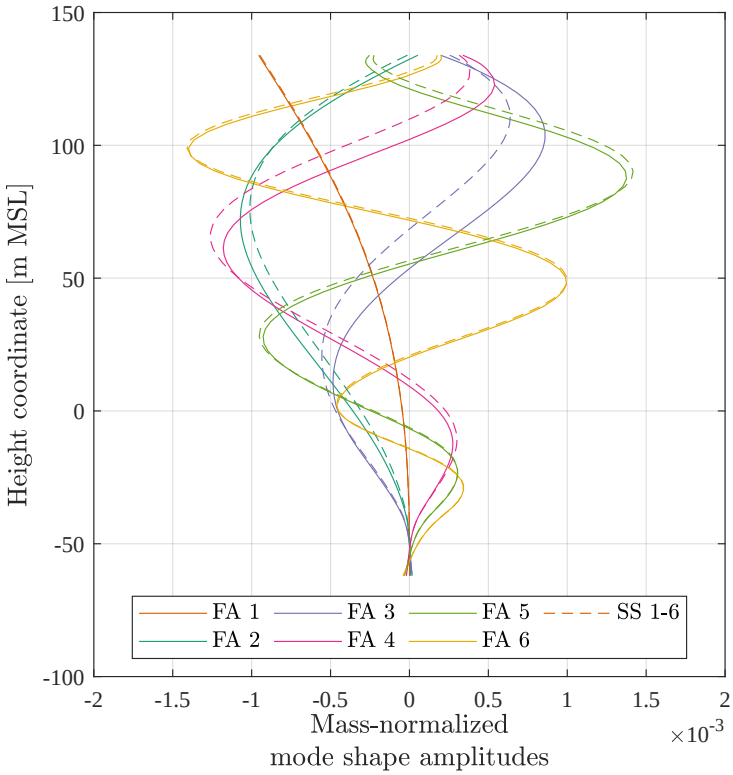


Figure 4.1: Mode shape amplitudes of the full-scale structural model in Fore-Aft (FA) and Side-Side (SS) direction.

To account for the wind in the experiments, a (shaft) force as an external (predefined) force and added modal aerodynamic damping in the numerical domain were applied. To generate a representative shaft force, fully-coupled BHawC simulations were performed. The simulations considered a wind shear law as defined in IEC 61400-3-1 (2019). The wind profile was defined for an averaged wind speed of 12 m s^{-1} at hub height, a reference height of roughly 139 m above MSL, a power law coefficient of 6, a roughness length of 0.09, and a turbulence intensity of 0.104. In addition, and as recommended by IEC

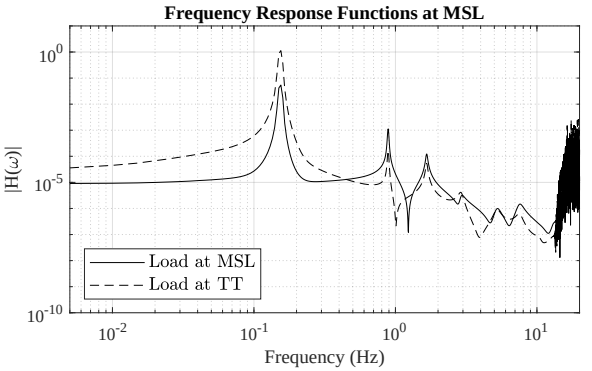


Figure 4.2: Application of sine sweep functions at MSL and TT reveal the frequency response functions of the offshore wind structure.

61400-3-1 (2019), a uniform shear Mann turbulence model was applied. Aerodynamics were modeled by the blade element momentum theory and further considerations as described in Chapter 6. Finally, the shaft force in fore-aft direction at the hub flange was extracted. Note that no cross-directional shaft forces were considered as the application would have unnecessarily complicated the analysis of ice-induced load effects in the cross-direction. Only a portion of the extracted time series from BHawC could be used because the microcontroller of the test setup had a limit of 2000 entries (i.e. 20 s at 100 Hz). The mean shaft force was subtracted to minimize the static deflection of the hybrid test setup, which would not affect the interaction with the ice. The shaft force time series subtracted by its mean is henceforth called wind fluctuation. As test durations were longer than 20 s, the predefined wind fluctuations are repeatedly applied at tower top (TT) as can be seen for a loading scenario without ice in Figure 4.3. The figure presents post-processed structural displacements at the ice action point (here: MSL) in the wind load direction (here: x) for a 90°-misaligned scenario in an open-water experiment and compares those to numerically determined displacements. The wind load repetition cycle of 20 s can be observed, which was limited by the processing capacity of the microcontroller. The Power Spectral Density (PSD) of the applied wind force is provided in Figure 4.4.

The linearized aerodynamic damping was determined by comparing the results of a modal analysis under operational condition for an averaged wind speed of 12 m s^{-1} and an idling condition in BHawC. The determined linearized aerodynamic damping is added to the modal damping in the direction of the applied wind fluctuations (Table 4.1, $\zeta_{\text{aero}} = \zeta_{\text{oper}} - \zeta_{\text{idl}}$).[1]

A summary of the structural parameters fbias used during the experiments is given

[1] Note that the majority of this subsection has been extracted from the journal paper *Experimental study into the effect of wind-ice misalignment on the development of ice-induced vibrations of offshore wind turbines* which is presented in the next chapter(Hammer and Hendrikse, 2023b).

in Table 4.1. Here, the structural frequency is f, ζ_{idl}, and ζ_{oper} are the damping in idling and operational conditions, respectively, and ϕ is the mass-normalized eigenvalue at the mean sea level (MSL) and tower top (TT) in x- and y-direction. Global bending modes up to 20 Hz natural frequency were considered as advised for analysis of dynamic ice-structure interaction in ISO 19906:2019(E) (2019).

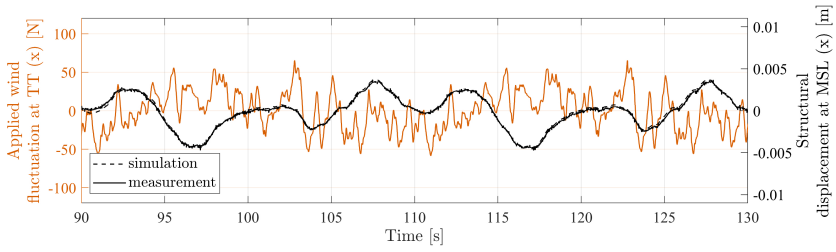


Figure 4.3: Wind load fluctuations applied at tower top (TT) and wind-induced displacements of the structure at the ice action point (here: MSL) as numerically determined and measured in a test without ice present (Test ID 380).

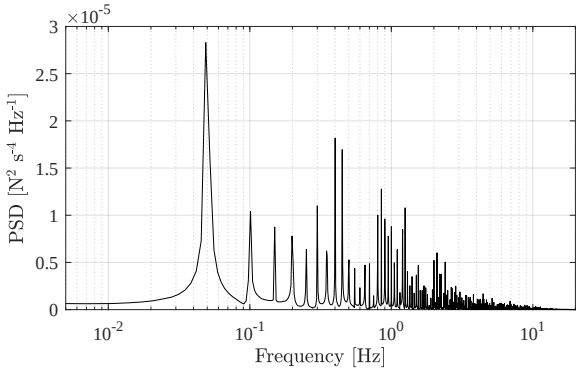


Figure 4.4: Power Spectral Density (PSD) of the applied wind load fluctuations.

4.2.2. HARDWARE-IN-THE-LOOP SYSTEM

A photograph of the setup in the basin is shown in Figure 4.5, combined with a schematic overview of the different components. The hybrid testing technique applied in the experiments is described in detail in Chapter 3. However, a small summary is given here. An aluminum, vertical cylindrical pile with a diameter of 200 mm penetrated the ice sheet. The motion of the pile matched the displacements of the simulated structure at the ice action point. Ice loads were identified from pile strains measured with strain gauges located above the ice action point. The response of the simulated structure to the measured ice loads was numerically simulated on a micro-controller. The calculated

Table 4.1: Scaled modal information at ice-structure interaction point and tower top for the lumped mass model of an offshore wind turbine ($\lambda_F = 1700$). Subscripts *idl* and *oper* indicate idling and operational scenarios, respectively. Subscript *MSL* indicates modal amplitudes at Mean Sea Level, and subscript *TT* at Tower Top.

Structural Mode	f [Hz]	ζ_{idl} [%]	ζ_{oper} [%]	$\phi_{x,\text{MSL}}$ [10^{-3} kg$^{-0.5}$]	$\phi_{y,\text{MSL}}$ [10^{-3} kg$^{-0.5}$]	$\phi_{x,\text{TT}}$ [10^{-3} kg$^{-0.5}$]	$\phi_{y,\text{TT}}$ [10^{-3} kg$^{-0.5}$]
1	0.153	0.8	1.0	-1.86	0.00	-39.10	0.00
2	0.154	0.8	10.2	0.00	1.88	0.00	39.39
3	0.824	1.2	1.8	12.66	0.00	0.52	0.00
4	0.888	1.3	4.4	0.00	-14.79	0.00	2.20
5	1.50	2.6	3.4	19.29	0.00	-10.55	0.00
6	1.66	1.9	5.9	0.00	-18.72	0.00	8.14
7	2.72	5.4	5.8	9.49	0.00	13.00	0.00
8	2.91	4.1	5.8	0.00	-7.53	0.00	-13.93
9	5.11	5.4	5.8	-9.39	0.00	-9.24	0.00
10	5.21	5.4	5.8	0.00	-10.04	0.00	-10.44
11	7.46	5.4	5.8	18.6	0.00	-7.25	0.00
12	7.54	5.4	5.8	0.00	18.54	0.00	-8.23
13	10.5	5.4	5.8	-2.35	0.00	-6.83	0.00
14	10.5	5.4	5.8	0.00	-1.95	0.00	-7.66
15	13.4	5.4	5.8	-16.12	0.00	-4.29	0.00
16	13.4	5.4	5.8	0.00	16.08	0.00	4.70
17	15.2	5.4	5.8	0.00	-7.03	0.00	-3.73
18	15.3	5.4	5.8	6.14	0.00	3.43	0.00
19	17.3	5.4	5.8	-9.17	0.00	4.98	0.00
20	17.3	5.4	5.8	0.00	8.70	0.00	-5.51

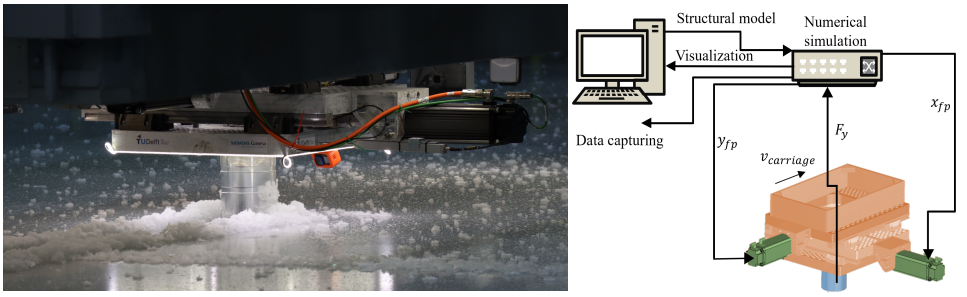


Figure 4.5: Left: Photograph of the hybrid test setup during testing, showing the cylindrical pile interacting with the ice. Right: Adjusted schematic overview of the hybrid test setup (Hammer *et al.*, 2021).

structural displacement at the ice action point was applied to the pile by two linear actuators. The pile displacements were measured by displacement sensors. The test setup was mounted to a carriage. The carriage was mounted to a bridge spanning the ice tank. Ice drift was simulated by moving the carriage along the bridge with pre-defined speeds. The resulting apparent ice drift (simulated by the moving carriage and the stationary ice sheet) was then opposite to the carriage movement direction. Herein, the

movement of the carriage is described as ice drift. The physical substructure of the hybrid test setup is described as the structure. The measured pile displacements relative to the carriage supporting the hybrid test setup are described as the structural displacements. During the tests, the global ice forces and structural responses were measured with load cells, strain gauges, accelerometers, and displacement sensors as further described in Chapter 3 and Hammer *et al.* (2021). The analyses presented here use the unfiltered measured global ice force and structural displacement.

4.2.3. SCALING

The scaling applied during the test campaign has been described in detail in Chapter 2. For the tests used in this section, the scale factor was defined as $\lambda_F = 1700$. This value was obtained using an estimate for the full-scale mean brittle crushing of 1.7 MN and an estimate for the mean brittle crushing load in the basin of 1 kN. The full-scale load was based on a scenario representative of 50 year return period Southern Baltic Sea design conditions ($h_{50} = 0.4$ m, $CR_1 = 1$ MPa), which are in line with the data presented in Tikanmäki and Heinonen (2021) and Willems and Hendrikse (2019), noting that these parameters will vary from site to site. During testing, it was found that the mean load was actually higher than initially estimated, which makes the experimental results represent a scenario with a higher (≈ 2.2 MN) mean brittle crushing load.

4.3. RESULTS

First, the results from constant deceleration tests are shown which were used to identify the ice drift speeds for which different regimes of ice-induced vibrations developed. Based on these tests several ice drift speeds were selected for constant speed tests to obtain long time series allowing to analyze the vibrations in more detail. Results for constant ice drift experiments with the idling and operational turbine are presented side-by-side to show the effect of the simulated wind loading and added aerodynamic damping on the ice-structure interaction.

4.3.1. CONSTANT DECELERATION TESTS

Figure 4.6 and Figure 4.7 show the results for an idling and operational turbine, respectively, during a constant deceleration test reducing the ice drift speed from 80 mm s^{-1} to 0 mm s^{-1} with a deceleration of approximately 0.2 mm s^{-2}. As the velocity decreases, the interaction can be clearly seen to change in both the ice load and structural response plots. At high speed (a), the response amplitude of the structural displacement is small in the case of idling, and dominated by the wind load in the case of operation. As there is no apparent amplification of the ice load, and the structural response is not dominated by any particular mode, the interaction is deemed to be continuous brittle crushing. In both operational states for an ice speed below 50 mm s^{-1}, an amplified second mode response is observed with some higher load peaks indicating interaction between ice and structure (b). For an ice drift speed of around 20 mm s^{-1} this interaction changes again showing a saw-tooth-like pattern in both the load and response with a clear first mode contribution as seen in the wavelet plot (c). When the speed gets close to zero, the ice load increases to the highest magnitude and the period of the observed saw-tooth becomes longer than the first natural period of the structure (d). In these ranges of speeds (b)–(d), ice-induced vibration regimes different from continuous brittle crushing are observed. To allow for the identification of these regimes, long runs with constant speed were performed, and the results are shown in the next section.

4.3.2. CONSTANT ICE DRIFT SPEED TESTS

From the deceleration tests, a total of eight ice speeds were chosen for long constant speed runs. Here the analysis focuses on several cycles of the observed interaction for the ice speeds of 5 mm s^{-1} , 20 mm s^{-1} , 40 mm s^{-1} , and 70 mm s^{-1} . These time series were illustrative of the four different regimes of ice-induced vibrations encountered during the experiments. The square root of power spectral densities (amplitude spectral density (ASD)) is presented to minimize the influence of initial vibrations on the spectra in the following figures.

INTERMITTENT CRUSHING

For low ice drift speeds (here: 5 mm s^{-1}), sawtooth displacement patterns and a corresponding load signal are found representative of intermittent crushing (see Figure 4.8). The amplitude spectral densities of both global ice load and structural displacement show peaks somewhat below the first linearized natural frequency, which are associated with the periodicity of the larger sawtooth observable in the time series. Comparing the

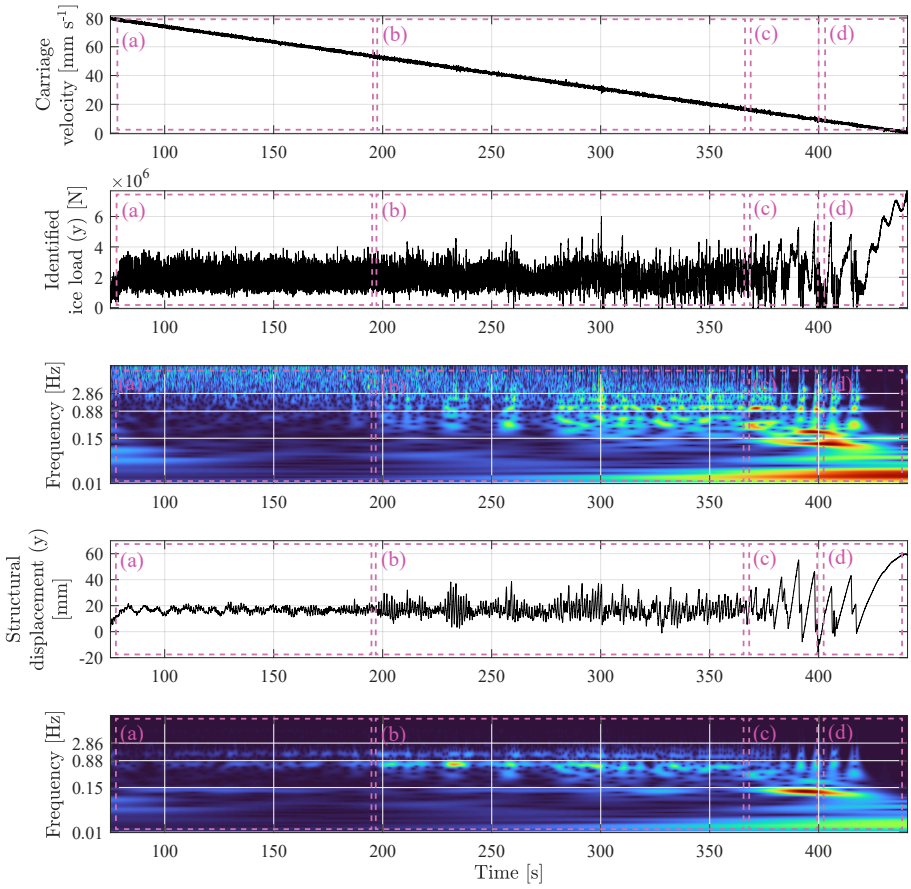


Figure 4.6: Results from a constant deceleration test for an idling wind turbine . From top to bottom: Low-pass filtered carriage velocity, identified ice load, structural displacement at the ice action point, wavelet plot of the structural displacement and ice load indicating the frequencies of the first three eigen modes on the ordinate axis. Different regimes of ice-induced vibrations are approximately indicated with (a) to (d).

operational to the idling case, the oscillations in the relative velocities seem to be reduced, which could be related to the higher damping suppressing higher mode oscillations of the structure. The wind load fluctuations do not appear to have a large effect on the overall interaction between the ice and the turbine in this regime.

Multi-Modal (ice-structure) Interaction with First Mode Amplified Response

A slightly higher ice drift speed (here: 20 mm s^{-1}) results in a structural response dominated by an amplified first mode response (see Figure 4.9). The global ice load pattern shows a saw-tooth-like shape; however, the main periodicity is closer to the first natural

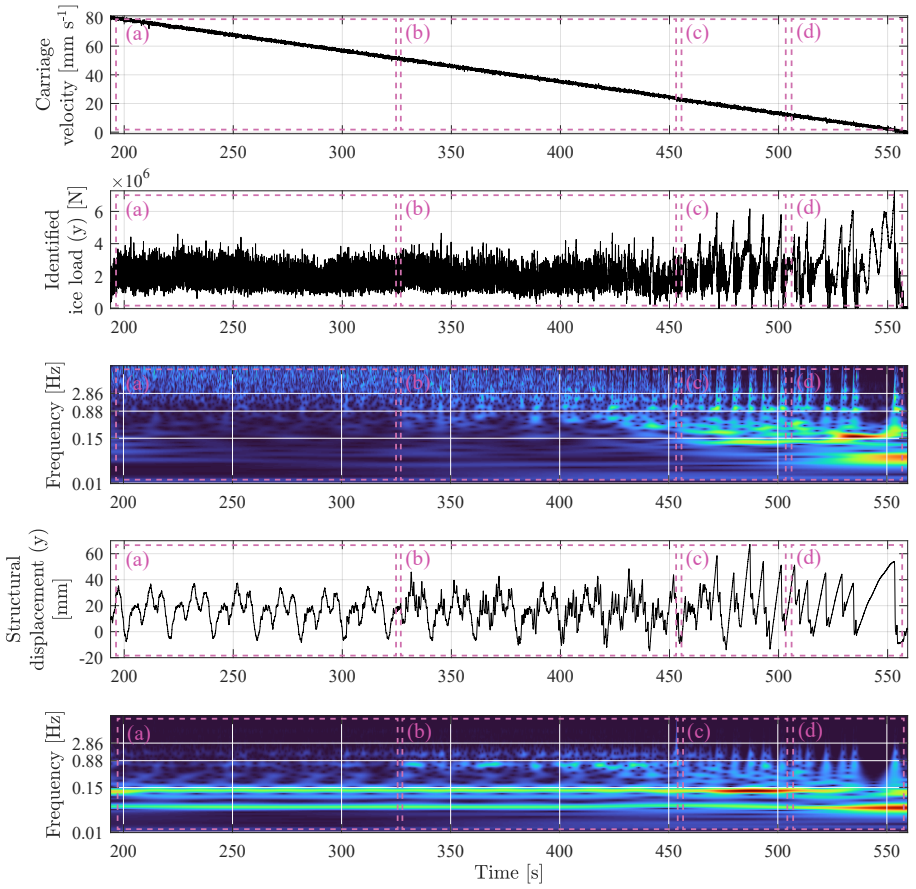


Figure 4.7: Results from a constant deceleration test for an operational wind turbine . From top to bottom: Low-pass filtered carriage velocity, identified ice load, structural displacement at the ice action point, wavelet plot of the structural displacement and ice load indicating the frequencies of the first three eigenmodes on the ordinate axis. Different regimes of ice-induced vibrations are approximately indicated with (a) to (d).

period of the structure when compared to Figure 4.8. The regime does not fall within the definitions for ice-induced vibrations adopted in ISO 19906:2019(E) (2019), IEC 61400-3-1 (2019) or literature (Hendrikse, 2017; Sodhi, 2001). The response of the structure is not dominated by a harmonic response in a single mode, which would characterize it as frequency lock-in. Instead, the second and third modes of the turbine get involved once the structure moves back to its origin after an event of global ice failure. The possibility for multi-modal ice-induced vibrations to develop has been observed during experiments conducted by Määttänen (1983), though not in a situation with a controlled indentation

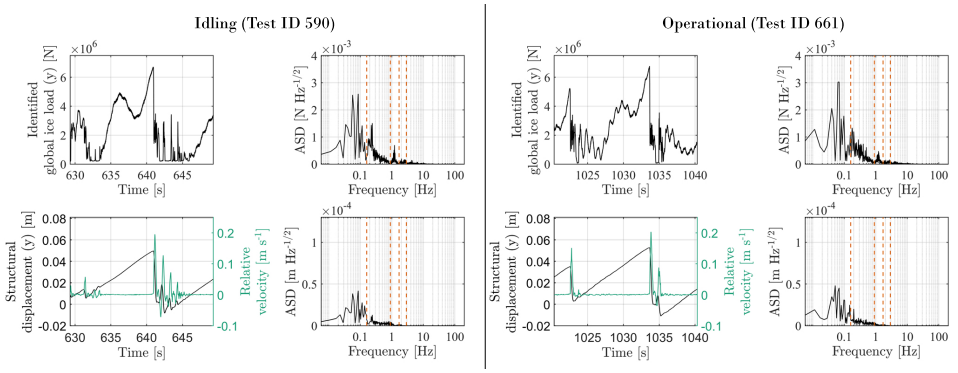


Figure 4.8: Time series of ice load, structural displacement and relative velocity and amplitude spectral densities of ice load and structural displacement of an idling (left) and operational (right) turbine for a constant ice drift speed test (here: 5 mm s^{-1}).

speed[2]. The short period of the second-mode vibration may develop because of the low frequency of the first mode oscillation. When the structure returns to the equilibrium after large global ice failure, the oscillations in relative velocity indicate short instances of frequency lock-in in the second mode to develop. As there is enough time during half a period of the first mode vibration (approximately 3 s) for several cycles of second-mode oscillation to develop, it is made impossible for 'classical' frequency lock-in to develop for the first mode. In a way, the motions in the second mode, and to some extent the third mode, act as a disturbance. Comparing the results for the idling and operational turbine, no clear differences are observed except for the peak in the ASD plot of the structural displacement at a frequency of 0.05 Hz, which relates to the imposed fluctuating wind load.

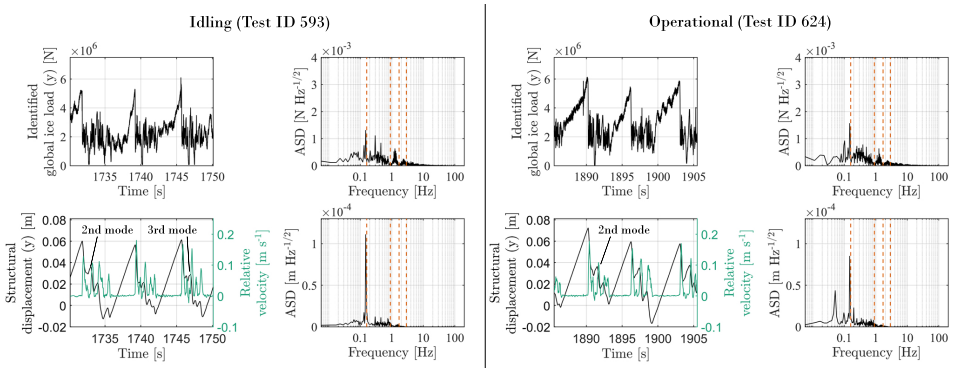


Figure 4.9: Time series of ice load, structural displacement and relative velocity and amplitude spectral densities of ice load and structural displacement of an idling and operational turbine for a constant ice drift speed test (here: 20 mm s^{-1}).

[2]The observations of Määttänen (1983) are discussed in Section 7.1

'FREQUENCY LOCK-IN'

For intermediate ice drift speeds in the experiment (here: 40 mm s^{-1}), a near-harmonic oscillation with a frequency slightly below the second natural frequency of the structure is found, which classifies as frequency lock-in[3] (see Figure 4.10). Some short moments of third mode interaction can be seen to develop for low relative velocities (around minima of the displacement signal).The global ice load is periodic, but with smaller peak load amplitudes than observed for the lower speeds. For this type of interaction, the wind-induced response is clearly visible in the displacement signal during the operational case. The effect on the ice load and relative velocity between ice and structure seems to be minimal. For confirmation of the qualification as frequency lock-in, the structural peak velocities in the direction of the ice motion v_{peak} for all tested ice drift speeds v_{ice} are shown in Figure 4.11. A linear relation between these two parameters (β) can be used to identify frequency lock-in (Hendrikse, 2017; Toyama *et al.*, 1983):

$$v_{peak} = \beta v_{ice} \tag{4.1}$$

with β between 1.0 and 1.5. The peak velocity was calculated for the 99th quantile of the last half of the time series to cover a steady-state response. Based on Figure 4.11, frequency lock-in occurs for an ice drift speed between 20 mm s^{-1} and 50 mm s^{-1}. However, the time series clearly indicate that the structure experiences a different type of vibration pattern for an ice drift speed of 20 mm s^{-1}. As the method is based on single-degree of freedom structures, this method might be insufficient when applied to multi-degree of freedom structures, though it still gives a reasonable indication if (temporary) lock-in might have developed.

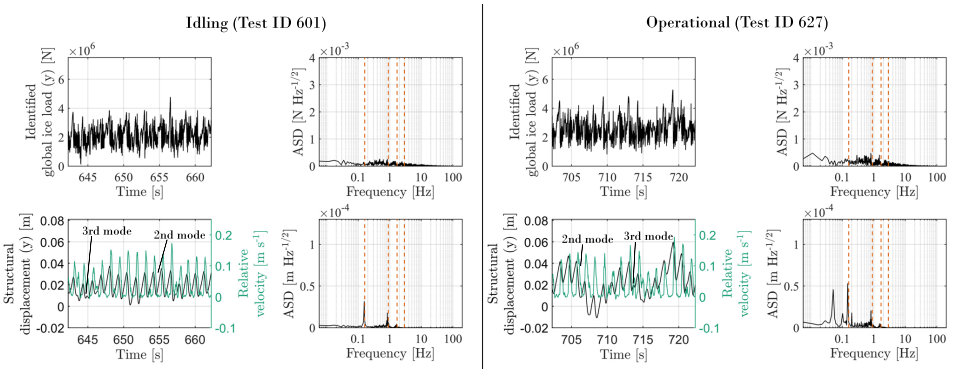


Figure 4.10: Timeseries of ice load, structural displacement and relative velocity and amplitude spectral densities of ice load and structural displacement of an idling and operational turbine for a constant ice drift speed test (here: 40 mm s^{-1}).

[3] The observed regime differs from the classical definition of 'frequency lock-in' as the response is definitely influenced by vibrations with a frequency close to the third eigenfrequency. The regime should rather be referred to as 'multi-modal (ice-structure) interaction-II'. However, the nomenclature of frequency lock-in is continued to not unnecessarily confuse the reader.

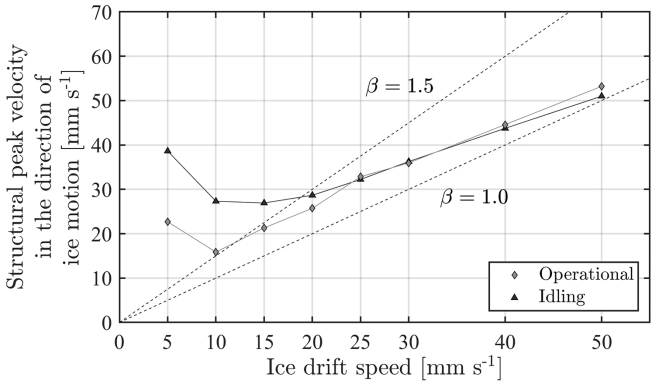


Figure 4.11: Structural peak velocities in the direction of ice motion are presented for eight tested constant ice drift speeds.

The differences in the structural peak velocity between the idling and operational scenarios can be explained by the difference in aerodynamic damping. An ice drift speed between 5 mm s^{-1} and 20 mm s^{-1} causes ice-induced vibrations with a frequency close to the frequency of the first eigenmode. As the aerodynamic damping is highest for this eigenmode, vibrations are significantly damped. Differences for higher ice drift speeds are marginal as the effect of aerodynamic damping on the structural peak velocity reduces due to a different type of structural response. The amplitude spectral density of the structural displacement in Figure 4.10 shows a contribution of the first mode during frequency lock-in. This is explained by the experiments not lasting long enough for the effects due to initial conditions to diminish.

CONTINUOUS BRITTLE CRUSHING

For the highest ice drift speeds included in the experiments, no significant structural vibrations and a characteristic stochastic load around a mean level are obtained (see Figure 4.12). For an operational turbine, the numerically applied wind load fluctuations at tower top can be recognized in the structural response at the ice action point. Neither the idling nor the operational ice load spectrum indicates any specific ice breaking frequency in this regime.

4.4. DISCUSSION

The discussion focuses on the observed regimes of ice-induced vibrations, generalization of the results, and limitations of the experiments.

ICE-INDUCED VIBRATIONS OF OFFSHORE WIND TURBINES

For the most part, the vibrations observed in the experiments for offshore wind turbines are similar to those observed for existing structures in the past. Intermittent crushing

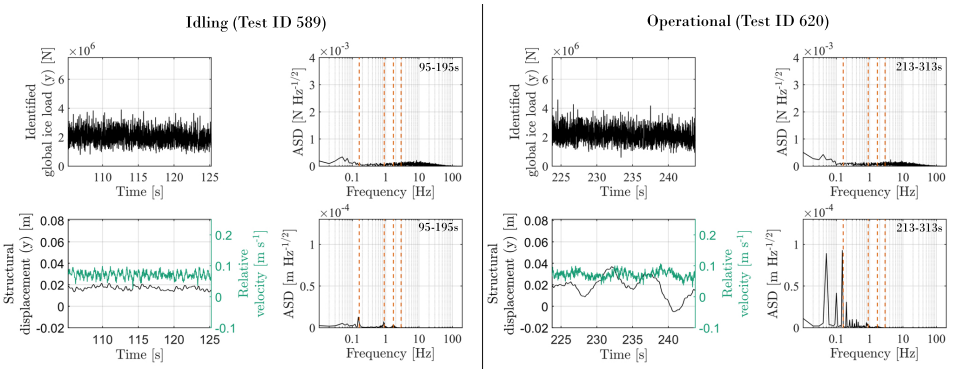


Figure 4.12: Time series of ice load, structural displacement and relative velocity and amplitude spectral densities of ice load and structural displacement of an idling and operational turbine for a quasi-constant high ice drift speed test (here roughly: 80 mm s^{-1}).

develops at low ice drift speeds, frequency lock-in at intermediate speeds, and continuous brittle crushing at high speeds. The results from the constant deceleration tests show transitions from one regime to the other which are comparable to the early observations on slender piles in Cook Inlet by Blenkarn (1970), and for example the Molikpaq May 12th event (Jefferies and Wright, 1988). As offshore wind turbines are relatively compliant structures, it is understandable that these will show severe ice-induced vibrations in much milder ice conditions when compared to, for example, the Molikpaq. However, there are two clear differences when comparing the wind turbine results to observations for other types of structures: 1) a multi-modal type of interaction leading to a non-harmonic amplified first mode response develops in between intermittent crushing and frequency lock-in, and 2) frequency lock-in develops mainly in the second global bending mode rather than the first. The multi-modal type of interaction is shown in Figure 4.9 and develops for both an idling and operational turbine. The response is characterized by a main period roughly equal to the first natural period of the structure, with contributions of the second and third mode during half the cycle when the main direction of motion of the structure is towards the ice. The response of the structure not being harmonic, makes this interaction not fit with the definition of frequency lock-in. The interaction not being quasi-static makes it not fit with the classical definition of intermittent crushing. This regime is perhaps best qualified as 'something in between'. The occurrence of this regime can be explained based on the particular modal properties of an offshore wind turbine. It is generally known that the periodicity in the ice load and structural response, provided ice-induced vibrations develop, decreases with increasing ice drift speed. Once the periodicity gets close to that of one of the structural modes, the interaction may change from intermittent crushing into frequency lock-in. This only happens if the structural mode is lightly damped, (and) if the frequency is relatively low (<10 Hz is a commonly used threshold (ISO 19906:2019(E), 2019), and if the mode can be easily excited by the ice. For lighthouses and channel markers, only the first mode typically fulfills these criteria, resulting in lock-in in the first mode only when the ice conditions are severe enough. For offshore wind turbines, the first mode fulfills these criteria, but the

second and third modes do as well. Specifically, after a moment of global ice failure, the structure starts to move towards the ice, increasing the relative velocity between ice and structure. When the relative velocity becomes higher than the incident ice drift speed, the conditions for lock-in in the second or third global bending mode are created. As these modes have significantly shorter periods than the first mode and low damping, the interaction develops quickly and for a couple of cycles. This 'lock-in' with the second or third mode disturbs the development of a quasi-harmonic first mode response of the structure, causing the response pattern to look different from what is typically observed in frequency lock-in. For frequency lock-in in the second mode, developing at higher ice speeds, this interference effect of higher modes is much more limited. Still some third mode oscillations were observed, but in general, the response was much closer to harmonic as known for other offshore structures. It is noted that the relative velocities do not need to be constant for a long time to lead to increased load peaks and vibration amplification, as can be seen from the constant deceleration tests in Figure 4.6 and Figure 4.7.

4.4.1. GENERALIZATION OF RESULTS

The results presented are specific to the case considered in this study in terms of absolute numbers for both the experiments and the numerical simulations. Qualitatively though, these can be generalized for monopile support structures of offshore wind turbines. Most support structures for offshore wind turbines have the second or third global bending mode excited 'easily' at the ice action point, and therefore, the interaction can be expected to develop as observed in the experiments. For larger turbines, the third mode influence is likely to become more significant as the mode shapes shift with respect to each other with the height of the support structure.[4]. For 'smaller' turbines, such as those currently installed in the Baltic Sea, higher mode vibrations will mainly manifest in the second global bending mode. Regardless of the modes involved in the interaction, low ice speeds will always result in the largest structural response. In terms of ice conditions, it is more challenging to generalize the results, though for more severe ice conditions than those scaled in the tank, the boundaries between different interaction regimes will theoretically shift to higher ice drift speeds and vice versa (Owen and Hendrikse, 2019).

4.4.2. LIMITATIONS

In the experiments, no buckling failure was observed, a failure mode which had complicated model-scale experiments in the past (Barker *et al.*, 2005; Hendrikse *et al.*, 2018), owing to the relatively high strength of the cold model ice. The initial impact between the ice and the structure at the start of a test would often result in oscillations with a frequency associated to the first mode. This transient effect took time to disappear owing to the long natural period and low damping. As a consequence, there was often not enough test length in the tank during high-speed tests to reach a state where the first mode was no longer visible in the response of the structure. Though in reality, such effects would also occur when ice first impacts a turbine support structure, the analysis of the results in the frequency domain is somewhat complicated by this as it cannot be confirmed if the

[4] An additional study was performed to investigate higher mode vibrations for 'tall' structures (Section 6.5)

first mode contribution is just transient or an essential part of the steady-state response. To reduce the effect of initial vibrations on the visualization of the spectrum analysis, amplitude spectral densities instead of power spectral densities have been shown and only the last half of the data was used for frequency analysis.

This chapter did not investigate how structural properties, non-linear effects, soil or passive dampers, and rotor-nacelle-assembly related aspects such as blade pitch angles, yaw errors and blade passing influence the ice-structure interaction. Inclusion of such effects in the experiments is theoretically possible with the hybrid test setup but was omitted as it was expected to significantly complicate the interpretation of the results. At the time of development of this work the IEA 15 MW turbine model (Gaertner *et al.*, 2020) was not available yet.[5].

4.5. CONCLUSION

Ice basin tests for offshore wind turbines with a monopile foundation in ice conditions representative of severe Southern Baltic Sea conditions have shown the development of all known regimes of ice-induced vibrations and, in addition, a multi-modal type of interaction regime. This multi-modal (ice-structure) interaction developed for both an idling and operational turbine at ice speeds between those for which quasi-static intermittent crushing and frequency lock-in in the second global bending mode were observed. The interaction is characterized by an amplified oscillations of the first eigenfrequency. During the reversal phase of the structure, oscillations with the second and third eigenfrequency were observed. Higher mode vibrations seem to be initiated by a change in the relative velocity between structure and ice. From the experiments, the effect of the wind load fluctuations during operation on the interaction between ice and structure seemed to be minimal when compared to an idling scenario. The relative contributions of different modes to the structural response changes due to higher aerodynamic damping, but all regimes of ice-induced vibrations showed to develop for both scenarios. For a high ice drift speed, the structural response at the ice action point during operation reflects the wind load fluctuations, whereas at low speeds when severe ice-induced vibrations develop, the response shows to be controlled by the ice.

[5] Note that the IEA 15 offshore wind turbine is an extremely stiff reference turbine. It resembles a design more realistic for extreme harsh ice conditions. Such experiments were performed during the second SHIVER model test campaign (Chapter 3) and confirmed the development of multi-modal ice-structure interaction (see Figure 3.11).


X
TUDelft
Aalto University
School of Engineering
SIEMENS Gamesa

5

EFFECT OF WIND-ICE MISALIGNMENT ON ICE-INDUCED VIBRATIONS

The present chapter is an extension of the previous chapter on ice-induced vibrations of offshore wind turbines (Chapter 4) and aims to analyze the effect of misalignment between wind and ice on the development of ice-induced vibrations of offshore wind turbines. Although the reader is recommended to read Chapter 4 before reading this chapter, it can also be read independently. The chapter first investigates the effect of the misalignment on the development of specific ice-induced vibrations and then focuses on how the ice, surrounding the support structure, is affected by wind-induced motions and vice versa.

5.1. INTRODUCTION

Offshore wind turbines experience significant wind loads in addition to ice loads acting on the structure. Those wind loads can act directionally misaligned to the ice load direction, potentially influencing the development of ice-induced vibrations. Multidirectional, environmental loading of offshore wind turbines is commonly considered when wind and wave loading is addressed (Passon *et al.*, 2015). In the case of wind and ice loading, this is far less common, and it is often assumed that ice and wind act on the structure from the same direction while studies of sea ice dynamics suggest differently (Leppäranta and Myrberg, 2009). Focusing for example on the Baltic Sea, the region with the most ongoing and planned offshore wind developments with seasonal sea ice in Europe, deviation angles (here: misalignment angles) typically vary between 22° and 30° (Leppäranta, 2005;

This chapter has been published in **Engineering Structures** as *Experimental study into the effect of wind-ice misalignment on the development of ice-induced vibrations of offshore wind turbines* in 2023 (Hammer and Hendrikse, 2023b). Redundant chapters in the introduction and methods have been removed. Textual passages may vary. Data for this chapter have been collected during **the first SHIVER model test campaign** and have been published separately (Hendrikse *et al.*, 2021; Hendrikse *et al.*, 2022a). Data from other sources are indicated as such.

Leppäranta and Myrberg, 2009). These misalignment angles are related to site-specific currents, and Coriolis and tilt effects that act directly on the ice independently of the wind direction. Additionally, high inertia of the ice prevents it from quickly following changes in wind direction. As a result, misalignment angles between wind and ice of up to 90° have been observed in the data collected during the STRICE campaign in the Baltic Sea (Ervik *et al.*, 2019; Gedikli *et al.*, 2020).

Ice-induced vibrations of a multi-degree-of-freedom representation of an offshore wind turbine have been investigated in Chapter 4. However, these experiments focused on aligned conditions between wind and ice only. So far it has been neither experimentally nor numerically investigated how a misaligned wind-ice scenario affects the development of ice-induced vibrations of an offshore wind turbine. Furthermore, it is currently unknown how wind-induced structural displacements originating from the tower and rotor-nacelle-assembly interacting with the wind would affect the development of ice-induced vibrations.

First, an operational scenario is compared to misalignment scenarios (30° and 90°). Next a 90°-misaligned operational scenario is compared with an aligned idling scenario in an attempt to separately assess the effect of wind-induced motion perpendicular to the ice drift direction on the ice loads, structural displacement, and spatial distribution of the ice load. The results, reliability of the data, and generalization of results are discussed. Note that the term 'ice' as used in the study is a replacement for first-year sea-ice, as seasonal ice regions such as the Baltic Sea are considered.

5.2. EXPERIMENTAL CAMPAIGN

Experiments were conducted with the same hybrid test setup configuration, structural model and wind load representation as presented in Chapter 4. In the present chapter the effect of simultaneous bi-directional loading of an offshore structure is investigated. Bi-directional response and loading in the hybrid experiments were enabled by the installation of two electrical actuators, which were positioned perpendicular to each other. More specifically, this arrangement allowed to test misalignment scenarios between wind and ice loading direction typical for seasonal ice regions such as the Baltic Sea.

5.2.1. MISALIGNMENT ANGLES

During testing, the direction of indentation into the ice could not be changed. Coordinate transformations were therefore made in the numerical domain to account for wind-ice misalignment (Figure 5.1). First, the measured ice load was projected on the structure coordinate system (x_s, y_s), after which the structure response was determined, combining both physical ice and numerical wind loading. The resulting response was converted back to the pile coordinate system (x_p, y_p) before being applied by the actuators. For example, measured ice loads in y_p-direction are applied in x_s-direction for a 90°-misaligned scenario ($F_{yp} = F_{xs}|\varphi = 90°$). During the campaign, misalignment angles of $\varphi = (0°, 30°, 90°)$ were tested. When not mentioned otherwise, the turbine tested was in operational mode (wind load fluctuations applied and aerodynamic damping added). For an idling scenario,

neither wind load fluctuations were applied nor was aerodynamic damping added to the structural damping. An overview of the different scnearios is visualized in Figure 5.2.

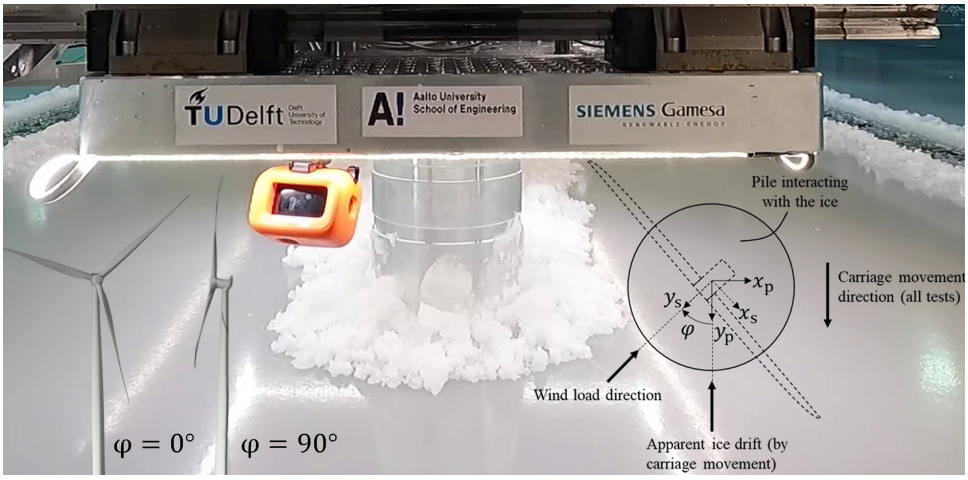


Figure 5.1: Wind load fluctuations applied at tower top (TT) and wind-induced displacements of the structure at the ice action point (here: MSL) as numerically determined and measured in a test without ice present (Test ID 380).

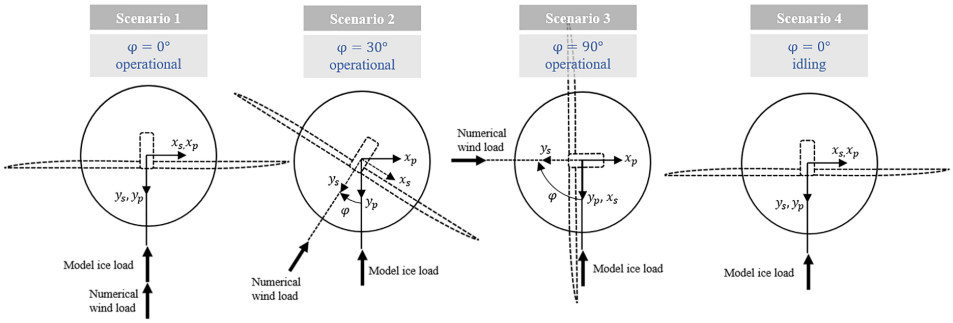


Figure 5.2: Aligned and misaligned scenarios considered in the experiments.

5.3. WIND-ICE MISALIGNMENT

Statistics of measured resultant global ice load ($F_{\text{res}} = \sqrt{F_{x_p}^2 + F_{y_p}^2}$) and measured resultant structural displacement ($d_{\text{res}} = \sqrt{d_{x_p}^2 + d_{y_p}^2}$) of a 0°-, 30°-, and 90°-misaligned scenario (further: 0°, 30° and 90° scenario) are shown in Figure 5.3. Maximum, mean, and standard deviation are shown for eight tested ice drift speeds in a 0° and 90° scenario and for four tested ice drift speeds in a 30° scenario.

Focusing on the ice load in Figure 5.3 first, the highest maximum resultant ice load develops for the lowest ice drift speed tested (here: 5 mm s^{-1}), independent of the misalignment angle. The highest maximum load over all misalignment angles can be found for the largest misalignment angle. The difference in the highest maximum ice load between an aligned and a misaligned scenario is larger than the difference between the highest maximum ice load of the two misaligned scenarios. Differences in the resultant ice load between the 0° and 90° scenarios can be partly explained by the variation in ice thickness (shift of the mean ice load) during the experiments, but are also related to the different manifestation of ice-induced vibrations for the different misalignment angles as discussed in more detail below. Overall, a decreasing trend of all statistics over all scenarios from low ice drift speeds to higher ice drift speeds is recognized. However, three exceptions can be observed. The first exception, observable in the 30° and 90° scenarios, occurs for an ice drift speed of 10 mm s^{-1} as a drop in the ice load statistical measures can be observed here. The second exception occurs for the highest ice drift speed tested (here: 50 mm s^{-1}) in the 0° and 90° scenarios. An increase in the statistical measures is noticed. The third exception is that the mean ice loads for 90° scenarios are rather constant for intermediate ice drift speeds.

Analysing statistical measures of the structural displacement in Figure 5.3, the largest maximum structural displacement per misalignment angle occurs for the lowest ice drift speed tested (here: 5 mm s^{-1}) in the 0° and 30° scenarios, while it occurs for an ice drift speed of 15 mm s^{-1} in the 90° scenario. This displacement is also the largest displacement of the three presented scenarios. The mean resultant displacements are largest for the lowest ice drift speed for all three scenarios. Differences of mean displacements and standard deviations between the three scenarios are smaller in comparison to differences in the maximum displacement. A decreasing trend of all statistical measures in 0° and 30° scenarios was found from low ice drift speeds to higher ice drift speeds, while the trend levels off for higher ice drift speeds. As a main exception, the 90° scenarios show an increased magnitude in all statistics at ice drift speeds of 15 mm s^{-1} and 20 mm s^{-1}. At an ice drift speed of 5 mm s^{-1}, an increase in maximum structural displacements for the 0° and the 90° scenarios is observable. Data points for the 30° scenario at an ice drift speed of 15 mm s^{-1} are labeled as outliers because the malfunction of one of the water spray nozzles created an artificially large ice thickness, which influenced the development of ice-induced vibrations significantly (see Section 5.5.5).

The identified differences in the trends for the statistical measures between the three scenarios are investigated by analyzing the specific time series.
First, the ice load decrease in the 90° scenario for an ice drift speed of 10 mm s^{-1} is considered. The time series of resultant global ice load and structural displacement for that ice drift speed are shown in Figure 5.4.

The figure shows that large-amplitude multi-modal vibrations occur for all misalignment angles tested, but a steady-state load and response is only obtained in the 90° scenario. One might explain the difference in the steadiness of the interaction by lower damping in the direction of ice loading in the 90° scenario. Peak loads in the 0° and 30° scenarios are larger than in the 90° scenario at an ice drift speed of 10 mm s^{-1}, which

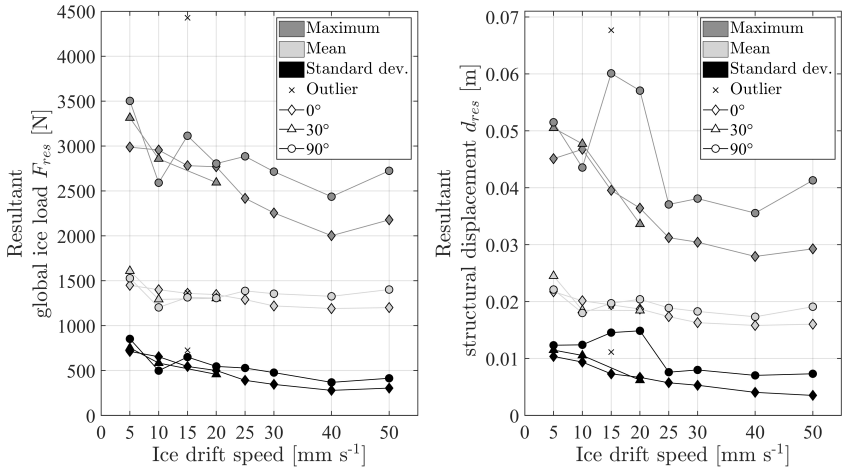


Figure 5.3: Statistics of resultant ice loads (left) and resultant structural displacements (right) for three different misalignment scenarios.

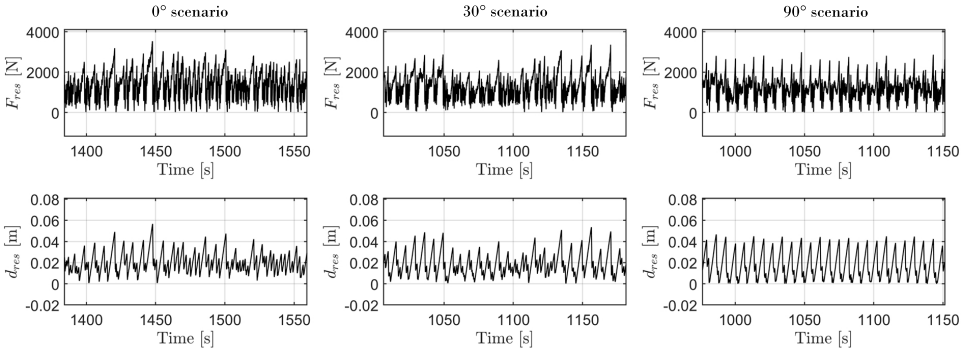


Figure 5.4: Time series of resultant global ice load and structural displacement for a 0°, 30°, and 90° scenario for an ice drift speed of 10 mm s^{-1}.

seems to be related to short instances of intermittent crushing, characterized by a saw-tooth load and response pattern with a period longer than the first natural period. Intermittent crushing resulted in larger peak loads compared to peaks from the multi-modal (ice-structure) interaction in the 90° scenario (Figure 5.4). It is possible that the variation in ice properties, such as thickness and strength, plays a role here. Thicker and stronger ice would result in a change in the interaction, which may cause a shift to a different regime of ice-induced vibrations. However, as the ice thickness in the 0° and 30° scenarios was slightly smaller than that during the 90° scenario, this explanation is unlikely true. Another explanation is that the structural motion due to the predefined wind force interferes with the synchronization between ice and structure and therefore inhibits the

development of the ice-induced vibration regime. This explanation is further investigated in Section 5.4.

The 90° scenario resulted in large displacements for ice drift speeds of 15 mm s^{-1} and 20 mm s^{-1} for which time series of the latter are shown in Figure 5.5.

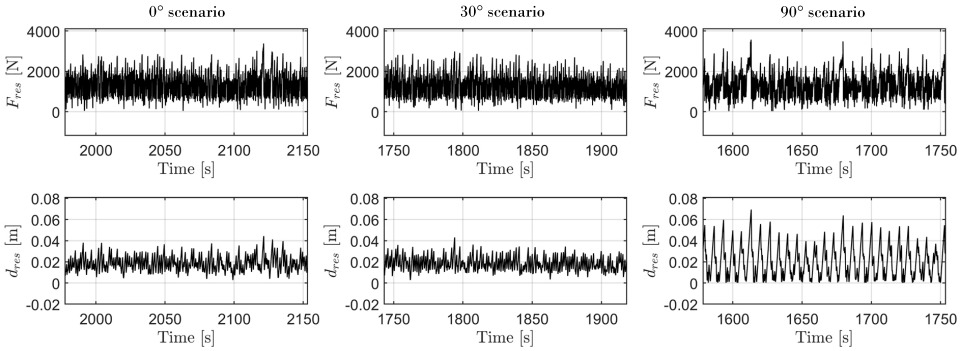


Figure 5.5: Time series of resultant global ice load and structural displacement for a 0°, 30°, and 90° scenario for an ice drift speed of 20 mm s^{-1}.

The comparison reveals that the 90° scenario results in multi-modal interaction with a strong amplified first-global-bending-mode response, whereas the 0° and 30° scenarios result in short periods of frequency lock-in in the second and third global bending mode. This result can be explained by the difference in the aerodynamic damping, which dampens the first mode oscillations significantly for the 0° and 30° scenarios where the ice is more aligned with the wind. The effect of higher aerodynamic damping in the 0° scenario compared to the 90° scenario can further be seen for the ice drift speed of 50 mm s^{-1} (Figure 5.6), where frequency lock-in in the second global bending mode still develops for short periods of time at this high speed in the 90° scenario while in the 0° scenario only continuous brittle crushing is observed.

For the 0° scenario, a peak in the brittle crushing load can be observed around t=860 s, which is related to the artificially high ice thickness created by the malfunction of one of the water spray nozzles as discussed in Section 5.5.5.

To summarize, the differences in vibrations between the three different scenarios seem to be mainly caused by the lower total damping in ice load direction when misalignment between wind and ice direction was tested, with some effect of variation in ice properties always present. For the 90° scenario, sustained vibrations are more likely to develop, and the regimes of ice-induced vibrations develop up to higher ice drift speeds. This is a common observation for structures with low damping interacting with ice.

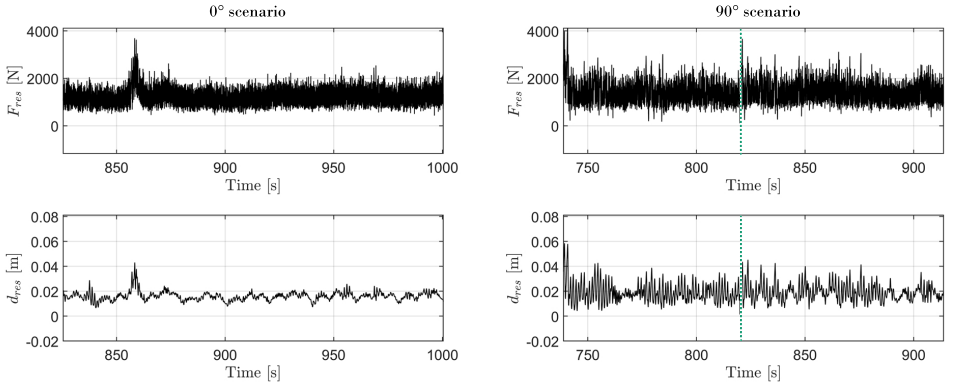


Figure 5.6: Time series of resultant global ice load and structural displacement for a 0° and 90° scenario for an ice drift speed of 50 mm s^{-1}. The green light line indicates where two test IDs have been merged.

5.4. WIND-INDUCED STRUCTURAL MOTION

5.4.1. INLINE MOTION

In this section, it is investigated if the response of the structure to the predefined wind load can interfere with the quasi-static load build-up process in the ice, thereby reducing the ice-load level and maximum structural displacements of aligned or slightly misaligned scenarios, when compared to highly misaligned scenarios for the lowest ice drift speed tested (Figure 5.3 at 5 mm s^{-1}).

To investigate the effect of wind-induced structural motion on the ice-structure interaction, time series and corresponding amplitude spectral densities (ASD) between a 0°, idling scenario and a 0°, operational scenario for intermittent crushing (here at 5 mm s^{-1}) are comapred in Figure 5.7. The ice load time series of the operational scenario shows lower ice load peaks and a difference in the amplitude spectral density of the ice load compared to that of the idling scenario. The spectrum of the ice load for the idling scenario shows content for low frequencies (quasi-static) and frequencies slightly above the first eigenfrequency. Note that the first two structural eigenfrequencies are indicated with green vertical lines. The spectrum of the operational scenario shows several peaks and a smaller contribution of lower natural frequencies when compared to that of the idling scenario.

Analysing the applied wind load fluctuation in the frequency domain, it can be noticed that the frequencies present are also present in the amplitude spectral density of the ice load for the operational scenario (e.g., 0.09 Hz and 0.25 Hz, which are highlighted by dashed, black vertical lines). This is an indication that the structural vibrations due to the applied wind load are present at the ice action point and thus in the ice load signal. As the ice-structure interaction is highly sensitive to the relative velocity between ice and structure, higher mode vibrations will have an effect during the load build-up phase

of intermittent crushing. It is assumed that peak loads for aligned, idling scenarios are higher than in aligned, operational scenarios as (wind-forced) vibrations are changing the relative velocity during interaction, provoking a premature global ice load failure. This observation could also explain why aligned or slightly misaligned scenarios fail to result in steady-state ice-induced vibrations as shown in Figure 5.4. However, a general conclusion for all types of ice-induced vibrations cannot be provided, as the aerodynamic damping was present in the ice drift direction and thus influenced the vibrations once regimes different from intermittent crushing occurred.

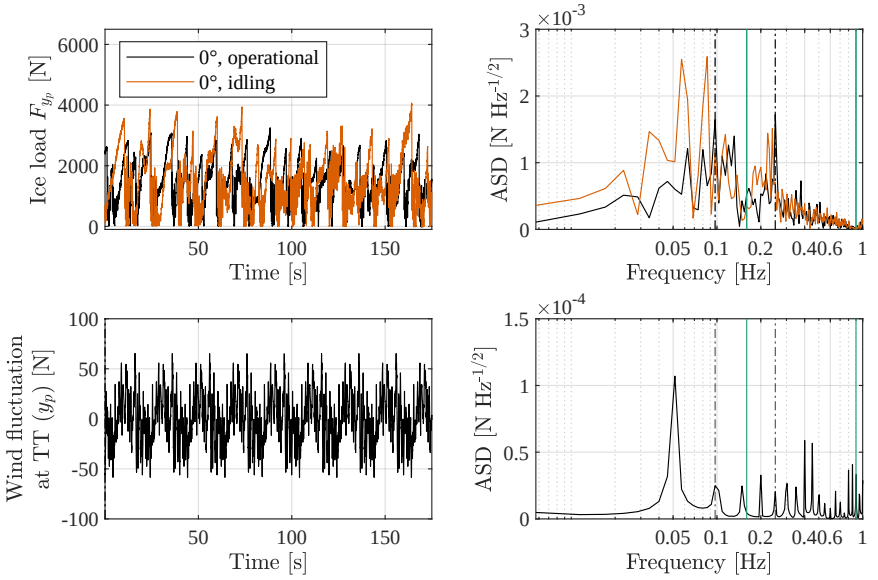


Figure 5.7: Ice load and wind fluctuation time series and corresponding amplitude spectral densities of 0°, idling and 0°, operational scenarios. The first and second natural frequencies are indicated by vertical green lines.

The results presented in Section 5.3 do not allow to identify to what extent the additional wind-induced displacement in x_p-direction (*crosswise*) influences the development of ice-induced vibrations in inline direction. Thus, in the next section, it is investigated if the wind-induced motions cause crushing of the ice *perpendicular* to the ice drift direction (x_p-direction) in a misaligned scenario, thereby potentially influencing the global ice load, structural response, or spatial distribution of the ice load.

5.4.2. CROSSWISE MOTION

When the ice drift and wind direction are misaligned by 90°, wind-induced displacements at the ice-action point, when inducing large enough stress, could theoretically cause crushing of the ice at the sides of the structure. To investigate if the ice in lateral direction is indeed crushed, test results of a 90° scenario are compared to an aligned (0°), idling

baseline scenario.

ICE LOAD AND STRUCTURAL DISPLACEMENT IN x_p- AND y_p-DIRECTIONS

First, the statistics of the ice loads in x_p- and y_p-directions are compared in Figure 5.8. The resultant load on the structure is, for a large part, defined by the load in the ice drift direction (y_p) as the different scale of the y-axis shows. The wind-induced displacements in the 90° scenario cause lower minima and higher maxima in the ice loads perpendicular to the ice drift direction (x_p) at low ice drift speeds. The opposite is true for the loads in the ice drift direction (y_p). For higher ice drift speeds, the effect of the wind seems negligible from the statistical measures.

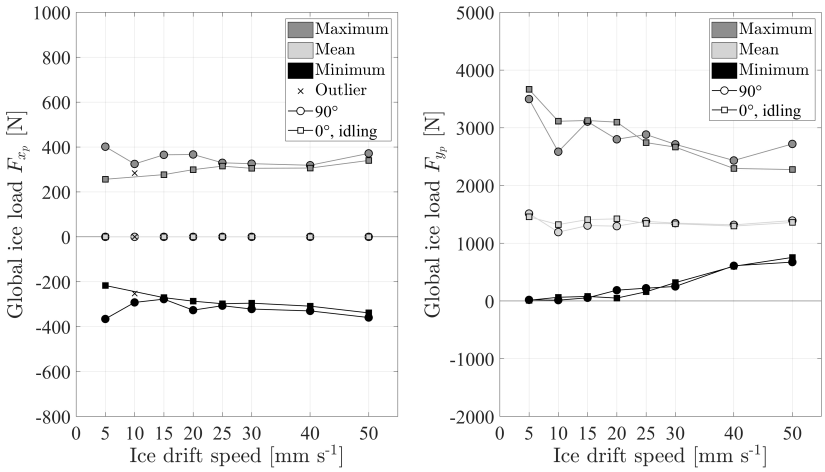


Figure 5.8: Statistics of global ice loads in x_p- and y_p-directions for a 90° misaligned and an aligned, idling scenario.

Second, the statistics of the structural displacements in x_p- and y_p-directions are compared in Figure 5.9. The maximum and minimum of wind-induced displacement at the ice action point in the absence of ice are shown in Figure 5.9 by dashed lines. Comparing the maximum and minimum displacements in the 90° scenario to those in the absence of ice shows that the measured displacements do not reach the numerical open-water amplitude for low ice drift speeds as the ice is constraining the structural motion in x_p-direction. At higher ice drift speeds, this constraining effect seems to be less than at lower speeds, which could relate to the fast repetitive failure of the ice at high ice drift speed allowing the structure to move freely in the clearing created in the ice. The statistical measures of displacements in y_p-direction do not show any remarkable difference between the idling and the 90° misaligned scenario, in the same manner as for the loads in Figure 5.8.

Figure 5.10 shows time series of structural displacement in x_p- and y_p-directions, as

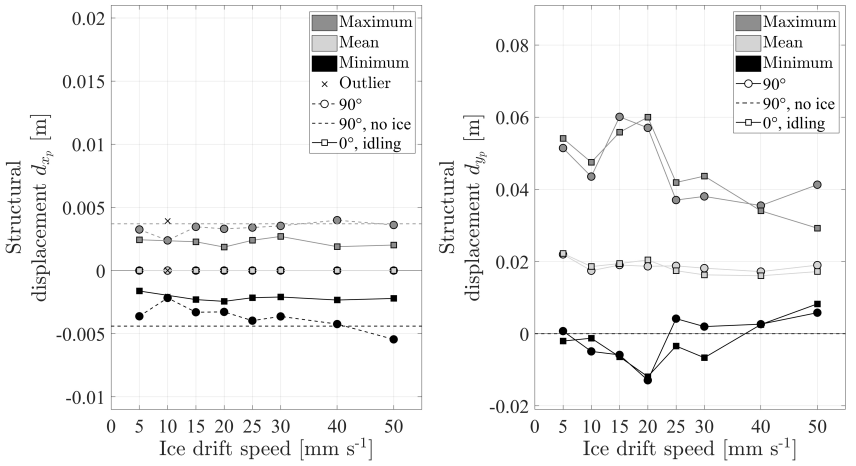


Figure 5.9: Statistics of displacements in x_p- and y_p-directions for a 90° misaligned and an aligned, idling scenario.

well as the numerical wind-induced displacement at the ice action point in x_p-direction in the absence of ice for an aligned, idling scenario at an ice drift speed of 5 mm s^{-1}. Note that the two y-axes have a factor ten difference in their limits. A case of intermittent crushing is found for this speed during which the motions of the structure in x_p-direction occur mainly after moments of global ice failure and into different directions quasi-randomly. As this observation is interpreted as such that the structure is moving into the space created at the moment the ice fails locally, it is shown that cascading failure (not purely instantaneous, simultaneous failure)[1] across the circumference of the pile takes place.

Equivalent to Figure 5.10, Figure 5.11a shows reuslts for a 90° scenario at the same ice drift speed (5 mm s^{-1}). The figure shows that the structure is following the wind-induced displacement only immediately after a global ice failure (e.g., at t = 720s). During the load build-up phases, it can be seen that the structure is moving due to the wind load, but its motion at the ice action point is clearly constrained by the ice (e.g., 750s - 760s). For a high ice drift speed (40 mm s^{-1}) as shown in Figure 5.11b, the motion in x_p-direction starts to approach the wind-induced displacements for an ice-free scenario. This can be explained by the events of ice failure following one another more rapidly at this speed (i.e., reduced contact area and confinement by the ice), creating the space for the structure to vibrate.

Finally, the attention is raised to the effect of small(er) misalignment angles (here $\varphi = 30°$) on the development of ice-induced vibrations in the direction perpendicular to

[1] Intermittent crushing is commonly referred to as a mode of simultaneous ice failure, while continuous brittle crushing is related to non-simultaneous ice failure relative to intermittent crushing. However, also during intermittent crushing the ice seems to not fail purely instantaneous but in a cascade of events.]

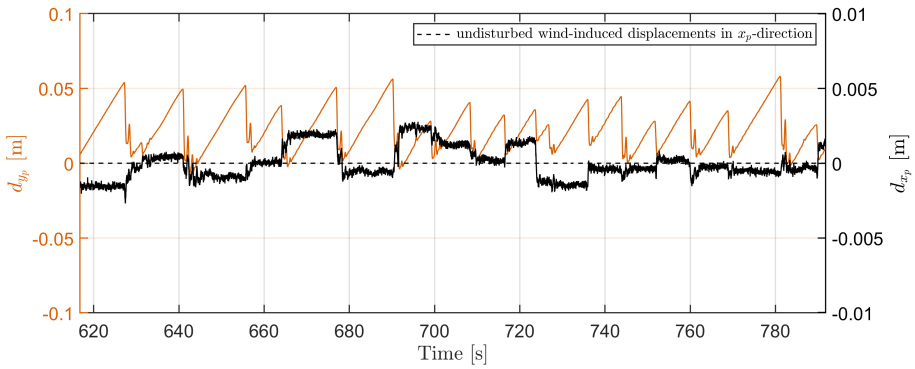


Figure 5.10: Time series of structural displacement in x_p- and y_p-directions for an ice drift speed of 5 mm s^{-1} for an aligned, idling scenario (Test ID 590).

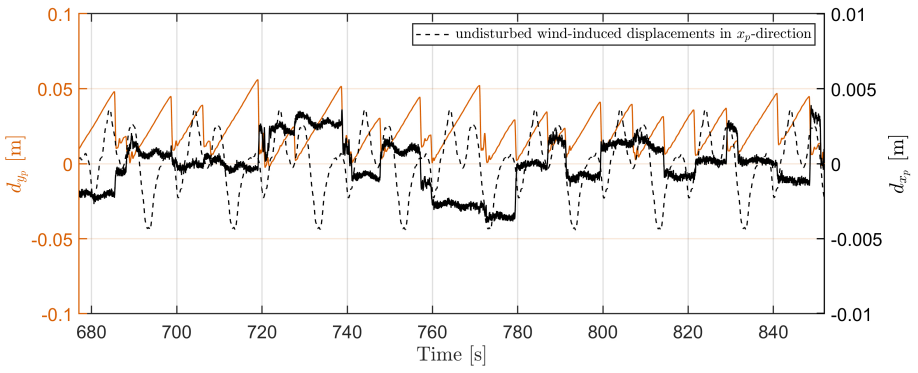
the wind (see Figure 5.12).

In the 30° scenario, the ice, now crushing slightly misaligned against the structure, causes a loading of the structure in x_s- and y_s-directions. As the aerodynamic damping is added to the structural damping in wind-direction (here: y_s), structural vibrations in x_s-direction consequently do not experience aerodynamic damping. The effect of the low damping on the structural vibrations on the projected x_p-direction, can be observed in Figure 5.12 as vibrations of higher frequency occur once the structure springs forward after a global ice failure event. However, it is striking that the structure vibrates with a low amplitude (0.5 mm) while still being constrained by the ice. Figure 5.13 reveals that the frequency of the low amplitude vibration (≈ 1.1 Hz) is higher than the second eigenfrequency and lower than the third eigenfrequency of the implemented structure. Thus, it is surmised that the intact ice is in contact with the structure and does not break for low amplitude forcing and high frequency but rather causes an added stiffness effect from the perspective of the structure. Added stiffness here means that the structure is experiencing constant constraining by the ice in the lateral direction. The frequency observed is that of the combined ice-structure system (see also Section 3.4.1).

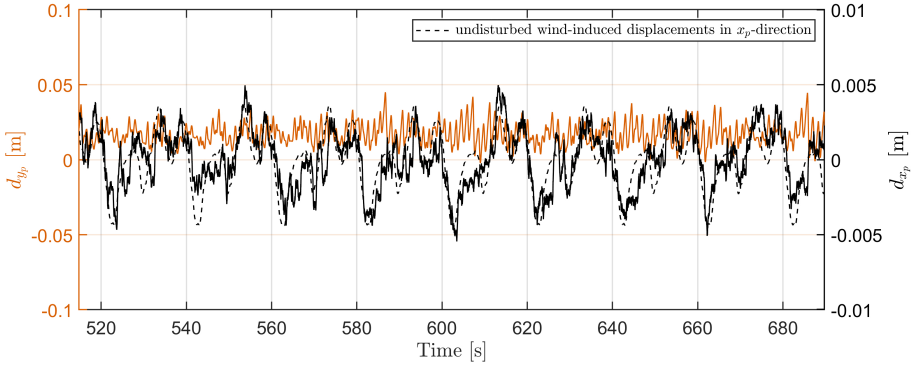
However, it is uncertain if the clearing of ice at the structural sides is caused by wind-induced motion or by the ice-induced motion solely. To address this question, the spatial distribution of the ice loads around the circumference of the structure is analyzed next.

SPATIAL DISTRIBUTION OF THE ICE LOAD

Normalized probability distributions of the resultant ice loading direction across the pile circumference are shown for the eight tested ice drift speeds for the 90° scenario and the aligned (0°) idling scenario in Figure 5.14. For normalization, the number of elements per bin c_i has been divided by the number of elements for the chosen input data N. For quantification of differences, three intervals along the structural surface (I = [340° to 358°], II = [359° to 1°], III = [2° to 20°]) have been defined. For each interval, the cumulative



(a)



(b)

Figure 5.11: Time series of structural displacement in x_p- and y_p-directions for an ice drift speed of 5 mm s^{-1} (Figure 5.11a) and 40 mm s^{-1} for a 90° scenario (Figure 5.11b) (Test ID 387 and 407).

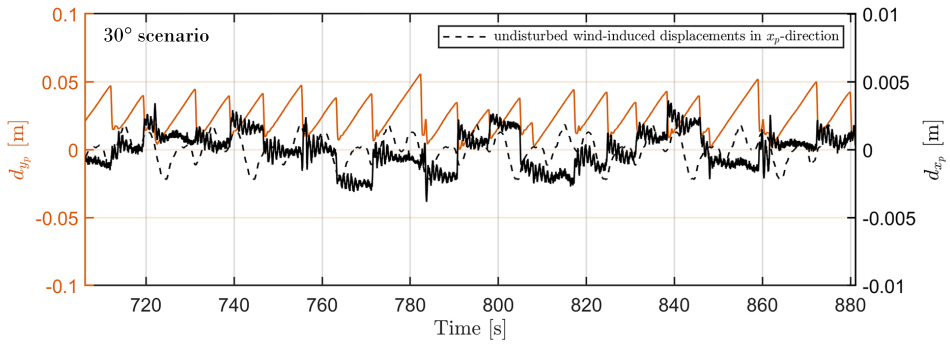


Figure 5.12: . Time series of structural displacements in the pile coordinate system for a small misalignment angle (Test ID 392).

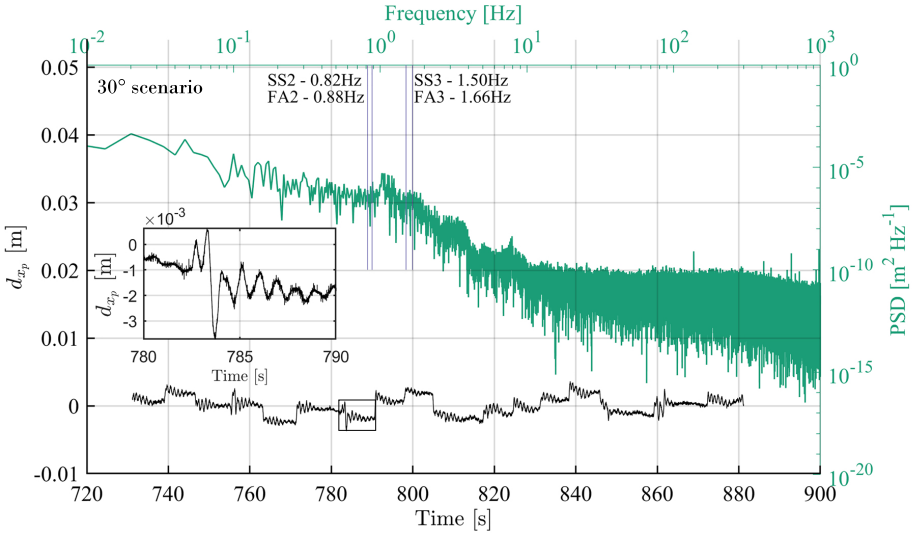


Figure 5.13: Power spectral density and time series of the structural displacement in x_p-direction indicating the natural frequencies (Test ID 392).

probability is given in percentages.

The normalized probability distributions of the resultant ice loading direction reveal that the structure, independent of the misalignment angle and ice drift speed, is mostly loaded in the direction of the ice drift. Values associated with interval II decrease for the 0°, idling scenario from lower to higher ice drift speeds (33% to 21%). Instead of being loaded in the main ice-drift direction as for low ice drift speeds, the structure at high ice drift speeds is more likely to be loaded in interval I and III as here values increase from 26% (I) and 28% (III) to 39% for both. This shift of values relates to the change in

ice-structure interaction from intermittent crushing to continuous brittle crushing where for the former, long load build-up phases are associated with loading in the direction of ice drift. Further note that the structure at low ice drift speeds shows an increased normalized probability distribution of the resultant ice loading direction outside of the defined intervals. The reason here is the added lateral confinement of the ice, increasing the probability of loading at the structural sides (see Figure 5.8-left). The effect of a wind-ice misalignment on the normalized probability distributions of the resultant ice loading direction is largest for low ice drift speeds ($5\,\mathrm{mm\,s^{-1}} - 20\,\mathrm{mm\,s^{-1}}$). Once the wind is acting on the turbine, the structure is loaded in interval I and III more frequently when compared to the 0°, idling scenario. The normalized probability distributions become left-skewed as the mean load of the applied wind fluctuation is positive, thereby causing a positive offset into the direction of wind load application. For the highest ice drift speed, the occurrence probabilities of the aligned and misaligned scenario are almost fully overlapping. The wind-caused displacement in x_p-direction does not seem to have any effect on the resultant ice load direction. From this it is concluded that the wind-induced motions do not crush the ice at the sides of the structure to any significant extent, which would have otherwise resulted in a different distribution of the normalized probability of the resultant ice load when compared to an idling scenario.

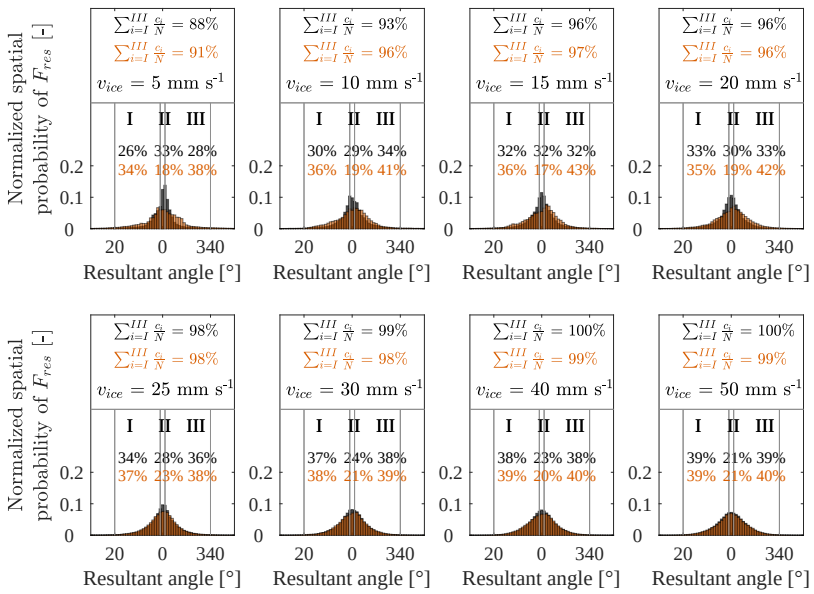


Figure 5.14: Normalized resultant ice load probabilities over the resultant direction angle. Results of a 0°, idling scenario are shown in grey, and in orange for a 90° scenario

5.5. DISCUSSION

5.5.1. EFFECTS OF WIND-ICE MISALIGNMENT ON THE DEVELOPMENT OF ICE-INDUCED VIBRATIONS

The results shown in Section 5.3 align with the general understanding of ice-induced vibrations that lower damping leads to high-amplitude structural vibrations. In the case of an offshore wind turbine, wind adds aerodynamic damping to the system. As the wind is primarily acting at the top of the structure, vibrations related to modes with a high mode shape amplitude at the tower top (e.g. first eigenmode) are more significantly damped during the ice-structure interaction. This explains the findings in Figure 5.3 and Figure 5.4, as ice-induced vibration regimes related to first-mode vibrations (90°, 15 mm s^{-1} and 20 mm s^{-1}) start to appear with an increase in the misalignment angle. However, the aerodynamic damping cannot explain the observed increase of maximum ice loads during intermittent crushing (5 mm s^{-1}) when the misalignment angle increases (see Figure 5.3). It is assumed that the increase in ice load with increasing misalignment angle during intermittent crushing is instead related to the absence of wind-induced structural displacements interfering with the interaction between ice and structure as explored in Section 5.4.1. It is unknown to what extent this interference would remain when the full interaction between wind and RNA is included in an experiment (or numerical simulation).

5.5.2. ICE DEFORMATION AND CRUSHING AT THE SIDE OF THE STRUCTURE

It was shown that the ice is confining the structure for low relative velocity (see Figure 5.10 and Figure 5.11). Once the relative velocity between the structure and the ice increases (e.g., at an unloading phase during intermittent crushing or during continuous brittle crushing), confinement reduces (see Figure 5.11). Structural displacements in x_p- direction at low ice drift speeds (see Figure 5.10, Figure 5.11a, and Figure 5.12) showed that the structure moves out of the main ice-drift direction once it snaps forward after a global ice failure. The direction of deviation seems random. The measured displacement in x_p- direction does not match exactly the expected open-water wind-induced displacement at high relative ice drift speed in operational scenarios (Figure 5.11b). At some instances, the structure is still confined, while at other instances the measured displacement exceeds the open-water wind-induced displacement (see Figure 5.11b, $t = 605$ s). It is speculated that the latter events are caused by the superposition of responses caused by wind and ice.

Analysis of structural responses in x_p-direction revealed that a misalignment angle between 0° and 90° leads to high frequency and low amplitude vibration in the cross-direction (see Figure 5.12 and Figure 5.13). As those vibrations did not match one of the natural frequencies of the implemented structure, it is reasonable to assume ice-structure coupling.

It was suggested that the structure at high relative velocities crushes the ice at the structural side, providing conditions allowing the open-water wind-induced motion to develop. In Figure 5.14, it is shown that the spatial probability of the resultant ice load

of the 0°, idling scenario is nearly the same as for the 90° scenario. However, loading does not necessarily reveal information about the failure of ice. Nevertheless, the ice does constrain the wind-induced motion for low ice drift speeds (see Figure 5.9). Thus, wind-induced motions do not manage to crush ice at the structure side for these ice drift speeds. As the wind-induced motion does not change for higher ice drift speeds, the phenomenon of ice crushing at the structure side is caused by the non-simultaneous ice failure across the circumference of the pile, not by the wind. In addition, it could be argued that the overall stress level of the wind-induced displacements is ultimately too low to crush the ice. However, this argument would require to identify local stresses and associate those to single crushing failures.

5.5.3. GENERALIZATION OF RESULTS

In the present chapter, a lumped mass model of a 14 MW offshore wind turbine was used, instead of a full offshore wind turbine in a fully- coupled aeroelastic solver. A full aeroelastic code and structural model, including blades, could be theoretically implemented in a microcontroller and may be considered in future experiments. This method could be used to investigate if the effect of wind interference on the development of ice-induced vibrations still takes place when the full RNA is accounted for non-linearly. During the test campaign the analysis focused on one wind speed and, respectively, on one set of linearized wind load fluctuations and aerodynamic damping at rated wind speed. Wind sets with smaller aerodynamic damping are expected to result in smaller differences between a misaligned and aligned load scenario, and higher vibrations for an aligned case. Wind sets with higher aerodynamic damping are expected to result in larger differences between a misaligned and aligned load scenario, and lower vibrations for an aligned case. A minor amplitude change of the wind-induced displacement at the ice action point is not likely to have any effect on the development of ice-induced vibrations. A static wind load at tower top, thus a wind-induced mean offset at waterline, was neglected as it was not expected to have a significant influence on the development of ice-induced vibrations. For the overall analysis of a support structure of an offshore wind turbine, and the relative importance of the different alignment scenarios for design, it is important to consider this load contribution as well.

5.5.4. DATA RELIABILITY

5.5.5. SENSITIVITY OF RESULTS TO LOCAL CHANGES IN ICE PROPERTIES AND EQUIPMENT MALFUNCTION

It was attempted to keep the properties of the ice constant during the campaign and to change only the wind-ice misalignment angle. However, it is possible that slight differences in (ice) temperature could have affected the development of ice-induced vibrations. One example of the influence of a substantial change in (ice) temperature on the development of ice-induced vibrations during this campaign was discussed by Hendrikse *et al.* (2022a) and is further discussed in this thesis (Chapter 7). Large differences in the ice thickness could also significantly influence the development of ice-induced vibrations. According to Figure 5.2, differences in the measured ice thickness were relatively large (σ = 3.4 mm). The measurement of the ice thickness was challenging as additional ice

growth under the sprayed ice thickness occurred during the day which had to be manually removed during the measurement, thereby introducing an error and deviation in the measurements.

A significant local ice thickness variation (ice inclusion) was seen to influence the development of ice-induced vibrations. The outlier, identified for the 30° scenario at an ice drift speed of 15 mm s^{-1} (see Figure 5.3), is caused by a sudden change in ice thickness. A defect in a water spray nozzle resulted in a linear band of stronger ice as can be seen in Fig. 7 from Hendrikse *et al.* (2021). While the ice thickness change has a limited effect on the brittle crushing load (quasi-static response in Figure 5.6), time series for lower ice drift speeds (dynamic response) show that the increased thickness introduces a phase of transient ice-induced vibrations which eventually disappear again after about 100 s (see Figure 5.15 at the green dotted line).

Another example of an outlier can be seen for the 0°, idling scenario at an ice drift speed of 10 mm s^{-1} in Figure 5.16. The reason for the increased structural displacement is that the electrical actuator in x_p-direction stopped working during testing. A larger load drop occurred once the test was continued the test at $t = 925$ s, as the ice already had been damaged, thereby providing an artificially high contact area as it was smoothened by previous contact with the structure. The outlier is marked as such in Figure 5.8-left.

Showing these two exemplary events, it is emphasized that maximum ice loads should be considered with care. To minimize the effect of local fluctuations in ice thickness and ice strength on the statistics, 99% and 1% percentiles were used as maximum and minimum in the present study. Statistics were based on the last 175 s of a time series to minimize the effect of initial vibrations on the statistics measured. However, ice crushing tests are limited by the available length of ice, which is why initial vibrations with low frequency are still observable in some time series.

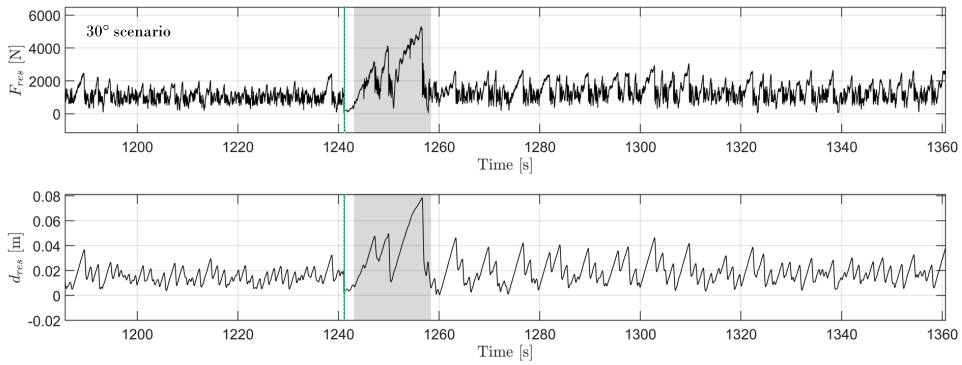


Figure 5.15: An artificially high ice thickness (shaded in grey) introduced a new phase of transient ice-induced vibrations (Test ID 394). The green line indicates where measurements of two Test IDs have been merged.

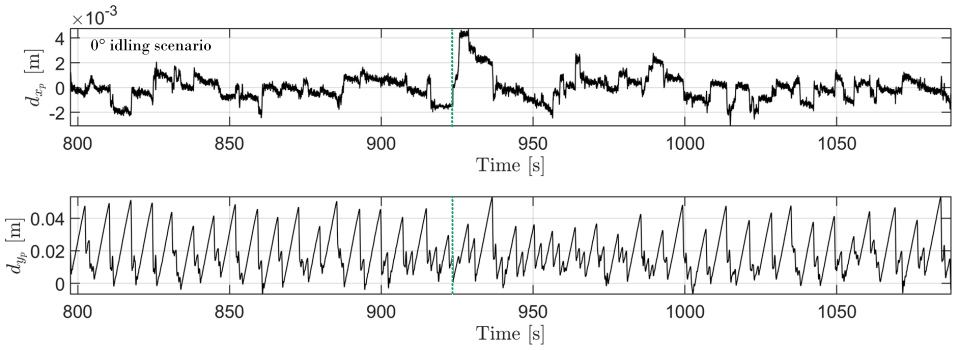


Figure 5.16: Smoothened ice due to a system stop introduces a locally increased structural displacement once resumed (Test ID 591). Here the green line indicates where two tests have been merged and consequently where the test resumed.

5

While post-processing the raw data, it was noticed that ice was 'crawling up' the pile during experiments. Once the ice came close to one of the strain gauge rings and caused temperature-induced strain, an artificial bending stress was included in the measurement. The tested pile was sensitive to those stresses as aluminium provides a high thermal conductivity and the strain gauge bridge in the inside of the pile was relatively large. A photograph of the pile and corresponding load data of an 'ice crawling' event is shown in Figure 5.17. The ice pieces close to the strain gauge ring shift the identified load direction by about 20° for the ring closest to the ice (Ring 2) and by about 12° for the ring with maximum distance to the ice (Ring 1). The load cells attached to the actuators show that the true loading direction had no such offset. It was possible to quantify the offset error in the strain gauge measurements by comparing the medians between the strain gauge and load cell measurements. The median was compared because the load cells measure additional inertial loading (higher peaks). The median is not as sensitive to increased peak measurements as a mean value would be. The calculated difference was substracted for both x_p- and y_p-directional loads in the present chapter. It was observed that the error due to 'crawling' ice in y_p-direction was small compared to the error in x_p-direction. Using the determined load offset, the corresponding offset for the structural displacement was calculated and applied using the numerical structural model. As the ice was 'crawling' during a single test, thereby slightly changing the temperature-induced bending stress amplitude over time, a linear detrend function (MATLAB R2021a) on the data in x_p-direction was applied. As the compensation for the crawling was not solved during the test campaign, but only during the post-processing, it is undeniable that the hybrid test method is influenced by this error. However, it is assumed that this error does not significantly influence the results, as no significant influence of the crushing on the vibration pattern was observed although the load in x_p-direction could have been overestimated. The statistical value of the data can be questioned as the limited test length inhibited test repetitions. Instead of repetition, it was decided to increase the test duration of single tests, allowing to use only the last 175 s of a single test which was more likely to be representative of a steady-state structural response. The full time series of the

measurements can be found in the supplementary material of Hammer and Hendrikse (2023b), indicating the data used in the analysis.

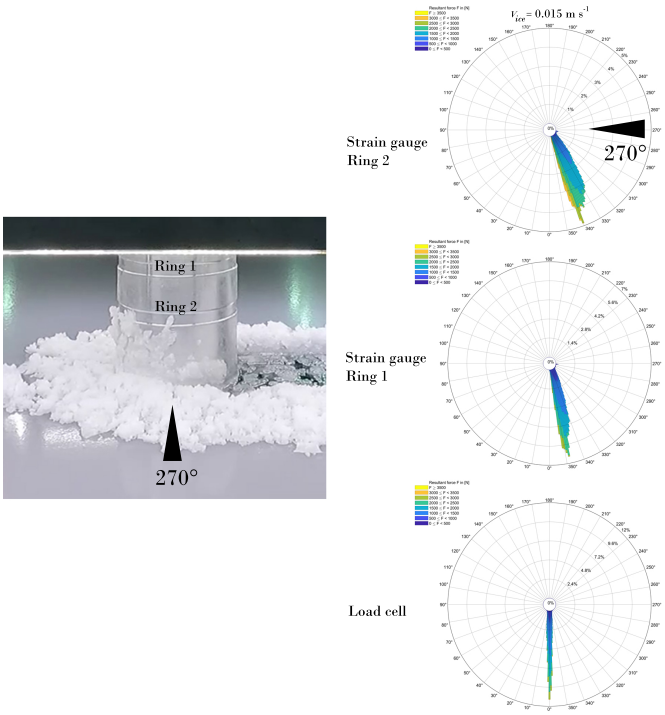


Figure 5.17: Ice attached to the pile influenced the strain gauge measurements. The data shown here are based on the last 100 s of data of test ID 384 and are based on the wind rose tool from Pereira (2022).

5.6. CONCLUSION

An experimental study was conducted to investigate the effect of wind-ice misalignment on the development of ice-induced vibrations of offshore wind turbines. Experiments were based on a hybrid testing technique implementing a linearized modal lumped mass representation of an offshore wind turbine. The structural model excluded blade interaction but included virtual wind loading and aerodynamic damping. The results demonstrate that, in a misaligned scenario, steady-state high-amplitude ice-induced vibrations could develop more pronounced when compared to an aligned scenario. This can be explained by the absence of aerodynamic damping in the direction of ice drift and ice loading. The wind-induced displacements at the ice-action point do not seem to have a significant effect on the development of ice-induced vibrations in a misaligned scenario, though there are indications that the wind-induced displacements can disturb the interaction process in an aligned scenario. At least it was found that structural vibrations due to wind loading interfere with the development of a quasi-static load

build-up in some tests. The ice was found to constrain the lateral structural motion for low ice drift speeds in a misaligned scenario, whereas for high ice drift speeds the open-water wind-induced displacement of the support structure is visible in the response of the structure. This is explained by the rapid succession of failure events in the ice (i.e. crushing of the ice edge) during continuous brittle crushing and clearing of the ice for the structure to move in cross ice-drift direction. A 30°-misaligned scenario resulted in lateral vibrations of the structure of relatively low amplitude and high frequency. For this scenario, the wind-induced motion was still constrained by the ice. The experimental results provide a basis for further studies of the response of offshore wind turbines to misaligned wind and ice loading.



6

IMPLICATIONS OF ICE-INDUCED VIBRATIONS FOR THE DESIGN OF OFFSHORE WIND TURBINES

This chapter delves into the implications that ice-induced vibrations of offshore wind turbines impose on design relevant aspects. The present chapter introduces a matrix for qualitative classification of ice-induced vibrations. Then, a numerical case study is performed to assess the design bending moments of a 14 MW offshore wind turbine in severe ice conditions in the Southern Baltic Sea. Thereby numerical simulations utilize the phenomenological ice model developed by Hendrikse and Nord (2019), which is fully-coupled to BHawC, a proprietary aeroelastic software package from Siemens Gamesa Renewable Energy. Numerical findings are substantiated by a qualitative validation of the implemented ice model with experimental results. Next, a sequential design approach (quasi-coupled) is applied to simulate design loads for the same structure and ice conditions. These results are compared with results based on fully-coupled simulations. Following this, an experimental study investigated the effect of larger tower deflection associated to higher structural modes at the ice action point, mirroring recent size developments of offshore wind turbines. Finally, the classification of ice-induced vibrations, ice-induced vibration mitigation measures, different foundation types under ice loading, and a design generalization are discussed and a conclusion is given.

6.1. INTRODUCTION

Focusing on cold regions, the challenge for offshore engineers lies in designing wind turbines capable of withstanding dynamic ice loads to a specified probability of occurrence. Initially, insights drawn from the utilization of offshore structures in the oil and gas sector (ISO 19906:2019(E), 2019) were used as first input for a design guideline of fixed offshore wind turbines in ice-prone areas (IEC 61400-3-1, 2019). However, as the number of planned wind farms in cold regions increased, concerns emerged regarding the applicability of these initial recommendations (Hendrikse, 2019; Kärnä *et al.*, 2013; Määttänen *et al.*, 2011). In contrast to these studies, the present chapter does not delve

into the specific application of design methodologies. Instead, it concentrates on broader debated topics[1]. These topics often arise in conferences or lengthy correspondences between certification bodies, support structure designers, and turbine manufacturers. Some of the underlying questions of those discussions were formulated below:

Section 6.2: How can ice-induced vibrations (IIV) of offshore wind turbines be classified?[2]

Section 6.3: How can ice-induced vibrations be modelled and which is the most critical ice-induced vibration regime for the design of offshore wind turbines?[3]

Section 6.4: How does the numerical coupling during dynamic ice-structure interaction simulations affect the bending moments along the support structure?

Section 6.5: How does an increase in tower top height affect the development of higher mode ice-induced vibrations?[4]

6.2. CLASSIFICATION OF ICE-INDUCED VIBRATIONS REGIMES OF OFFSHORE WIND TURBINES

In this section, four distinct regimes of ice-induced vibrations for offshore wind turbines are outlined and visualized in Figure 6.1. It should be noted that the descriptions of intermittent crushing and continuous brittle crushing, align with those existing for single-degree-of-freedom structure representations as presented in Section 1.1.

Continuous brittle crushing

The ice load is characterized as a stochastic crushing process around a roughly constant mean value[5]. The order of load magnitude is lowest of all ice-induced vibration regimes. The load signal has no obvious periodicity, and neither does the ice-induced structural displacement. The structural displacement is typically characterized by a small-amplitude oscillation of the structure around a mean displacement. Relatively high and nearly constant relative velocity between structure and the ice occurs.

Multi-modal (ice-structure) interaction-II (also: Frequency lock-in)[6]

The structural response shows a clear periodicity which is also apparent in the ice load

[1] encountered by the author during his studies and time at Siemens Gamesa Renewable Energy

[2] This section has been published in the **peer-reviewed Proceedings of the ASME 2022 41st International Conference on Ocean, Offshore and Arctic Engineering (OMAE)** in a study on the *Classification of ice-induced vibration regimes of offshore wind turbines* in 2022 (Hammer *et al.*, 2022).

[3] This section has been published in **Marine Structures** as part of the study on *Dynamic ice loads for offshore wind support structure design* in 2023 (Hammer *et al.*, 2023).

[4] This section has been published in the **peer-reviewed Proceedings of the 27th International Conference on Port and Ocean Engineering under Arctic Conditions (POAC)** in a study focusing *On the dependency of the development of frequency lock-in on the [tower deflections associated to] higher structural modes* in 2023 (Hammer and Hendrikse, 2023c)

[5] This statement is mainly valid for ice tank experiments. The mean would fluctuate in full-scale due to inhomogeneous properties (e.g., ice thickness, ice strength).

[6] It should be noted that the terms of MMI-II and FLI can be found to be interchangeable in this thesis.

time series. The structure (here: offshore wind turbine) vibrates with the second, and third eigenmode contributing. At the moment of simultaneous ice failure (unloading phase), the structural displacement has a slightly steeper slope than during the loading phase. The latter loading phase can be characterized as the phase during which the relative velocity between the ice and structure remains around zero, causing peak ice loads to occur. Both the presence of higher mode vibrations initiated by a change in relative velocity during the unloading phase of the structure, and the difference in the slope of structural response during the loading and unloading phases are a distinction from the general description of frequency lock-in for single-degree of freedom structures.

Multi-modal (ice-structure) interaction-I
The regime results in largest structural displacements. Peak loads develop after a long phase of low relative velocity between the ice and structure. During the unloading phase the ice load and structural displacement resembles that of multi-modal interaction-II being superposed on a low frequency oscillation. The reason for this observation seems to be that, the relative velocity between the structure and the ice during the unloading phase stays in the range where second and third mode vibrations can be excited. It is expected that this characteristic would not be observed for structures with a much faster first mode oscillation as the relative velocity between ice and structure increases in such cases. The ice load signal shows that phases of contact loss are minimized. The general structural response indicates periodic saw-tooth patterns near the first mode. The loading and unloading phase almost have the same steepness.

Intermittent crushing
This quasi-static regime shows long phases of load build-up with severe, rapid load drops upon global ice failure. After a load drop, the structure crushes through the ice with a high relative velocity. The high relative velocity results in short phases of brittle crushing. Once the structure moves in the same direction as the ice, contact might be lost. During the decay of the structural vibration, several events of contact loss can occur, resulting in load drops to zero or more specifically to the sum of remaining external loads. The frequency of global ice failures is well below the natural frequency of the structure.

In general, ice-induced vibrations of offshore wind turbines can be classified by periodicity of the response and load signal as summarized in Figure 6.1. If neither the time series of structural displacement nor the time series of a global ice load indicate periodicity, the structure and ice do not interact significantly with each other. That situation is here defined as an action rather than an interaction, which is referred to as continuous brittle crushing (CBR) in existing design standards. Once any periodicity is observable, interaction is likely to have taken place between ice and structure. If the global frequency of interaction is well below the first eigenfrequency of the structure, the vibration can be classified as intermittent crushing (ICR) as commonly done. If any interaction at frequencies close to a natural frequency occurs, vibrations can either be classified as multi-modal (ice-structure) interaction (MMI) or as frequency lock-in (FLI), depending on the number of modes of the structure contributing to the interaction. If the structural response does show vibration of a single mode only, thereby resulting in a near-harmonic

structural response, the vibration is classified as frequency lock-in. Once frequencies of multiple modes are present in the structural response, the vibration is classified as multi-modal interaction. As time series of multi-modal interaction can vary significantly, their classification is extended by a numeral, indicating the dominant structural mode (MMI-*n*), e.g., MMI-I in the case of major periodicity in the load and response signals being around the period of the first structural mode. Additionally, the relative velocity between the structure and ice should be around zero, indicating ice-structure synchronization [7]. Also higher mode vibrations must be investigated to distinguish free vibrations from higher mode lock-in vibrations.

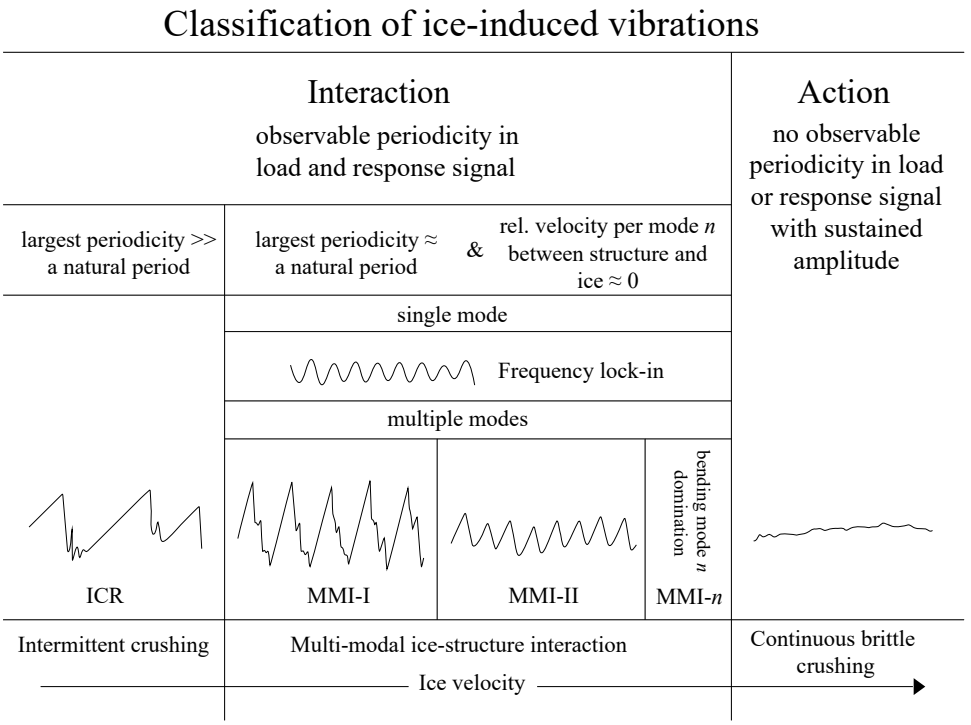


Figure 6.1: Matrix for application of qualitative classification of ice-induced vibrations of offshore wind turbines.

[7] More specifically spatial synchronization can be assumed to occur for the lowest relative velocity at which the ice load still increases during rigid indenter experiments caused by simultaneous ice failure. In this thesis, the value was found to be 1 mm s^{-1} to 2 mm s^{-1}.)

6.3. FULLY-COUPLED ICE-STRUCTURE INTERACTION SIMULATIONS

In this section, ice-induced vibrations of an offshore wind turbine are numerically simulated and analyzed. Furthermore, the global bending moments along the support structure of an offshore wind turbine are analyzed for classified ice-induced vibrations regimes. Numerical results are qualitatively compared to experimental results (presented in Chapter 4) for validation.

A phenomenological ice model from literature (see Appendix A), specifically developed for the simulation of dynamic ice-structure interaction, which was coupled to the Bonus Horizontal axis wind turbine Code (BHawC) by Willems and Hendrikse (2019), was used for simulating ice-induced vibrations of offshore wind turbines. The approach chosen allows a realistic estimation of the bending moments that develop over the support structure at the cost of limited reproducibility. It is noted that the ice model is public and input parameters for the simulations are provided below. As BHawC was used for verification and validation of an open-source code (Guntur *et al.*, 2017), the ice model can be coupled to an open-source aeroelastic software to obtain qualitatively similar results as presented in this section.

6.3.1. ICE MODEL

The ice model used for this work is defined in detail in Hendrikse and Nord (2019). A brief description of the ice model can be found in Appendix A. The applied ice model is a phenomenological model which defines the global ice load on a vertically sided structure as a result of interaction with level ice. The model uses input parameters which define the ductile and brittle behavior of the ice and the ice drift speed. Values for these parameters can be determined based on the method described in Hendrikse and Nord (2019) and also described in Appendix A. Values used here are listed in Table 6.1.

The characteristic peak design load during continuous brittle crushing is obtained based on ISO 19906:2019(E) (2019) and local ice conditions as:

$$F_G = h_w C_R \left(\left(\frac{h}{h_1} \right)^n \cdot \left(\frac{w}{h} \right)^m + f_{AR} \right) \tag{6.1}$$

where F_G is the peak global ice load during continuous brittle crushing, w is the projected width of the structure, h is the ice thickness, h_1 is a reference thickness of 1 m, n and m are empirical coefficients, f_{AR} an empirical term, and C_R is the ice strength coefficient. This formula gives a deterministic estimate of the peak brittle crushing load which can be used for design, but not necessarily the true load on the structure in the given scenario. For the ice model, the parameters are chosen such that during continuous brittle crushing, the peak load obtained from Equation (6.1) has a 50 % probability of exceedance in the simulation of a standard crushing event. The standard crushing event is characterized by an ice drift speed and crushing length. The choice of parameters must guarantee a period of stable continuous brittle crushing. This approach is comparable to that used to define

the C_R coefficient by Kärnä and Qu (2009). The standard stable brittle crushing event was defined here based on full-scale data as a crushed length of 90 m at an ice speed of 150 mm s^{-1}. The input parameters for the simulations as given in Table 6.1 are then obtained by substituting the 50-year ice thickness h_{50} = 0.4 m, and 1-year ice strength coefficient $C_{R,1}$ = 1.38 MPa[8] into Equation (6.1) to obtain the target peak brittle crushing load in the standard crushing event. The somewhat high value of $C_{R,1}$ used here, when the Southern Baltic Sea is concerned, is chosen to have the corresponding full-scale load as during the ice tank experiments. Due to its phenomenological nature, certain physical effects are likely to not be captured in the model. As indicated in a recent analysis by Gagnon (2022), the instantaneous removal of failed ice results in an underprediction of the damping from the ice. This will have to be addressed in a future update of the model. However, for the purpose of this study, the important aspect is that the ice model used captures all relevant regimes of ice-induced vibrations as observed in the experiments (see Section 4.3).

Table 6.1: Ice model parameters with SI units.

Ice model parameters	K_1 [N m^{-1}]	K_2 [N m^{-1}]	C_1 [N m^{-1} s]	C_2 [N^3 m^{-1} s]	N [-]	δ_f [mm]	$r_{\max}$ [mm]
	8.52×10^6	3.26×10^7	3.06×10^7	1.11×10^{18}	58	0.004	0.006

6.3.2. WIND TURBINE MODEL

The ice model is fully-coupled to the Bonus Horizontal axis wind turbine Code (BHawC), which is a nonlinear aeroelastic tool for the dynamic analysis of offshore wind turbines developed by Siemens Gamesa Renewable Energy. BHawC solves substructures for foundation, tower, nacelle, shaft, hub, and blades using a co-rotational formulation, allowing for geometric nonlinearity (Rubak and Petersen, 2005). In more detail, the structural model is implemented as a combination of the stiffness matrix and section force recovery formulation (Krenk and Couturier, 2017) and a stiffness proportional damping formulation (Couturier and Skjoldan, 2018). Aerodynamics are modeled based on the blade element momentum theory, which has been expanded for skewed and unsteady inflow. Corrections for Prandtl's tip loss and thrust at high induction values are implemented. Aerodynamic forces are based on 3D-corrected coefficients for stationary airfoil data and are corrected by a Beddoes-Leishman-type model. Furthermore, tower shadow effects are included, and aerodynamics on the nacelle and tower are calculated. For further details on the aerodynamics, reference is made to Skjoldan (2011). Displaced and contained water as well as marine growth on the support structure are modeled as distributed added mass. A sketch of the wind turbine model and the first three mode shapes of global bending modes are shown in Figure 6.2. The implemented structural model in this case study is representative of a 14 MW wind turbine on a monopile foundation with a diameter of 7.5 m at mean sea level (MSL). The tower top is roughly 134 m above MSL, and the interface between the tower and transition piece is at 14 m above MSL. The water depth was assumed arbitrarily as 30 m, resulting in the pile tip at 62 m below MSL.

[8] $C_{R,1}$ is not determined based on location specific data but rather from the experiments and scaling factor applied. The resulting value is within regular ranges of values used in the Baltic Sea.

The structural model consists of 92 Equilibrium-Based Nonhomogeneous Anisotropic Beam Elements, resulting in a model with 547 degrees of freedom. The soil is represented by linearized p-y-curves representative for the Baltic Sea. The damping (log. dec.) for the foundation and tower were tuned to 5.0 % and 8.3 % for the first and second natural frequencies, respectively (i.e., Rayleigh damping). The model was implemented such that boundary conditions prevent translational and rotational motion in the z-direction at the pile tip.

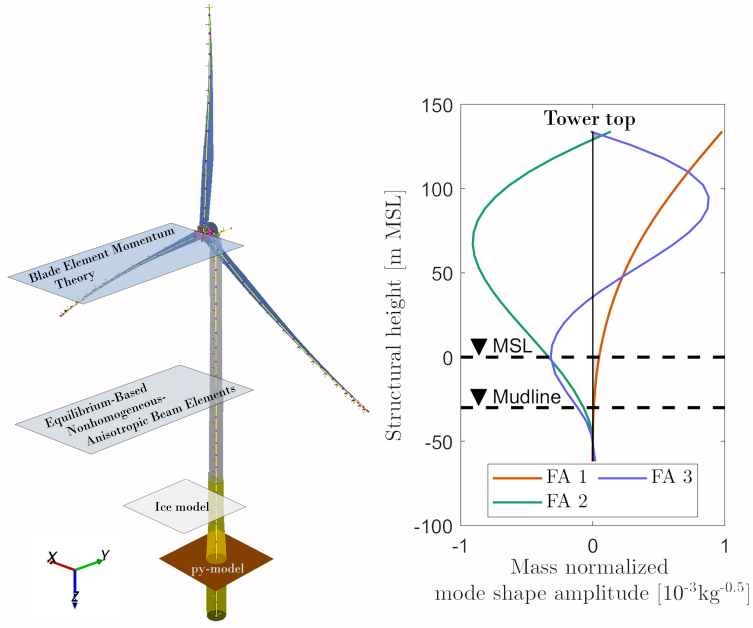


Figure 6.2: Left: Wind turbine model. Right: The first three global bending modes of the modelled structure. The fore-aft direction is denoted FA.

6.3.3. SIMULATION MATRIX

The numerical simulation matrix is given in Table 6.2. As for the experiments, both an operational and idling case are considered. The operational case is representative for design load case (DLC) D3 at rated wind speed in IEC 61400-3-1 (2019). The Wind Turbine Generator (WTG) is in normal power production at rated wind speed, with a normal turbulence model (NTM). The idling case is representative of design load case D8 in IEC 61400-3-1 (2019). The wind turbine is idling at a wind speed below the cut-in wind speed (i.e., the speed above which the turbine starts to produce power), with an extreme wind model (EWM). Relevant ice drift speed intervals for the simulations were defined based on the results from the experimental campaign. A simulation duration of 900 s was chosen to minimize the effect of initial conditions after an initialization time of 300 s. For all simulations, it is assumed that ice drift and wind directions are aligned. Frequency spectra of the numerical data are based on the last 175 s of the data.

Table 6.2: Information on numerical simulations performed.

Turbine state	Representative DLC in IEC 61400-3-1 (2019)	Ice drift speed [mm s^{-1}] (start:step:end)	Wind speed [m s^{-1}] (# seeds)
Operational	D3	(2:1:5), (10:2:70), (70:10:150)	12 (6)
Idling	D8	(2:1:5), (10:2:70), (70:10:150)	1 (6)

6.3.4. NUMERICAL ICE-INDUCED VIBRATIONS REGIMES

Figure 6.3 (idling scenario) and Figure 6.4 (operational scenario) provide an overview of the numerically obtained ice-induced vibration regimes for different ice speeds in the same format as Figure 4.8 to Figure 4.12 for the experimental results. For both an idling and an operational turbine, all four experimentally identified regimes of ice-induced vibrations were found in the numerical simulations. For the idling turbine, intermittent crushing developed for an ice speed of 5 mm s^{-1}. An example of multi-modal (ice-structure) interaction-I has been selected for an ice speed of 38 mm s^{-1}. An example of multi-modal (ice-structure) interaction-II is shown for an ice speed of 48 mm s^{-1}, and at higher speeds (e.g., 150 mm s^{-1}), the simulation resulted in continuous brittle crushing. For the operational turbine, similar results were obtained, with the effect of wind loading clearly visible for the higher ice speeds simulated. A difference between the numerical and experimental results for the operational turbine is the mean offset of the displacement, which was not included in the experiments to avoid having to offset the electrical actuators in the test campaign. Another difference is that in idling scenarios, ice-induced vibration regimes could be observed to occur up to higher ice drift speeds.

6

6.3.5. BENDING MOMENTS ALONG THE SUPPORT STRUCTURE

The absolute maximum bending moments over the height of the support structure are presented in Figure 6.5. These are the maxima from six simulations with different wind seeds for the idling and operational cases as introduced in Table 6.2. Local maxima per cross-section are indicated in purple. It is found that, regardless of the operational state, the maximum bending moments per cross-section occur when the ice drift speeds are low, in the range of 2 mm s^{-1} up to 40 mm s^{-1} approximately. These ice drift speeds correspond to the regimes of intermittent crushing and multi-modal interaction-I as can be seen in Figure 6.3 and Figure 6.4. The effect of the wind load is clearly seen in the results as bending moments over the height of the support structure are much larger for the operational scenario when compared to the idling scenario.

6.3.6. QUALITATIVE ICE MODEL VALIDATION

Qualitatively, numerical results match the experimental observations well as an exemplary comparison in Figure 6.6 shows. Thus, the findings for the bending moments along the support structure are substantiated. Note that the time axes were changed for some regimes to visualize single vibration cycles. It should also be noted that the numerical model results in more regular load and displacement patterns as the model assumes perfectly homogeneous ice, whereas real ice and model ice in comparison to numerical ice are characterized as a relatively inhomogeneous material with both thickness and strength varying across the ice sheet.

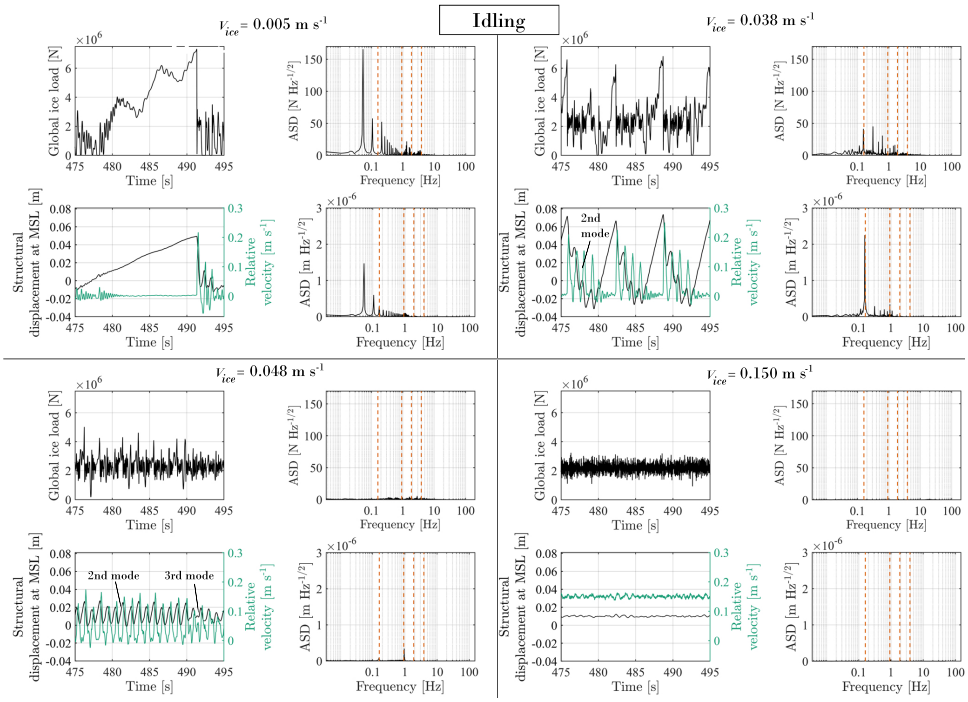


Figure 6.3: Characteristics of global ice load and structural displacement at the mean sea level (MSL) for four representative ice drift speeds for an idling turbine. For each ice drift speed four plots represent the ice load time series (top left), amplitude spectral density of the ice loads (top right), structural displacement time series (bottom left) and amplitude spectral density of structural displacement (bottom right). Dashed orange lines mark the first four structural eigenfrequencies.

6.3.7. CONCLUSION

Numerical simulations of ice-induced vibrations of offshore wind turbines have been qualitatively validated against results from experimental model ice experiments.
Validated numerical simulations have shown that the interaction at low ice drift speeds resulting, in intermittent crushing and multi-modal interaction-I, give rise to the largest bending moments along the full support structure, illustrating the relevance of these ice-induced vibration regimes for the design of offshore wind turbines in cold regions.

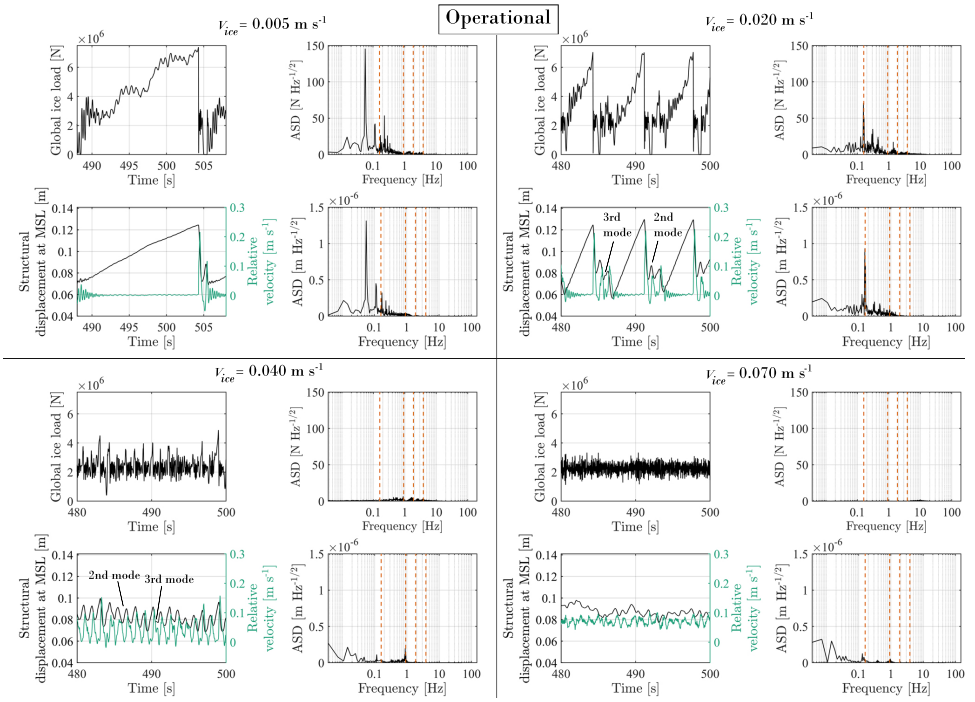


Figure 6.4: Characteristics of global ice load and structural displacement at the mean sea level (MSL) for four representative ice drift speeds for an operational turbine. For each ice drift speed four plots represent the ice load time series (top left), amplitude spectral density of the ice loads (top right), structural displacement time series (bottom left) and amplitude spectral density of structural displacement (bottom right). Dashed orange lines mark the first four structural eigenfrequencies.

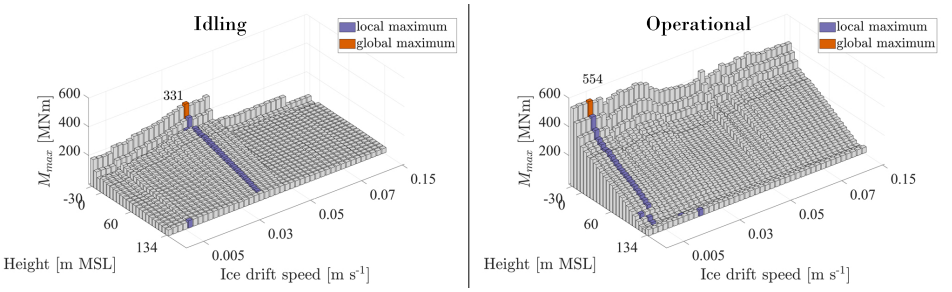


Figure 6.5: Maximum bending moment over the height of the support structure for different design load cases and simulated ice drift speeds.

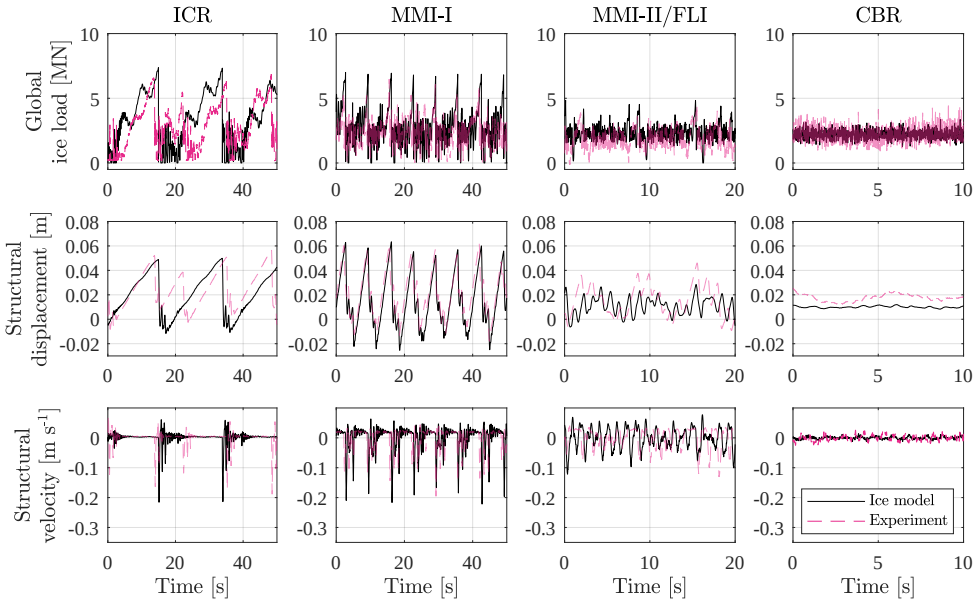


Figure 6.6: Qualitative validation of the fully-coupled simulations for an idling scenario. Note the differences in the time scale. Experimental results are upscaled to full-scale.

6.4. ICE MODEL COUPLING EFFECTS ON ICE-INDUCED VIBRATIONS OF AN OFFSHORE WIND TURBINE

The IEC 61400-3-1 (2019) offers simplified equations for evaluating dynamic ice load effects on offshore wind turbines when statistical data, advanced numerical models, or measurements are unavailable. These simplified equations propose the identification of critical frequencies that might initiate frequency lock-in of the structure. Once these frequencies are identified, they are supposed to be utilized to develop and implement periodic forcing functions when analyzing dynamic ice loading scenarios of offshore wind turbines. However, in the offshore wind industry, forcing functions are commonly determined through numerical simulations of ice-structure interaction. This procedure involves the coupling of ice models to linearized structural models of offshore wind turbines. Once coupled, numerical simulations result in ice load time series, which are then utilized as input for sophisticated software to design the support structures for offshore wind turbines. This design approach is known as a sequential or quasi-coupled design method. The utilization of linearized (or predefined) time series, as commonly applied in dynamic simulations of offshore wind turbines, stems from the field of hydrodynamics. Yet, the application of this method to investigate ice loading scenarios raises debate. This is because ice loads and interaction patterns demonstrate significant dependence on structural motion and vice versa. The difference between a fully-coupled and quasi-coupled design method in application of ice loading is schematically shown in Figure 6.7.

The extent to which a simplified design method, assuming a linear relationship between ice, structure, and wind, can capture all ice-structure interaction regimes and subsequently can determine the design bending moment sufficiently remains unknown.

This section assesses the suitability of a quasi-coupled method considering the general non-linear nature of ice loads during ice-structure interaction. Comparisons are made between results of fully-coupled simulations and quasi-coupled simulations to assess the suitability of the quasi-coupled method. Both design methods employ the phenomenological ice model described in Section 6.3.1. The method for fully-coupled simulations was previously outlined in Section 6.3 and is not repeated here. Predefined time series as input for the quasi-coupled method are based on a linearized structural model of the offshore wind turbine as used in the fully-coupled simulations. The linearized structural model consisted of structural eigenfrequencies up to 20 Hz. When simulating operational scenarios, linearized aerodynamic damping was applied. The predefined ice load time series have been implemented as load input for the aeroelastic simulations in BHawC. All simulations consider a simulation time of 900 seconds. Maximum values for bending moments and structural velocities are based on six repetitions of the simulations with varying wind seed whereby only the last 600 seconds of the signal are considered during the postprocessing.

6.4.1. COMPARISON OF LOCAL MAXIMUM BENDING MOMENTS IN IDLING

In Figure 6.8, the local maximum bending moments of each structural cross section are compared during an idling scenario. Also, relative differences between these maxima

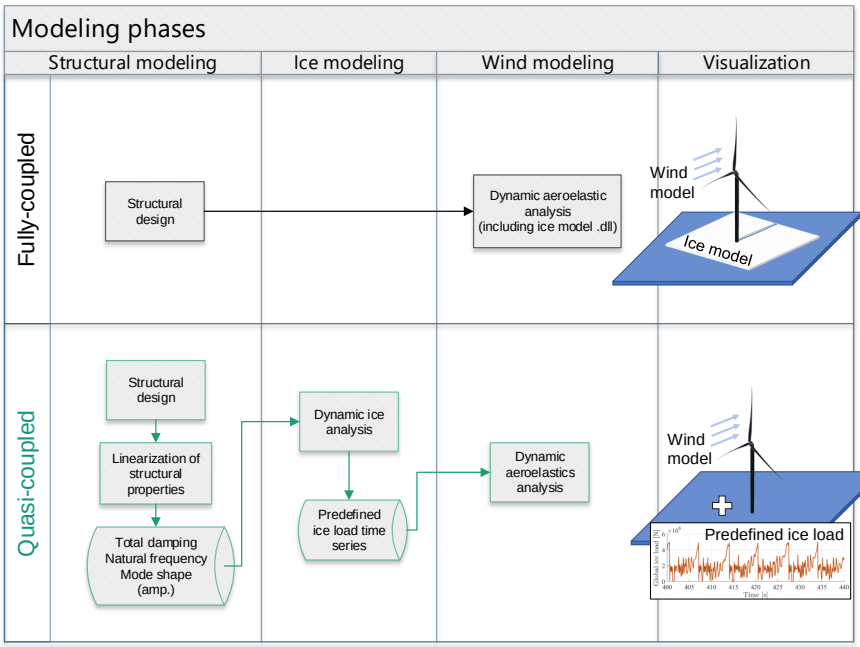


Figure 6.7: Fully-coupled and quasi-coupled design methods for ice-structure interaction analysis of offshore wind turbines.

are calculated per cross section, depicted with colors to indicate which method yielded higher bending moments. Upon examination, neither method consistently generated notably higher or lower bending moments. The quasi-coupled method tended to result in higher bending moments for cross sections above 60 m MSL and two cross sections below the mudline. Conversely, the fully-coupled method tended to result in higher bending moments for cross sections between -10 m MSL and 60 m MSL.

6.4.2. COMPARISON OF BETA-PLOTS IN IDLING

To identify the origins of these differences in bending moments, further analysis is focused on structural velocities at the mean sea level (MSL). Figure 6.9 displays the average peak structural velocity at MSL concerning ice drift speeds for both the fully-coupled and the quasi-coupled method under an idling load scenario. The dotted lines representing $\beta = 1.5$ and $\beta = 1.0$ indicate the range wherein frequency lock-in (FLI) might arise for a single-degree-of-freedom structure representation, as per Hendrikse (2017) and Toyama *et al.* (1983).

Structural velocities for ice drift speeds ranging between $0.01\,\mathrm{m\,s^{-1}}$ to $0.02\,\mathrm{m\,s^{-1}}$ in

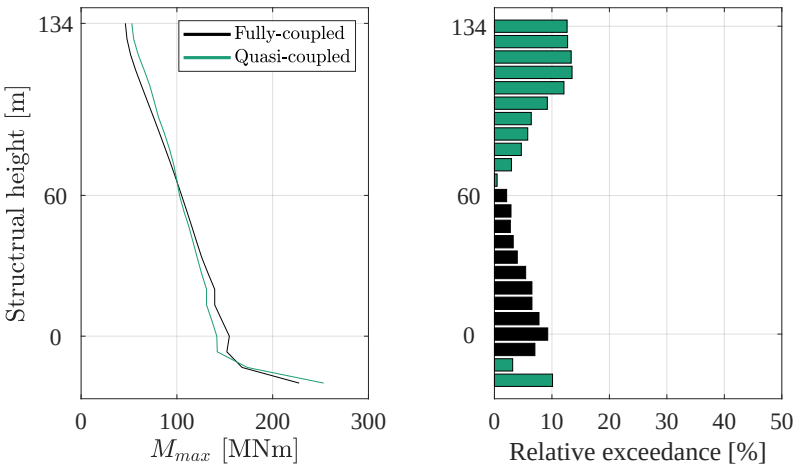


Figure 6.8: Comparison of the local maximum bending moments for each structural cross section of the offshore wind turbine during idling between the two applied methods.

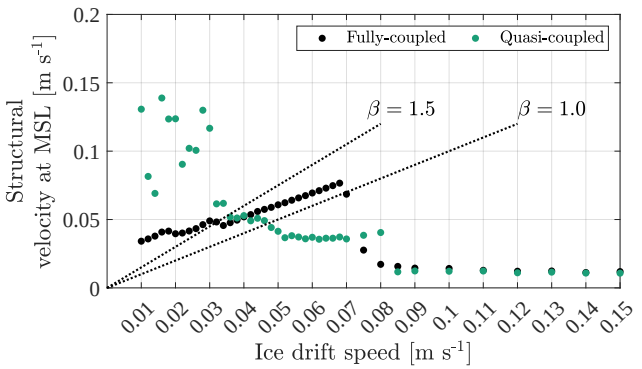


Figure 6.9: Comparison of structural peak velocities at MSL between the two applied methods. The dotted lines representing $\beta = 1.5$ and $\beta = 1.0$ indicate the range wherein frequency lock-in (FLI) might arise for a single-degree-of-freedom structure representation, as per Hendrikse (2017) and Toyama *et al.* (1983).

Figure 6.9 are expected to relate to intermittent crushing. Structural velocities for ice drift speeds ranging between 0.02 m s^{-1} to 0.03 m s^{-1} are expected to relate to multi-modal interaction-I. The fully-coupled method portrays a pattern of steadily increasing structural velocities in these two ranges. Conversely, structural velocities caused by the quasi-coupled method are scattered without a distinct trend. Structural velocities of the quasi-coupled method exhibit significantly higher magnitudes compared to those observed in the fully-coupled method. Moreover, the fully-coupled simulations show a larger range of cases involving frequency lock-in, while peak velocities during continuous brittle crushing remain relatively consistent between both methods.

6.4.3. COMPARISON OF TIME SERIES IN IDLING

In order to characterize the disparities in structural velocities caused by the two methods, time series and their corresponding amplitude spectral densities (ASD) of the global ice load and structural displacement at MSL are displayed in Figure 6.10 for an idling scenario with an ice drift speed of 0.01 $\mathrm{m\,s^{-1}}$. During intermittent crushing, both methods demonstrate similar levels of ice loading. However, structural displacements look significantly different. In the fully-coupled method, structural energy contribution in the displacement signal manifests around a frequency slightly below the first eigenmode. For the quasi-coupled method, the observed pattern comprises a superposition of vibrations involving the first and a higher structural mode. The occurrence of a high mode vibration in quasi-coupled simulations explains the high structural peak velocities observed in Figure 6.9. The frequency of the high mode vibration closely aligns with the frequency of the second global bending mode, suggesting that the predefined time series provoked second mode vibrations. The forced vibrations could be explained by the substantial tower deflection and relatively low damping associated to the second eigenmode at MSL.

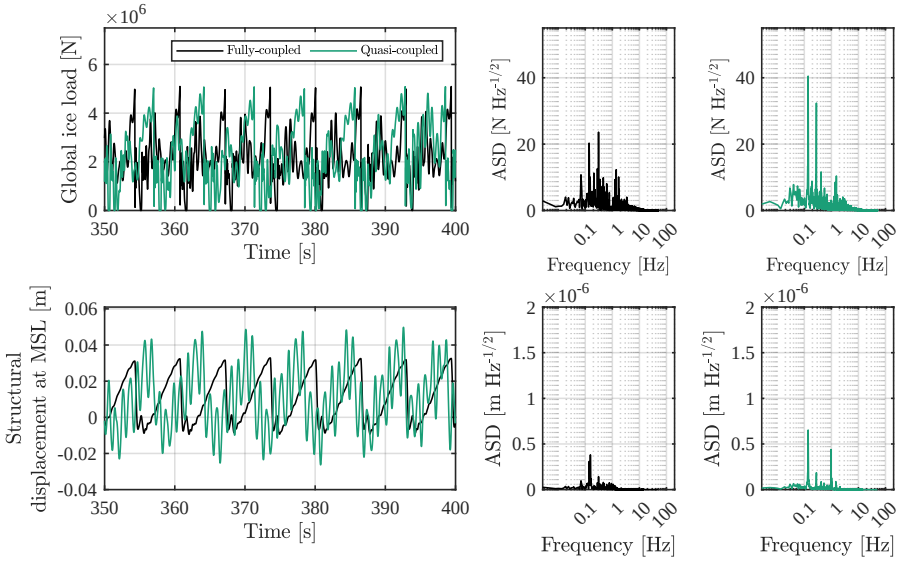


Figure 6.10: Comparison of global ice load, structural displacement and corresponding amplitude spectral densities during intermittent crushing between results of the two applied methods.

In order to distinguish the disparities in structural velocities associated with ice drift speeds related to multi-modal interaction-I, time series and corresponding ASD for global ice load and structural displacement at MSL are shown in Figure 6.11 for an ice drift speed of 0.026 $\mathrm{m\,s^{-1}}$. During the multi-modal interaction, both methods demonstrate similar levels of ice loading. Notably, the quasi-coupled method showed instances of full contact losses, recognizable by load drops to zero. The fully-coupled method resulted in similar load drops, although here the load did not drop to zero. Although the struc-

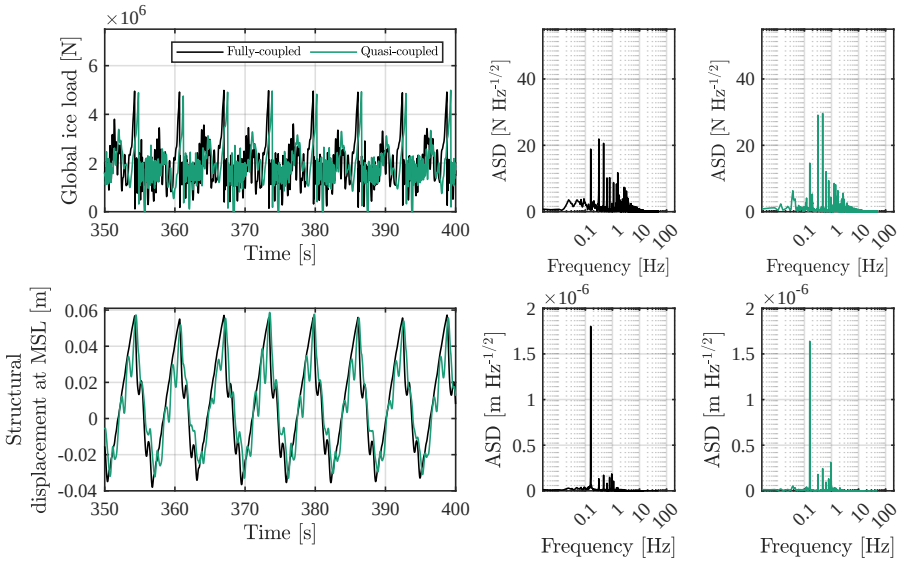


Figure 6.11: Comparison of global ice load, structural displacement and corresponding amplitude spectral densities during multi-modal interaction-I between results of the two applied methods.

tural displacement predominantly exhibited first mode dominance in both methods, the quasi-coupled method causes second eigenmode vibrations within the whole phase of the structural response, akin to the earlier observations during intermittent crushing. The first mode response was not fully developed and was most likely disturbed by the second mode vibrations. However, the discrepancies between the methods were less pronounced compared to the intermittent crushing results. Once again, the combination of first and second mode responses accounted for the notably high structural peak velocities observed in Figure 6.9 for the quasi-coupled method.

6.4.4. COMPARISON OF LOCAL MAXIMUM BENDING MOMENTS IN OPERATION

Upon comparing bending moments between the two methods for an operational scenario (at the rated wind speed) in Figure 6.12, it becomes apparent that the quasi-coupled method consistently underestimates the resulting bending moment. This observation aligns with expectations as aerodynamic damping during operation mitigates the effects of higher mode vibrations. The remaining disturbance in synchronization, assumed to be caused by non-physical loading phases (i.e., loading at phases when the ice and structure would loose contact during fully-coupled simulations), restrains the development of ice-induced vibrations associated with the first bending moment. Consequently, this reduces the magnitude of the resulting bending moment.

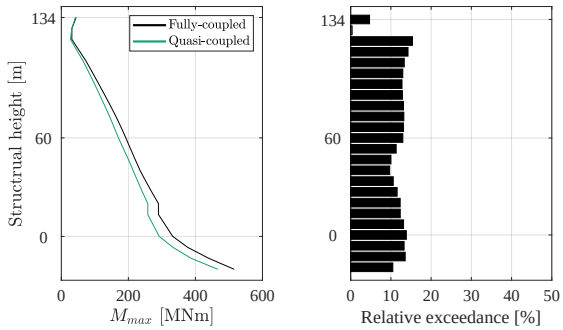


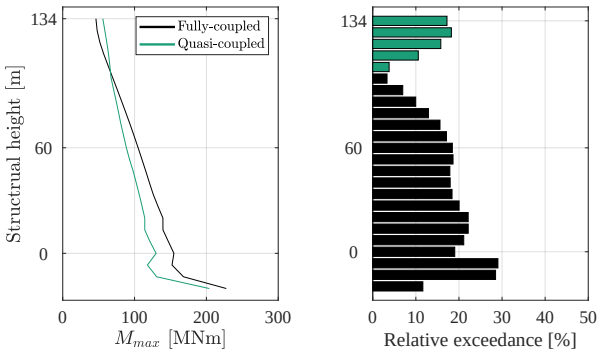
Figure 6.12: Comparison of bending moments along the structural height of the offshore wind turbine during operation for the two applied methods.

6.4.5. LINEARIZED STRUCTURAL MODEL

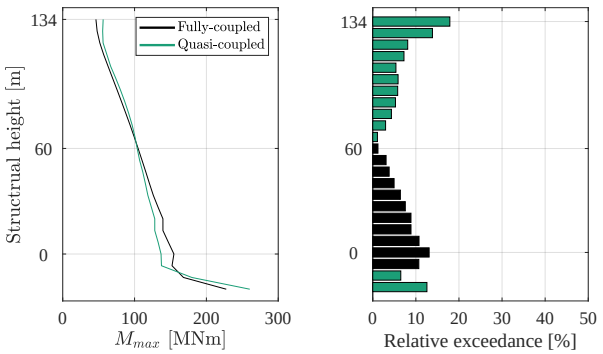
The predefined ice load time series utilized in quasi-coupled simulations are commonly derived from simulations incorporating a truncated, linearized structural model of an offshore wind turbine. This section delves into the effect on design driving bending moments when the structural modes included in these models are altered. Two distinct cases were chosen for the comparison. In the first case, the structural model accounts solely for the linearized properties of the four global bending modes. In the second case, structure modes were expanded to encompass 98% of the global structure stiffness, involving modes up to 2.5 Hz. Simulations conducted for the first case, as depicted in Figure 6.13a, revealed that most global bending moments are underestimated when the quasi-coupled method is applied. This observation suggests that the structural representation, limited to the initial four bending modes, proves to be too stiff to experience the typical ice-induced vibration regimes observed in offshore wind turbines. The second scenario resulted in a comparable state to that of the full structural model (compare Figure 6.13b to the results presented in Figure 6.8).

6.4.6. DISCUSSION

The investigation revealed that quasi-coupled simulations induce forced vibrations in the second global bending mode during idling scenarios. In contrast to fully-coupled simulations, the quasi-coupled approach yielded higher bending moments at cross sections positioned farthest from local maxima of the second global bending mode shape. As aerodynamic damping increases, the damping effect on higher mode vibrations becomes pronounced. Consequently, in these scenarios, the artificial coupling between the ice and structure disrupts the synchronization process during ice-structure interaction, leading to a reduction in bending moments. The outcomes of this study are corroborated by the time series shown by Granlund *et al.* (2023) in Figure 11-left. Although not mentioned by Granlund *et al.* (2023), the excitation of the second mode of the structure can be observed upon the application of predefined load time series in quasi-coupled simulations.



(a) The linearized structural model consists of structure properties of the four global bending modes only.



(b) The linearized structural model consists of structure properties to cover 98% of the total structural stiffness.

Figure 6.13: Comparison of bending moments along the structural heights of the offshore wind turbine during idling for the two applied methods.

The wind industry often refers to the fully-coupled method as a fully-integrated approach. However, the two terms are not interchangeable as discussed by Popko (2020) in the context of ice-structure interaction. The interaction between an external ice model functioning as a dynamic library link (DLL) and an aeroelastic software, as applied in the present study, is defined as fully-coupled and not as fully-integrated because both models communicate based on a numerical solver with invariant time steps. To capture the smallest ice failure events in between these time steps, the solver interpolates the structural velocity between these time steps if required. For large time steps ice failures could be missed. In a fully-integrated method, the models are solved for the same time step and no interpolation is required (i.e., no ice failures are missed). However, during the verification phase of the fully-coupled software as used in this thesis, simulations employing infinitesimally small initial time steps revealed that industry-standard time

steps (e.g., dt = 0.01 s) are adequate to capture the majority of rapid ice failures; the differences observed in comparison to fully-integrated simulations were negligible.

6.4.7. CONCLUSION

It cannot be generalized that a quasi-coupled design method consistently leads to either lower or higher bending moments. The non-physical coupling between ice and structure, where ice loads are applied even when the turbine and ice are not in contact, introduces non-physical coupling effects. The application of predefined time series induces forced vibrations. For the offshore wind turbine investigated in this thesis, these vibrations typically provide a frequency close to the second eigenfrequency. While the fully-coupled method results in a synchronization between the structure and the ice, reaching an optimal state where the contact time and subsequent energy transfer are maximized, the quasi-coupled method fails to achieve full synchronization, evident in the lower energy content within the first mode of the structural response, contact losses, and disturbed ice-induced vibration patterns. Differences compared to a fully-coupled method are contingent on factors such as wind speeds (aerodynamic damping), the chosen linearized structural model, and the cross section of interest. Neglecting the non-linear characteristics of the ice-structure interaction can introduce inaccuracies in the coupled kinematics, synchronization, ice-induced vibration regimes, and subsequently, bending moments.

6.5. ICE-INDUCED VIBRATIONS OF "XXL" TURBINES

Over the last two decades, offshore wind turbines have substantially increased in height, significantly altering their structural properties. This evolution has led to the observation of multi-modal interactions involving higher structural modes during numerical and experimental simulations of ice-structure interaction in this thesis.

As offshore wind turbine sizes continue to grow, it is anticipated that the impact of higher mode vibrations on overall interaction will be further magnified, corresponding to increased tower deflection at the ice action point. Motivated by this projection, experimental investigations were conducted to explore how altering the mode shape amplitude ratio associated to higher structural modes, specifically at the water level within a multi-degree-of-freedom structure representation characterized by low natural frequencies, influences the development of higher mode vibrations during ice-structure interaction.

6.5.1. METHOD

The analysis was conducted with the same experimental setup as used in Chapter 4. As a hybrid test setup allowed full control over the structural properties, specific mass-normalized mode shape amplitudes ϕ_i^* per mode i were numerically tuned, while the total structural stiffness k_{tuned} was kept equal to the original total structural waterline stiffness k_{total}:

$$k_{\text{total}} = \left(\sum_{i=1}^{n} \frac{(\phi_i^*)^2}{4\pi^2 f_i^2} \right)^{-1} = k_{\text{tuned}} \tag{6.2}$$

where f_i is the structural frequency per mode i. Using Equation (6.2), structural properties were scaled for four different configurations, which are summarized in Table 6.3.

All configurations consisted of the first four global bending modes of an offshore wind turbine representation (see Chapter 4). Structural frequencies and damping were kept constant for all configurations. The regular scenario was tested as a reference configuration $\phi_{y,\text{ref}}^*$. For the row of $\phi_{y,\text{eq}}^*$ in Table 6.3, mode shape amplitudes of the second and third global bending modes at MSL were scaled to be of equal magnitude; for the row of $\phi_{y,23}^*$, the second mode shape amplitude was a magnitude larger than for the third mode shape amplitude; and for the row of $\phi_{y,32}^*$, it was vice versa. As one example, the tuning of the third mode shape amplitude for the scaled structure $\phi_{y,32}^*$ is shown:

$$\phi_{y,32,3}^* = \sqrt{\frac{k_{\text{total}}^{-1} - \frac{(\phi_1^*)^2}{4\pi^2 f_1^2} - \frac{(\phi_4^*)^2}{4\pi^2 f_4^2}}{\frac{0.01}{4\pi^2 f_2^2} + \frac{1}{4\pi^2 f_3^2}}} \tag{6.3}$$

An overview of the conducted tests can be found in Table 2 of Hammer and Hendrikse (2023c). Each structure was tested for four different ice drift speeds on the 23.06.2021. All tests were conducted within two runs of the same ice sheet at an ambient temperature T of $-11\,^{\circ}\text{C}$ in cold model ice.

Table 6.3: Table 1. Overview of structures considered in the present study.

	Structural mode i:	1	2	3	4
	f_i [Hz]	0.154	0.888	1.66	2.91
	ζ_i [%]	0.8	1.3	1.9	4.1
Case 1	$\phi^*_{y,\mathrm{ref}}$ [$10^{-3}\,\mathrm{kg}^{-0.5}$]	1.88	14.79	18.72	7.53
Case 2	$\phi^*_{y,\mathrm{eq}}$ [$10^{-3}\,\mathrm{kg}^{-0.5}$]	1.88	15.75	15.75	7.53
Case 3	$\phi^*_{y,23}$ [$10^{-3}\,\mathrm{kg}^{-0.5}$]	1.88	17.83	1.78	7.53
Case 4	$\phi^*_{y,32}$ [$10^{-3}\,\mathrm{kg}^{-0.5}$]	1.88	3.29	32.86	7.53

6.5.2. EXPERIMENTAL RESULTS

In this section, the results of measured structural displacements d_y, ice load F_y, and corresponding frequencies over time for each tested case are analyzed separately. Only the last 50 seconds of the full time series (≈100 s) are shown in the result sections to minimize the influence of transient vibrations on the results. When frequencies or vibrations are related to global bending modes, the frequencies (and vibrations with such frequencies) are related to the eigenfrequencies associated to the specific global bending mode.

CASE 1 - REFERENCE STRUCTURE

First, a reference structural model consisting of the first four global bending modes of an offshore wind turbine model was tested using hybrid simulations in cold model ice. Experimental results (d_y, F_y) for an ice drift speed of 30 mm s^{-1} are shown in Figure 6.14a. The measured structural displacement d_y showed that the tested structure experienced ice-induced vibrations. More specifically, the structural displacement showed mode contributions of at least three different modes. Analyzing the time series in the frequency domain, those structural modes can be quantified. For better mode identification, the chosen grid illustrates the structural frequencies as listed in Table 6.3. Note that the resampling of the data results in a lower resolution of the frequency output and thus in small differences between structural frequencies in Table 6.3 and indicated frequencies in the figure.

The results show that the structure, over the full test length, oscillated with a frequency slightly below the first eigenfrequency. Additionally, it can be seen that the structure, especially in the beginning and in the end of the test, vibrated in a frequency below the second eigenfrequency. In addition to oscillations of the second eigenfrequency, the structure experienced vibrations with oscillation slightly below the third eigenfrequency. It was observed that third mode vibrations mainly occurred or interfered with the development of sole second mode vibrations, once the structure and ice were moving on average in opposite directions, thus with increasing relative velocity. The change in relative velocity seemed to induce the development of third mode vibrations. Focusing on the measured ice load F_y in Figure 6.14a, it was noticed that single load peaks occurred once the structure experienced second mode oscillations. It is also interesting to observe

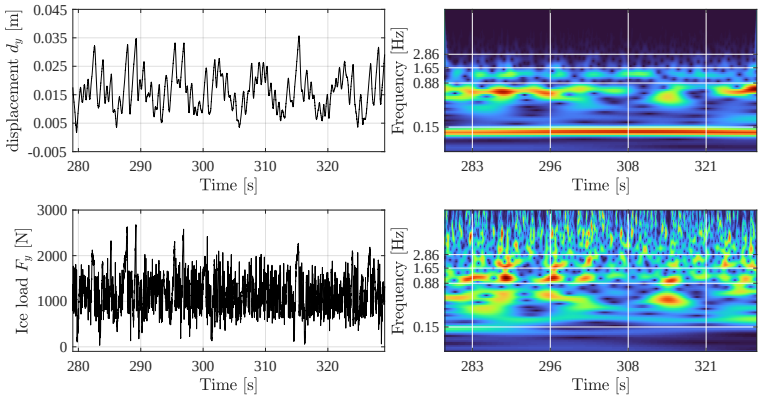
that single instances existed when the measured ice load almost dropped to zero. These load drops did not occur directly after the load peak, but after some time when the ice and structure moved in the same direction. Once the structure moved faster than the ice (negative relative velocity), the ice and structure lost contact. When analyzing the load time series in the frequency domain, a large contribution of frequencies that are significantly higher than the structural eigenfrequencies can be found. Those frequencies were not observed in the frequency analysis of the structural displacement. Thus, either the structure or the measurement system acted as a low-pass filter on the displacement signal. But also vibrations close to the structural eigenfrequencies were found in the frequency domain of the ice load time signal, although the measured frequencies were either slightly higher or lower than the corresponding structural eigenfrequency.

CASE 2 - EQUALIZED MODE SHAPE AMPLITUDES

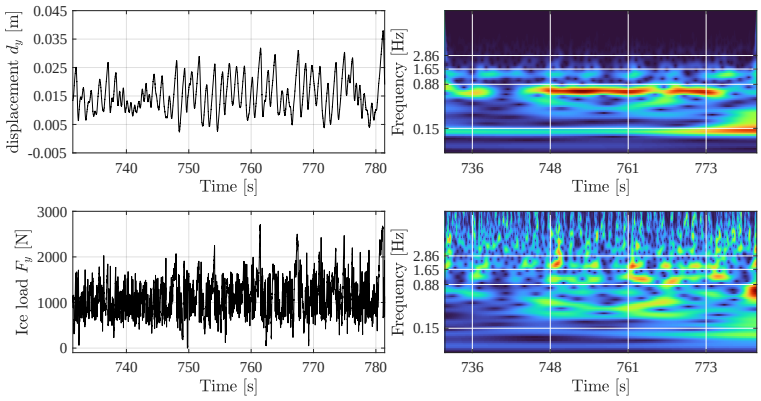
For the next case, the mode shape amplitudes of the second and third eigenmode at water level were equalized, while the total structural stiffness and damping of the structure were kept constant. Experimental results for a test with an ice drift speed of 30 mm s^{-1} are shown in Figure 6.14b. The measured structural displacement showed that the structure underwent oscillations of two frequencies mainly. The analysis in the frequency domain showed that the active frequencies were close to the second and third eigenfrequencies. But again it can be observed that the oscillation frequencies were slightly below the structural eigenfrequencies. In comparison to the previous case, durations of single mode vibrations in this case were more continuous, and the structure tended to vibrate in the second eigenmode mainly. While the first mode was less pronounced in this instance compared to the initial case, the ice load time series in the second case exhibited results similar to those in the first case. However, in the present scenario, load peaks and contact losses occurred more regularly. When examining the load time series in the frequency domain, frequencies slightly lower or higher than the natural structural frequencies were still recognizable, although not as prominently as observed in the first case.

CASE 3 – LARGE SECOND MODE SHAPE AMPLITUDE

For the third case, the mode shape amplitudes of the second and third mode were tuned so that the magnitude of the second mode exceeded the mode shape amplitude of the third mode by a factor of ten while keeping the total structural stiffness and damping of the structure constant. The measured structural displacement in Figure 6.15a for an ice drift speed of 50 mm s^{-1} shows the presence of oscillations of two frequencies mainly. The analysis in the frequency domain revealed that those are related to the first and second structural eigenfrequencies. Note that the measured frequencies were again slightly lower than the structural eigenfrequencies. The load time series shows peak loads and significant load reduction in phases of negative relative velocity. The frequency analysis showed that a frequency below or above the second eigenfrequency was present in the measured ice load signal. No significant contribution of the third eigenfrequency could be observed either in the displacement or in the load signal.



(a) Experimental results of the structural displacement d_y and ice load F_y and corresponding wavelet transformations for Case 1.

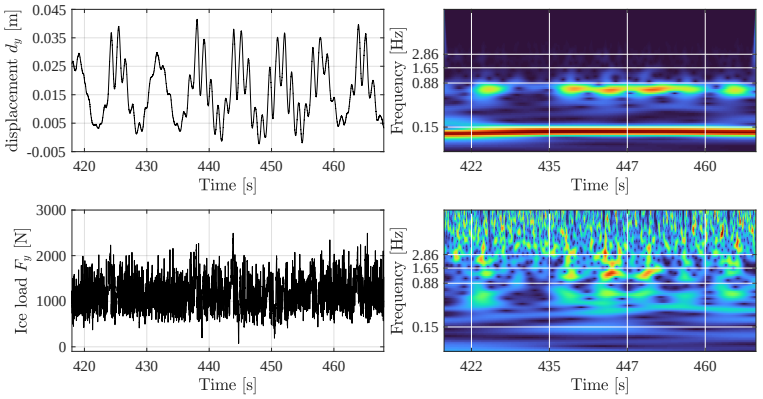


(b) Experimental results of the structural displacement d_y and ice load F_y and corresponding wavelet transformations for Case 2.

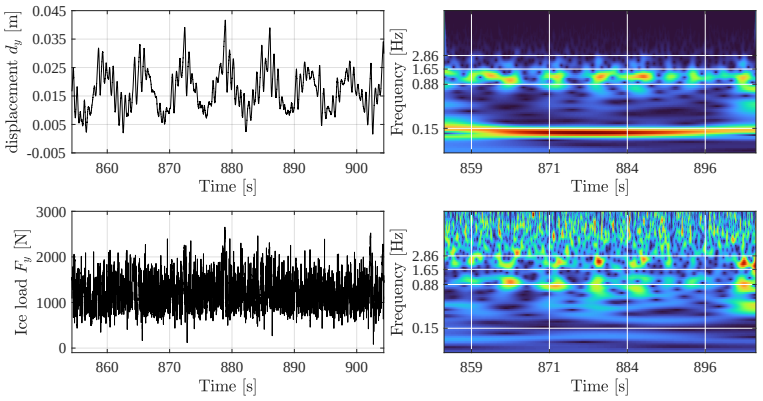
Figure 6.14: Experimental results for Case 1 and Case 2. Note that the resampling of the data results in a lower resolution of the frequency output and thus does not allow to indicate the same structural frequencies as in Table 6.3 on the y-axis.

CASE 4 - LARGE THIRD MODE SHAPE AMPLITUDE

Conversely to the third case, the mode shape amplitudes of the second and third mode were tuned, so that the third mode shape amplitude exceeded the mode shape amplitude of the second mode by a factor of 10, while keeping the waterline stiffness and damping of the structure constant. The measurement displacement in Figure 6.15b for a speed of 50 mm s^{-1} shows that the structure underwent oscillations of mainly two frequencies. The analysis of the time signal in the frequency domain showed that the frequencies measured are slightly lower than the first and third structural mode. While only slightly recognizable in the time series, the frequency analysis revealed that the structure even



(a) Experimental results of the structural displacement d_y and ice load F_y and corresponding wavelet transformations for case 3.



(b) Experimental results of the structural displacement d_y and ice load F_y and corresponding wavelet transformations for case 4.

Figure 6.15: Experimental results for case 3 and case 4.

experienced single cycles of fourth mode vibrations. The load time series of Case 4 looked similar to that of Case 3. However, the load time signal showed a higher number of load peak cycles due to the increased frequency of the lock-in phenomenon.

6.5.3. MULTI-MODAL INTERACTION

Finally, the measured structural displacement between three different multi-modal interaction regimes are compared in Figure 6.16. For the lowest ice drift speed (Figure 6.16-left), the first mode became excited during a phase of low relative velocity. When the relative velocity increased, because the structure crushed through the ice in the opposite drift di-

rection, the next higher mode became excited (second mode). When testing with a higher ice drift speed (Figure 6.16-center), the second mode became excited during the phase of low relative velocity. Again, when the relative velocity increased, because the structure crushed through the ice in the opposite drift direction, the mode with the largest mode shape amplitude became excited (third mode). When testing with the highest ice drift speed (Figure 6.16-right), the structure vibrated in the third eigenfrequency during the phase of low relative velocity. Only in this case did the structure not follow the trend and did not experience sustained fourth mode vibrations during the phase of higher relative velocity as to be expected. Instead only a single cycle of fourth mode vibrations was observed at the end of the shown signal. However, Figure 6.16 illustrates that ice-induced vibrations of multi-degree-of-freedom structures are highly dependent on the relative velocity between the ice and structure and thus on the superposition of higher mode oscillations with lower mode oscillations.

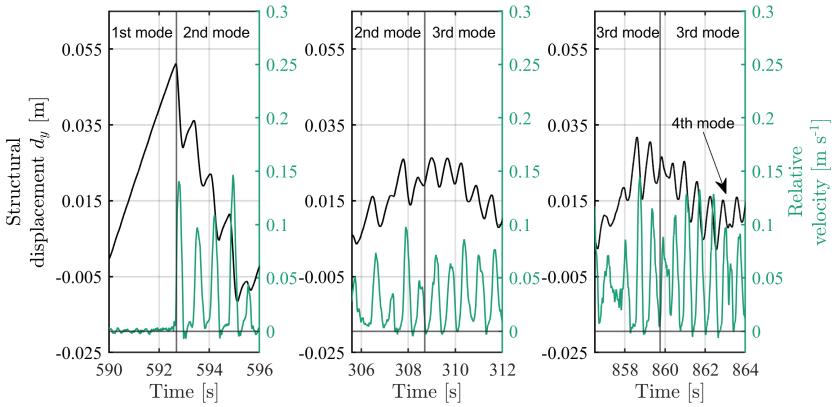


Figure 6.16: Measured structural displacement of three different multi-modal interaction regimes.

After presenting the results of ice-induced vibrations experiments of four different structural configurations, it can be summarized that:

- A frequency lock-in competition between second and third mode vibrations occurred for the structural reference case (Case 1). Once the mode shape amplitudes were equalized (Case 2), the structure tended to undergo oscillations with a frequency close to the second eigenfrequency superposed on a first mode oscillation.
- The structure experienced sustained frequency lock-in vibrations, superposed on first mode oscillations, in a frequency corresponding to the mode shape amplitude of artificially high magnitude (Case 3 & 4).
- Increased maxima of the measured structural displacement and increased maxima and standard deviations of the measured ice load occurred once either the second or the third mode shape amplitude exceeded the other by a factor 10 (case 3 & 4)[9].

[9] Corresponding results have not been shown here but can be found in Hammer and Hendrikse (2023c)

Furthermore, it was found that:

- All tested structures resulted in ice-induced vibrations characterized by multiple structural frequencies excited, wherein frequencies of the measured structural displacement were slightly lower than the eigenfrequencies, and frequencies within the ice load signal were either lower or higher than the eigenfrequencies.
- Case 3 and Case 4 resulted in sustained ice-induced vibrations up to higher ice drift speeds, e.g., showing contributions of first mode structural vibrations up to higher ice drift speeds.

6.5.4. DISCUSSION

ICE-STRUCTURE COUPLING

Identified frequencies in the measured structural response were lower than the natural frequencies. Frequency analysis of the ice load time series showed frequencies at the lower and upper boundary of the eigenfrequency, and a clear absence of any natural frequency content. This observation showed that ice-structure interaction should consider the coupling between structure and ice. Ice load signals recorded from Nord *et al.* (2013) and Nord *et al.* (2015a) indicated that the coupled frequencies were below the natural frequency as can be seen from Figure 4 and Figure 5 in their publications, respectively. However, here it can only be concluded that the ice load explicitly did not show a frequency contribution at exactly the linearized structural eigenfrequencies.

HIGHER MODE VIBRATIONS

As the total structural stiffness was kept constant but solely the mass-normalized mode shape amplitude was changed, it is emphasized that observations presented are neither related to a change in stiffness nor change in frequency. Consequently, the conclusion of Nord *et al.* (2015a) can be updated in a way that it is the distribution of mass-normalized mode shape amplitudes of higher modes that shifts the transition speed from first to second (or third) mode vibrations. Further, the observation of Nord *et al.* (2013) can be confirmed, which stated that the maximum ice load increases when the response has more than one major frequency component active and that the ice-induced load (standard deviation) and maximum displacement depends on the number of activated modes.

6.5.5. LIMITATIONS

It could not be distinguished if the first structural mode vibrated because of the set of initial conditions or because of the set of tested parameters. Dedicated tests with longer test length could be conducted to improve these insights. However, the full time series indicated that the effect of transient vibrations could be negligible. To investigate if the presented results could be generalized for higher structural modes, tests with structures consisting of higher structural modes could be conducted. However, such experiments could bring the complexity of data analysis to a point where distinction

between oscillation of single structural modes is not possible and instabilities of the hybrid simulations in ice are provoked (see Chapter 3).

6.5.6. CONCLUSION

To investigate the influence of a sole change of tower deflection on the development of multi-modal ice-structure interaction, small-scale experiments of a vertical structure in model ice were performed. Numerical models with exclusively-tuned mode shape amplitudes at the water level were implemented in hybrid simulations to analyze the development of multi-modal vibrations. Higher mode oscillation was controlled by a sole change of mass-normalized mode shape amplitude, while keeping stiffness and damping constant. Ice-induced vibrations of multi-degree-of-freedom structures are highly dependent on the relative velocity between the ice and structure. Higher mode vibrations are thus highly dependent on the low-frequency oscillation of the structure.

6.6. DISCUSSION

The preceding sections addressed the primary questions outlined in Section 6.1, particularly concerning the implications of ice-induced vibrations for the design of offshore wind turbines. The following is a discussion of those implications.

CLASSIFICATION OF ICE-INDUCED VIBRATIONS

In the context of the classification of ice-induced vibration regimes, it is important to note that this study has up to now only provided a qualitative classification algorithm. Granlund *et al.* (2023) introduced a quantitative classification scheme aiming to categorize ice-induced vibration regimes based on normalized structure accelerations. Despite the claim by the authors that "no information about the modal properties of the structure [is] required," it is important to highlight that key parameters for the algorithm were identified "by visually inspecting various time series data" and "by analyzing a time series of [ICR] and measuring the ratio of the duration of the build-up phase to the complete cycle." These parameters are subject to change with alterations of the structure. Therefore, the classification algorithm implicitly depends on structural properties embedded within the response of the structure and time series data, although indeed does not require external information about the modal properties when applying the algorithm. Additionally, it is worth noting that the proposed classification scheme might categorize second mode resonance as frequency lock-in since it lacks parameters to investigate synchronization between the structure and the ice. Covering this aspect, a quantitative classificaiton scheme is presented next, which, contrary to Granlund *et al.* (2023) requires external information (i.e., eigenfrequencies) of the structure of interest and can only applied when multi-modal interaction develops. The method computes the cumulative Power Spectral Density ($cPSD$) of simulated time series to investigate the periodicity of the simulated signals. Upon reaching a specific percentile of the maximum $cPSD$ during summation, a corresponding percentile frequency f_{perc} could be established and be compared against the eigenfrequencies of mode n (f_n). Considering ice-structure coupling, the coupled vibration frequency might differ within a coupling interval CI

compared to the linearized bending mode frequency (see also Section 2.6). To explore the development of frequency lock-in, a check on the relative velocity becomes necessary. Here, the relative velocity between the structure and ice is investigated. The regime can be classified as MMI once it is shown that the relative velocity is at or below the velocity v_1 at which ice begins causing a load peak increase before simultaneous ice failure. The algorithm involves sorting the time series $x(t)$ from lowest to highest ice velocity across the index i. The following statements have been implemented to classify the numerically simulated ice-induced vibrations as visualized in Figure 6.17:

$$x(t)_i \in \begin{cases} \text{MMI}_n \text{ and flag} \rightarrow 1 & \text{if } CI(1) \cdot f_n < f_{\text{perc}} < CI(2) \cdot f_n \textit{ and } v_{rel_n}(t) \overset{t=[0,\frac{1}{f_n}]}{\rightarrow} v_1 \\ & \textit{and } cPSD_{norm;i} > cPSD_{norm;CBR} \\ \text{ICR} & \text{if } f_{\text{perc}} < CI(2) \cdot f_1 \\ \text{CBR} & \text{if flag} == 1 \text{ and } x(t)_i \notin \{\text{MMI}_n, \text{ICR}\} \end{cases} \tag{6.4}$$

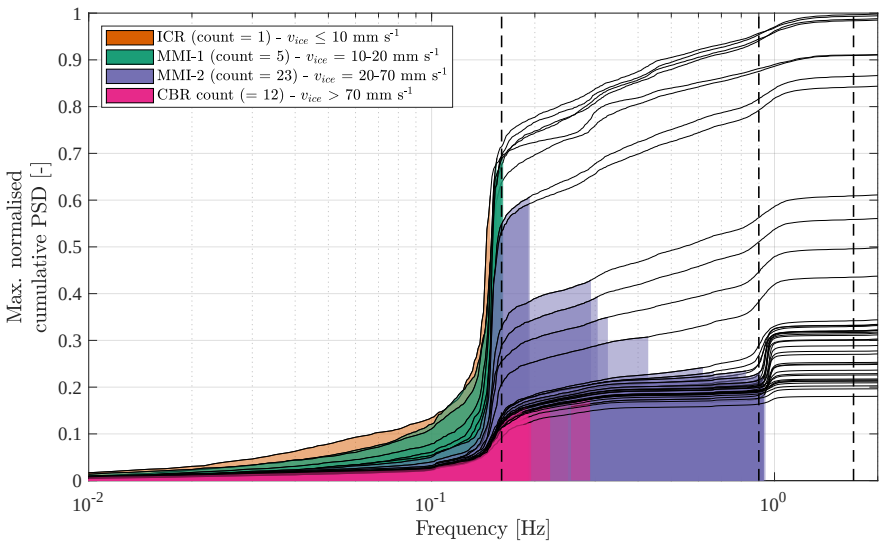


Figure 6.17: Results after application of the classification algorithm to fully-coupled simulations of ice-induced vibrations of an offshore wind turbine. However, transition regimes cannot be accurately classified.

While examining fully-coupled simulations, the algorithm demonstrated robust outcomes for this choice of values: CI = [0.95, 1.05], $f_{perc} = f_{70}$, and $cPSD_{norm;CBR}$ = 0.25. Nonetheless, considerable uncertainty persists within the algorithm. Factors such as the selection of the coupling interval CI, the percentile threshold (*perc*) for f_{perc}, and the velocity v_1 vary with ice characteristics, quality of time series, and structural frequency

composition.

Overall, the author believes that, while quantitative regime classification algorithms serve as valuable industry tool, it remains crucial not to assume that ice-induced vibrations can be universally and definitively classified.

OFFSHORE WIND TURBINE SPECIFICS

This thesis notably omitted the impact of several factors such as blades (e.g., blade pitch, passing), soil, gravity, varying wind speeds, yaw errors, marine growth, water depth, and others on the development of ice-induced vibrations and thus on the offshore wind turbine design loads. If deemed relevant, it appears to be more practicable to explore such effects through numerical case studies based on simulations with a validated, fully-coupled ice model.

ICE-INDUCED VIBRATION MITIGATION

This thesis did not delve into ice-induced vibration mitigation methods, such as the installation of conical structures. Cones alter the failure mode of drifting ice from crushing to bending, potentially reducing the loads on the structure, and thus supposedly reducing the occurrence of ice-induced vibrations. However, this broad assumption does not entirely align with the understanding of the author. To the author's knowledge, conical structures still could experience ice-induced vibrations, albeit caused by bending failure of the ice instead of crushing. This alteration shifts the mechanism from spatial synchronization to a temporal synchronization problem, as over time, the structure could start to vibrate with the frequency of the bending failure (forced vibration). Additionally, it should be noted that during the bending of ice, short phases of crushing could occur (Petry *et al.*, 2023). While the author agrees that cones most likely change the development of ice-induced vibrations, it would be surprising if structures like offshore turbines would show no form of ice-induced vibrations during the ice-structure interaction. Additionally, the added mass of the cone alters the structural stiffness and thus eigenfrequencies, a factor to consider when evaluating the impact of conical structures on mitigating ice-induced vibrations. The installation of conical structures extends the effective foundation diameter, potentially increasing long-term damage from waves and currents, and affecting both transportation and installation. Perhaps more sophisticated methods could be applied to mitigate ice-induced vibrations, for example, by tuning of the mode shape amplitudes at the ice action point to promote a mode competition (refer to Figure 6.14a). This competition might disrupt the development of sustained vibrations, thus reducing overall damage to the offshore wind turbine. Further, active blade controllers could be used to dampen second mode vibrations, as flap yaw blade modes are often coupled to the second eigenmode of offshore wind turbines.

FOUNDATION TYPES

This thesis focused on offshore wind turbines with monopile foundations. In regions with severe ice conditions and shallow water depths—where sea ice development is more likely—there is a potential emergence of gravity-based foundations for offshore wind

turbines. These foundations, offering relatively high structural eigenfrequencies, could serve as a viable solution to mitigate pronounced ice-induced vibrations. However, as turbine sizes increase, eigenfrequencies are set almost *below* the peak frequencies of wave and wind spectra. Gravity foundations might realign structural eigenfrequencies into the wind and wave spectra, potentially amplifying accumulated fatigue damage. The increased effective width of gravity foundations could increase damage from waves and currents over their lifespan. Other scenarios could be that the ice rides up the gravity foundation and interacts with the turbine directly.

Jacket structures bring forth novel ice failure and loading phenomena such as splitting, jamming, shielding, and mixed mode ice failures on steep conical structures. While jamming might be less of a problem (Lelieveld, 2021), local structural elements like braces can be expected to result in local frequency lock-in (Hoek, 2021). The incorporation of asymmetric foundation types could intensify vibrations in torsional structural modes and pose challenges during installation.

The understanding of ice-induced vibrations for floating offshore wind turbines remains uncertain. Speculating, the relationship between mooring line or anchor capacity and ice compressive strength might drive the static load scenario. Both static and dynamic design considerations could depend upon the pitch of the offshore wind turbine under loading as an increased vertical ice load angle might lead to ice failure in bending rather than crushing. However, if crushing were to occur, it could cause severe multi-modal interactions due to the relatively low natural frequencies of floating structures (e.g. depending on higher mode damping). Dynamic effects in the mooring line (i.e. nonlinear stiffness) are expected to influence the development of ice-induced vibrations.

DESIGN GENERALIZATION

The identification of critical ice-induced vibration scenarios for design purposes relied on analyzing the maximum bending moment (ULS) in a specific case study under Southern Baltic Sea conditions. The Baltic Sea is characterized by generally mild wave and wind loads, making ice load scenarios influential in the design of offshore wind turbines in these regions. Ice, wave, and wind conditions are interconnected, especially in fetch-limited or sheltered seas like the Baltic, where limited wave heights allow for undisturbed ice growth. As ice grows, it dampens the waves, and strong winds remove snow from the ice, promoting further ice growth. Wind can also detach landfast ice in the spring, initiating ice drift towards wind farms. However, it is essential to note that certain regions or scenarios may prioritize design considerations based on wind and wave loads rather than level ice. Future projects in the Northern Baltic Sea might encounter design driving loading scenarios caused by ice ridge formations.

In cases of intermittent crushing, the ULS loads typically govern the design for the foundation. However, multi-modal interaction can shift the ULS envelope, making ice loads dominant at the interface between the foundation and tower. This is a crucial aspect of the design because, in such scenarios, the bottom flange of the tower is affected by ice loads, expanding the scope beyond the foundation alone. This observation could

become particularly significant for XXL turbines, where multi-modal interaction, such as MMI-II or MMI-III (refer to Section 6.5) could cause the ice loads to dominate a larger part of the tower.

For a more extensive analysis of the viability of monopile foundations for offshore wind installations across the entire Baltic Sea, incorporating considerations of ice-induced vibrations, the reader is referred to van der Stap *et al.* (2023). The study also underlines the considerable impact of fatigue damage resulting from ice-induced vibrations on the design of offshore wind turbines, particularly when offshore wind turbines are planned to be build in more northern regions with increased exposure to ice.

6.7. Conclusion

The analysis and discussion of fully- and quasi-coupled simulations as well as hybrid simulations for larger offshore wind turbines leads to the following conclusions:

1. Ice-induced vibration regimes of offshore wind turbines can be categorized into intermittent crushing, multi-modal (ice-structure) interaction-I, multi-modal (ice-structure) interaction-II (or frequency lock-in), and continuous brittle crushing.

2. Design-driving bending moments primarily stem from intermittent crushing and multi-modal interaction-I, rather than frequency lock-in. However, multi-modal (ice-structure) interaction-II can significantly contribute to fatigue-driven design in regions with more frequent ice occurrence. Therefore, industry-implemented ice models should be capable to replicate all four regimes of ice-induced vibrations.

3. The application of a sequential ice-structure design method resulted in forced vibrations, disrupting the synchronization process of ice-induced vibrations. Due to this non-physical coupling, results may either underestimate or overestimate resulting bending moments when compared to design bending moments derived from fully-coupled simulations, contingent on the cross-section height.

4. Future offshore wind turbines are anticipated to exhibit amplified multi-modal ice-induced vibrations. Additionally, it is expected that multi-modal interaction-III could be predicted to develop when future generation offshore wind turbines are implemented in ice-structure interaction simulations.


Shivor

7

DISCUSSION & CONCLUSION

Ice modeling is one of the most powerful tool[s] to make our field progress but under the condition that it is used properly for what it is intended to do with its laws very well understood.

Prof. Dr. Eng. Bernard Michel in a discussion on ice modeling in hydraulic engineering during the first IAHR symposium on ice in 1970.[1]

[1] Michel (1970)

The present chapter comprises two parts. The first part focuses on the discussion and is divided in four sections. First, it is discussed why ice-induced vibrations of offshore wind turbines show a multi-modal character and why it was decided to introduce the term of multi-modal ice-structure interaction (Section 7.1). Second, it is discussed why the time- and rate-dependent behavior of sea ice must be considered when scaling ice-induced vibrations (Section 7.2). Third, differences between full-scale measurements and presented model-scale and simulated results are anticipated (Section 7.3). Finally, it is discussed to what extent fully-coupled ice models can be used to simulate ice-induced vibrations of offshore structures (Section 7.4). The second part of this chapter outlines specific conclusions derived in this thesis (Section 7.5), addressing the research questions as posed in Section 1.7.

7.1. MULTI-MODAL (ICE-STRUCTURE) INTERACTION

It was observed that ice-induced vibrations for multi-degree of freedom structures were not necessarily dominated by the mode associated with the lowest natural frequency, as described by Kärnä *et al.* (2003), but rather by the most critical combination of mode shape, relative velocity between ice and structure, and modal damping. A similar conclusion was derived by Hendrikse (2017) after analysing simulations of the ice-structure interaction of an offshore wind turbine, which was represented by a 1D-beam model.

In the present thesis, the observed ice-induced vibration regimes of offshore wind turbines were classified into distinct categories: intermittent crushing, multi-modal (ice-structure) interaction-I, multi-modal (ice-structure) interaction-II (also known as frequency lock-in), and continuous brittle crushing. These regimes are believed to emerge due to an energy exchange between the structure and ice, primarily influenced by synchronization, which, in turn, could be determined by the contact time and area between the structure and ice. During contact periods with a high contact ratio (akin to quasi-static loading), the structure deforms quasi-linearly until the ice fails and the structure freely vibrates occasionally crushing the ice (intermittent crushing). It is assumed that at a certain combination of contact duration and area, the ice and structure synchronize, resulting in a minimization of contact losses over the full crushing period (multi-modal interaction-I). When time and contact area are insufficient to excite the lowest structural frequency, higher structural modes which are more susceptible to ice-induced vibrations get excited (e.g., multi-modal interaction-II). This phenomenon is assumed to occur because less contact time between the ice and structure is needed to gather the energy for the self-excitation of this particular structural mode. In fact, the mode of vibration has been actively controlled by artificially increasing mode shape amplitudes while keeping total structural stiffness, eigenfrequencies, and damping constant (refer to Section 6.5), which supports this idea.

Combining these observations with the findings by Määttänen (1983), it is agreed that higher mode vibrations can be expected to occur when higher ice drift speeds are tested. However, those higher modes do not necessarily become the single mode vibrating during the interaction. Rather, higher mode oscillations seem to be caused by and

are thus superposed with lower mode oscillations. A similar observation was made by Nord *et al.* (2015a) who found that during the ice-structure interaction, more than one mode of the structure can be excited simultaneously. But also this description can be misleading. During the ice-structure interaction, the structural response associated to a low frequency changes the relative velocity and thus changes the effectiveness of the energy transfer during the interaction. This observation differs from the observation of multiple structural modes vibrating after the structure "springs out" after global ice failure as described by Määttänen (1975b).

Observations collected and analyzed in the previous chapters resemble those observed for flexible free-hanging cylindrical tension riser systems under current loading. For a change of constant flow velocity, multiple modes were observed to vibrate, whereby often one dominant mode was present (Chaplin *et al.*, 2005; Huera Huarte *et al.*, 2006; Violette *et al.*, 2010; Zhu *et al.*, 2019). The primary mode of vibrations switched once the constant flow rate was changed, an observation titled *mode switching* (Chaplin *et al.*, 2005). This phenomenon was even observed to occur spatially along the riser, attributed to the exponential shear forcing (Zhu *et al.*, 2019). Another study underlined the observation that the dominant frequency in the response can change by a slight change of boundary conditions (e.g., by small vibrations of the carriage) and introduced the term *time sharing*. Similarly, the term of *mode competition* was introduced to describe the observation that two modes were competing for dominance in the structural response without any clear change of conditions (Li *et al.*, 2018). Note that a mode switching also has been documented in this thesis (e.g., Section 6.5.3).

However, the observations of mode switching, time sharing, and mode competition were all related to the phenomenon of vortex-induced vibrations. The mechanisms causing such vibrations fundamentally differ from those causing ice-induced vibrations. While vortex-induced vibrations are caused by the vortex shedding frequency, there is no apparent frequency in the ice when it is crushing against a rigid and immovable structure (see Figure 4.12). For ice-induced vibrations, it was shown that the effectiveness of the energy transfer between the structure and the ice, meaning the time at low relative velocity between structure and ice, determines the vibration regime. In other words, vortex-induced vibrations are caused by a vortex shedding frequency, ice-induced vibrations by a self-excitation after spatial synchronization between the structure and the ice. The term of multi-modal ice-structure interaction (short: multi-modal interaction) was thus introduced to underline this distinction in mechanism. Multi-modal ice-structure interaction is a specific form of a multi-modal vibration.

It is proposed that historical test campaigns in model ice (Kärnä *et al.*, 2003; Määttänen, 1983; Määttänen *et al.*, 2012) overemphasized the development of frequency lock-in of offshore structures, as tested eigenfrequencies of the prototypes were too high. First-mode oscillations in the present study changed the relative velocity between the ice and structure, thus initiating different modal vibrations of higher frequency at different time instances within a single first-mode structural oscillation. Full-scale structures like the Kemi-I lighthouse might never have resulted in multi-modal interaction as the lowest

eigenfrequency was too high to change the relative velocity, during the reversal phase of the structure, into a regime that would cause second mode vibrations. It is expected that it is unlikely that a modern offshore wind turbine will ever experience frequency lock-in in a single (dominant) frequency. This observation motivated the author to replace the term of frequency lock-in with multi-modal ice-structure interaction, adding an indicator for the dominant mode (Section 6.2). It can be imagined that the idea of a dominant single mode vibration during frequency lock-in for a multi-degree-of-freedom structure could also originate from the choice of model ice tested. As will be shown in the next section, the 'standard' model ice used in past experiments significantly enhances the development of frequency lock-in.

7.2. SCALING OF ICE-INDUCED VIBRATIONS

First, the Buckingham Pi theorem was applied in an attempt to identify dimensionless parameters governing ice-induced vibrations Section 2.1. Yet, the study uncovered the insufficiency of the state-of-the-art understanding to derive fundamental dimensionless numbers for scaling of ice-induced vibrations. Instead, a detailed analysis of observations from full- and model-scale measurements was conducted, leading to the development of a theoretical framework outlining the mechanisms relevant to scaling of ice-induced vibrations (Chapter 2). This approach is occasionally referred to as case-based scaling in existing literature (von Bock und Polach *et al.*, 2020). However, the term 'scaling' inherently suggests condensing a complex phenomenon into a specific, small-scale scenario. Consequently, the nomenclature of 'case-based scaling' could be considered a tautology and was not used in this thesis. Nonetheless, the author agrees with von Bock und Polach *et al.* (2020) on the crucial notion that descriptions of reality are scaled and not reality itself.

This thesis introduced a scaling approach founded on the concept that ice-induced vibrations arise from the energy transfer between the ice and structure during phases of low (relative) velocity. It is suggested that the development of these vibrations is governed by the contact area and contact time and thus by the spatial synchronization between structure and ice. And although it may not necessarily be the contact as recently discussed by Owen (2024), the main message that the effectiveness of the energy transfer is driving the ice-induced vibration remains. In the following sections, cases will be discussed where the effectiveness of energy transfer is supposedly scaled, potentially impacting the development of ice-induced vibrations.

7.2.1. SCALED TIME- AND RATE-DEPENDENT BEHAVIOR OF ICE

Drawing from theoretical understanding, it was derived that the behavior of ice, which is time- and rate-dependent, could be defined to some extent by a transition speed (The transition speed, in the present thesis, is defined as the indentation speed at which the macroscopic creep changes to a fracture dominated failure of the ice.). Consequently, severe ice-induced vibrations are expected when testing with structures in model ice which has a relatively high transition speed. Thus magnified ice-induced vibrations were

expected to occur when testing in standard model ice, which is commonly employed in ship model experiments (measured: σ_f = 100 kPa, E = 230 MPa) and is assumed to have a higher transition speed when compared to that of cold model ice.

Results of ice-induced vibration experiments with the same structural model conducted in both cold and standard model ice are shown in Figure 7.1. As expected, the standard model resulted in sustained frequency lock-in vibrations, which are also initiated at a higher ice drift speed when compared to the initiation speed in cold model ice. Notably, the standard model ice fails to exhibit a peak load increase at the lowest ice drift speeds, thereby falling short of meeting the scaling criteria outlined in Section 2.2.

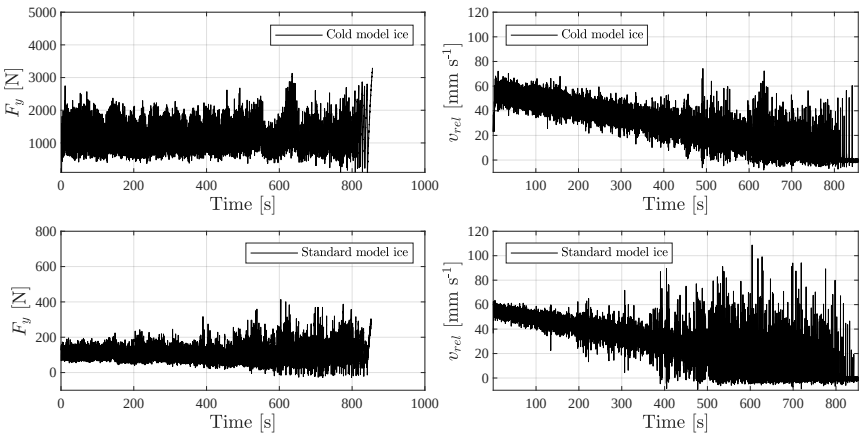


Figure 7.1: Ice loads F_y and relative velocities v_{rel} for deceleration experiments in cold and standard model ice (measured: σ_f = 100 kPa, E = 230 MPa)

Focusing on the specifics of a frequency lock-in event in Figure 7.2, an intriguing similarity is noticeable in the signal patterns for both model ice types. This resemblance implies that both regimes stem from the same or similar mechanism, evidenced by the velocity effect observed in both scenarios. However, in rigid indentation experiments using the standard model ice, there was no clear manifestation of the velocity effect (Figure 7.3). This observation can be explained in three possible ways. First, the standard model ice may trigger the velocity effect only if the initiation time is shorter than the time required for the ice to buckle or bend (which is a common ice failure mode for the standard model ice when interacting with a vertically sided structure). Second, the effect could occur when there is a preceding phase of rapid loading. Third, the increase in peak load might not have been captured during the rigid indenter experiments, as the sensors were calibrated for larger (cold) mean ice loads. Without deeper analysis, it remains unclear how dynamic experiments initiate the velocity effect while rigid indentation experiments at low velocities do not.

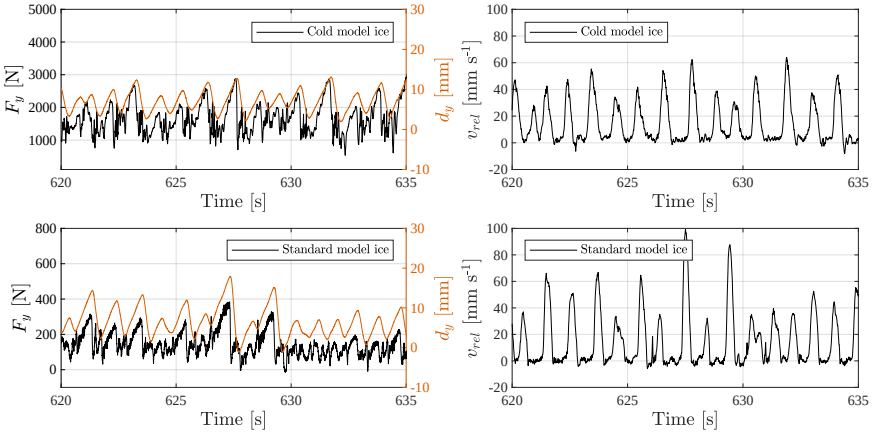


Figure 7.2: Ice loads F_y, structural displacements in ice loading direction d_y, and relative velocities v_{rel} for experiments in cold and standard model ice during frequency lock-in.

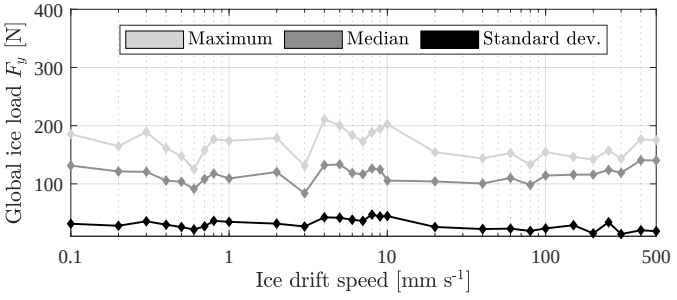


Figure 7.3: Rigid indentation experiments in standard model ice.

7.2.2. SCALED STRUCTURAL FREQUENCIES

Using any model ice that meets the criteria outlined in Chapter 2 while upscaling the structural frequencies is anticipated to lead to an underestimation of the development of ice-induced vibrations. This expectation arises from the likelihood that, even if a comparable contact area to full-scale could be attained, the contact time would be shortened. This is due to the structure moving faster and consequently crushing the ice earlier than it would in reality. It is expected that significantly lower constant ice drift speeds would be necessary to induce ice-induced vibrations. However, the relation between these values and values in full-scale remains unknown, mirroring the uncertainty surrounding the physical scaling of the energy transfer.

Moreover, this thesis revealed that the low mode responses alter the dynamics during the interaction between ice and multi-degree-of-freedom structures, resulting in specific multi-modal (ice-structure) interaction regimes. Thus, the experimental modeling of

such multi-modal responses becomes unfeasible when eigenfrequencies of the prototype structure are significantly increased as witnessed by Määttänen (1983). The research of Määttänen (1983) involved testing multi-degree-of-freedom structural models with scaled-up structural frequencies, where he observed that frequency lock-in transitions from one mode to another when the ice drift speed was increased. Thus, the upscaling of structural frequencies not only alters the threshold of ice drift speeds initiating ice-induced vibrations but also fundamentally modifies the nature of these vibrations. Hence, the observation of multi-modal interaction-I becomes impossible because the motion associated with an upscaled lowest eigenfrequency cannot initiate higher mode vibrations showing that the chosen and applied scaling approach might be flawed.

Using any model ice that meets the criteria outlined in Chapter 2 while reducing the structural frequencies is expected to lead to an overestimation of the intensity of ice-induced vibrations. This scenario anticipates ice-induced vibrations occurring at higher constant ice drift speeds than in full-scale situations.

Summarizing, it can be underlined that the usage of 'standard' model ice in model-scale experiments for analysis of ice-induced vibrations overemphasized the importance of frequency lock-in, complicated to relate intermittent crushing to the structure of interest and inhibited the observation of multi-modal (ice-structure) interaction-I. One plausible explanation is that the standard model ice generates an artificially high contact area, improving the effectiveness of energy transport between ice and structure into the system compared to the cold model ice. This observation could explain why experiments in standard model ice resulted in sustained vibrations of frequency lock-in (Hendrikse *et al.*, 2022b; Määttänen, 1983; Ziemer, 2021), while experiments in the cold model ice did not. Another explanation is that the viscosity of the ice increased with increased model ice temperature and thus improved the effectiveness of energy transport between structure and ice. Note that the former explanation could be caused by the latter. The reader is referred to Owen (2024) for further results and discussion on ice mechanics in ice-induced vibrations.

It can also be discussed if sustained vibrations in standard model ice are caused by a scaling effect or can be expected to occur in full-scale as well. On the one hand full-scale structures have been observed to experience frequency lock-in vibrations when the ice was relatively warm; Bjerkås *et al.* (2013) documented that "major observations of ice-induced vibrations were done from 10[th] March on. Then intense vibrations were detected after a time period with air temperatures in the range of 0°C to +10°C." Kärnä (2011a) formulated that "a detailed analysis of this phenomenon [...] suggests that some ice mechanical phenomena promotes the arise of high vibrations in warm ice.", also adding that "[p]otential explanations are not suggested in this report". On the other hand, it seems logical that ice-induced vibrations mainly occur at higher air temperatures in the spring season as the landfast ice is otherwise not detached from the shore and thus few observations on drift ice can be made. Additionally, full-scale structures as the Norströmsgrund lighthouse or Molikpaq never experienced sustained vibrations as have been observed when testing in standard model ice. It remains unknown if this observa-

tion is related to the homogeneous conditions in small-scale experiments or due to a scaling effect caused by the ice temperature. The author can thus not conclude if higher mode vibrations in standard model ice are a scaling effect or have full-scale relevance for frequency lock-in vibrations.

7.2.3. SCALING LAWS AND THE FUTURE OF ICE MODEL TESTING

When presenting numerical findings, it often comes with a demand for experimental validation. However, what scientists should first try to seek is validation through field measurements. This experience illustrates a common trend: scaling methods, once defined as scaling "laws" are often taken for granted and applied almost universally across research disciplines. Similar behavior emerged in the study of ice-induced vibrations. Scaling methods derived from ship-towing experiments— Froude and Cauchy scaling — were applied to ice-induced vibrations, although the phenomenon of interest was different. As the model ice weakened, it struggled to withstand substantial stresses at lower relative velocities between the ice and the structure, leading to premature ice failure. The «ice community» had extended the use of «scaling laws» far beyond their original context, introducing new concepts that diverged significantly from or exaggerated the intended purpose of these contents. Replacing the first term highlighted by « » with «movie industry» and the second term with «the motives», one finds a description of the phenomenon of "jumping the shark" in the film industry. Maybe one should consider to use the term 'scaling jaws'[2] instead of scaling laws once such a state of scaling law application is reached. The term captures the essence of applying scaling laws beyond their intended purpose.

On a different note, and given the demonstrated capability of numerical models to qualitatively predict the development of ice-induced vibrations, there is a valid query regarding the continued necessity of experimental ice test facilities. Why not consider constructing a digital twin of an ice tank as proposed by Tian *et al.* (2023)? This approach might be particularly relevant considering the flawed repeatability of ice tank experiments due to changing initial conditions as highlighted by van den Berg *et al.* (2020). However, an ice tank only exists because ice and the effect of ice on structures is not fully understood yet. This is why, on the one hand, the author of this thesis believes that digital twins of ice tanks are unnecessary as the conduction of *experimental research* within ice test facilities cannot be replaced. Here, experimental research is defined as research aiming to reveal novel physical phenomena or to derive and validate physical mechanisms experimentally. On the other hand, the author also believes that *experimental testing* will shift towards the numerical domain, as shown for example in von Bock und Polach *et al.* (2023). In this thesis, *experimental testing* refers to experiments aiming to ascertain particular values often regulated by guidelines (e.g., compressive ice strength, fatigue damage simulation).

However, the focus should be to improve the fundamental mechanism behind numeri-

[2] The term 'jaws' was adopted from the movie *Jaws* (1975)

cal models rather than modeling an ice tank with insufficient 'numerical ice'. *Experimental research* could focus on finding the fundamental process explaining the time- and rate behavior of ice. In the meantime, a combination of physical prototypes, numerical simulations and tailored model ice can be used to investigate specific phenomena as observed in nature. Following the same analogy, it is thus concluded that not 'digital twins' but that 'replicants'[3] should be developed. Consequently, hybrid simulations are assumed to become pivotal in future model testing by combining advanced numerical models with physical loading scenarios, as they offer the advantage of isolating physical components for analysis in a controlled environment. The versatility, reproducibility, adaptability, and repeatability of these simulations mark a significant leap forward. The method allows to switch structural models numerically, enabling numerous experiment repetitions and thus reducing the impact of initial conditions on the results. Hybrid simulations of offshore structures already do and could even involve further physical load measurements, collecting those (such as ice, wind, wave, and soil pressures) in different test facilities at the same time. However, the development of such systems will depend on the reduction of rise times of measurement systems (for spatial pressure or load determination) and the reduction of delays during transmission of the data.

7.3. EXPECTED RESULTS OF FULL-SCALE MEASUREMENTS

This section addresses assumptions made to reduce the physical event of ice-induced vibrations of an offshore wind turbine in the field to an idealized model-scale scenario as done in this thesis. The assumptions are addressed by anticipating how full-scale measurements would differ from the results and conclusions.

Most likely, full-scale data will show the result of an ice floe slowing down against an offshore wind turbine, which is why only a couple of cycles of ice-induced vibrations are expected to be recorded. Rafted ice, ice inclusions or ice ridges, and natural variations in thickness and strength could change the mean ice load level and thus the ice-induced vibration regime, even for a constant ice drift speed. Ice ridges could lead to significantly larger mean and maximum ice loads in quasi-static scenarios. Extruded ice and ice rubble could induce additional damping to the system. Formed rubble piles might initiate a deformation or failure of the ice sheet. The ice could be predamaged and thus show an increased first load peak (increase in contact area) or only partially load the circumference of the structure which could affect the mean load level and thus the development of ice-induced vibrations. The ice could rotate around the support structure and induce friction forces to the turbine. Neighboring turbines could jam the ice sheet in place, resulting in temperature induced ice loading (caused by thermal expansion) to the structure. Tidal effects (arch effects) could induce loads to the turbines. Near-shore turbines will most likely be frozen in, until the ice sheet starts to move as a whole.

All in all it must be understood that the results of this thesis are limited to the idealized case of a homogeneous, infinite and isotropic level ice floe of continuous thickness, drift-

[3] The term 'replicant' was adopted from the movie *Bladerunner (1982)*.

ing without forcing limits and solely crushing against a single idealized offshore wind turbine support structure, with a vertically sided interface at the waterline.

7.4. ENGINEERING CONFIDENCE

It is assumed that the qualitatively validated ice model increases the confidence in engineering offshore wind turbines in cold regions. When planning offshore wind turbines in regions with more frequent sea ice occurrence compared to the Southern Baltic, incorporating the side-side confinement as observed during the experiments (Section 5.4.2) into a numerical model is anticipated to decrease the overall fatigue damage, particularly in misaligned scenarios. Moreover, the ice confinement might alter the lateral eigenfrequencies of the turbine, potentially affecting design considerations. Hence, for a quantitative validation of ice-structure interaction models, incorporating ice confinement should be achieved.

Additionally, a more extensive focus on environmental data could offer insights into alternative limiting mechanisms during simulations of offshore wind turbine ice-structure interactions. However, achieving a balance between phenomenological and physical modeling is crucial. As an initial step, exploring simulations of velocity profiles involving velocity rates, rather than simulating for constant drift speeds, could be considered to mimic diverse or limiting forcing mechanisms. Notably, it has been demonstrated that design-driving interaction regimes, such as multi-modal interaction-I, can occur within a single cycle (Figure 4.6). This approach should thus not affect the ULS design but could significantly reduce the total simulation time.

7.5. CONCLUSION

Current generations of offshore wind turbines are expected to experience intermittent crushing, multi-modal (ice-structure) interaction-I, multi-modal (ice-structure) interaction-II, and continuous brittle crushing when interacting with a sea ice floe crushing against a vertically sided support structure of an offshore wind turbine. This thesis introduced a hybrid testing technique in model ice and developed a scaling method to incorporate the time- and rate dependent behavior of sea ice during the ice-structure interaction. It enables scientists to systematically test ice-induced vibrations of vertically sided structures in model ice experiments; it enables engineers to gain confidence in applying numerical simulations for prediction of design relevant ice-induced vibrations regimes of offshore wind turbines, and it hopefully inspires the transfer of the insights to a multi-disciplinary scale.

The posed research questions (Section 1.7) are answered as follows:

RQ1: *How can ice-induced vibrations of vertically sided offshore structures be scaled?*

Ice-induced vibrations of offshore structures could be investigated in model-scale experiments when replica ice modeling and preservation of kinematics were com-

bined. The replica modeling results in a mean pressure similarity[4], while the preservation of kinematics denies any scaling of time components (either of the structure or of the ice). The mean pressure similarity allows to scale the numerical structural properties based on the ratio between a measured model-scale and an estimated full-scale mean ice load. It was essential that the model ice failed in crushing, showed a velocity effect, and had a similar transition speed as sea ice. 'Crushing' was thereby imposed by avoiding buckling, submergence during interaction, very wet material extrusion, or large plastic deformation of the ice in compression at high speed. The transition speed[5] was chosen as a representative parameter to incorporate the time- and rate dependent behavior of sea ice during modeling. Any model ice type that can fulfill the criteria formulated in Chapter 2 is believed to result in representative ice-induced vibrations if structural kinematics can be preserved during testing.

RQ2: *How can offshore structures with low and multiple eigenfrequencies be tested in ice tank experiments*

The application of hybrid simulations allows for analysis of multi-degree-of-freedom and low frequency structure representations in model ice experiments. Limitations were analyzed and related to experiments with low signal-to-noise ratios and scaling of offshore wind turbines for extreme (high) full-scale mean ice load values.

RQ3: *What types of ice-induced vibrations can an offshore wind turbine experience?*

Dynamic ice loads caused by drifting level sea ice crushing against the vertical sided support structure of an offshore wind turbine can result in intermittent crushing, multi-modal (ice-structure) interaction-I, multi-modal (ice-structure) interaction-II (also: frequency lock-in), and continuous brittle crushing. Multi-modal (ice-structure) interaction regimes are not recognized based on past experience and are not included in standard methods, which could result in the omission of design-critical ice-induced vibration regimes.

RQ4: *What is the effect of wind-ice misalignment on the development of ice-induced vibrations of offshore wind turbines?*

Misalignment between wind and ice promotes the development of ice-induced vibrations due to the change in aerodynamic damping in the direction of ice loading. The ice was found to confine wind-induced structure motion during misaligned loading scenarios. Indications were found that wind-induced displacements disturb the development of ice-induced vibration but do not suppress those.

[4] when assuming that the physical driver are on a geometrical scale significantly smaller than tested

[5] The transition speed is defined as the indentation speed at which the macroscopic creep changes to a fracture dominated failure of the ice.

EPILOGUE

Years come and go unnoticed in this world of ice, and we have no more knowledge here of what these years have brought to humanity than we know of what the future ones have in store.

Dr. Fridtjof Nansen

When the ice crushes into pieces, I realize,
that structure and ice start to synchronize,
now I hear the song, it was a dance all along:
ice-induced vibrations, a majestic phenomenon.

Tim Christopher Hammer

ACKNOWLEDGEMENTS

The start of the COVID pandemic, in the third month of my PhD, brought unforeseen challenges. My girlfriend and I, then residing in the Netherlands for two months, suddenly found ourselves isolated from our social circle and families, transitioning to remote work which should last for 1 1/2 years. Conferences were canceled, and virtual interactions replaced face-to-face connections, leading to a gradual fading of our faces from the memories of our colleagues.

These acknowledgements are primarily addressed to people that helped me through the period of that isolation as I could have never completed the thesis without their help.

My main supervisor, Hayo, deserves immense acknowledgements for guiding me through this journey. You not only brought a German to a job interview, but you also trusted me with a topic in structural dynamics and ice-structure interaction despite my limited background in these areas. Your patience in reviewing my chaotic manuscripts, along with your professional and honest feedback, was invaluable. Your approach of gradually entrusting me with more responsibility significantly contributed to my growth as a scientist. Your support and motivation, especially during the isolating times of COVID, were crucial to *finish* this thesis. You even established an 'ice family' which created a socially safe hub for me. I value your extraordinary personal commitment in your daily care for your PhD-students more than a victory in a boardgame against you.

The 'ice family' also owe[n]s its existence to my fellow PhD candidate, Cody. Thank you for generously sharing your online library, thesis template, and VANILLA code versions with me. Thank you for all your help during the two test campaigns, setup development and shaping of manuscripts. Your selflessness and philanthropic nature make you a standout example of a scientist. Your support, especially in enhancing my English proficiency, deserves great respect. Our philosophical discussions, shared YouTube discoveries, and our time in the saunas were moments I will never forget. Being your paranymph and friend fills me with pride.

I would like to extend my gratitude to Laura. Your role in the success of the second SHIVER model test campaign was remarkable. Your warmth and care for our well-being made a significant difference. Your little gestures, such as reaching out to the Easter bunny and Sinterklaas, meant a lot to me.

Despite the brief time that Marnix spent in on our team, his support in updating the numerical model of the hybrid test setup proved invaluable. Your implementation of the forward-prediction saved both test campaigns. Personally, I am grateful for your

sacrifice of privacy, sharing a bedroom for weeks with me during the first SHIVER model test campaign. Also thank you for pushing us to our limits on bike and on foot. I also want to thank Nick for his contribution to the first SHIVER model test campaign.

My time at the Stevin lab of the TU Delft, dedicated to develop the hybrid test setup, was made possible with the steady assistance of Jeroen Koning and Kees van Beek. Jeroen, your expertise in the mechanical setup and the development of the 3D-printed piles were essential. Kees, your support in configuring and troubleshooting the hybrid test setup was indispensable. Without the collaborative efforts of both of you, the realization of the hybrid test setup would not have been possible.

I extend my gratitude to my fellow PhD colleagues, with whom I shared delightful conversations and enjoyable moments during our gatherings for drinks and chats at PSOR. These interactions added immense value to my journey and my propositions.

I would like to express my gratitude to Andrei for his role as my promotor throughout my PhD journey. I highly acknowledge your trust in Hayo, Cody, and me. Your guidance refined my scientific understanding, and your approach to lectures and speeches served as an inspiration, motivating me to engage more effectively with my audience. Never give up your charm and fridge.

I wish to extend my gratitude to all my colleagues at Siemens Gamesa Renewable Energy (SGRE) for their support throughout my PhD journey, particularly during the challenging COVID period. I always felt integrated and warmly welcomed to the SGRE family. I wish to thank Tom, my initial supervisor at SGRE, for your support during the first 1 1/2 years of my PhD. Your guidance significantly enhanced my MATLAB programming skills, enabling the numerical studies for both fully-coupled and quasi-coupled simulations. Your assistance during the first SHIVER model test campaign, the development of the post-processor, and the drone footage are deeply appreciated. Without your cooking skills, we would probably have developed diabetes or scurvy (or both) during our time in Finland. Not a single tear shed was wasted once you decided to move on and I am proud of the friendship we developed.

I extend my gratitude to Jeffrey, who began as a master student alongside us, for being an inspiration on how structured work can look like. Your assistance during the second test campaign made it possible to run NREL experiments. Your passionate expertise in ice studies at SGRE and engaging discussions on industry-relevant ice topics are highly valued.

I also want to thank Sebastian for supervising the final two years of my PhD - I enjoyed our talks about scientific offshore wind turbine topics. I also would like to thank Maarten and Dion for sharing their enthusiasm about dynamic ice loads on offshore wind turbines with me.

Many thanks go out to all my other colleagues at SGRE for their support whenever

expertise in waves, soil, aerodynamics, structure design, or control was needed. I believe that the offshore group at SGRE rightfully deserves the title of ‘offshore wind university’. The camaraderie we shared, from ’botje’ and table tennis matches to car rallies and Christmas parties, created great memories for me.

Finally, I want to thank Colinda for her first words she ever spoke to me; Mauk, Jan-Bart and David for their trust in Hayo and me, supporting the co-financing of the SHIVER project. I also would like to emphasize David’s mission to "leave the planet in a better shape than [we] found it and dare to have some serious fun while doing it." as I fully support it.

I would like to express my gratitude to everyone I met during the model test campaigns at the Aalto University. Teemu and Lasse, your support and innovative ideas throughout the test campaigns were of immense importance. Otto, I appreciate your insights and help during the conceptualization of the test campaigns. Our discussions on model ice scaling were highly motivating to me. Additionally, I extend my gratitude to Alice for her invaluable assistance during the second SHIVER model test campaign and for sharing experiences with 3D-printed structures in ice with us. Your sense of humor and knack for scientific memes are appreciated—please never lose them. I want to thank Arttu for his support throughout the SHIVER project, as well as our engaging discussions on movies. I am thankful to Jukka and Arttu for the honest feedback they gave me during my stay in Finland writing part of this thesis. Both Arttu and Jukka also deserve many thanks for initiating the trip to the *Discovery* during our time in Glasgow, and for sharing personal stories with me. Lastly, I want to express my gratitude to Pentti for his comments on our work during my first in-person conference presentation at OMAE in Hamburg in 2022 and Jukka for his compliment on the failure mode of the cold model ice. Both compliments held great significance for me. Similarly, I extend my thanks to Mikko for his supportive words.

I would like to express my gratitude to my Norwegian colleagues whom I initially encountered during the FATICE project. Specifically, I extend my thanks to Knut for his initiative in organizing regular FATICE meetings, even after the project was terminated, providing a platform for presenting and discussing ice-related subjects. I also want to thank Knut for his valuable contribution to the discussions about scaling of ice-induced vibrations. I am grateful to Vegard, whom I initially met during the FATICE meetings, for being a great friend, often surprising me with little gifts he brought from Norway. Thank you for sharing your field experience and insights gathered from simulations in Copernicus with me. Our shared adventures in Svalbard, Trondheim, Montreal and Glasgow are unforgettable. I also want to thank Aleksey and Sveinung for taking me to the field in Svalbard and sharing your stories with me. I am glad that people still work with ice.

Close to the end, I extend my thanks to Vroukje and Bárbara for providing continuous mental support to our research group. Your backing made the success of our test campaigns possible.

I want to thank all the people that sent little care packages and cards during the COVID period and beyond.

Robi, Vito and Basti thank you for the friendship and always reminding me that I can do this.

Thank you Jan for being the role model you are.

Finally, I want to highlight the incredible contribution of Rieke. You took a risk by following me to the Netherlands without a job position at that time. Your presence was essential in helping me maintain a healthy life throughout my PhD journey. Your reminders to take breaks, stay hydrated, and prioritize self-care were invaluable. You never challenged my long trips to Svalbard or Finland. You never complained when we would visit or meet research fellows in our private holidays. Thank you for standing up to my unnecessary discussions and still never giving up on me. You are *everything I wanted*.

A

APPENDIX

A.1. NUMERICAL ICE MODEL

The implemented numerical ice model as used in Chapter 6 was adopted from Hendrikse and Nord (2019) and the description below is a condensed version of the descriptions provided in Hendrikse and Metrikine (2016b), Hendrikse and Nord (2019), and Hendrikse *et al.* (2018). The phenomenological ice model considers a rate-dependent failure length of local elements resulting in a nonlinear global force (F_{ice}) dependence on ice drift speed (v_{ice}).

A.1.1. MODELING APPROACH

A rheological model (i.e., modified Burgers model[1] is used to model each single, independent, and local element[2] i with three degrees of freedom: $u_{i,1}$, $u_{i,2}$, and $u_{i,3}$ (see Figure A.1). Several of these elements (number defined as N) are introduced to capture the stochastic nature of the ice load in the brittle regime observed in full- and model-scale measurements. The elements are one-dimensional and thus is the coupling between the ice and the structure. In summary, the ice model uses several elements, each represented by a Burgers model, to mimic ice crushing and the transition from simultaneous to non-simultaneous global ice failure with increasing interaction speeds.]

Zooming into the modified Burgers model, the elements are coupled via the linear front spring K_2 to the structure. The spring captures the local elastic deformation of ice in interaction with a structure. Once a critical load level is reached, the spring exceeds a critical deformation and fails. However, the time until failure is depending on the rate of loading of the total element. Reason for that are the centre linear spring K_1 and dashpot C_1 in parallel (i.e. Voigt element), and a non-linear rear dashpot C_2 to mimic the power-law creep deformation of the ice.

[1] The components of the Burger model are linear (i.e., the Maxwell model (a linear spring in series with a linear dashpot) and the Kelvin-Voigt model (a linear spring in parallel with a linear dashpot)). Here the rear dashpot is non-linear and the front spring cannot be loaded in tension and has a discrete failure limit.

[2] Here: Ice element. However, to minimize confusion an interpreting it as a physical ice element, 'element' is used instead.

The ice is modelled as a semi-infinite ice sheet in the present thesis, but can also be coupled as finite ice floe including and current and wind forces ($F_{current}$ and F_{wind} as visualized in Figure A.1 and presented by Hendrikse and Nord (2019).

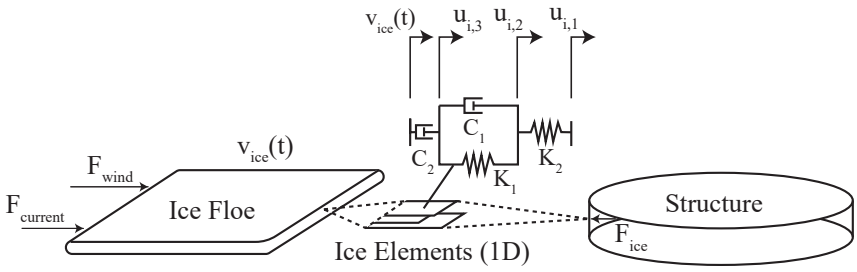


Figure A.1: Visualization of the phenomenlogical ice model. Reprodued from Hendrikse and Nord (2019).

The equations of motion per element based on the structural displacement u_s are defined as (see also Figure A.1):

$$u_{i,1} = \begin{cases} u_{i,2} & \text{if } u_i < u_s \\ u_s & \text{if } u_{i,1} \geq u_s \end{cases} \tag{A.1}$$

$$\dot{u}_{i,2} = \frac{K_2}{C_1}(u_{i,1} - u_{i,2}) + \frac{K_1}{C_1}(u_{i,3} - u_{i,2}) + v_{\text{ice}} - \frac{1}{C_2}\left(K_2(u_{i,2} - u_{i,1})\right)^3 \tag{A.2}$$

$$\dot{u}_{i,3} = v_{\text{ice}} - \frac{1}{C_2}\left(K_2(u_{i,2} - u_{i,1})\right)^3 \tag{A.3}$$

where overdots represent time-derivates of the displacements. Integrating the local loads as induced by each element in contact with the structure, the global ice load is given as:

$$F_{\text{ice}}(u_s, t) = \sum_{i=1}^{N} F_{t,i} = \sum_{i=1}^{N} K_2(u_i - u_{i,1})H(u_{i,1} - u_s) \tag{A.4}$$

where $F_{t,i}$ is the ice load from an individual element and H is the Heaviside step which determines whether contact between an ice element and structure exists.

A.1.2. INPUT PARAMETERS

The phenomenological model requires seven input parameters (i.e., δ_f, K_2, K_1, C_2, C_1, N, r_{max}), which are proposed to be based upon ice load measurements on rigid (e.g., immobile) structures. The determination of the input parameters requires that the ice (during the measurements) failed in crushing purely and was rate-unaffected (e.g., by ice extrusion). Six of the seven parameters can be directly determined by defining Figure A.2 for a given scenario (i.e., ice conditions and structure geometry):

$$r_{\max} = \delta_f \left(\frac{F_t}{2\mu_{\text{cbr}}} - 2 \right) \tag{A.5}$$

$$N = \frac{(\frac{2F_t}{3\mu_{\text{cbr}}} - 1)}{\left(\frac{\sigma_{\text{cbr}}}{\mu_{\text{cbr}}}\right)^2} \tag{A.6}$$

$$K_2 = \frac{F_t}{\delta_f N} \tag{A.7}$$

$$C_2 = \frac{F_t^3}{N^3 v_t} \tag{A.8}$$

Note that the equation of C_2 has been corrected in Hendrikse and Nord (2020). The input parameters for K_1 and C_1 can be determined iteratively by solving eq. (A.4) setting u_s to zero:

$$\mu_1(v_1) = \frac{F_t}{\delta_f} \frac{\int_0^{t_f(v_1)} u_{i,2}(t)\mathrm{d}t}{\frac{0.5 r_{max}}{v_1} + t_f(v_1)} \tag{A.9}$$

$$\mu_2(v_2) = \frac{F_t}{\delta_f} \frac{\int_0^{t_f(v_2)} u_{i,2}(t)\mathrm{d}t}{\frac{0.5 r_{max}}{v_2} + t_f(v_2)}. \tag{A.10}$$

whereas t_f is the time between initial contact and failure for an indidicual ice element at the reference ice drift speed v_{ice} associated to the mean load level, and r_{max} is the maximum offset of an element with respect to the structure.

The last parameter δ_f can be determined by a probabilistic analysis of the rigid load measurements tracking the time between initiation of local loading and failure as presented in Figure 12 of Hendrikse *et al.* (2018).

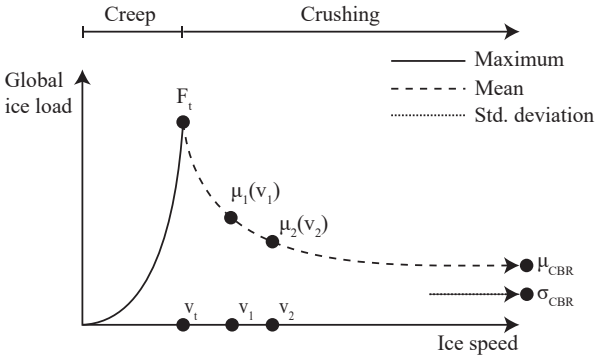


Figure A.2: Aligned and misaligned scenarios considered in the experiments.

The reader can find a hands-on example on the determination of the input parameters for the ice model in Hendrikse *et al.* (2018).

A.1.3. INITIAL ROUGHNESS AND ICE FAILURE

The elements are implemented with an initial offset to the structure. The offset is based on a uniform distribution U, creating an effective roughness (i.e., non-simultaneous loading). The additional offset of $v_{ice} t_f$ is added to consider that the ice elements during the crushing motion already moved by that offset before failing and being replaced. Once the critical deformation of a single element is exceeded, the element is removed, simulating local ice failure, and replaced with an element which is given a new offset with respect to the structure based on an initial position with respect to the structure:

$$u_{i,1} = u_{i,2} = u_{i,3} = \begin{cases} u_{s,0} - U(0, r_{max} + v_{ice} t_f) & \text{during the initial offset.} \\ u_{s,0} - U(0, r_{max}) & \text{during crushing.} \end{cases} \tag{A.11}$$

A.1.4. LIMITATIONS AND DISCUSSION

The model is not mass-conservative as ice is removed from the simulation without consequences. The model does not consider any other failure modes than crushing which is defined as a pulverization of the ice in compression. The pulverized ice (ice rubble) is not considered.

The input parameters are depending on the ice, and on the structure used during the crushing experiments. The model assumes that the the mean load level can be used as scaling origin, which considers no influence of the aspect ratio, rate-dependent loads at high ice speed, additional damping of the rubble, or temperature. The person applying the model should consider to what extend the reproduced load levels (see Figure A.2) mimic the behavior of the ice under consideration in full-scale. For example, the present thesis discussed that the transition speed (v_t) is supposed to shift to higher ice drift speed with an increase of the (model) ice temperature, implying that for a different temperature a different curve as shown in Figure A.2 would have to be defined.

B

APPENDIX

B.1. A SCALING EXAMPLE OF ICE-INDUCED VIBRATIONS

This section describes the scaling method as applied to reproduce ice-induced vibrations of the Molikpaq platform under crushing ice in the Beaufort Sea (see Section 2.6.1). An adapted version of Table 2.3 is populated to compare full-scale and small-scale physical quantities. Furthermore, the overall test and scaling procedure is described chronologically.

The Molikpaq structure was treated as a SDOF structure. The structural properties of the Molikpaq platform were chosen as: f= 1.3 Hz, ζ_{crit} = 20 %, and mass-normalized mode shape amplitude of 8.1681e-05. The full-scale mean brittle cruising ice load was observed to be 50 MN (Gagnon, 2012; Kärnä, 2011b; Owen and Hendrikse, 2021).

A diameter for the physical test structure is chosen, which in combination with the ice thickness, does not result in buckling of the strong and cold model ice when tested in crushing indenter experiments. The grain size of the model ice should be significantly smaller than the diameter. The transition speed from macroscopic creep to a fracture based crushing of the model ice should be in the range of observed full-scale data.

Next, a crushing indenter experiment is performed at an ice drift speed of 100 mm s^{-1}. The recorded data is analyzed in-situ. The mean brittle crushing model ice load was determined to 1122 N. The mean value is used next to calculate the scaling factor λ_F, resulting in this example in λ_F = 44130. Following, λ_F is used to adjust the structural properties of the Molikpaq platform. The scaled structural model is finally used in hardware-in-the-loop experiments in crushing model ice.

Table B.1: Population of Table 2.3

Physical quantity	Unit	Full-scale	Small-scale	Scaling
		Structure		
Frequency	[s^{-1}]	1.3	1.3	1
Modal damping	[%]	20	20	1
Mass-normalized mode shape	[$kg^{-0.5}$]	8.1681e-05	0.017157	$\sqrt{44130}$
Mass	[t]	~150000	3.397	44130
Stiffness	[$MN\,m^{-1}$]	10000	0.2266	44130
Damping	[$MN\,s\,m^{-1}$]	~489.7	0.011	44130
		Ice		
Transition speed*	[$m\,s^{-1}$]	0.08	0.1	1
Ice drift speed	[$mm\,s^{-1}$]	60 to 0	60 to 0	1
Grain Size	[mm]	2-12	1	D/D_{gr} (300 > 25)
Strength	[MPa]	1-4	1	Only crushing
Thickness	[m]	2	0.025	Only crushing
Aspect ratio	[-]	25	8	Only crushing

*As discussed in Section 2.7.1

BIBLIOGRAPHY

Abbiati, G., Covi, P., Tondini, N., Bursi, O. S., & Stojadinović, B. (2020). A Real-Time Hybrid Fire Simulation Method Based on Dynamic Relaxation and Partitioned Time Integration. *Journal of Engineering Mechanics*, *146*(9). https://doi.org/10.1061/(asce)em.1943-7889.0001826

Amaducci, R., Reyes-Sanchez, M., Elices, I., Rodriguez, F. B., & Varona, P. (2019). RThybrid: A standardized and open-source real-time software model library for experimental neuroscience. *Frontiers in Neuroinformatics*, *13*(March), 1–14. https://doi.org/10.3389/fninf.2019.00011

Atkins, A. G., & Caddell, R. M. (1974). The laws of similitude and crack propagation. *International Journal of Mechanical Sciences*, *16*(8), 541–548. https://doi.org/10.1016/0020-7403(74)90019-8

Bachynski, E. E., Thys, M., Sauder, T., Chabaud, V., & Sæther, L. O. (2016). Real-time hybrid model testing of a braceless semi-submersible wind turbine. Part II: Experimental Results. *Proceedings of the ASME 2016 35th International Conference on Ocean, Offshore and Arctic Engineering*, (1), 1–12.

Baker, W. E., Westine, P. S., & Dodge, F. T. (1991). *Similarity methods in engineering dynamics* (Revised Ed). Elsevier Science Publishers B.V.

Barker, A., Timco, G. W., Gravesen, H., & Vølund, P. (2005). Ice loading on Danish wind turbines. Part 1: Dynamic model tests. *Cold Regions Science and Technology*, *41*(1), 1–23. https://doi.org/10.1016/j.coldregions.2004.05.002

Bjerkås, M. (2006). *Ice actions on offshore structures with applications of continuous wavelet transforms on ice load signals* [Doctoral dissertation, Norwegian University of Science and Technology].

Bjerkås, M., Meese, A., & Alsos, H. S. (2013). Ice induced vibrations - Observations of a full scale lock-in event. *Proceedings of the 23rd International Offshore and Polar Engineering Conference*, *9*, 1272–1279.

Blanchet, D., Churcher, A., Fitzpatrick, J., & Badra-Blanchet, P. (1988). An analysis of observed failure mechanisms for laboratory, first-year and multi-year ice. In H. Saeki & K.-i. Hirayama (Eds.), *Proceedings of the 9th iahr international symposium on ice* (pp. 89–136). IAHR.

Blenkarn, K. A. (1970). Measurement and analysis of ice forces on cook inlet structures. *Proceedings of the Annual Offshore Technology Conference*, *2*, 365–378. https://doi.org/10.4043/1261-ms

Böhm, A. M., Herrnring, H., & von Bock und Polach, R. U. F. (2022). Lessons learned: The influence of testing properties on uniaxial compression tests of ice. *Proceedings of the ASME 2022 41st International Conference on Ocean, Offshore and Arctic Engineering*, 1–9.

Bonnet, P. A. (2006). *The Development of Multi-Axis Real-Time Substructure Testing* [Doctoral dissertation, University of Oxford].

Carrion, J. E., & Spencer, B. F. (2007). *Model-based Strategies for Real-time Hybrid Testing* (tech. rep.). University of Illinois at Urbana-Champaign.

Chaplin, J. R., Bearman, P. W., Huera Huarte, F. J., & Pattenden, R. J. (2005). Laboratory measurements of vortex-induced vibrations of a vertical tension riser in a stepped current. *Journal of Fluids and Structures*, *21*(1 SPEC. ISS.), 3–24. https://doi.org/10.1016/j.jfluidstructs.2005.04.010

Chen, P. C., & Chen, P. C. (2023). Real-time hybrid simulation for seismic control performance evaluation of an active inerter damper system. *Engineering Structures*, *294*(January), 116760. https://doi.org/10.1016/j.engstruct.2023.116760

Christensen, F. T., Timco, G. W., & Nwogu, O. G. (1995). Compliant model tests with the Great Belt West bridge piers in ice part II: Analyses of results. *Cold Regions Science and Technology*, *23*(2), 165–182. https://doi.org/10.1016/0165-232X(94)00013-N

Cole, D. M. (2021). A constitutive model for sea ice: physical basis, formulations, examples and applications. *Proceedings of the 26th International Conference on Port and Ocean Engineering under Arctic Conditions*, 1–12.

Cole, D. M., & Durell, G. D. (1995). The cyclic loading of saline ice. *Philosophical Magazine A*, *72*(1), 209–229. https://doi.org/10.1080/01418619508239591

Cornett, A. M., & Timco, G. W. (1998). Ice loads on an elastic model of the Molikpaq. *Applied Ocean Research*, *20*(1-2), 105–118. https://doi.org/10.1016/S0141-1187(98)00006-6

Couturier, P. J., & Skjoldan, P. F. (2018). Implementation of an advanced beam model in BHawC. *Journal of Physics: Conference Series*, *1037*(6), 0–10. https://doi.org/10.1088/1742-6596/1037/6/062015

Engelbrektson, A. (1977). Dynamic ice loads on a lighthouse structure. *Proceedings of the 4th International Conference on Port and Ocean Engineering under Arctic Conditions*, 654–663.

Enkvist, E., & Makinen, S. (1984). A fine-grain model ice. *Proceedings of the 7th IAHR International Symposium on Ice*, 217–227.

Ervik, Å., Nord, T. S., Høyland, K. V., Samardzija, I., & Li, H. (2019). Ice-ridge interactions with the Norströmsgrund lighthouse: Global forces and interaction modes. *Cold Regions Science and Technology*, *158*(August 2018), 195–220. https://doi.org/10.1016/j.coldregions.2018.08.020

Evers, K.-U., & Jochmann, P. (1993). An advanced technique to improve the mechanical properties of model ice developed at the HSVA Ice Tank. *Proc. of The 12th International Confere4nce on Port and Ocean Engineering under Arctic Conditions*, (August), Vol. 2, pp. 877.

Fransson, L. (2004). Mechanical properties of ice at Norströmsgrund, Tests 2003. *Technical Report of the STRICE project*, 1–30.

Frederking, R. M. W., & Timco, G. (1983). Uniaxial compressive strength and deformation of Beaufort Sea ice. *Proceedings of the 7th International Conference on Port and Ocean Engineering under Arctic Conditions*, 89–98.

Gaertner, E., Rinker, J., Sethuraman, L., Anderson, B., Zahle, F., & Barter, G. (2020). *IEA Wind TCP Task 37: Definition of the IEA 15 MW Offshore Reference Wind Turbine* (tech. rep.).

Gagnon, R. (2022). Spallation-based numerical simulations of ice-induced vibration of structures. *Cold Regions Science and Technology*, *194*(August 2021), 103465. https://doi.org/10.1016/j.coldregions.2021.103465

Gagnon, R. E. (2011). A numerical model of ice crushing using a foam analogue. *Cold Regions Science and Technology*, *65*(3), 335–350. https://doi.org/10.1016/j.coldregions.2010.11.004

Gagnon, R. E. (2012). An explanation for the Molikpaq May 12, 1986 event. *Cold Regions Science and Technology*, *82*, 75–93. https://doi.org/10.1016/j.coldregions.2012.05.009

Gao, X. S., & You, S. (2019). Dynamical stability analysis of MDOF real-time hybrid system. *Mechanical Systems and Signal Processing*, *133*, 106261. https://doi.org/10.1016/j.ymssp.2019.106261

Gedikli, E. D., Bjerkås, M., Høyland, K. V., Hornnes, V., & Turner, J. (2020). On the ice and wind conditions in the northern part of the Gulf of Bothnia leading ice-induced vibrations. *Proceedings of the 25th IAHR International Symposium on Ice*, (November 2019), 1–10.

Granlund, V., Schümann, B., & Hoek, J. (2023). Comparison of sequential and coupled approaches for dynamic ice loads by regime extent analysis. *Proceedings of the 27th International Conference on Port and Ocean Engineering under Arctic Conditions*, (June).

Gravesen, H., & Kärnä, T. (2009). Ice loads for offshore wind turbines in southern Baltic Sea. *Proceedings of the 20th International Conference on Port and Ocean Engineering under Arctic Conditions (POAC)*, 1–12.

Guntur, S., Jonkman, J., Schreck, S., Jonkman, B., Wang, Q., Sprague, M., Hind, M., & Sievers, R. (2017). A validation and code-to-code verification of FAST for a megawatt-scale wind turbine with aeroelastically tailored blades. *34th Wind Energy Symposium*, 443–468. https://doi.org/10.2514/6.2016-1008

Hakuno, M., Shidawara, M., & Hara, T. (1969). Dynamic destructive test of a cantilever beam, controlled by an analog-computer. *Proceedings of the Japan Cociety of Civil Engineers*, 1–9.

Hammer, T. C., Beek, K. V., Koning, J., & Hendrikse, H. (2021). A 2D test setup for scaled real-time hybrid tests of dynamic ice- structure interaction. *Proceedings of the 26th International Conference on Port and Ocean Engineering under Arctic Conditions*, 1–13.

Hammer, T. C., & Hendrikse, H. (2023a). Data for the publication: Scaling of ice-induced vibrations. *4TU.ResearchData. dataset.* https://doi.org/https://doi.org/10.4121/6a696ee6-bed5-48b6-84cd-11385da2ee56

Hammer, T. C., & Hendrikse, H. (2024a). Data for the publication: Hardware-in-the-Loop experiments in model ice for analysis of ice-induced vibrations of offshore structures. *4TU.ResearchData. dataset.* https://doi.org/https://doi.org/10.4121/be53fc9d-3d5a-4aee-b694-cd92c66e6403

Hammer, T. C., & Hendrikse, H. (2024b). Hardware-in-the-Loop experiments in model ice for analysis of ice-induced vibrations of offshore structures. *Scientific Reports*, 1–17. https://doi.org/10.1038/s41598-024-68955-x

Hammer, T. C., & Hendrikse, H. (2023b). Experimental study into the effect of wind-ice misalignment on the development of ice-induced vibrations of offshore wind turbines. *Engineering Structures*, *286*, 1–17. https://doi.org/10.1016/j.engstruct.2023.116106

Hammer, T. C., & Hendrikse, H. (2023c). On the dependency of the development of frequency lock-in on the mode shape amplitude for higher structural modes. *Proceedings of the 27th International Conference on Port and Ocean Engineering under Arctic Conditions*.

Hammer, T. C., Owen, C. C., van den Berg, M., & Hendrikse, H. (2022). Classification of ice-induced vibration regimes of offshore wind turbines. *Proceedings of the ASME 2022 41st International Conference on Ocean, Offshore and Arctic Engineering*, 1–8. https://doi.org/10.1115/OMAE2022-78972

Hammer, T. C., Puolakka, O., & Hendrikse, H. (2024). Scaling ice-induced vibrations by combining replica modeling and preservation of kinematics. *Cold Regions Science and Technology*, *220*(January), 104127. https://doi.org/10.1016/j.coldregions.2024.104127

Hammer, T. C., Willems, T., & Hendrikse, H. (2023). Dynamic ice loads for offshore wind support structure design. *Marine Structures*, *87*, 1–19. https://doi.org/10.1016/j.marstruc.2022.103335

Hendrikse, H. (2017). Ice-induced vibrations of vertically sided offshore structures. https://doi.org/doi.org/10.4233/uuid:325ebcfb-f920-400c-8ef6-21b2305b6920

Hendrikse, H. (2019). Dynamic ice actions in the revision of iso 19906. *Proceedings of the 25th International Conference on Port and Ocean Engineering under Arctic Conditions*, (June).

Hendrikse, H. (2024). Ice engineering challenges for offshore wind development in the Baltic Seale. *Proceedings of the 27th IAHR International Symposium on Ice*.

Hendrikse, H., Hammer, T. C., Berg, M. v. d., Willems, T., Owen, C. C., van Beek, K., Ebben, N. J., Puolakka, O., & Polojärvi, A. (2022a). Experimental data from ice basin tests with vertically sided cylindrical structures. *Data in Brief*, *41*, 1–18. https://doi.org/10.1016/j.dib.2022.107877

Hendrikse, H., Hammer, T. C., Owen, C. C., Puolakka, O., & Willems, T. (2022b). Ice basin tests for ice-induced vibrations of offshore structures in the SHIVER project. *Proceedings of the ASME 2022 41st International Conference on Ocean, Offshore and Arctic Engineering*, 1–9. https://doi.org/10.1115/OMAE2022-78507

Hendrikse, H., Hammer, T. C., van den Berg, M., Willems, T., Owen, C. C., & van Beek, K. (2021). Data from ice tank tests with vertically sided structures collected during the SHIVER project. *4TU.ResearchData. dataset*. https://doi.org/10.4121/17087462.v1

Hendrikse, H., & Metrikine, A. (2015). Interpretation and prediction of ice induced vibrations based on contact area variation. *International Journal of Solids and Structures*, *75-76*, 336–348. https://doi.org/10.1016/j.ijsolstr.2015.08.023

Hendrikse, H., & Metrikine, A. (2016a). Edge indentation of ice with a displacement-controlled oscillating cylindrical structure. *Cold Regions Science and Technology*, *121*, 100–107. https://doi.org/10.1016/j.coldregions.2015.10.013

Hendrikse, H., & Metrikine, A. (2016b). Ice-induced vibrations and ice buckling. *Cold Regions Science and Technology*. https://doi.org/10.1016/j.coldregions.2016.09.009

Hendrikse, H., & Nord, T. S. (2019). Dynamic response of an offshore structure interacting with an ice floe failing in crushing. *Marine Structures*, *65*, 271–290. https://doi.org/10.1016/j.marstruc.2019.01.012

Hendrikse, H., & Nord, T. S. (2020). Corrigendum to "Dynamic response of an offshore structure interacting with an ice floe failing in crushing" [Mar. Struct. 65 (2019) 271–290](S0951833918303496)(10.1016/j.marstruc.2019.01.012). *Marine Structures*, *70*(January), 102706. https://doi.org/10.1016/j.marstruc.2019.102706

Hendrikse, H., Ziemer, G., & Owen, C. C. (2018). Experimental validation of a model for prediction of dynamic ice-structure interaction. *Cold Regions Science and Technology*, *151*, 345–358. https://doi.org/10.1016/j.coldregions.2018.04.003

Hirayama, K.-i. (1983). *Properties of urea-doped ice in the CRREL test basin* (tech. rep.). U.S. Army Cold Regions Research and Engineering Laboratory. Hanover, New Hampshire, USA.

Hirayama, K.-i., Schwarz, J., & Wu, H.-C. (1974). *An investigation of ice forces on vertical structures* (tech. rep.). Iowa Institute of Hydraulic Research, The University of Iowa. Iowa City, Iowa, USA.

Hoek, J. (2021). Dynamic ice-structure interaction for jacket substructures. *Master thesis*.

Horiuchi, T., Inoue, M., Konno, T., & Namita, Y. (1999). Real-time hybrid experimental system with actuator delay compensation and its application to a piping system with energy absorber. *Earthquake Engineering and Structural Dynamics*, *28*(10), 1121–1141. https://doi.org/10.1002/(SICI)1096-9845(199910)28:10<1121::AID-EQE858>3.0.CO;2-O

Hornnes, V., Hammer, T. C., Høyland, K. V., & Hendrikse, H. (2022). On the use of drift ice thickness statistics from a Copernicus reanalysis product for fatigue damage calculation. *In Proceedings of the 26th IAHR International Symposium on Ice*, (June), 1–11.

Høyland, K. V., Nord, T., Turner, J., Hornnes, V., Gedikli, E. D., Bjerkås, M., Hendrikse, H., Hammer, T. C., Ziemer, G., Stange, T., Ehlers, S., Braun, M., Willems, T., & Fischer, C. (2021). Fatigue damage from dynamic ice action - the FATICE project. *Proceedings of the 26th International Conference on Port and Ocean Engineering under Arctic Conditions*.

Huang, Y., Shi, Q., & Song, A. (2007). Model test study of the interaction between ice and a compliant vertical narrow structure. *Cold Regions Science and Technology*, *49*, 151–160. https://doi.org/10.1016/j.coldregions.2007.01.004

Huera Huarte, F. J., Bearman, P. W., & Chaplin, J. R. (2006). On the force distribution along the axis of a flexible circular cylinder undergoing multi-mode vortex-induced vibrations. *Journal of Fluids and Structures*, *22*(6-7), 897–903. https://doi.org/10.1016/j.jfluidstructs.2006.04.014

IEC 61400-3-1. (2019). Wind energy generation systems - Part 3-1: Design requirements for fixed offshore wind turbines.

Inoue, M., & Koma, N. (1985). Field Indentation Tests on Cylindrical Structures. *Proceedings of the 8th International Conference on Port and Ocean Engineering under Arctic Conditions, 2*, 555–568.

Insam, C., Ballat, L. M., Lorenz, F., & Rixen, D. J. (2021). Hardware-in-the-loop test of a prosthetic foot. *Applied Sciences (Switzerland), 11*(20), 1–16. https://doi.org/10.3390/app11209492

ISO 19906:2019(E). (2019). Petroleum and natural gas industries — Arctic offshore structures.

ITTC. (2021). Recommended Procedures and Guidelines - Test Methods for Model Ice Properties. *International towing tank conference*, 1–19.

Izumiyama, K., Irani, M. B., & Timco, G. W. (1994). Influence of compliance of structure on ice load. *Proceedings of the 12th IAHR International Symposium on Ice, 1*, 229–238.

Izumiyama, K., & Uto, S. (1997). Ice loading on a compliant indentor. In H. Yamaguchi, K. Izumiyama, D. S. Sodhi, W. A. Nixon, & H. Kitagawa (Eds.), *Proceedings of the 16th international conference on offshore mechanics and arctic engineering* (pp. 431–436, Vol. 4). OMAE.

Jalonen, R., & Ilves, L. (1990). Experience with a chemically-doped fine-grained model ice. *Proceedings of the 10th IAHR International Symposium on Ice*, 639–651.

Jefferies, M. G., & Wright, W. H. (1988). Dynamic response of Molikpaq to ice-structure interaction. *Proceedings of the 7th International Conference on Offshore Mechanics and Arctic Engineering, 4*, 201–220.

Jefferies, M., Kärnä, T., & Løset, S. (2008). Field data on the magnification of ice loads on vertical structures. *Proceedings of the 19th IAHR International Symposium on Ice*, 1325–1343.

Jordaan, I. J. (2001). Mechanics of ice-structure interaction. *Engineering Fracture Mechanics, 68*(17-18), 1923–1960. https://doi.org/10.1016/S0013-7944(01)00032-7

Kamesaki, K., Yamauchi, Y., & Kärnä, T. (1996). Ice force as a function of structural compliance. *Proceedings of the 13th IAHR International Symposium on Ice, 1*, 395–402.

Kärnä, T., Andersen, H., Gürtner, A., Metrikine, A., Sodhi, D. S., Loo, M., Kuiper, G., Gibson, R., Fenz, D., Muggeridge, K., Wallenburg, C., Wu, J.-F., & Jefferies, M. G. (2013). Ice-induced vibrations of offshore structures - looking beyond ISO 19906. *Proceedings of the 22nd International Conference on Port and Ocean Engineering under Arctic Conditions*, 1–12.

Kärnä, T., Gravesen, H., Fransson, L., & Løset, S. (2010). Simulation of multi-modal vibrations due to ice actions. *Proceedings of the 20th IAHR International Symposium on Ice*, (August).

Kärnä, T., & Jochmann, P. (2003). Field observations on ice failure modes. *Proceedings of the 17th International Conference on Port and Ocean Engineering under Arctic Conditions*, (1-10).

Kärnä, T. (2011a). *Full-scale data analyses of frequency lock-in* (tech. rep.).

Kärnä, T. (2011b). *Validation of predictive IIV HM-model* (tech. rep.).

Kärnä, T., Guo, F., Løset, S., & Määttänen, M. (2008). Small-scale data on magnification of ice loads on vertical structures. In M. Jasek (Ed.), *Proceedings of the 19th iahr international symposium on ice* (pp. 1313–1324, Vol. 2).

Kärnä, T., Kamesaki, K., & Tsukuda, H. (1999). Numerical model for dynamic ice-structure interaction. *Computers and Structures, 72*(4), 645–658. https://doi.org/10.1016/S0045-7949(98)00337-X

Kärnä, T., Kolari, K., Jochmann, P., Evers, K.-U., & Bi, X. (2003). Tests on dynamic ice-structure interaction. *Proceedings of the 22nd International Conference on Offshore Mechanics and Arctic Engineering*, 1–7.

Kärnä, T., & Muhonen, A. (1990). Preliminary results from ice indentation tests using flexible and rigid indentors. *Proceedings of the 10th IAHR International Symposium on Ice, 3*, 261–275.

Kärnä, T., & Qu, Y. (2009). Analysis of the size effect in ice crushing. *Internal report*, (2), 1–167.

Knut, V., Torodd, S., Hendrikse, H., Tuhkuri, J., Polojärvi, A., von Bock und Polach, R. U. F., Heinonen, J., Johannessen Eik, K., & Teigen, S. H. (2023). Delft University of Technology Challenges with sea ice action on structures for Offshore wind. *Proceedings of the 27th International Conference on Port and Ocean Engineering under Arctic Conditions (POAC)*.

Kong, V., Cassidy, M. J., & Gaudin, C. (2015). Development of a real-time hybrid testing method in a centrifuge. *International Journal of Physical Modelling in Geotechnics, 15*(4), 169–190. https://doi.org/10.1680/ijpmg.14.00021

Korzhavin, K. (1962). *Action of Ice on Engineering Structures* (tech. rep.). Siberian Branch of USSR Academy of Sciences.

Krenk, S., & Couturier, P. J. (2017). Equilibrium-based nonhomogeneous anisotropic beam element. *AIAA Journal, 55*(8), 2773–2782. https://doi.org/10.2514/1.J055884

Lau, M., Wang, J., & Lee, C. (2007). Review of ice modeling methodology. *Proceedings of the International Conference on Port and Ocean Engineering under Arctic Conditions, POAC*, 350–362.

Lee, C., & Tu, J. Y. (2014). Preliminary comparison of hybrid testing techniques. *Procedia Engineering, 79*(1st ICM), 490–494. https://doi.org/10.1016/j.proeng.2014.06.370

Lelieveld, T. (2021). Influence of ice jams on ice- induced vibrations of multi-legged sub-structures. *Master thesis*.

Leppäranta, M. (2005). *The Drift of Sea Ice*.

Leppäranta, M., & Myrberg, K. (2009). *Physical Oceanography of the Baltic*. Springer-Verlag Berlin Heidelberg. https://doi.org/10.1007/978-3-540-79703-6

Li, Y., Guo, S., & Chen, W. (2018). Analysis on multi-frequency vortex-induced vibration and mode competition of flexible deep-ocean riser in sheared fluid fields. *Journal of Petroleum Science and Engineering, 163*(January), 378–386. https://doi.org/10.1016/j.petrol.2018.01.008

Linderholt, A., Allen, M. S., & D'Ambrogio, W. (2020). *Dynamic Substructures, Volume 4*. Springer Nature Switzerland AG.

Liu, J., Silva, C. E., Dyke, S. J., Wu, Y., & Liu, H. (2024). Using real-time hybrid simulation for active mass damper experimentation and validation. *Mechanism and Machine*

Theory, *191*(September 2023). https://doi.org/10.1016/j.mechmachtheory.2023.105474

Løset, S., Shkhinek, K. N., Gudmestad, O. T., & Høyland, K. V. (2006). *Actions from ice on Arctic offshore and coastal structures* (N. M. Bashakova, N. K. Beliakova, & O. V. Shilkova, Eds.).

Luan, C., Gao, Z., & Moan, T. (2018). Comparative analysis of numerically simulated and experimentally measured motions and sectional forces and moments in a floating wind turbine hull structure subjected to combined wind and wave loads. *Engineering Structures*, *177*(7491), 210–233. https://doi.org/10.1016/j.engstruct.2018.08.021

Määttanen, M. (1981). Laboratory tests for dynamic ice-structure interaction. *Engineering Structures*, *3*(2), 111–116. https://doi.org/10.1016/0141-0296(81)90037-7

Määttänen, M. (1975a). Experience of Ice Forces Against a Steel Lighthouse Mounted on the Seabed and Proposed Construction Refinements. *Proceedings of the 3rd International Conference on Port and Ocean Engineering under Arctic Conditions*, 857–869.

Määttänen, M. (1975b). Ice forces and vibrational behaviour of bottom-founded steel lighthouses. *Proceeding of the 3rd IAHR International Symposium on Ice*, 345–355.

Määttänen, M. (1978). *On conditions for the rise of self-excited autonomous oscillations in slender marine piles* (Publication No. 25) [Doctoral dissertation, University of Oulu].

Määttänen, M. (1979). Laboratory tests for dynamic ice-structure interaction. *Proceedings of the 5th Port and Ocean Engineering under Arctic Conditions*, 1139–1153.

Määttänen, M. (1983). *Dynamic ice-structure interaction during continuous crushing* (tech. rep.). U.S. Army Cold Regions Research and Engineering Laboratory. Hanover, New Hampshire, USA.

Määttänen, M. (2015). Ice induced frequency lock-in vibrations - converging towards consensus. *Proceedings of the 23rd International Conference on Port and Ocean Engineering under Arctic Conditions*, 1–11.

Määttänen, M., Løset, S., Metrikine, A., Evers, K.-U., Hendrikse, H., Lønøy, C., Metrikin, I., Nord, T. S., & Sukhorukov, S. (2012). Novel ice induced vibration testing in a large-scale facility: Deciphering ice induced vibrations, part 1. *Proceedings of the 21st IAHR International Symposium on Ice*, 946–958.

Määttänen, M., Marjavaara, P., Saarinen, S., & Laakso, M. (2011). Ice crushing tests with variable structural flexibility. *Cold Regions Science and Technology*, *67*(3), 120–128. https://doi.org/10.1016/j.coldregions.2011.03.004

Maghareh, A. (2017). *Nonlinear Robust Framework for Real-Time Hybrid Simulation of Structural Systems : Design , Implementation , and Validation* [Doctoral dissertation, Purdue University].

Maghareh, A., Dyke, S., Rabieniaharatbar, S., & Prakash, A. (2016). Predictive stability indicator: a novel approach to configuring a real-time hybrid simulation. *Earthquake Engineering & Structrual dynamics*, (056), 1–6. https://doi.org/10.1002/eqe

Matlock, H., Dawkins, W. P., & Panak, J. J. (1969). A model for the prediction of ice-structure interaction. *Proceedings of the Annual Offshore Technology Conference*, *May*, 687–694. https://doi.org/10.4043/1066-ms

McCrum, D. P., & Williams, M. S. (2016). An overview of seismic hybrid testing of engineering structures. *Engineering Structures*, *118*, 240–261. https://doi.org/10.1016/j.engstruct.2016.03.039

Mergny, E., & Franssen, J. M. (2022). Multi-degree-of-freedom Hybrid Fire Testing of a Column in a Non-linear Environment. *Fire Technology*. https://doi.org/10.1007/s10694-022-01258-7

Michel, B. (1970). Ice modeling in hydraulic engineering. *Proceedings of the 1st IAHR International Symposium on Ice*, 1–12.

Miraglia, G., Petrovic, M., Abbiati, G., Mojsilovic, N., & Stojadinovic, B. (2020). A model-order reduction framework for hybrid simulation based on component-mode synthesis. *Earthquake Engineering and Structural Dynamics*, *49*(8), 737–753. https://doi.org/10.1002/eqe.3262

Najafi, A., Fermandois, G. A., & Spencer, B. F. (2020). Decoupled model-based real-time hybrid simulation with multi-axial load and boundary condition boxes. *Engineering Structures*, *219*(October 2019). https://doi.org/10.1016/j.engstruct.2020.110868

Nakashima, M., Kato, H., & Takaoka, E. (1992). Development of real-time pseudo dynamic testing. *Earthquake Engineering & Structural Dynamics*, *21*(1), 79–92. https://doi.org/10.1002/eqe.4290210106

Neumann, C., Simpson, B., Schellenberg, A., Lomonaco, P., & You, S. (2023). Hydrodynamic Real-Time Hybrid Simulation Demonstrated for Cascading Seismic and Tsunami Events. *Journal of Waterway, Port, Coastal, and Ocean Engineering*, *149*(1). https://doi.org/10.1061/(asce)ww.1943-5460.0000733

Nord, T. S., Lourens, E. M., Määttänen, M., Øiseth, O., & Høyland, K. V. (2015a). Laboratory experiments to study ice-induced vibrations of scaled model structures during their interaction with level ice at different ice velocities. *Cold Regions Science and Technology*, *119*, 1–15. https://doi.org/10.1016/j.coldregions.2015.06.017

Nord, T. S., Lourens, E. M., Øiseth, O., & Metrikine, A. (2015b). Model-based force and state estimation in experimental ice-induced vibrations by means of Kalman filtering. *Cold Regions Science and Technology*, *111*, 13–26. https://doi.org/10.1016/j.coldregions.2014.12.003

Nord, T. S., Määttänen, M., & Øiseth, O. (2013). Frequency domain force identification in ice-structure interaction. *Proceedings of the 22nd International Conference on Port and Ocean Engineering under Arctic Conditions*, 10.

Nord, T. S., Samardžija, I., Hendrikse, H., Bjerkås, M., Høyland, K. V., & Li, H. (2018). Ice-induced vibrations of the Norströmsgrund lighthouse. *Cold Regions Science and Technology*, *155*(August), 237–251. https://doi.org/10.1016/j.coldregions.2018.08.005

Nordlund, O., Kärnä, T., & Järvinen, E. (1988). Measurements of ice-induced vibrations of channel markers. *Proceedings of the 9th IAHR International Symposium on Ice*, *1*, 537–548.

Owen, C. C. (2024). *On ice mechanics in ice-induced vibrations* [Doctoral dissertation, Delft University of Technology].

Owen, C. C., Hammer, T. C., & Hendrikse, H. (2022). Test setup for compressive loading of confined ice thick sections viewed with in-situ cross-polarization imaging. *Proceeding of the 26th IAHR International Symposium on Ice*, (July), 1–10.

Owen, C. C., Hammer, T. C., & Hendrikse, H. (2023a). Hysteresis and dichotomous mechanics in cyclic crushing failure of confined freshwater columnar ice. *Cold Regions Science and Technology*, *209*, 1–18. https://doi.org/10.1016/j.coldregions.2023.103816

Owen, C. C., Hammer, T. C., & Hendrikse, H. (2023b). Peak loads during dynamic ice-structure interaction caused by rapid ice strengthening at near-zero relative velocity. *Cold Regions Science and Technology*, *211*(January), 103864. https://doi.org/10.1016/j.coldregions.2023.103864

Owen, C. C., & Hendrikse, H. (2019). A study of the transition ice speed from intermittent crushing to frequency lock-in vibrations based on model-scale experiments. *Proceedings of the 25th International Conference on Port and Ocean Engineering under Arctic Conditions*, 1–14.

Owen, C. C., & Hendrikse, H. (2021). Simulation and analysis of ice-induced vibrations experienced by Molikpaq during the May 12 , 1986 event. *Proceedings of the 26th International Conference on Port and Ocean Engineering under Arctic Conditions*, (July).

Palacio-Betancur, A., & Gutierrez Soto, M. (2023). Recent Advances in Computational Methodologies for Real-Time Hybrid Simulation of Engineering Structures. *Archives of Computational Methods in Engineering*, *30*(3), 1637–1662. https://doi.org/10.1007/s11831-022-09848-y

Palmer, A., & Dempsey, J. (2009). Model tests in ice. *Proceedings of the 20th International Conference on Port and Ocean Engineering under Arctic Conditions*, 1–10.

Palmer, A., Qianjin, Y., & Fengwei, G. (2010). Ice-induced vibrations and scaling. *Cold Regions Science and Technology*, *60*, 189–192. https://doi.org/10.1016/j.coldregions.2009.11.005

Park, J., Park, M., Chae, Y., & Kim, C. Y. (2023). Real-time hybrid simulation for investigating the influence of vertical ground motions on the lateral response of RC piers. *Earthquake Engineering and Structural Dynamics*, (April), 2928–2944. https://doi.org/10.1002/eqe.3902

Passon, P., Branner, K., Larsen, S. E., & Rasmussen, J. H. (2015). *Offshore Wind Turbine Foundation Design* [Doctoral dissertation].

Pereira, D. (2022). Wind Rose.

Petry, A., Hammer, T. C., Hendrikse, H., & Puolakka, O. (2023). Ice basin experiments on mixed-mode failure on ice cones. *Proceedings of the 27th International Conference on Port and Ocean Engineering under Arctic Conditions*.

Peyton, H. (1968). Sea ice forces. *Proceedings of Conference on Ice Pressures Against Structures*, 117–123.

Popko, W. (2020). Impact of Sea Ice Loads on Global Dynamics of Offshore Wind Turbines. *Leibniz Universität Hannover (Doctoral thesis)*.

Rubak, R., & Petersen, J. (2005). Monopile as part of aeroelastic wind turbine simulation code. *Proceedings of Copenhagen Offshore Wind*, 1–10.

Ruffini, V., Szczyglowski, C., Barton, D. A., Lowenberg, M., & Neild, S. A. (2020). Real-Time Hybrid Testing of Strut-Braced Wing Under Aerodynamic Loading Using an Electrodynamic Actuator. *Experimental Techniques*, *44*(6), 821–835. https://doi.org/10.1007/s40799-020-00394-5

Sauder, T., Chabaud, V., Thys, M., Bachynski, E. E., & Sæther, L. O. (2016). Real-time hybrid model testing of a braceless semi-submersible wind turbine: Part I: The hybrid approach. *Proceedings of the ASME 2016 35th International Conference on Ocean, Offshore and Arctic Engineering*, 1–13.

Schwarz, J. (1975). On the flexural strength and elasticity of saline ice. *Proceedings of the 3rd IAHR International Symposium on Ice*, 373–386.

Schwarz, J., & Jochmann, P. (2001). Ice force measurements within the LOLEIF-project. *Proceedings of the 16th International Conference on Port and Ocean Engineering under Arctic Conditions (POAC'01)*, *2*, 669–682.

Silva, C. E., Gomez, D., Maghareh, A., Dyke, S. J., & Spencer, B. F. (2020). Benchmark control problem for real-time hybrid simulation. *Mechanical Systems and Signal Processing*, *135*, 106381. https://doi.org/10.1016/j.ymssp.2019.106381

Singh, S. K., Timco, G. W., Frederking, R. M. W., & Jordaan, I. J. (1990). Tests of ice crushing on a flexible structure. *Proceedings of the 9th Offshore Mechanics and Arctic Engineering Symposium*, *4*, 89–94.

Skjoldan, P. F. (2011). Aeroelastic modal dynamics of wind turbines including anisotropic effects. *Danmarks Tekniske Universitet, Risø Nationallaboratoriet for Bæredygtig Energi, Risø-PhD,*

Sodhi, D. S. (1991). Ice-structure interaction during indentation tests. In S. Jones, R. F. McKenna, J. Tillotson, & I. Jordaan (Eds.), *Proceedings of the iutam-iahr symposium on ice-structure interaction* (pp. 619–640). Springer-Verlag Berlin Heidelberg. https://doi.org/10.1007/978-3-642-84100-2{_}31

Sodhi, D. S. (1992). Ice-structure interaction with segmented indentors. *Proceedings of the 11th IAHR International Symposium on Ice*, 909–929.

Sodhi, D. S. (1995). An ice-structure interaction model. In A. P. S. Selvadurai & M. J. Boulon (Eds.), *Mechanics of geomaterial interfaces* (pp. 57–75, Vol. 42). Elsevier Science B.V. https://doi.org/10.1016/S0922-5382(06)80006-1

Sodhi, D. S. (2001). Crushing failure during ice-structure interaction. *Engineering Fracture Mechanics*, *68*(17-18), 1889–1921. https://doi.org/10.1016/S0013-7944(01)00038-8

Stange, T., Ziemer, G., & von Bock und Polach, R. U. F. (2020). Development of an experimental setup to investigate the impact of higher structural modes on dynamic ice-structure interaction. *Proceeding of the 25th IAHR International Symposium on Ice*, (November), 23–25.

Sun, C., Song, W., & Jahangiri, V. (2022). A real-time hybrid simulation framework for floating offshore wind turbines. *Ocean Engineering*, *265*(August), 112529. https://doi.org/10.1016/j.oceaneng.2022.112529

Suominen, M., Karhunen, J., Bekker, A., Kujala, P., Elo, M., von Bock und Polach, R. U. F., Enlund, H., & Saarinen, S. (2013). Full-scale measurements on board PSRV S.A. Agulhas II in the Baltic Sea. *Proceedings of the 22nd International Conference on Port and Ocean Engineering under Arctic Conditions*, 1–13.

Takanashi, K., & Ohi, K. (1983). Earthquake response analysis of steel structures by rapid computer-actuator on-line system. *Transactions of the Architectural Institute of Japan*, 103–109.

Takanashi, K., Udagawa, K., Seki, M., Okada, T., & Tanaka, H. (1975). Non-linear Earthquake Response Analysis of Structures by a Computer-Actuator On-Line System. *Transactions of the Architectural Institute of Japan, 229*(March 1975), 1–17. https://doi.org/10.3130/aijsaxx.229.0

Takeuchi, T., Sakai, M., Akagawa, S., Nakazawa, N., & Saeki, H. (2001). On the factors influencing the scaling of ice forces. In J. P. Dempsey & H. H. Shen (Eds.), *Proceedings of the iutam symposium on scaling laws in ice mechanics and ice dynamics* (pp. 149–160). IUTAM.

The Baltic Sea Energy Security Summit. (2022). The Marienborg Decleration.

Thys, M., Sauder, T., Chabaud, V., Eliassen, L., Sæther, L. O., & Magnussen, Ø. B. (2018). Real-time hybrid model testing of a semi-submersible 10MW floating wind turbine and advances in the test method. *ASME 2018 1st International Offshore Wind Technical Conference, IOWTC 2018*, (November). https://doi.org/10.1115/IOWTC2018-1081

Tian, Y., Huang, Y., & Li, W. (2019). Experimental Investigations on Ice Induced Vibrations of a Monopile-type Offshore Wind Turbine in Bohai Sea. *Proceedings of the 29th International Ocean and Polar Engineering Conference*, 327–334.

Tian, Y., Yang, D., Gang, X., Yu, C., Ji, S., & Yue, Q. (2023). Development of a Numerical Ice Tank Based on DEM and Physical Model Testing: Methods, Validations and Applications. *Journal of Marine Science and Engineering*, *11*(7). https://doi.org/10.3390/jmse11071455

Tikanmäki, M., & Heinonen, J. (2021). Estimating extreme level ice and ridge thickness for offshore wind turbine design: Case study Kriegers Flak. *Wind Energy*, (September), 1–21. https://doi.org/10.1002/we.2690

Timco, G. W. (1980). The mechanical properties of saline-doped and carbamide (urea)-doped model ice. *Cold Regions Science and Technology*, *3*(1), 45–56. https://doi.org/10.1016/0165-232X(80)90006-3

Timco, G. W. (1991). Laboratory observations of macroscopic failure modes in freshwater ice. *Proceedings of the 6th International Cold Regions Engineering Conference*, 605–614.

Timco, G. W., Wright, B., Johnston, M., & Frederking, R. M. W. (1999). First-Year Ice Ridge Loads on the Molikpaq. *Proceedings 4th International Conference on Development of the Russian Arctic Offshore*, (July), 172–179.

Timco, G. W. (1984). Ice fores on structures: physical modelling techniques. *Proceedings of the 7th IAHR International Symposium on Ice*, 117–150.

Timco, G. W. (1986). EG/AD/S: A new type of model ice for refrigerated towing tanks. *Cold Regions Science and Technology*, *12*(2), 175–195. https://doi.org/10.1016/0165-232X(86)90032-7

Timco, G. W., Irani, M. B., Tseng, J., Liu, L. K., & Zheng, C. B. (1992). Model tests of dynamic ice loading on the Chinese JZ-20-2 jacket platform. *Canadian Journal of Civil Engineering, 19*, 819–832.

Timco, G., Nwogu, O., & Christensen, F. (1995). Compliant model tests with the Great Belt West Bridge piers in ice part I: Test methods and key results. *Cold Regions Science and Technology*, *23*(2), 149–164. https://doi.org/10.1016/0165-232X(94)00012-M

Toyama, Y., Sensu, T., Minami, M., & Yashima, N. (1983). Model tests on ice-induced self-excited vibration of cylindrical structures. *Proceedings of the 7th International Conference on Port and Ocean Engineering under Arctic Conditions*, *2*, 834–844.

Tsuchiya, M., Kanie, S., Ikejiri, K., Yoshida, A., & Saeki, H. (1985). An experimental study on ice-structure interaction. *Proceedings of the 7th Offshore Technology Conference*, 312–327. https://doi.org/https://doi.org/10.4043/5055-MS

van den Berg, M., Lubbad, R., & Løset, S. (2020). Repeatability of ice-tank tests with broken ice. *Marine Structures*, *74*(July). https://doi.org/10.1016/j.marstruc.2020.102827

van den Berg, M., Owen, C. C., & Hendrikse, H. (2022). Experimental study on ice-structure interaction phenomena of vertically sided structures. *Cold Regions Science and Technology*, *201*(May), 103628. https://doi.org/10.1016/j.coldregions.2022.103628

van der Stap, F. L., Nielsen, M. B., Owen, C. C., van der Male, P., & Hendrikse, H. (2023). On the feasibility of monopile foundations for offshore wind in the Baltic Sea. *Proceedings of the 27th International Conference on Port and Ocean Engineering under Arctic Conditions*, 1–14.

Violette, R., de Langre, E., & Szydlowski, J. (2010). A linear stability approach to vortex-induced vibrations and waves. *Journal of Fluids and Structures*, *26*(3), 442–466. https://doi.org/10.1016/j.jfluidstructs.2010.01.002

von Bock und Polach, R. U. F., & Ehlers, S. (2015). On the scalability of model-scale ice experiments. *Journal of Offshore Mechanics and Arctic Engineering*, *137*, 1–8. https://doi.org/10.1115/1.4031114

von Bock und Polach, R. U. F., Ehlers, S., & Kujala, P. (2013). Model-scale ice - Part A: Experiments. *Cold Regions Science and Technology*, *94*, 74–81. https://doi.org/10.1016/j.coldregions.2013.07.001

von Bock und Polach, R. U. F., Ettema, R., Gralher, S., Kellner, L., & Stender, M. (2019). The non-linear behavior of aqueous model ice in downward flexure. *Cold Regions Science and Technology*, *165*(May), 102775. https://doi.org/10.1016/j.coldregions.2019.05.001

von Bock und Polach, R. U. F., Klein, M., Reimer, N., & Hartmann, M. (2023). Estimation of model ice properties in ice tank operations with numerical models. *Proceedings of the 27th International Conference on Port and Ocean Engineering under Arctic Conditions*.

von Bock und Polach, R. U. F., & Molyneux, D. (2017). Model ice: A review of its capacity and identification of knowledge gaps. *Proceedings of the 36th International Conference on Offshore Mechanics and Arctic Engineering*, 1–10. https://doi.org/10.1115/OMAE2017-61808

von Bock und Polach, R. U. F., Ziemer, G., Klein, M., Hartmann, M. C., Toffoli, A., & Monty, J. (2020). Case based scaling: Recent developments in ice model testing technology. *Proceedings of the International Conference on Offshore Mechanics and Arctic Engineering - OMAE*, *7*, 1–9. https://doi.org/10.1115/omae2020-18320

Wallace, M. I., Sieber, J., Neild, S. A., Wagg, D. J., & Krauskopf, B. (2004). Stability analysis of real-time dynamic substructuring using delay differential equation models. *pre-print*.

Wallace, M. I., Sieber, J., Neild, S. A., Wagg, D. J., & Krauskopf, B. (2005). Stability analysis of real-time dynamic substructuring using delay differential equation models. *Earthquake Engineering and Structural Dynamics*, *34*(15), 1817–1832. https://doi.org/10.1002/eqe.513

Wang, G., Zhang, D., Yue, Q., & Yu, S. (2022). Study on the Dynamic Ice Load of Offshore Wind Turbines with Installed Ice-Breaking Cones in Cold Regions. *Energies*, *15*(9). https://doi.org/10.3390/en15093357

Wang, X., Kim, R. E., Kwon, O.-S., Yeo, I.-H., & Ahn, J.-K. (2019). Continuous Real-Time Hybrid Simulation Method for Structures Subject to Fire. *Journal of Structural Engineering*, *145*(12), 1–12. https://doi.org/10.1061/(asce)st.1943-541x.0002436

Wei, M., Prasanna, M., Cole, D. M., & Polojärvi, A. (2022). Response of Dry and Floating Saline Ice to Cyclic Compression. *Geophysical Research Letters*, *49*, 1–10. https://doi.org/10.1029/2022GL099457

Willems, T., & Hendrikse, H. (2019). Coupled simulation of ice-structure interaction of offshore wind turbines in BHawC using VANILLA. *Proceedings of the 25th International Conference on Port and Ocean Engineering under Arctic Conditions*, (June).

WindEurope. (2019). *Boosting offshore wind energy in the Baltic Sea* (tech. rep. No. November).

Witteveen, W., & Koller, L. (2023). FRF-based non-simultaneous real-time hybrid testing of multiple subsystems with moderate nonlinearities. *Mechanical Systems and Signal Processing*, *188*(January 2022), 109944. https://doi.org/10.1016/j.ymssp.2022.109944

Wu, H., Huang, Y., & Li, W. (2018). Experimental study on the ice load of large-diameter monopile wind turbine foundations (In Chinese). *The Ocean Engineering (Chinese)*, *36*(2), 1–9.

Wu, H., Chang, K., & Schwarz, J. (1976). Fracture in the compression of columnar gained ice. *Engineering Fracture Mechanics*, *8*(2), 365–370. https://doi.org/10.1016/0013-7944(76)90016-3

Wu, T., & Song, W. (2019). Real-time aerodynamics hybrid simulation: Wind-induced effects on a reduced-scale building equipped with full-scale dampers. *Journal of Wind Engineering and Industrial Aerodynamics*, *190*(October 2018), 1–9. https://doi.org/10.1016/j.jweia.2019.04.005

Xu, N., Yuan, S., Liu, X., Ma, Y., Shi, W., & Zhang, D. (2020). Risk assessment of sea ice disasters on fixed jacket platforms in Liaodong Bay. *Natural Hazards and Earth System Sciences*, *20*(4), 1107–1121. https://doi.org/10.5194/nhess-20-1107-2020

Yap, K. T. (2011). *Level ice-vertical structure interaction : Steady-state self-excited vibration of structures* [Doctoral dissertation, National University of Singapore].

Yap, K. T., & Palmer, A. C. (2013). A model test on ice-induced vibrations: Structure response characteristics and scaling of the lock-in phenomenon. *Proceedings of the 22nd International Conference on Port and Ocean Engineering under Arctic Conditions, POAC*, (109), 11.

Yu, S., Zhang, D., Wang, S., Wang, G., Wang, G., Yue, Q., & Li, G. (2020). Field monitoring of offshore wind turbine foundations in ice regions. *Journal of Coastal Research*, *104*(sp1), 343–350. https://doi.org/10.2112/JCR-SI104-063.1

Yue, Q., & Bi, X. (2000). Ice-induced jacket structure vibrations in Bohai Sea. *Journal of Cold Regions Engineering*, *14*(2), 81–92. https://doi.org/10.1061/(ASCE)0887-381X(2000)14:2(81)

Yue, Q., Bi, X., Zhang, X., & Kärnä, T. (2002). Dynamic ice forces caused by crushing failure. In V. Squire & P. Langhorne (Eds.), *Proceedings of the 16th iahr international symposium on ice* (pp. 231–237, Vol. 3). IAHR.

Yue, Q., Guo, F., & Chu, S. (2006). Laboratory tests of ice induced structure vibrations. *Proceedings of the 18th IAHR International Symposium on Ice*, *1*, 191–198.

Zhang, Z., Basu, B., & Nielsen, S. R. (2019). Real-time hybrid aeroelastic simulation of wind turbines with various types of full-scale tuned liquid dampers. *Wind Energy*, *22*(2), 239–256. https://doi.org/10.1002/we.2281

Zhao, J., French, C., Shield, C., & Posbergh, T. (2003). Considerations for the development of real-time dynamic testing using servo-hydraulic actuation. *Earthquake Engineering and Structural Dynamics*, *32*(11), 1773–1794. https://doi.org/10.1002/eqe.301

Zhou, H., Shao, X., Zhang, B., Tan, P., & Wang, T. (2023a). Relative stability analysis for robustness design of real-time hybrid simulation. *Soil Dynamics and Earthquake Engineering*, *165*(May 2022), 107681. https://doi.org/10.1016/j.soildyn.2022.107681

Zhou, Z., Zhang, D., Zhang, Y., Gao, S., Yue, Y., & Li, N. (2023b). Real-time hybrid simulation for fluid-structure interaction: Structures under seismic and hydrodynamic forces. *Earthquake Engineering and Structural Dynamics*, (December 2022), 1–18. https://doi.org/10.1002/eqe.3978

Zhu, H., Lin, P., & Gao, Y. (2019). Vortex-Induced Vibrations of A Long Flexible Cylinder in Linear and Exponential Shear Flows. *Journal of Fluids and Structures*, *33*(1), 44–56. https://doi.org/10.1007/s13344-019-0005-9

Ziemer, G. (2019). Utilization of tactile sensors to investigate local ice pressure in scale model tests. *The 6th International Conference on Advanced Model Measurement Technology for The Maritime Industry*, 12.

Ziemer, G. (2021). *Ice-Induced Vibrations of Vertical Structures* [Doctoral dissertation, Technische Universität Hamburg]. https://doi.org/10.15480/882.4018

Ziemer, G., & Evers, K.-U. (2016). Model Tests With a Compliant Cylindrical Structure to Investigate Ice-Induced Vibrations. *Journal of Offshore Mechanics and Arctic Engineering*, *138*(4). https://doi.org/10.1115/1.4033712

SAMENVATTING

De wereldwijd toenemende vraag naar energieonafhankelijkheid en hernieuwbare energie heeft geleid tot de ontwikkeling van offshore windparken in subarctische gebieden, zoals de Baltische Zee in Europa en de Bohai Zee in China. De trilling van offshore constructies veroorzaakt door ijs wanneer het ijs tegen de constructive faalt heeft in het verleden geleid tot het fallen van (delen van) deze constructies.

Wanneer het ijs tegen de verticale zijde van een offshore wind turbine botst ('crushed'), kunnen de meest extreme ijs geïnduceerde trillingen optreden. Helaas is er geen veld data beschikbaar om dit fenomeen te onderzoeken. Daarbij bestaan er twijfels of inzichten over dit fenomeen opgedaan uit de olie- en gas industrie of metingen op vuurtorens toepasbaar zijn op offshore windturbines, vanwege de aanzienlijke verschillen in constructieve eigenschappen tussen deze constructies. Door het gebrek aan veld metingen kunnen numerieke modellen die ijs geïnduceerde trillingen simuleren nog niet gevalideerd worden. Daarnaast zijn inzichten uit experimenten op kleine schaal beperkt, omdat deze experimenten andere ijsfaalmechanismen opleverden dan die in werkelijkheid werden waargenomen.

Het doel van dit proefschrift was daarom om een benchmark dataset van modelschaal offshore windturbines die ijs geïnduceerde trillingen ondergaan te genereren en te analyseren. Het hoofddoel was om het model ijs zo aan te passen dat toepassing van de schaalmethode op constructies waar metingen uit het veld beschikbaar van zijn zou leiden tot gelijke observaties in de ijstank. Daarnaast was het doel om de experimentele bevindingen te vergelijken met die uit een state-of-the-art numeriek model en daarmee de gevolgen voor het ontwerp van offshore windturbines bedoelt voor koude gebieden.

Om dit doel te bereiken is een schalingsmethode ontwikkeld waarmee offshore windturbines in modelijsexperimenten konden worden onderzocht. De methode was gebaseerd op de aanname dat ijs geïnduceerde trillingen voornamelijk gebaseerd zijn op het falen van het ijs, het gemiddelde ijs belastingsniveau en de tijd- en snelheidsafhankelijke eigenschappen van het ijs. Er werd een koud modelijs ontwikkeld dat hetzelfde snelheidsafhankelijke gedrag vertoonde als zeeijs en dat bij de test tot breuk leidde. De offshore-constructies werden geschaald voor een verhouding tussen de gemeten gemiddelde ijsbelasting van het model en de geschatte gemiddelde ijs belasting voor een overeenkomstig scenario op ware grootte. Het toepassen van de schaling resulteerde in amplitudes en frequenties van de constructierespons op ware grootte. Hierbij zijn praktische beperkingen bij het testen van constructies met een lage eigenfrequentie (bijvoorbeeld 0.15 Hz voor een offshore windturbine) overwonnen door het innovatieve gebruik van real-time hybride simulaties in ijs.

Real-time hybride simulaties zijn gebaseerd op de substructureringstechniek, die het mogelijk maakt om de structurele interface onder belasting los te koppelen van de volledige constructie. In dit proefschrift werd alleen de structurele interface in contact met het ijs fysiek getest, terwijl het volledige structuurmodel numeriek werd geïmplementeerd. De gemeten ijsbelastingen tijdens de experimenten konden dus worden gebruikt om de volledige constructierespons numeriek op te lossen, die uiteindelijk in real-time werd opgelegd door twee elektrische actuatoren.

De resultaten van deze real-time hybride simulaties onthulden de ontwikkeling van multi-modale ijs geïnduceerde trillingen van een offshore windturbine onder dynamische ijsbelasting. In totaal werden vier soorten trillingen waargenomen: intermittent crushing, multi-modal interaction-I, multi-modal interaction-II (ook wel bekend als frequency-lock-in), en continuous brittle crushing. Verhoogde aerodynamische demping en door wind veroorzaakte verplaatsingen beïnvloedden de kenmerken van ijs geïnduceerde trillingen, maar veranderen deze niet significant. Experimenten voor scenario's met niet-uitgelijnde wind-ijs belasting toonden het effect van lage aerodynamische demping in de richting van ijsbelasting op de ontwikkeling van deze trillingen, en lieten zien dat door wind veroorzaakte verplaatsingen werden beperkt door het ijs.

Vergelijking van de experimentele en numerieke resultaten laat zien dat het bestaande model de interactie voldoende accurraat beschrijft. Het effect van de inklemming van de constructie door het ijs in de richting loodrecht op die van beweging van het ijs moet echter worden toegevoegd om een goede inschatting van de vermoeiing van het materiaal te krijgen onder ijsbelasting. Verder onderzoek toonde aan dat maximale buigmomenten in de constructie verband houden met de ontwikkeling van multi-modale interactieregimes. De multi-modale interacties worden op dit moment niet erkend in ontwerpstandaarden en methoden die gebaseerd zijn op observaties van bestaande constructies anders dan offshore wind turbines. Een vergelijking tussen volledig gekoppelde en sequentiële simulaties toonde aan dat deze laatste moeite hadden met het nauwkeurig simuleren van (ontwerp-gedreven) multi-modale ijs-structuur interactieregimes.

LIST OF PUBLICATIONS

JOURNAL PUBLICATIONS

1. **Hammer**, **T. C.**, Willems, T., & Hendrikse, H. (2023). Dynamic ice loads for offshore wind support structure design. *Marine Structures*, *87*, 1–19. https://doi.org/10.1016/j.marstruc.2022.103335
2. **Hammer**, **T. C.**, & Hendrikse, H. (2023b). Experimental study into the effect of wind-ice misalignment on the development of ice-induced vibrations of offshore wind turbines. *Engineering Structures*, *286*, 1–17. https://doi.org/10.1016/j.engstruct.2023.116106
3. **Hammer**, **T. C.**, Puolakka, O., & Hendrikse, H. (2024). Scaling ice-induced vibrations by combining replica modeling and preservation of kinematics. *Cold Regions Science and Technology*, *220*(January), 104127. https://doi.org/10.1016/j.coldregions.2024.104127
4. **Hammer**, **T. C.**, & Hendrikse, H. (2024b). Hardware-in-the-Loop experiments in model ice for analysis of ice-induced vibrations of offshore structures. *Scientific Reports*, 1–17. https://doi.org/10.1038/s41598-024-68955-x
5. Hendrikse, H., **Hammer**, **T. C.**, Berg, M. v. d., Willems, T., Owen, C. C., van Beek, K., Ebben, N. J., Puolakka, O., & Polojärvi, A. (2022a). Experimental data from ice basin tests with vertically sided cylindrical structures. *Data in Brief*, *41*, 1–18. https://doi.org/10.1016/j.dib.2022.107877
6. Owen, C. C., **Hammer**, **T. C.**, & Hendrikse, H. (2023b). Peak loads during dynamic ice-structure interaction caused by rapid ice strengthening at near-zero relative velocity. *Cold Regions Science and Technology*, *211*(January), 103864. https://doi.org/10.1016/j.coldregions.2023.103864
7. Owen, C. C., **Hammer**, **T. C.**, & Hendrikse, H. (2023a). Hysteresis and dichotomous mechanics in cyclic crushing failure of confined freshwater columnar ice. *Cold Regions Science and Technology*, *209*, 1–18. https://doi.org/10.1016/j.coldregions.2023.103816

CONFERENCE PUBLICATIONS

1. **Hammer**, **T. C.**, Beek, K. V., Koning, J., & Hendrikse, H. (2021). A 2D test setup for scaled real-time hybrid tests of dynamic ice- structure interaction. *Proceedings of the 26th International Conference on Port and Ocean Engineering under Arctic Conditions*, 1–13
2. **Hammer**, **T. C.**, Owen, C. C., van den Berg, M., & Hendrikse, H. (2022). Classification of ice-induced vibration regimes of offshore wind turbines. *Proceedings of the ASME 2022 41st International Conference on Ocean, Offshore and Arctic Engineering*, 1–8. https://doi.org/10.1115/OMAE2022-78972
3. **Hammer**, **T. C.**, & Hendrikse, H. (2023c). On the dependency of the development of frequency lock-in on the mode shape amplitude for higher structural modes. *Proceedings of the 27th International Conference on Port and Ocean Engineering under Arctic Conditions*

4. Hendrikse, H., **Hammer**, **T. C.**, Owen, C. C., Puolakka, O., & Willems, T. (2022b). Ice basin tests for ice-induced vibrations of offshore structures in the SHIVER project. *Proceedings of the ASME 2022 41st International Conference on Ocean, Offshore and Arctic Engineering*, 1–9. https://doi.org/10.1115/OMAE2022-78507

5. Petry, A., **Hammer**, **T. C.**, Hendrikse, H., & Puolakka, O. (2023). Ice basin experiments on mixed-mode failure on ice cones. *Proceedings of the 27th International Conference on Port and Ocean Engineering under Arctic Conditions*

6. Owen, C. C., **Hammer**, **T. C.**, & Hendrikse, H. (2022). Test setup for compressive loading of confined ice thick sections viewed with in-situ cross-polarization imaging. *Proceeding of the 26th IAHR International Symposium on Ice*, (July), 1–10

7. Hornnes, V., **Hammer**, **T. C.**, Høyland, K. V., & Hendrikse, H. (2022). On the use of drift ice thickness statistics from a Copernicus reanalysis product for fatigue damage calculation. *In Proceedings of the 26th IAHR International Symposium on Ice*, (June), 1–11

8. Høyland, K. V., Nord, T., Turner, J., Hornnes, V., Gedikli, E. D., Bjerkås, M., Hendrikse, H., **Hammer**, **T. C.**, Ziemer, G., Stange, T., Ehlers, S., Braun, M., Willems, T., & Fischer, C. (2021). Fatigue damage from dynamic ice action - the FATICE project. *Proceedings of the 26th International Conference on Port and Ocean Engineering under Arctic Conditions*

CURRICULUM VITAE

Tim Christopher Hammer

16-04-1994 Born in Flensburg, Germany

EDUCATION

2013–2017 Bachelor of Science
Civil- and Environmental Engineering
Leibniz University Hannover
Faculty of Civil Engineering and Geodetic Science
Ludwig Franzius Institute of Hydraulic, Estuarine and Coastal Engineering

2016–2019 Master of Science (with distinction)
Water Management, Environmental and Coastal engineering
Leibniz University Hannover
Faculty of Civil Engineering and Geodetic Science
Ludwig Franzius Institute of Hydraulic, Estuarine and Coastal Engineering

2020–2024 Doctor of Philosophy Research
Ice-induced vibrations of offshore wind turbines
Delft University of Technology
Faculty of Civil Engineering and Geosciences
Section of Offshore Engineering